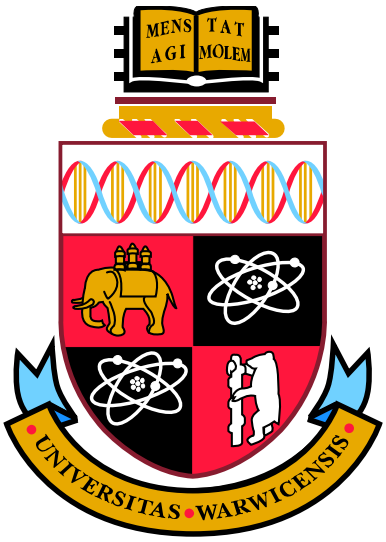

Magnetic resonance studies of point defects in diamond

by

Bradley Lyall Cann

Thesis

Submitted to the University of Warwick

for the degree of

Doctor of Philosophy

Department of Physics

July 2009

THE UNIVERSITY OF WARWICK

Contents

List of Tables **ix**

List of Figures **xi**

Acknowledgments **xv**

Declaration and published work **xvii**

Abstract **xxi**

Glossary and abbreviations **xxiii**

Chapter 1 Introduction **1**

1.1 History of Diamond 1

1.2 Natural diamond formation 2

1.3 Diamond Structure 2

1.4 Defects and Impurities 3

1.4.1 Diamond Classification 4

1.5 Synthetic diamond 6

1.6 Diamond properties and its uses 6

1.7 EPR in the study of Diamond 7

1.8 Thesis outline 8

References 10

Chapter 2 Literature review **13**

2.1 Hybridisation of carbon 13

2.2 Synthetic diamond 14

2.2.1 High pressure high temperature diamond synthesis 14

2.2.2 Chemical vapour deposition diamond synthesis 16

2.3 Nitrogen-related defects 19

2.3.1 Single substitutional nitrogen 19

2.3.2 The nitrogen-vacancy centre 20
2.4 Hydrogen in diamond 21
2.4.1 The vacancy-hydrogen complex 21
2.4.2 The nitrogen-vacancy-hydrogen complex 22
2.5 Vacancy clusters 24
References 26

Chapter 3 Theory **29**
3.1 Overview 29
3.2 EPR - A historical perspective 30
3.3 EPR theory 31
3.3.1 Zero-field interaction 33
3.3.2 Dipolar interaction 34
3.3.3 The spin Hamiltonian 36
3.3.3.1 Nuclear Zeeman interaction 36
3.3.3.2 Hyperfine interaction 37
3.3.3.2.1 Isotropic hyperfine interaction 37
3.3.3.2.2 Anisotropic hyperfine interaction 37
3.3.3.3 Quadrupole interaction 38
3.3.4 Transition probabilities 39
3.3.5 Relaxation 40
3.3.5.1 The Bloch model 40
3.3.6 Rapid passage 41
3.4 Symmetry 42
3.5 Annealing 46
3.5.1 First order reaction 47
3.5.2 Second order reaction 47
3.5.3 Experimental methods 48
References 49

Chapter 4 Experimental details **51**
4.1 The electron paramagnetic resonance spectrometer 51
4.1.1 The external magnetic field 51

4.1.2 The microwave source . . . 52
4.1.3 Detection of the EPR signal . . . 54
4.1.3.1 Automatic frequency control (AFC) . . . 55
4.1.4 EPR spectrometer detail . . . 55
4.1.5 Resonant cavities . . . 56
4.1.5.1 Quality factor . . . 56
4.1.5.2 E and B field components of the microwave radiation 57
4.1.6 Quantitative EPR . . . 58
4.1.7 Variable temperature EPR . . . 59
4.1.7.1 Optical illumination . . . 61
4.2 Annealing . . . 61
References . . . 63

Chapter 5 Quantitative rapid passage EPR 65
5.1 Overview . . . 65
5.1.1 Historical review . . . 66
5.1.2 Detection limits . . . 66
5.1.3 Rapid passage . . . 67
5.1.4 Theoretical description of RP-EPR . . . 68
5.2 Experimental details . . . 68
5.3 Results . . . 70
5.3.0.1 Detection limits . . . 73
5.4 Discussion . . . 75
5.5 Conclusions and further work . . . 76
References . . . 78

Chapter 6 Charge transfer and trapping in nitrogen doped CVD diamond 79
6.1 Overview . . . 79
6.1.1 Examples of charge transfer . . . 80
6.1.2 Mechanisms . . . 82
6.1.3 Chapter aims . . . 84
6.2 Experimental . . . 84

6.2.1 Samples . . . 85
6.3 Results . . . 86
6.3.1 Variation in N_S^0 . . . 86
6.3.2 Variation in NVH^- . . . 89
6.3.3 Other contributing defects . . . 92
6.3.4 Illumination . . . 93
6.3.5 Thermo-chromic and visual variations . . . 94
6.3.6 The 3123 cm^{-1} absorption line and the NVH defect . . . 97
6.3.7 Additional IR features . . . 100
6.4 Discussion . . . 101
6.4.1 Other contributing defects . . . 104
6.4.2 The 3123 cm^{-1} absorption line . . . 104
6.5 Conclusion . . . 105
References . . . 107

Chapter 7 A preferentially aligned defect in CVD diamond 109
7.1 Overview . . . 109
7.1.1 Hydrogen in diamond . . . 109
7.1.2 CVD Diamond growth . . . 109
7.1.2.1 Mono-hydride dimer model . . . 110
7.1.3 Preferentially aligned defects in diamond . . . 110
7.2 Experimental details . . . 112
7.2.1 CVD growth conditions . . . 112
7.2.2 Experimental apparatus . . . 113
7.3 Results . . . 113
7.3.1 Samples and defect concentrations . . . 113
7.3.2 EPR - WAR2 characterisation . . . 115
7.3.3 EPR high resolution . . . 119
7.3.4 High temperature annealing . . . 122
7.3.5 Heat treatment . . . 125
7.3.5.1 Sample A . . . 125
7.3.5.2 Sample C . . . 128
7.3.5.3 Samples B and H . . . 128

7.3.6 Supporting data 130
7.4 Discussion 130
7.4.1 Charge state 131
7.4.1.1 Temperature Region 1 in Sample A 131
7.4.1.2 Temperature Region 2 in Sample A 132
7.4.1.3 Temperature Region 3 in Sample A 132
7.4.1.4 Dual sector model - inhomogeneous distribution of defects 133
7.4.1.5 Samples B, C and H 133
7.5 Proposed model for WAR2: (V-(CH)-V)^0 135
7.5.1 Potential incorporation mechanism 139
7.5.2 The stability of (V-(CH)-V)^0 140
7.6 Conclusion 140
7.7 Further work 141
References 142

Chapter 8 Nitrogen Interstitial 145
8.1 Overview 145
8.2 Experimental 150
8.3 Results 152
8.3.1 EPR measurements 152
8.3.1.1 Optical 157
8.4 Discussion 159
8.4.1 WAR9 model 162
8.4.1.1 WAR10 model 163
8.5 Conclusion 165
References 166

Chapter 9 WAR5 169
9.1 Overview 169
9.1.1 Effect of oxygen on CVD growth 169
9.1.2 Oxygen related defects 171
9.1.2.1 OV^0 versus NV$^-$ 172

9.2 Experimental 177
9.3 Results 177
9.3.1 EPR - WAR5 defect 177
9.3.2 WAR5 ^{13}C hyperfine satellites 178
9.3.3 Photoluminescence 184
9.4 Discussion 184
9.4.1 Comparison of the OV^0 to the NV^- defect 186
9.4.2 WAR5 ^{13}C hyperfine satellites 187
9.5 Conclusion and further work 190
References 192

Chapter 10 V_nH^- ^{13}C satellites **195**
10.1 Overview 195
10.2 Results 196
10.3 Discussion 198
10.4 Conclusion and further work 201
References 202

Chapter 11 Summary **203**
11.1 Identification and characterisation 203
11.1.1 Defects in nitrogen doped HPHT diamond 203
11.1.2 Defects in diamond grown by CVD 204
11.2 Charge transfer 205
11.3 Sub ppb EPR detection of N_S^0 205
References 207

Appendix A Samples **209**

List of Tables

1-1 Classification of diamond, by nitrogen content 4

3-1 Point group nomenclature given by the Schoenflies notation 43

4-1 Frequency bands commonly used in EPR 53

4-2 Names and descriptions of EPR resonant cavities used in this Thesis. . . 57

5-1 Samples used in this Chapter for the quantitative investigation of RP-EPR. 69

5-2 Optimum RP-EPR conditions determined for two different spectrometer configurations (see Section 4.1.4), compared to typical SP-EPR conditions. 70

6-1 Previously published examples of charge transfer work 83

6-2 Defect concentrations determined for samples used in the charge transfer study 86

6-3 Determined activation energies and final concentrations for charge transfer resulting from heat treatment 90

6-4 Defect concentrations and absorption intensities determined from UV-Vis absorption, before and after heat treatment 94

7-1 Samples observed to contain the WAR2 defect 113

7-2 Spin Hamiltonian parameters determined for WAR2 121

8-1 Concentrations of defects observed in Sample P 154

8-2 The spin Hamiltonian parameters for the ^{15}N, WAR9 and WAR10 defects 157

9-1 Defect concentrations in samples which contain WAR5 178

9-2 Spin Hamiltonian parameters for the WAR5 defect compared to those of V_nH^- and NV^- 180

9-3 WAR5 ^{13}C hyperfine parameters 182

9-4 Calculated ^{13}C hyperfine parameters for the nearest neighbour carbon atoms, labelled as in the literature 183

10-1 ^{13}C hyperfine parameters for the V_nH^- defect 199

A-1 Table of sample used in this work, see relevant chapter for defect concentrations. Mass is given to the nearest mg and the diamond type as synthetic CVD or HPHT. 209

List of Figures

1-1 The diamond unit cell 3

2-1 The formation of sp^2 and sp^3 orbitals 14
2-2 A belt HPHT cell 15
2-3 The sectors of a HPHT synthetic diamond 16
2-4 A schematic of a typical microwave plasma CVD reactor 17
2-5 Cartoon depictions of the V_nH^- defect in diamond 23

3-1 Graphical depiction of the swept external magnetic field 32
3-2 An energy level diagram of a system with $S = 1$, displaying a zero field interaction 34
3-3 Graphical description of symmetry operations key to defects in diamond 43
3-4 $^{14}N_S^0$ simulated spectra at principal orientations 45
3-5 Four possible occupation sites for N_S^0 45

4-1 Block diagram of the EMX Bruker spectrometer 54
4-2 Graphical representation absorption 55
4-3 Labelled photographs of super high Q and high temperature cavities . . . 57
4-4 Graphical description of the magnetic and electric field lines in a TE_{011} cavity 58
4-5 Ramp up and down rates of the high temperature cavity 60
4-6 Labelled diagram of the 'Elite' tube furnace 62

5-1 Variation in signal strength with microwave power attenuation in the SHQ cavity. 71
5-2 Signal-to-noise ratio comparison between SP-EPR and RP-EPR 72
5-3 Variation in rapid passage signal intensity with N_S^0 concentration from a single sample in the high temperature cavity. 73
5-4 Rapid passage integrated intensity versus $[N_S^0]$ over a range of samples . . 74
5-5 Variation of the signal-to-noise ratio from rapid passage with $[N_S^0]$ after 40,000 scans 74

6-1 Schematic of riser and terrace growth during CVD diamond 84
6-2 Variation of $[N_S^0]$ with isochronal heat treatment 87
6-3 Normalised variation of $[N_S^0]$ with isochronal heat treatment 87
6-4 First versus mixed order fits to isochronal heat treatment of Sample A . 88
6-5 Variation in the concentration of NVH^- with isochronal heat treatment . 91
6-6 Variation of defect concentrations in Sample J with isochronal heat treatment 93
6-7 Variation of $[N_S^0]$ in Sample A, after heat treatment, with illumination wavelength 95
6-8 Thermoluminescence glow curves versus $[N_S^0]$ isochronal variations 96
6-9 Images of samples H and J post-illumination and heat treatment 97
6-10 FTIR absorption spectra of Sample J before and after 850 K heat treatment 98
6-11 Variation in concentration of NVH^-, and the integrated absorption of the $3123\,cm^{-1}$ line, with increasing heat treatment temperature 99
6-12 The $3123\,cm^{-1}$ integrated absorption versus ΔNVH^- 99
6-13 The $3123\,cm^{-1}$ integrated intensity (FTIR) versus the NVH^0 (EPR) . . . 100
6-14 Isochronal variation in integrated intensity of 7354, 6857 and $6426\,cm^{-1}$ lines 101
6-15 Model for the change in concentration of acceptors 103
6-16 Model for the photo-excitation of charge from the defect, X_1, to N_S^+ . . . 103

7-1 A (001) mono-hydride reconstructed surface 111
7-2 Picture of Sample A 114
7-3 Pictures and diamond view images of Sample B 114
7-4 Pictures and diamond view images of Sample D 115
7-5 Comparison of slow and rapid passage scans of Sample B to disentangle defect spectra 116
7-6 Cartoon of a sample showing roadmap rotation planes 116
7-7 Roadmaps of the WAR2 defect at X-band 118
7-8 Roadmap of the WAR2 defect at Q-band 119
7-9 Cartoon energy level diagram of the WAR2 defect at X and Q-band . . . 120
7-10 Isochronal variation in defect concentrations in Sample A 121
7-11 Roadmap after heat treatment, indicating a lowering of symmetry to C_2 122
7-12 Comparison of C_2 and C_{2v} simulated spectra to experimental data 123
7-13 Cartoon describing the interactions of the WAR2 defect 123

7-14 Isothermal annealing decay curves of WAR2 124
7-15 Sample A. Fit to isochronal decay of $[N_S^0]$, [WAR2] and $[V_nH^-]$ with heat-treatment 126
7-16 Sample A. An example isothermal decay curve and the resulting N_S^0 Arrhenius plot 127
7-17 Sample C. Fit to isochronal decay of $[N_S^0]$, [WAR2] and $[V_nH^-]$ with heat- treatment 129
7-18 band-gap cartoon showing the suggested charge transfer processes 131
7-19 Potential defect concentrations in separate sectors in Sample A 134
7-20 (V-(CH)-V) model suggestion for WAR2 in an unreconstructed form . . . 136
7-21 (V-(CH)-V) model suggestion for WAR2 in an reconstructed form 137
7-22 Potential surface defect giving rise to the (V-(CH)-V) defect 138

8-1 Model of the nitrogen-split interstitial, N_I 148
8-2 Model of the nitrogen di-interstitial, (N_I-I_{001}) 149
8-3 EPR spectrum of Sample P after irradiation 151
8-4 Sample P after irradiation and annealing. Two sectors are simulated . . . 153
8-5 Picture of Sample P 154
8-6 Spectrum simplification of the $g \approx 2.00$ region resulting from simulating $^{14}N_S^0$ 155
8-7 Experimental spectra from Sample P in the $\{1\bar{1}0\}$ plane 156
8-8 Comparison of experiential data and simulated WAR9 and WAR10 spectra at X-band 158
8-9 Q-band EPR spectra, peak positions and the resulting roadmaps of WAR9 and WAR10 159
8-10 Simulated X-band spectrum for a non-isotopically enriched sample 160
8-11 Q-band experimental and simulated spectrum for WAR9, WAR10 and $^{14}N_S^0$, showing that a hyperfine interaction is required to describe the observed WAR10 spectra 161

9-1 Simplified Bachmann diagram 170
9-2 Cartoon depiction of the NV^- and OV^0 defects in diamond 173
9-3 Depiction of the energy states of a T_d and C_{3v} defect 174
9-4 Depiction of the energy levels of the NV^- and OV^0 defects 175

9-5 Half and full-field X-band roadmaps generated from Sample J in the $(1\bar{1}0)$ plane 179
9-6 Half field experimental and simulated spectra of the WAR5 defect and ^{13}C satellites 181
9-7 Full-field experimental and simulated spectra of the WAR5 defect and WAR5 ^{13}C satellites with the external magnetic field aligned parallel to $\langle 111 \rangle$ 183
9-8 PL spectrum of Sample J at 77 K 184
9-9 Cartoon depiction of the VO^0 defect in diamond and the surrounding lattice that will give rise to ^{13}C transitions 188

10-1 Half field experimental and simulated spectrum of the V_nH^- defect and ^{13}C satellites 197
10-2 Cartoon depictions of the V_nH^- defect in diamond and surrounding ^{13}C . 200

Acknowledgments

I would like to thank Dr. Mark Newton for his help, guidance and patience throughout my PhD.

The supporting cast of the Warwick Diamond Group each have helped invaluably with the completion of this work, I would like to thank all of them. Andy for his general wizardry, Solveig for her many explanations and patience, Steph for her cooking and squeezing, Bianca for not throwing anything too hard at me, Robin for his encouragement and enthusiasm, Ulrika for taking up the 'noise collection' and Chris for his wise words.

The extended Warwick diamond group family of Prof. Michael Baker and Dr. Jim Butler have proved invaluable in the formulation of defect models and interpretation of EPR data.

Staff at the DTC Research Centre and Element Six Ltd. are thanked for the provision of many interesting samples. In particular Dr. Riz Kahn, Dr. Philip Martineau, Dr. David Fisher and Dr. Daniel Twitchen are thanked for exuding enthusiasm to different parts of the work, and helping to paint the 'bigger picture' when morale was low.

External collaborators are thanked for their input to this work. The staff and students at both IMOMEC and LIMIP are thanked for the provision of samples and Dr. Jon Goss and Prof. Bob Jones for their theoretical input.

I thank Becca for being a source of constant love and support, seeming able to put up with any 'disaster'.

Finally I would like to thank my parents for continuing to look out for their 'eternal student' and Matt for keeping me company for four of my years at Warwick.

Declaration and published work

I declare that the work presented in this Thesis is my own except where stated, and was carried out entirely at the University of Warwick, during the period of September 2005 to June 2009, under the supervision of Dr. M. E. Newton. The research reported here has not been submitted, either wholly or in part, in this or any other academic institution for admission to a higher degree.

Some parts of the work reported and other work not reported in this Thesis have been published, as listed below:

Published papers

[1] R. U. A. Khan, P. Martineau, B. L. Cann, M. E. Newton, and D. J. Twitchen, J. Phys. C Solid State **21**, 364214 (2009).

[2] S. Felton, B. L. Cann, A. M. Edmonds, S. Liggins, R. J. Cruddace, M. E. Newton, D. Fisher, and J. M. Baker, J. Phys. Condens. Matter **21**, 364212 (2009).

Conference presentations

[1] B. L. Cann, A. M. Edmonds, S. Felton, M. E. Newton, P. M. Martineau, and D. J. Twitchen, *Lowering quantitative detection limits in EPR*, The 58$^{\text{th}}$ Diamond Conference, Warwick, poster presentation (2007).

[2] B. L. Cann, U. F. S. D'Haenens-Johansson, S. Felton, A. M. Edmonds, R. J. Cruddace, H. Newton, M. E. Murphy, J. Dodson, and D. J. Twitchen, *A reliable method for the detection of < 1 ppb single substitutional nitrogen in single crystal CVD diamond*, The 60$^{\text{th}}$ Diamond Conference, Warwick, poster presentation (2009).

[3] B. L. Cann, M. E. Newton, J. M. Baker, P. M. Martineau, R. U. A. Khan, and D. J. Twitchen, *An investigation of charge trapping in CVD diamond*, The 59$^{\text{th}}$ Diamond Conference, Oxford, oral presentation (2008).

[4] B. L. Cann, M. E. Newton, J. M. Baker, P. M. Martineau, and D. J. Twitchen, *An investigation of charge trapping in CVD diamond*, SBDD XIII, Hasselt (Belgium), oral presentation (2008).

[5] R. U. A. Khan, P. M. Martineau, B. L. Cann, M. E. Newton, and D. J. Twitchen, *Charge-transfer effects, photo- and thermochroism in single crystal CVD synthetic diamond*, The 60$^{\text{th}}$ Diamond Conference, Warwick, oral presentation by R. U. A. Khan (2009).

[6] S. Liggins, B. L. Cann, and M. E. Newton, *Assignment of the 3123 cm^{-1} absorption line to the NVH^0 centre*, The 60$^{\text{th}}$ Diamond Conference, Warwick, poster presentation by S. Liggins (2009).

[7] B. L. Cann, A. M. Edmonds, S. Felton, M. E. Newton, P. M. Martineau, J. M. Baker, and D. J. Twitchen, *EPR studies of a point defect grown into* {100} *single crystal CVD diamond with a preferred orientation*, The 58$^{\text{th}}$ Diamond Conference, Warwick, oral presentation (2007).

[8] B. L. Cann, A. M. Edmonds, S. Felton, M. E. Newton, J. M. Baker, K. Haenen, J. Achard, F. Silva, A. Gicquel, P. M. Martineau, et al., *Investigating the structure of a preferentially oriented hydrogen related defect in CVD diamond*, SBDD XIII, Hasselt (Belgium), poster presentation (2008).

[9] B. L. Cann, S. Felton, M. E. Newton, J. M. Baker, P. M. Martineau, and D. J. Twitchen, *Lowered symmetry of the WAR2 defect*, The 59$^{\text{th}}$ Diamond Conference, Oxford, poster presentation (2008).

[10] B. L. Cann, S. Felton, M. E. Newton, J. M. Baker, P. M. Martineau, and D. J. Twitchen, *Lowered symmetry of the WAR2 defect*, Frontiers of Magnetic Resonance Conference, Warwick, poster presentation (2008).

[11] S. Felton, B. L. Cann, R. J. Cruddace, M. E. Newton, and D. Fisher, *EPR measurements on the g=2.00 region of HPHT ^{15}N doped diamond*, The 57$^{\text{th}}$ Diamond Conference, Cambridge, poster presentation by S. Felton (2006).

[12] S. Felton, B. L. Cann, S. Liggins, R. J. Cruddace, A. M. Edmonds, M. E. Newton, D. Fisher, J. M. Baker, and J. E. Butler, *Identification of interstitial nitrogen defects in diamond*, 19th European Conference on Diamond, Diamond-Like Materials, Carbon Nanotubes, and Nitrides, Sitges, oral presentation by S. Felton (2008).

[13] S. Liggins, S. Felton, B. L. Cann, R. J. Cruddace, A. M. Edmonds, M. E. Newton, D. Fisher, J. M. Baker, and J. E. Butler, *Identification of interstitial nitrogen defects in diamond*, The 60$^{\text{th}}$ Diamond Conference, Warwick, oral presentation by S. Liggins (2009).

[14] S. Felton, B. Cann, and M. E. Newton, *EPR measurements on a new S=1 defect in diamond*, The 59$^{\text{th}}$ Diamond Conference, Oxford, oral presentation by S. Felton (2008).

[15] S. Felton, B. L. Cann, M. E. Newton, J. M. Baker, P. M. Martineau, and D. J. Twitchen, *EPR studies of vacancy-hydrogen centres in diamond*, The 59$^{\text{th}}$ Diamond Conference, Oxford, poster presentation by S. Felton (2008).

[16] S. Felton, B. L. Cann, M. E. Newton, J. M. Baker, P. M. Martineau, and D. J. Twitchen, *EPR studies of vacancy-hydrogen centres in diamond*, Frontiers of Magnetic Resonance Conference, Warwick, poster presentation by S. Felton (2008).

B. L. Cann

July 2009

Abstract

Electron paramagnetic resonance (EPR) has been used to study point defects in synthetic single crystal diamond. Newly observed defects are reported in high pressure high temperature (HPHT) and chemical vapour deposition (CVD) diamond.

HPHT diamond doped with ^{15}N has been used to investigate the g = 2 region of the EPR spectrum which is obscured when natural isotopic abundances are present. Two previously unreported defects labelled WAR9 and WAR10 are reported. The EPR data has been shown to be consistent with the neutral nitrogen interstitial, N_I^0 (WAR9), and neutral nitrogen di-interstitial, N_I-I_{001} (WAR10), defects respectively.

Two further defects observed in CVD diamond are reported here. The first labelled WAR2 is preferentially aligned with the direction of growth, [001]. The EPR data is consistent with a (V-(CH)-V)^0 structure although theoretical studies suggest that this structure is unstable at CVD growth temperatures. Growth mechanisms are suggested that would account for the observed preferential alignment. The second defect labelled WAR5, has been observed exclusively in samples grown using an experimental CVD chemistry containing oxygen. The EPR data is consistent with the OV^0 defect, although no confirming ^{17}O hyperfine structure has been observed. ^{13}C hyperfine data is also reported for the KUL1/V_nH^- defect (n = 1 or 2) but the new data is not sufficient to conclusively discount either the n = 1 or n = 2 models suggested for this defect.

Changes in defect concentrations in CVD diamond with thermal and illumination treatments has been investigated. Experimental data has indicated the presence of an unseen trap, common to CVD diamond, with concentrations comparable to that of N_S^0, and levels in the band-gap 0.5–1.2 eV above the top of the valence band.

The difficult quantification of sub part per billion defect concentrations, as observed in electronic grade material, is tackled with the use of rapid passage EPR. It is shown that with this technique it is possible to detect concentrations of single nitrogen in diamond at tens of parts per trillion, close to a factor of 100 improvement on the currently used slow passage EPR.

Glossary and abbreviations

A	Hyperfine interaction term
AFC	Automatic frequency control
B_0	Externally applied magnetic field
B_m	Magnetic field modulation amplitude
B_1	Magnetic field component of microwave radiation
CVD	Chemical vapour deposition
CL	Cathodoluminescence
CT	Conversion time
CW	Continuous wave
D	Zero-field interaction term
DFT	Density functional theory
E	Activation energy
EPR	Electron paramagnetic resonance
FTIR	Fourier transform infra-red spectroscopy
g_e	g value for the free-electron
g_N	Nuclear g value
$\mathscr{H}$	Spin Hamiltonian term(s)
HPHT	High-pressure high-temperature
HT	High temperature
HQ	High quality
I	Nuclear spin
II	Integrated intensity
I_{001}	$\langle 001 \rangle$–split self interstitial
k_B	Boltzmann constant
K	Decay rate
L	Orbital angular momentum
LT	Low temperature

M_S	Projection of electron spin (S) on z-axis
m_I	Projection of nuclear spin (I) on z-axis
m_e	Mass of electron
N_S	Substitutional nitrogen defect
M	Magnetisation
NIR	Near infra-red
N_I	interstitial nitrogen
N_I-I_{001}	nitrogen di-interstitial
N_{2I}	di-nitrogen interstitial
NV	Nitrogen-vacancy defect
NVH	Nitrogen-vacancy-hydrogen defect
P	Quadrupole interaction term
$P_{\mu w}$	Microwave power
PAS	Positron annihilation spectroscopy
PL	Photoluminescence
ppm	Parts per million carbon atoms
ppb	Parts per billion carbon atoms
PSD	Phase sensitive detection
q	Tsallis lineshape parameter
Q	Quality factor
RP	Rapid passage
SP	Slow passage
S	Electronic spin
SC-CVD	Single crystal diamond grown by chemical vapour deposition
SHQ	Super high quality
SIMS	Secondary ion mass spectroscopy
T	Temperature
TC	Time constant
TL	Thermoluminescence
$\mathbf{T}$	Anisotropic hyperfine matrix
TEM	Transmission electron microscopy

TM	Transverse magnetic
TE	Transverse electric
τ_1	Spin-lattice relaxation time
τ_2	Spin-spin relaxation time
UV	Ultra-violet
V	Isolated vacancy
V_nH	('n' Vacancies)-hydrogen defect
V-(CH)-V	Carbon-hydrogen di-vacancy
OV	Oxygen-vacancy defect
ZPL	Zero phonon line

γ_e	Gyromagnetic ratio
θ/ϕ	Angle
λ_{so}	Russell-Saunders spin-orbit coupling term
Λ	Spin orbit coupling matrix
μ	Magnetic dipole
μ_B	Bohr magneton
μ_N	Nuclear magneton
ν	Microwave frequency
ν_{res}	Resonant frequency
υ_0	Characteristic attempt frequency
ω_0	Lamour frequency
χ^2	Chi squared value (fit quality)

$\langle hkl \rangle$	A general hkl direction
$[hkl]$	A specific hkl direction
$\{hkl\}$	A general hkl plane
(hkl)	A specific hkl plane

Chapter 1

Introduction

In 1502 Leonardus suggested that diamond was a reliable cure for lunacy...
I am tempted to believe the contrary. [1]

1.1 History of Diamond

Since its discovery, diamond has been of interest to humanity due to its rarity, beauty and durability [2]. The name diamond derives from the Greek 'adamas' meaning 'the untameable'. The earliest record of diamond is from 1000 BC [2, 3] and ever since it has been sought after by rulers and historians alike.

In 1772 when it was found that diamond is composed of carbon, the sixth most common element in the universe, there was great surprise [2]. However, this has not detracted from its popularity and use in both commercial and industrial applications.

Many of the extreme properties of diamond, such as its durability and incompressibility are directly attributable to its structure. These properties have been recognised and exploited since Biblical times, where 'a pen of iron and a tip of diamond' is mentioned in Exodus XXVIII.18 and XXXIX.11 [3]. Furthermore, in the first detailed pseudo-scientific account of diamond, Pliny (AD23-AD79) [4] commented on the 'toughness' of diamond, although diamond is not considered tough by current definitions.

The exploitation of diamond's extreme properties is of great interest to both scientists and engineers. Interesting properties of diamond include very high thermal heat conductivity, high carrier mobility, extreme hardness, durability, an unreactive nature and optical transparency. It is in particular the combination of these properties that invites keen attention.

Whilst diamond has numerous industrial uses, it is most commonly considered

as a gemstone for jewellery. Historically, diamonds were worn by males as a 'magic amulet' to give them courage and were used as religious icons in ancient India [2]. The most frequent use of diamond in jewellery is in engagement and eternity rings as a symbol of commitment. The perception of diamond as a symbol of commitment and eternity has been strengthened through clever promotions by the major diamond distributor, De Beers. The marketing campaign, which famously declared 'a diamond is forever', first appeared in the mid-20th century and is still synonymous with diamond today [5]. This successful marketing has assisted the generation of a $62 billion per year gem stone market [6].

1.2 Natural diamond formation

For the formation of natural diamond the carbon source must be in the diamond-stable region of the phase diagram [7]. For natural diamond synthesis pressures are between 4.5 and 6 GPa and temperatures between 1200 and 1600 K. These conditions are found in the lithospheric mantle below relatively stable continental plates, one to two hundred kilometers below the surface. Diamonds are brought to the surface via deep volcanic eruptions and found in volcanic pipes. A good discussion of this process is given by Kirkley in *The nature of diamond* [8].

Isotopic dating of inclusions in natural diamonds, coupled with nitrogen aggregation studies indicate ages of between one and three billion years [9, 10]. Natural stones are formed below the surface of the earth under which diamond is the stable phase of carbon.

1.3 Diamond Structure

Diamond is composed of carbon and has a relatively simple crystal structure. The unit cell of diamond can be considered as two interpenetrating face centred cubic lattices, in which one lattice is displaced by $\frac{1}{4}$ of the main body diagonal from the other. The unit cell has a side length of 0.3567 nm [11], see Figure 1-1.

Each carbon atom is surrounded by four nearest neighbours, connected together by covalent sigma bonds. The distance between nearest neighbour atoms

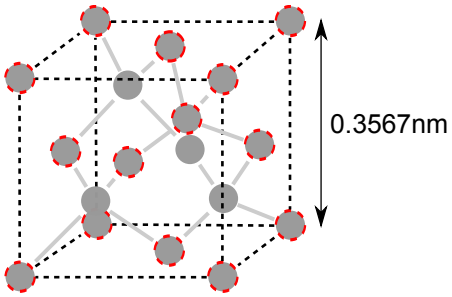

Figure 1-1: The diamond unit cell. One of the two interpenetrating face centred cubic lattices is shown by the (red when in colour) outlined atoms.

is 0.15445 nm at and the bonds make an angle of 109.5° with one another.

Diamond is a crystalline form of carbon that is metastable at atmospheric temperatures and pressures. This means that diamond is not thermodynamically stable under atmospheric conditions, but there is a large energy barrier preventing its conversion to graphite.

The structure of 'perfect' diamond results in many properties including:

1. High thermal conductivity - which arises from the strong carbon–carbon bonds, resulting in a very high Debye temperature and thus a low probability of Umklapp processes (which contribute to the thermal resistivity) at room temperature. ($2000\,\mathrm{Wm^{-1}K^{-1}}$ at room temperature, five times that of copper, $400\,\mathrm{Wm^{-1}K^{-1}}$ [12].)
2. Wide band-gap - 5.47 eV indirect band-gap [12]. This is a consequence of the large separation between bonding and anti-bonding orbitals.
3. Very low electrical conductivity. - Since there is a negligible probability of the excitation of electrons from the valence band to the conduction band at room temperature.
4. High carrier mobility. - Electrons and holes have carrier mobilities of 4500 and $3800\,\mathrm{cm^2V^{-1}s^{-1}}$ at room temperature respectively [13]. This is a result of weak phonon scattering.

However, when defects are present in the lattice the local symmetry is lowered and many properties are altered, for example the colour.

1.4 Defects and Impurities

Defects in the bulk of a crystal can be categorised as extended (voids or dislocations), point (impurities or vacancies) or surface defects. Point defects are of

Table 1-1: The diamond classification system based on the concentration and form of nitrogen impurities [14]. This classification is particularly useful for natural and HPHT synthetic stones [15].

Classification	Sub-classification	Defects present	N Concentration
I		Contain nitrogen - this includes 98% of all diamonds	>1 ppm
	Ia	Nitrogen impurities are aggregated / clustered together	>1 ppm
	IaA	Nearest-neighbor substitutional nitrogen pairs (A centres)	>1 ppm
	IaB	Centers comprising four nitrogen atoms symmetrically surrounding a vacancy (B centres)	>1 ppm
	Ib	N_S^0 - impurities are spread evenly throughout the lattice - these makeup less than 0.1% of diamonds	>1 ppm
II		Very few or no nitrogen atoms	<1 ppm
	IIa	Tiny concentrations of impurities	<1 ppm
	IIb	Boron - p-type semiconductor	

interest in this Thesis. Point defects can result from three basic components, as well as combinations of these.

1. Substitutional impurities - The presence of a different atom at a host lattice site.
2. Vacancy - The absence of a host or impurity atom at a lattice site.
3. Interstitial - The presence of a host or impurity atom not at a lattice site.

Even at very low concentrations (parts per billion) point defects can have a significant affect upon the properties of diamond. Impurities can be incorporated by the intentional doping of material or by accidental incorporation. In some cases specific impurities result in a specific sample colouration, for example boron gives a blue colour, while nitrogen can result in a canary yellow colour.

As a result of the comparable atomic size and its relative abundance in nature nitrogen is the most common impurity in diamond and thus is be basis for its classification [14, 15].

1.4.1 Diamond Classification

Diamond classification is based on the concentration and form of nitrogen in a sample, as shown in Table 1-1. Type I diamonds are the most common type and contain nitrogen in sufficient enough concentrations to be detected by infra-red

absorption spectroscopy. If nitrogen cannot be observed by this method then the diamond is considered to be type II. Type I diamonds are separated into two categories Ia and Ib. In type Ia diamond the nitrogen is aggregated, whereas in type Ib diamond the nitrogen is incorporated as isolated substitutional impurities. Type Ia diamonds are further categorised into IaA and IaB, where the final letter denotes the more abundant nitrogen aggregation centre. An A centre [16] is a nearest-neighbour substitutional nitrogen pair, whilst a B centre [17, 18] comprises four nitrogen atoms symmetrically surrounding a vacancy. Some natural diamonds are predominantly type IaA and some are predominantly type IaB, but the majority are a mixture of both types often labelled type IaAB. The optical N3 centre is another form of nitrogen aggregation, which consists of three nitrogen atoms surrounding a vacancy. This defect is not used in classification, but can have a large affect upon the colour of the diamond [19, 20].

Type II diamonds have a small concentration of nitrogen impurity. This type of diamond is divided into two; type IIa, those that contain no other dominant impurity; and type IIb, those that contain a larger concentration of boron than nitrogen [11]. With improvement in chemical vapour deposition (CVD) synthetic growth many more synthetic diamonds are being characterised as type IIa. Martineau *et al.* [21] have suggested an additional sample classification structure for CVD samples. The classifications are as follows; (i) nitrogen doped, (ii) nitrogen doped and subsequently high pressure high temperature (HPHT) annealed, (iii) boron doped and (iv) high purity. The final class is applied if exhaustive efforts have been taken to exclude any impurities, other than hydrogen, from the source material. Samples from the nitrogen doped and high purity categories have been investigated in this Thesis.

The colouration of a diamond is due to its defects and impurities. Many natural diamonds are brown; this is hypothesised to result from the presence of vacancy clusters generated by plastic deformation [22]. These defects can be 'healed' with HPHT annealing, potentially producing water clear or 'fancy' coloured diamonds [23]. It is of major concern to the gem market if low-value brown diamonds can be turned into more valuable clear or 'fancy' coloured diamonds. It is for this reason that researchers in the field of diamond are keen to find ways to distinguish

a 'treated' coloured diamond from a naturally coloured one. Techniques have thus been developed to identify such diamonds. These are outlined by Collins [24]. CVD diamond often displays a brown colouration of varying hues. Currently the origin of this colour is unclear and this is a major area of current work.

1.5 Synthetic diamond

The first reliable report of diamond synthesis was made in 1959 by General Electric [25, 26]. This used a HPHT method, which produces conditions where diamond is the stable form of carbon, typically above 5 GPa and 1500-2400 K [7] with a metal solvent (catalyst).

Another method of diamond synthesis is CVD which uses low pressures in the graphite stable region of the pressure-temperature phase diagram. The first example of growth using this method was patented by Eversole and Kenmore in 1958 [27, 28], who used atomic hydrogen to generate a hostile environment which etched both diamond and non-diamond carbon. However, the rate of diamond growth exceeded its etch rate, whilst for non-diamond carbon (e.g. graphite) the reverse is true.

1.6 Diamond properties and its uses

As mentioned in Section 1.3 diamond possesses a combination of extreme properties, which makes diamond an interesting material for technological development; a few possible applications are mentioned below.

1. Semiconductor - The high thermal conductivity, diffusivity, carrier mobilities, breakdown voltage and the wide band-gap of diamond makes the material a promising wide band semiconductor for use in high power and high frequency electronic applications.
2. Thermal management systems - At room temperature the thermal conductivity of diamond is five times that of copper, potentially making it a useful heat spreader [12].
3. Durable observation windows - Diamond has a high refractive index and

remains transparent over a wide wavelength range, even at elevated temperatures.

4. Radiation detectors - Diamond is radiation hard and so in extreme conditions such as the large hadron collider at CERN it will outlive other detectors such as silicon, which might only last a few months [29, 30].
5. Coatings - Diamond can be used as a hard or protective coating on a variety of surfaces [31].

Diamond is an attractive material for electronic applications at high temperatures, powers and frequencies. However, to exploit fully the semiconducting nature of diamond, material doped with relatively shallow donors (n-type) and acceptors (p-type) is required.

Boron is to the left of carbon in the periodic table, and of comparable size. This makes it a good choice as an acceptor impurity. With low boron concentrations the acceptor level is observed 0.3685(15) eV above the top of the valence band [32]. The activation energy has been shown to reduce with increasing boron concentration [33]. At sufficiently high boron concentrations, the doped diamond displays metallic properties. These metallic properties are the result of individual boron atoms being sufficiently close to interact, thus generating a defect band within the material; a good review is given in [34]

Finding a suitable donor, however, is more difficult. Nitrogen is to the right of carbon in the periodic table and of similar atomic size. However, its donor level is 1.7 eV below the bottom of the conduction band [35]. The depth of this donor is the result of lattice relaxation around the substitutional nitrogen centre, (see Chapter 2). This donor is too deep to be useful in most applications, leading to research into alternate donors being carried out. Many potential donors have been simulated but as yet a suitable candidate has not been found. Good reviews of the relevant research are given by Mainwood [36] and Goss *et al.* [37].

1.7 EPR in the study of Diamond

Electron paramagnetic resonance (EPR) is the main technique used in this Thesis. EPR, also known as electron spin resonance (ESR), is a bulk measurement

technique which is sensitive to paramagnetic defects at sub part per billion (ppb) concentrations. EPR is a non-destructive technique which involves the application of an external magnetic field to separate energy levels associated with the different spin states of a defect. Electromagnetic radiation (in the microwave region of the spectra) can be used to stimulate magnetic dipole transitions between the energy levels. The strength of the resulting absorption signal is proportional to the number of spins involved and thus the defect concentration. However, EPR can only be used to study defects with unpaired electrons (paramagnetic). Therefore, in order to build a detailed picture of a defect, EPR should be coupled with other techniques such as optical spectroscopy. Over 100 different defect centres in diamond have been observed by EPR and reported [38]. New defects are still being observed, as are reported in this Thesis.

1.8 Thesis outline

The remainder of this Thesis is laid out as follows:

- Chapter 2 - A literature review of the field of diamond, specifically involving a discussion of point defects in diamond that have specific relevance to the latter experimental chapters.
- Chapter 3 - An introduction to EPR theory, which is the main experimental technique used.
- Chapter 4 - A review of the experimental apparatus used in this work.
- Chapter 5 - The first experimental chapter which investigates rapid passage EPR as a quantitative technique, with a view to lowering the EPR detection limit for nitrogen in diamond.
- Chapter 6 - An investigation into the reversible transfer of charge between defects in CVD diamond. Such transfers are generated by heat treatments (<900 K) and ultra violet illumination.
- Chapter 7 - Reports the observation of a defect in [001] grown CVD diamond which displays preferential alignment with respect to the direction of growth.
- Chapter 8 - Reports the observation of two paramagnetic defects, in ^{15}N doped HPHT diamond. The defects are identified as the nitrogen interstitial

and interstitial nitrogen-carbon interstitial pair (nitrogen-di-interstitial).

- Chapter 9 - Reports the observation of a paramagnetic defect in CVD diamond and explains the identification of this defect as the oxygen-vacancy complex.
- Chapter 10 - Investigates the ^{13}C structure on the V_nH^- defect.
- Chapter 11 - Presents a summary of the results presented in the Thesis and suggestions for extensions.
- Appendix A - List of samples studied in this Thesis.

References

[1] C. Leonardus, *Speculum lapidum - The mirror of stones* (1502 Venice. (English translation (anon.) : 1750 London)).

[2] S. Tolansky, *The history and use of diamond* (Methuen & Co. Ltd., London, 1962).

[3] Jeremiah, *The Holy Bible, Revised version* (Tophi Books, 1994).

[4] Pliny (the elder), *Natural History, book 37* (AD 77).

[5] F. Gerety, *A diamond is forever*, N W Ayer advertising agency (1947).

[6] *Changing Facets*, The Economist. London: Feb 24, 2007. Vol. 382, Iss. 8517; pg. 68.

[7] F. P. Bundy, W. A. Bassett, M. S. Weathers, R. J. Hemley, H. U. Mao, and A. F. Goncharov, Carbon **34**, 141 (1996).

[8] M. B. Kirkley, *The Nature of Diamond* (Cambridge University Press, 1998).

[9] S. Richardson and J. Harris, Earth Planet. Sci. Lett. **151**, 271 (1997).

[10] S. Richardson, S. Shirey, J. Harris, and R. Carlson, Earth Planet. Sci. Lett. **191**, 257 (2001).

[11] J. E. Field, *The properties of natural and synthetic diamond* (Academic Press, 1992).

[12] R. Berman, in *The Properties of Natural and Synthetic Diamond*, edited by J. E. Field (Academic Press, London, 1992), chap. 7, pp. 291–300.

[13] S. Hadlington, IEE Review **51**, 30 (2005).

[14] R. Robertson, J. J. Fox, and A. E. Martin, Phil. Trans. R. Soc. A **232**, 463 (1934).

[15] A. T. Collins, Physica B **185**, 284 (1993).

[16] G. Davies, J. Phys. C: Solid State Phys. **9**, L537 (1976).

[17] J. Loubser and J. A. van Wyk, Diamond conf. abst. Reading (unpublished) (1981), the B centre in diamond.

[18] G. S. Woods, Proc. R. Soc. Lond. A. **407**, 219 (1986).

[19] C. M. Welbourn, M. Cooper, and P. M. Spear, Gems. Gemmol. **32**, 156 (1996).

[20] G. Woods and A. Collins, J. Gemmol. **20**, 75 (1986).

[21] P. M. Martineau, S. C. Lawson, A. J. Taylor, S. J. Quinn, D. J. F. Evans, and M. J. Crowder, Gems. Gemmol. **40**, 2 (2004).

[22] L. S. Hounsome, R. Jones, P. M. Martineau, D. Fisher, M. J. Shaw, P. R. Briddon, and S. Öberg, Phys. Status Solidi C **4**, 2950 (2007).

[23] A. T. Collins, H. Kanda, and H. Kitawaki, Diamond Relat. Mater. **9**, 113 (2000).

[24] A. T. Collins, Diamond Relat. Mater. **12**, 1976 (2003).

[25] H. P. Bovenkerk, F. P. Bundy, H. T. Hall, H. M. Strong, and R. H. Wentorf, Nature **184**, 1094 (1959).

[26] H. P. Bovenkerk, F. P. Bundy, R. M. Chrenko, P. J. Codella, H. M. Strong, and R. H. Wentorf, Nature **365**, 19 (1993).

[27] W. G. Eversole and N. Y. Kenmore (1958), US Patent 3030187.

[28] W. G. Eversole and N. Y. Kenmore (1958), US Patent 3030188.

[29] L. Allers, A. S. Howard, J. F. Hassard, and A. Mainwood, Diamond Relat. Mater. **6**, 353 (1997).

[30] A. Mainwood, L. . Allers, A. . Collins, J. F. Hassard, A. S. Howard, A. R. Mahon, H. L. . Parsons, T. Sumner, G. L. Scarsbrook, R. S. Sussmann, et al., J. Phys. D: Appl. Phys. **28**, 1279 (1995).

[31] P. Ball, New Scientist **2067**, 22 (1997).

[32] A. T. Collins and A. W. S. Williams, J. Phys. C: Solid State Phys. **4**, 1789 (1971).

[33] J. P. Lagrange, A. Deneuville, and E. Gheeraert, Diamond Relat. Mater. **7**, 1390

(1998).
[34] K. Thonke, Semicond. Sci. Tech. p. S20 (2003).
[35] R. G. Farrer, Solid State Commun. **7**, 685 (1969).
[36] A. Mainwood, J. Mater. Sci. Mater. Electron. **17**, 453 (2006).
[37] J. P. Goss, R. J. Eyre, and P. R. Briddon, Phys. Status Solidi B **245**, 1679 (2008).
[38] C. A. J. Ammerlaan, *Paramagnetic centers in diamond* (Springer, 2001).

Chapter 2

Literature review

The purpose of this chapter is not to review the entire field of research on diamond, but to introduce synthetic diamond growth processes and present the current knowledge of point defects which are relevant to the work discussed in this Thesis.

2.1 Hybridisation of carbon

The different structural forms of carbon arise because of the ability of carbon to form hybrid orbitals from the 2s and 2p atomic orbitals. The hybrid orbitals form a new basis set from which two and three dimensional structures can be built. The ground state of a carbon atom is $1s^2 2s^2 2p^2$. Thus two 2p orbitals (e.g. ϕ_{2p_x} and ϕ_{2p_y}) and the ϕ_{2s} orbital are available for the construction of hybrids. If the three hybrids are equivalent (e.g. make an angle of 120° with respect to one another, see Figure 2-1(a)) then it can be shown that:

$$\begin{aligned} h_1 &= \frac{1}{\sqrt{3}}\phi_{2s} - \sqrt{\frac{2}{3}}\phi_{2p_x} \\ h_2 &= \frac{1}{\sqrt{3}}\phi_{2s} + \sqrt{\frac{2}{3}}\left(\frac{1}{2}\phi_{2p_x} + \frac{\sqrt{3}}{2}\phi_{2p_y}\right) \\ h_3 &= \frac{1}{\sqrt{3}}\phi_{2s} + \sqrt{\frac{2}{3}}\left(\frac{1}{2}\phi_{2p_x} - \frac{\sqrt{3}}{2}\phi_{2p_y}\right) \end{aligned} \tag{2-1}$$

These are called sp^2-hybrids, the name reflecting the s:p composition ratio. A 2D sheet of graphite can thus be constructed where strong bonds are produced by overlap of these hybrids, see Figure 2-1(a). However, such sheets will be only weakly bonded to one another.

In order to produce three dimensional strong covalent bonds an electron has to be promoted from a ϕ_{2s}-orbital to a ϕ_{2p}-orbital (e.g. $1s^2 2s^2 2p^2 \rightarrow 1s^2 2s^1 2p^3$). This promotion costs energy, but when the carbon-carbon bonds are formed the cost

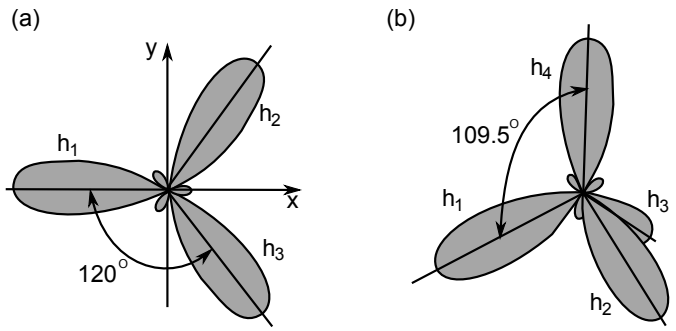

Figure 2-1: The formation of (a)sp^2 hybrid orbitals and (b) the sp^3 hybrid orbitals. Figures are adapted from [1].

is more than offset. The increased overlap of the sp^3-hybrids results in a strong three dimensional bonded structure and lower overall energy, see Figure 2-1(b). The sp^3-hybrids can be written as:

$$\begin{aligned} h_1 &= \phi_{2s} + \phi_{2p_x} + \phi_{2p_y} + \phi_{2p_z} \\ h_2 &= \phi_{2s} - \phi_{2p_x} + \phi_{2p_y} - \phi_{2p_z} \\ h_3 &= \phi_{2s} + \phi_{2p_x} - \phi_{2p_y} - \phi_{2p_z} \\ h_4 &= \phi_{2s} - \phi_{2p_x} - \phi_{2p_y} + \phi_{2p_z} \end{aligned} \tag{2-2}$$

Hybridisation does not take place in two steps (promotion and bonding), instead both steps occur together. For carbon, the tetrahedral structure (Figure 2-1(b)) occurs because the promotion of the electron takes place into an empty ϕ_{2p} orbital, thus four, rather than three covalent bonds can be formed. In the tetrahedral arrangement, the electrostatic repulsion between the electrons in the four bonds is minimised. Many of the properties of diamond are directly attributable to the strong bonding enabled by hybridisation.

2.2 Synthetic diamond

2.2.1 High pressure high temperature diamond synthesis

Direct conversion of graphite into diamond is energetically very expensive because of the need to change the long range order. This can result in only very small crystals being produced. HPHT synthesis with a solvent (e.g. Fe, Ni, Co) gets round this problem. Carbon dissolves into the solvent, and the saturated solvent

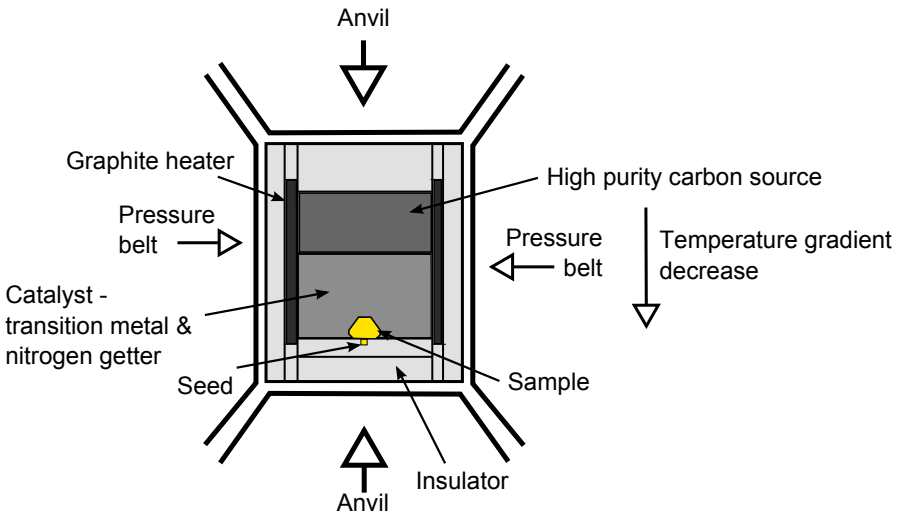

Figure 2-2: A schematic of a typical belt HPHT cell used for diamond growth [8].

allows crystallisation of diamond, atom by atom on the surface of a seed crystal, which is held at a lower temperature, see Figure 2-2.

Source materials used for HPHT synthesis contain significant concentrations of nitrogen. Unless efforts are made to remove nitrogen from the source material, nitrogen concentrations of hundreds of parts per million are common in HPHT diamond. Point defects which involve impurity atoms originating from the solvent are also common (see the review of EPR defects by Ammerlaan [2]). The concentration of nitrogen in the diamond can be reduced through the use of a 'getter' (e.g.Żr, Al, Ti) which has a strong affinity to nitrogen [3–5], thus preventing the incorporation of nitrogen into the diamond (i.e. locks the nitrogen in the solvent). Alternatively removing the nitrogen from the source material by replacing it with another gas (e.g. methane) can reduce the incorporation of nitrogen into the diamond [6].

The nitrogen incorporation efficiency depends upon the applied pressure and temperature of the synthesis as well as the direction of crystal growth. This means that different growth sectors can have different nitrogen concentrations. Typically the {111} sector has the highest uptake, followed by {100} then {113} and {110} sectors. The variation in nitrogen uptake between {111} and {110} sectors can be greater than a factor of 100 [7]. This variation in nitrogen uptake in HPHT synthetic diamond is shown graphically in Figure 2-3 where the shading / colour reflects the nitrogen concentration in each sector.

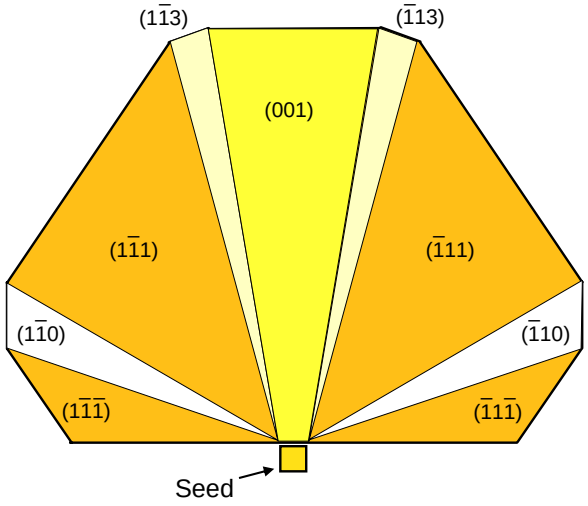

Figure 2-3: A schematic of the sectors of a HPHT synthetic diamond. The shade or colour of each sector reflects the nitrogen concentration. Reproduced from [9].

2.2.2 Chemical vapour deposition diamond synthesis

An alternative method of diamond synthesis is chemical vapour deposition (CVD). In CVD diamond is grown in the graphite-stable region of the phase diagram through the chemical interaction of carbon-containing source gases with the deposition surface. The first example of growth using this method was patented by Eversole and Kenmore in 1958 [10, 11]. However, growth rates of only 0.1μm/h were achieved. Subsequently, Angus *et al.* [12] and Derjaguin *et al.* [13] demonstrated that the presence of hydrogen at temperatures above 1000°C lead to the preferential removal of graphitic (sp^2) material over diamond (sp^3) material. Therefore, higher growth rates of diamond are achievable from hydrocarbon-hydrogen systems (e.g. H_2:CH_4).

Since 1958 different growth chemistries have been investigated in various attempts to increase growth rates and produce doped diamond. The most popular gas mixture for CVD growth is H_2 and CH_4, which involves carbon-containing radicals and atomic hydrogen. Much work has been carried out in an attempt to understand the microscopic mechanisms involved in CVD growth and has culminated in a 'standard model' of CVD diamond growth [14]. CVD diamond growth models are discussed by Goodwin and Butler [15], with more recent developments

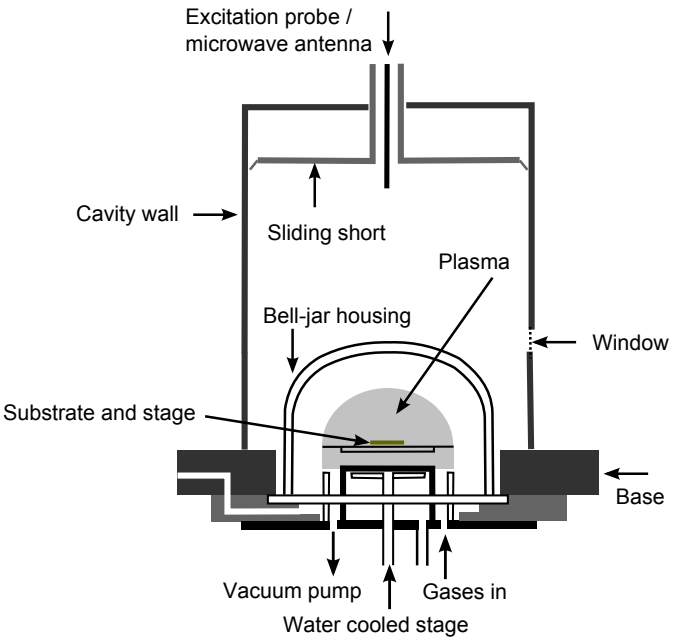

Figure 2-4: Schematic of a microwave plasma CVD reactor. Adapted from [18].

being discussed in [14].

For atomic hydrogen to be present in the reactor elevated temperatures are required. These temperatures can be generated by either:

1. A hot filament (~2000°C) which is placed close to the growth surface. This involves a relatively inexpensive experimental set-up where multiple filaments can allow a large deposition area. One major disadvantage is that the growth material can be contaminated with material from the filament. In addition, the growth rates are typically relatively low compared to microwave plasma CVD.
2. The microwave plasma (MP-CVD) method can offer a cleaner growth environment and was used to produce all the samples discussed in this Thesis. With MP-CVD high quality uniform films can be produced over large substrate areas. This method was first used by Kamo *et al.* [16] at 2.45 GHz, a frequency which has been widely adopted, although some lower frequency reactors with larger growth areas have been reported [17]. The reactor used in the work by King *et al.* [17] is depicted in Figure 2-4.

Nitrogen is readily incorporated into diamond grown by MP-CVD, although at far lower concentrations than in HPHT diamond grown without a 'getter'. Through the minimisation of reactor leaks and the removal source gas impurities, diamond containing less than 1 ppb of nitrogen defects can be produced (see

Chapter 5). However, very low concentrations of nitrogen in the source gases can dramatically increase the growth rate of diamond [19–21]. Nitrogen is incorporated into the sample in the form of single nitrogen (N_S) [22, 23] as well as other defects which can affect optical, thermal and electrical properties. The doping efficiency of nitrogen, i.e. the relative incorporation of a nitrogen atom to the incorporation of a carbon atom, has been determined by Samlenski *et al.* [24] and Tallier *et al.* [23] to be $(0.75 - 6) \times 10^{-4}$. Ultimately, a balance must be struck between the permissable level of nitrogen incorporation and the required growth rate. In this Thesis (Chapter 5) some very high purity samples ($N_S^0 < 1$ ppb) are studied where exhaustive efforts were taken to exclude nitrogen from the growth environment.

Any impurity introduced to the source gas could be incorporated into the growing crystal. For example, the doping efficiency of boron is $10^{-1} - 10^{-2}$, significantly higher than for nitrogen [22]. For both nitrogen and boron the incorporation efficiency is dependent upon the growth sector [22, 24], as well as the growth conditions of the diamond.

Other impurities observed in CVD diamond are phosphorous, where incorporation efficiencies have been determined to be between 0.15 and 0.04 [25, 26] and silicon, where incorporation efficiencies are lower than that of boron but greater than that of nitrogen on a {001} surface [27]. The incorporation of oxygen is considered in Chapter 9.

In 2002, Yan *et al.* [28] reported single crystal (SC) CVD diamond growth rates of 50–150 μm/h. Comparable growth rates have been reported by several groups subsequent to Yan *et al.* [29–32]. However, for CVD diamond the nitrogen impurity concentration in such material is typically high ($\lesssim$10 ppm) and the material is brown in colour. The brown colour is attributed to vacancy clusters grown into the diamond [33, 34]. Methods for the production of thick SC-CVD samples have also been patented by Element Six Ltd., as well as patents for the growth of very high purity SC-CVD diamond grown without the addition of nitrogen [35].

Recent work by Asmussen *et al.* [18] has discussed the use of MP-CVD reactors operating at 915 MHz [17] with a potential deposition area of 6-8 inches. Asmussen *et al.* [18] reported a deposition area of 100 mm diameter with an average growth

rate of 20.8 μm/h for SC-CVD diamond. Asmussen *et al.* [18] reported that over the deposition area there was a variation in the growth rate of 5%.

Other elements can be incorporated into the CVD growth environment for the purpose of deliberately doping the diamond (e.g. boron [22, 36]); to improve growth rates; or inhibit the incorporation of specific impurities [27].

2.3 Nitrogen-related defects

2.3.1 Single substitutional nitrogen

As early as 1959 [37] nitrogen was identified as the most common impurity in natural diamond. In as-grown CVD diamond, where nitrogen has not aggregated, the most common form of nitrogen is the single substitutional centre, which is EPR-active in its neutral charge state (N_S^0). Nitrogen in this form was first observed by Smith *et al.* in natural diamond [38] and has since been observed in HPHT and CVD synthetic diamond [39].

The structure of N_S^0 can be explained as follows. The substitutional nitrogen bonds with each of the four neighbouring carbon atoms. The additional electron localised in an anti-bonding orbital between the nitrogen and one of the carbon atoms (the unique carbon). This unique nitrogen-carbon bond is extended by 20–30% when compared with carbon-carbon bonds in the lattice [40–42]. Each of the other carbon-nitrogen bonds is slightly shorter than a carbon-carbon bond [43]. This produces a defect with C_{3v} symmetry and results in a deep donor state, 1.7 eV [44]. A review of EPR and ENDOR measurements on the N_S^0 centre is given by Cox. [45]

The N_S centre is observed optically in absorption spectroscopy. The neutral charge state (N_S^0) shows a continuum of optical absorption, beginning at ~1.7 eV and rising rapidly, with some sharp absorption lines at ~4 eV [46]. This continuum continues until it merges with the fundamental absorption edge at 5.5 eV [47]. This absorption spectra has been interpreted as transitions from the donor level into the conduction band (1.7 eV), and transitions from the valance band into the localised electronic level (~4 eV) [46, 47]. There are three broad bands at 3.3, 3.9 and 4.6 eV (376, 318 and 270 nm) [48] that have been connected with this centre and give rise

to the yellow colouration associated with N_S^0. The concentration of N_S^0 can be determined by fourier transform infra-red (FTIR) spectroscopy. N_S^0 also generates absorption in the one phonon region, with peaks at 1344 (sharp) and 1130 cm^{-1}. It has been shown that the concentration of N_S^0 is proportional to the absorption strength at these peaks. An absorption of 1 cm^{-1} at the 1130 cm^{-1} peak relates to a concentration of 25 ± 5 ppm of N_S^0 [49].

N_S^+ is also observed in FTIR and has been correlated [50] with the 1332 cm^{-1} line [51] with a correlation factor of 5.5(10) ppm / cm^{-1}. Other peaks have also been assigned to this defect: 1095(weak), 1050 and 950 cm^{-1} [50].

2.3.2 The nitrogen-vacancy centre

The nitrogen-vacancy centre (NV) is observed in both as-grown CVD and natural diamond. NV defects can also be formed in diamond which has been irradiated to form vacancies, and annealed at ~900 K [52] to allow them to migrate. When a vacancy is caught by an N_S centre, an NV centre is created. This is either negatively (NV^-) or neutrally (NV^0) charged depending on the availability of electron donors. The nitrogen-vacancy centre anneals out at ~1800 K, contributing to the aggregation of nitrogen into pairs known as A centres [53].

The NV centre was first observed optically [54] as the 637 nm line, which was studied in detail by Davies and Hamer [55] who suggested the NV model. Subsequently a defect with $S = 1$ and an $I = 1$ nucleus, C_{3v} symmetry and a large zero field splitting (2.88 GHz) was observed in EPR by Loubser and van Wyk [56]. Each of these characteristics is consistent with the NV model proposed for the 637 nm line. The EPR and optical observations were further connected through work by Reddy *et al.* [57] and Redman *et al.* [58].

The 575 nm line is observed in samples that have experienced the same treatments as those that display 637 nm line [59, 60]. From uniaxial stress measurements [55, 60] the 575 nm line was shown to originate from an E→A transition at a trigonal defect [59]. The authors suggested that this was the NV^0 centre. A subsequent correlation between the 637 and 575 nm lines was made by Mita [61], and confirmed that they are due to two different charge states of the same defect, 637 nm (NV^-) and 575 nm (NV^0). The NV^- defect is well documented and

its electronic structure is well understood. The similarities between NV^- and the WAR5 defect are further discussed in Chapter 9.

2.4 Hydrogen in diamond

As discussed in [14] and [62] hydrogen is a crucial component of the CVD source gas for diamond growth. The prevalence of hydrogen in the growth environment invites consideration of the incorporation of this impurity into the diamond. Hydrogen has been shown to have an affect on the electronic performance of diamond, for example, by compensating the substitutional boron acceptor [63]. Consequently, the trapping or release of hydrogen by point or extended defects is an important topic for research.

Hydrogen is observed in CVD diamond at the surface and crystal grain boundaries [64]. For example, the H1 EPR-active centre [65, 66] which involves a single hydrogen atom is present only at grain boundaries. Hydrogen can also be incorporated into the crystal bulk through growth errors, which are grown over resulting in a point defect [67].

Hydrogen-related defects are also observed optically; a review is given by Cruddace [68]. One prominent hydrogen-related optical transition is the $3107\,cm^{-1}$ absorption line which is commonly observed in natural and HPHT treated diamonds. The $3107\,cm^{-1}$ line is thought to originate from a carbon-hydrogen stretch mode [69, 70]. The $3123\,cm^{-1}$ absorption line, that will be discussed in Chapter 6 involves a hydrogen and a carbon atom but has no isotopic shift with ^{15}N enrichment [71].

Two routinely observed hydrogen containing EPR-active defects are reviewed here.

2.4.1 The vacancy-hydrogen complex

The V_nH^- defect is commonly observed in CVD diamond [72, 73]. The defect is labelled here with an unspecified number of vacancies 'n' as there are currently two models proposed for this defect. The first, initially proposed by Glover *et al.* [73], involves a hydrogen atom bonded to one of four carbon neighbours surrounding

a vacancy (n = 1), see Figure 10.2(b). However, density functional theory (DFT) calculations by Shaw *et al.* [72] predict that the hydrogen hyperfine interaction resulting from such a construction would be significantly larger than that observed by the experiment. They instead proposed that the experimentally observed hyperfine interaction is consistent with a dynamic defect. This second model suggests that the hydrogen atom is tunnelling between three equivalent dangling bonds at one end of a di-vacancy (n=2), see Figure 2.5(b).

EPR spectra recorded at temperatures in the range 4 K to 300 K have shown no evidence of motional averaging on an EPR time scale [73]. However, the tunneling between orbitals may have such a low energy barrier that it is unaffected by this temperature change. This means that we cannot differentiate between the models based on the available EPR data. The V_nH^- defect has also been observed in deuterium enriched samples (V_nD^-), but no splitting from the deuterium hyperfine interaction was resolved [68].

2.4.2 The nitrogen-vacancy-hydrogen complex

EPR spectra resulting from the negative nitrogen-vacancy-hydrogen NVH^- defect were first observed by Hunt, [50] and subsequently by Glover *et al.* [74]. The NVH^- defect is routinely observed in SC-CVD diamond, but has not been reported in natural or HPHT synthetic diamond. Cruddace [68] showed that the defect can be responsible for a significant fraction of the nitrogen in SC-CVD diamond (up to 10%). These measurements were made on samples with N_S^0 concentrations of 100–1000 ppb.

EPR measurements show that the NVH^- defect has an effective C_{3v} symmetry [74]. Theoretical DFT calculations by Kerridge *et al.* [75] and Shaw *et al.* [72] have predicted that the hydrogen would tunnel between three equivalent positions, where it bonds to one of the three carbon atoms surrounding the vacancy. The static configuration of the defect would have C_{1h} symmetry. Edmonds [76] has recently shown that the EPR observations are consistent with this dynamic model and that the observed EPR spectrum results from motional averaging of the configuration with C_{1h} symmetry.

The NVH^- defect is suggested to be infra-red active since there are no selection

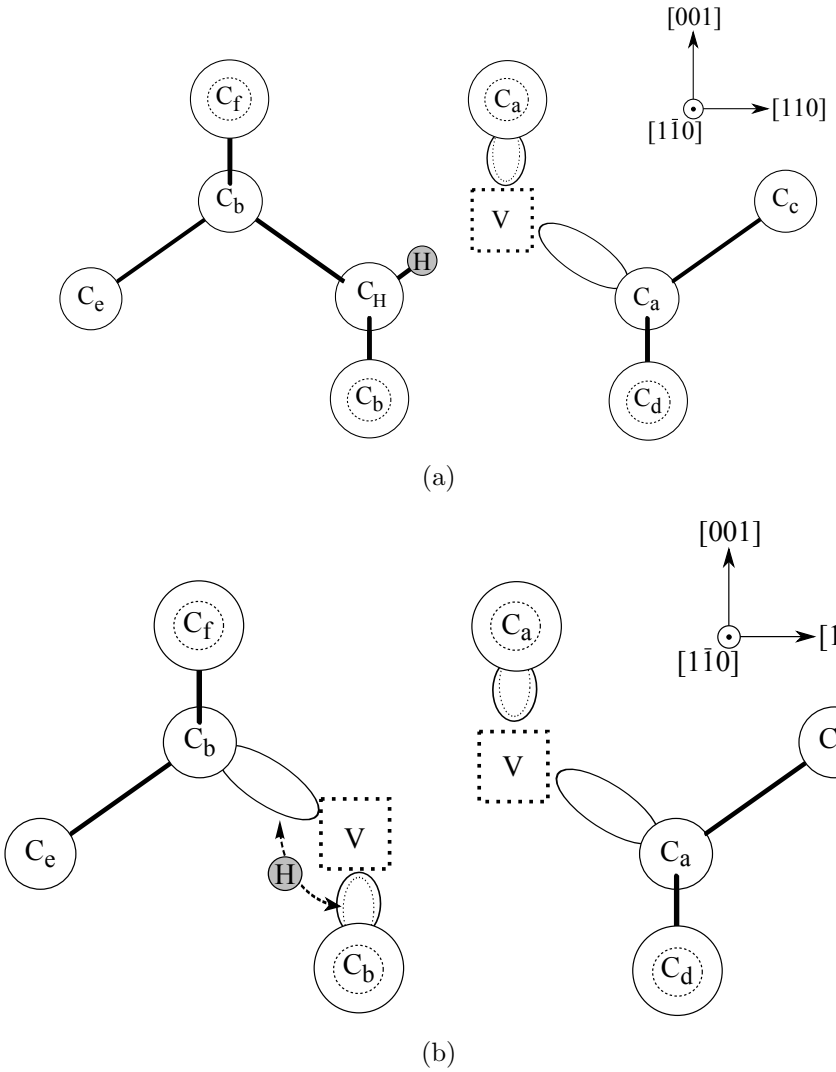

Figure 2-5: Cartoon depictions of the V_nH^- defect in diamond projected in the $(1\bar{1}0)$ plane. The larger circles represent those carbon atoms in the foreground, the smaller dotted circles represent those in the plane behind when viewed in this direction. (a) the V_1H model proposed by Glover *et al.* [73] and (b) the V_2H model proposed by Shaw *et al.* [72]. The neighbouring carbon atoms are labelled in groups with equivalent positions. The broken squares represent vacancies and the shaded circle a hydrogen atom. In the V_2H model the hydrogen atom is tunneling between the dangling bonds from the three C_b atoms, as indicated by the dashed arrow.

rules that forbid it [77]. Goss *et al.* [77] made predictions for the positions of the local vibrational mode, originating from a C-H stretch mode, of the NVH defect in both negative and neutral charge states at ~2827 cm^{-1} and ~2679 cm^{-1} respectively. Caution should be exercised here since these predictions are at best 'semi-quantitative' [77].

Cruddace [68] showed that the 3123 cm^{-1} absorption line resulted from a defect with C_{1h} symmetry and correlated its intensity with the concentration of NVH^- over four orders of magnitude. It was subsequently suggested by Meng *et al.* [78] that the 3124 cm^{-1} line[1] may be associated with the NVH^- defect.

2.5 Vacancy clusters

In natural brown diamonds it is presumed that vacancy clusters are formed by vacancy release during plastic deformation and subsequent aggregation to form clusters. In type IIa brown natural diamond the removal of vacancy clusters through HPHT annealing can result in a colourless diamond.

It has been proposed that vacancy clusters cause a brown colouration in both CVD synthetic and some natural diamonds [79, 80]. Vacancy clusters have been observed directly by transmission electron microscopy (TEM) [81]. The presence of vacancy clusters have also been inferred by positron annihilation spectroscopy (PAS), which can distinguish a single vacancy from a cluster by the extended positron lifetime [82].

The removal of the brown colouration from CVD diamond occurs at a lower temperature than that observed for natural diamond. PAS studies show that the smaller vacancy clusters are annealing out, but larger clusters are being produced that do not contribute to the colour [83]. The difference between the annealing behaviour of brown natural and CVD diamond may be related to the large concentrations of hydrogen. However, further work is required to reveal the details of the process.

It is possible that vacancy clusters are present in all SC-CVD diamond to

[1]Meng *et al.* [78] refer to this line as the 3124 cm^{-1}, whereas in this Thesis and other works the same line is referred to as the 3123 cm^{-1}line

some extent [84] and given their extended nature could act as multiple charge traps. The variation in the size of vacancy clusters may also result in different levels within the band-gap. Such extended defects could play an important role in any charge transfer experiments (see Chapter 6) and their presence could influence the performance of electronic devices fabricated from CVD diamond [84].

References

[1] P. W. Atkins, *Molecular Quantum Mechanics* (Clarendon Press, 1970).

[2] C. A. J. Ammerlaan, *Paramagnetic centers in diamond* (Springer, 2001).

[3] H. M. Strong (1978), US Patent 4082185.

[4] H. M. Strong and R. M. Chrenko, J. Phys. Chem. **75**, 1838 (1971).

[5] R. H. Wentorf, J. Phys. Chem. **75**, 1833 (1971).

[6] C. V. H. Stroemann, F. Tshisikhawe, J. O. Hansen, and R. C. Burns, *Synthesis of Diamond* (2006), Patent WO2006061672.

[7] R. C. Burns, V. Cvetkovic, C. N. Dodge, D. J. F. Evans, M. T. Rooney, P. M. Spear, and C. M. Welbourn, J. Cryst. Growth **104**, 257 (1990).

[8] Wedlake, in *Properties of Diamond*, edited by J. E. Field (Academic Press, London, 1979), chap. 16, pp. 501–535.

[9] C. M. Welbourn, M. Cooper, and P. M. Spear, Gems. Gemmol. **32**, 156 (1996).

[10] W. G. Eversole and N. Y. Kenmore (1958), US Patent 3030187.

[11] W. G. Eversole and N. Y. Kenmore (1958), US Patent 3030188.

[12] J. C. Angus, H. A. Will, and W. S. Stanko, J. Appl. Phys. **39**, 2915 (1968).

[13] B. V. Derjaguin, D. V. Fedoseev, V. M. Lukyanovich, B. V. Spitzin, V. A. Ryabov, and A. V. Lavrentyev, J. Cryst. Growth **2**, 380 (1968).

[14] J. E. Butler, Y. A. Mankelevich, A. Cheesman, J. Ma, and M. N. R. Ashfold, J. Phys. Condens. Matter **21**, 364201 (2009).

[15] D. G. Goodwin and J. E. Butler, in *Handbook of Industrial Diamonds and Diamond Films*, edited by M. A. Prelas, G. Popovici, and L. K. Bigelow (Marcel Dekker, New York, 1998), pp. 527–581.

[16] M. Kamo, Y. Sato, S. Matsumoto, and N. Setaka, J. Cryst. Growth **62**, 642 (1983).

[17] D. King, M. Yaran, T. Schuelke, T. Grotjohn, D. Reinhard, and J. Asmussen, Diamond Relat. Mater. **17**, 520 (2008).

[18] J. Asmussen, T. A. Grotjohn, T. Schuelke, M. F. Becker, M. K. Yaran, D. J. King, S. Wicklein, and D. K. Reinhard, Appl. Phys. Lett. **93**, 031502 (2008).

[19] W. Muller-Sebert, E. Worner, F. Fuchs, C. Wild, and P. Koidl, Appl. Phys. Lett. **68**, 759 (1996).

[20] A. Afzal, C. Rego, W. Ahmed, and R. Cherry, Diamond Relat. Mater. **7**, 1033 (1998).

[21] E. Butler, J and I. Oleynik, Phil. Trans. R. Soc. A **366**, 295 (2008).

[22] R. Samlenski, C. Haug, R. Brenn, C. Wild, R. Locher, and P. Koidl, Diamond Relat. Mater. **5**, 947 (1996).

[23] A. Tallaire, A. T. Collins, D. Charles, J. Achard, R. Sussmann, A. Gicquel, M. E. Newton, A. M. Edmonds, and R. J. Cruddace, Diamond Relat. Mater. **15**, 1700 (2006).

[24] R. Samlenski, C. Haug, R. Brenn, C. Wild, R. Locher, and P. Koidl, Appl. Phys. Lett. **67**, 2798 (1995).

[25] S. Koizumi, M. Kamo, Y. Sato, H. Ozaki, and T. Inuzuka, Appl. Phys. Lett. **71**, 1065 (1997).

[26] M. Katagiri, J. Isoya, S. Koizumi, and H. Kanda, Phys. Status Solidi A **201**, 2451 (2004).

[27] S. D. Williams, D. J. Twitchen, P. M. Martineau, G. A. Scarsbrook, and I. Friel (2007), UK Patent Application: GB 2428690 A.

[28] C. S. Yan, Y. K. Vohra, H.-k. Mao, and R. J. Hemley, Proc. Natl. Acad. Sci. **99**, 12523 (2002).

[29] Y. Mokuno, A. Chayahara, Y. Soda, Y. Horino, and N. Fujimori, Diamond Relat. Mater. **14**, 1743 (2005).
[30] A. Tallaire, J. Achard, F. Silva, R. S. Sussmann, and A. Gicquel, Diamond Relat. Mater. **14**, 249 (2005).
[31] H. Sternschulte, T. Bauer, M. Schreck, and B. Stritzker, Diamond Relat. Mater. **15**, 542 (2006).
[32] S. Ho, C. Yan, Z. Liu, H. Mao, and R. Hemley, Ind. Diamond Rev. **66**, 28 (2006).
[33] L. S. Hounsome, R. Jones, P. M. Martineau, D. Fisher, M. J. Shaw, P. R. Briddon, and S. Öberg, Phys. Rev. B **73**, 125203 (2006).
[34] D. Fisher, D. J. F. Evans, C. Glover, C. J. Kelly, M. J. Sheehy, and G. C. Summerton, Diamond Relat. Mater. **15**, 1636 (2006).
[35] G. A. Scarsbrook and P. M. Martineau (2001), Patent Application: WO 0196633.
[36] G. A. Scarsbrook, P. M. Martineau, T. D. J., A. J. Whitehead, and M. A. Cooper (2003), Patent WO03052174.
[37] W. Kaiser and W. L. Bond, Phys. Rev. **115**, 857 (1959).
[38] W. V. Smith, P. P. Sorokin, I. L. Gelles, and G. J. Lasher, Phys. Rev. **115**, 1546 (1959).
[39] I. Watanabe and K. Sugata, Jpn. J. Appl. Phys. Pt1 **27**, 1808 (1988).
[40] A. R. Lang, M. Moore, A. P. W. Makepeace, W. Wierzchowski, and C. M. Welbourn, Phil. Trans. R. Soc. A **337**, 497 (1991).
[41] S. A. Kajihara, A. Antonelli, J. Bernholc, and R. Car, Phys. Rev. Lett. **66**, 2010 (1991).
[42] P. R. Briddon, M. I. Heggie, and R. Jones, in *Proc. 2nd int. conf. on new diamond science and technology*, edited by R. Messier, T. J. Glass, J. E. Butler, and R. Roy (Material Research Society, Pittsburg, 1991), p. 63.
[43] O. D. Tucker, M. E. Newton, and J. M. Baker, Phys. Rev. B **50**, 15586 (1994).
[44] R. G. Farrer, Solid State Commun. **7**, 685 (1969).
[45] A. Cox, M. E. Newton, and J. M. Baker, J. Phys. Condens. Matter **6**, 551 (1994).
[46] A. Mainwood, J. Phys. C: Solid State Phys. p. 2543 (1979).
[47] H. B. Dyer, F. A. Raal, L. du Preez, and J. H. N. Loubser, Phil. Mag. **11**, 763 (1965).
[48] J. Koppitz, O. F. Schirmer, and M. Seal, J. Phys. C: Solid State Phys. **19**, 1123 (1986).
[49] G. S. Woods, J. A. van Wyk, and A. T. Collins, Phil. Mag. B **62**, 589 (1990).
[50] D. Hunt, D. Phil. Thesis, University of Oxford (1999).
[51] S. C. Lawson, D. Fisher, D. C. Hunt, and M. E. Newton, J. Phys. Condens. Matter **10**, 6171 (1998).
[52] G. Davies, S. C. Lawson, A. T. Collins, A. Mainwood, and S. J. Sharp, Phys. Rev. B **46**, 13157 (1992).
[53] A. T. Collins, J. Phys. C: Solid State Phys. **13**, 2641 (1980).
[54] L. du Preez, Ph.D. thesis, University of the Witwatersrand, Johannesburg (1965).
[55] G. Davies and M. F. Hamer, Proc. R. Soc. Lond. A. Mat. **348**, 285 (1976).
[56] J. H. N. Loubser and J. A. van Wyk, Diamond Research **11**, 11 (1977).
[57] N. R. S. Reddy, N. B. Manson, and E. R. Krausz, J. Lumin. **38**, 46 (1987).
[58] D. A. Redman, S. Brown, R. H. Sands, and S. C. Rand, Phys. Rev. Lett. **67**, 3420 (1991).
[59] A. T. Collins and S. C. Lawson, J. Phys. Condens. Matter **1**, 6929 (1989).
[60] G. Davies, J. Phys. C: Solid State Phys. **12**, 2551 (1979).
[61] Y. Mita, Phys. Rev. B **53**, 11360 (1996).

[62] T. R. Anthony, Vacuum **41**, 1356 (1990).
[63] J. Chevallier, A. Lusson, D. Ballutaud, B. Theys, F. Jomard, A. Deneuville, M. Bernard, E. Gheeraert, and E. Bustarret, Diamond Relat. Mater. **10**, 399 (2001).
[64] N. Mizuochi, H. Watanabe, J. Isoya, H. Okushi, and S. Yamasaki, Diamond Relat. Mater. **13**, 765 (2004).
[65] X. Zhou, G. D. Watkins, K. M. M. Rutledge, R. P. Messmer, and S. Chawla, Phys. Rev. B **54**, 7881 (1996).
[66] D. F. Talbot-Ponsonby, M. E. Newton, J. M. Baker, G. A. Scarsbrook, R. S. Sussmann, A. J. Whitehead, and S. Pfenninger, Phys. Rev. B **57**, 2264 (1998).
[67] J. E. Butler, R. L. Woodin, L. M. Brown, and P. Fallon, Phil. Trans. R. Soc. A **342**, 209 (1993).
[68] R. J. Cruddace, PhD. Thesis, University of Warwick (2007).
[69] G. S. Woods and A. T. Collins, J. Phys. Chem. Solids **44**, 471 (1983).
[70] R. M. Chrenko, R. S. McDonald, and K. A. Darrow, Nature **213**, 474 (1967).
[71] F. Fuchs, C. Wild, K. Schwarz, W. Muller-Sebert, and P. Koidl, Appl. Phys. Lett. **66**, 177 (1995).
[72] M. J. Shaw, P. R. Briddon, J. P. Goss, M. J. Rayson, A. Kerridge, A. H. Harker, and A. M. Stoneham, Phys. Rev. Lett. **95**, 105502 (2005).
[73] C. Glover, M. E. Newton, P. M. Martineau, S. Quinn, and D. J. Twitchen, Phys. Rev. Lett. **92**, 135502 (2004).
[74] C. Glover, M. E. Newton, P. Martineau, D. J. Twitchen, and J. M. Baker, Phys. Rev. Lett. **90**, 185507 (2003).
[75] A. Kerridge, A. H. Harker, and A. M. Stoneham, J. Phys. Condens. Matter **16**, 8743 (2004).
[76] A. M. Edmonds, PhD. Thesis, University of Warwick (2008).
[77] J. P. Goss, P. R. Briddon, R. Jones, and S. Sque, J. Phys. Condens. Matter **15**, S2903 (2003).
[78] Y. Meng, C. Yan, J. Lai, S. Krasnicki, H. Shu, T. Yu, Q. Liang, H. Mao, and R. J. Hemley, Proc. Natl. Acad. Sci. U S A. **105**, 17620 (2008).
[79] A. Pu, T. Bretagnon, D. Kerr, and S. Dannefaer, Diamond Relat. Mater. **9**, 1450 (2000).
[80] V. Avalos and S. Dannefaer, Physica B **340-342**, 76 (2003).
[81] U. Bangert, R. Barnes, L. S. Hounsome, R. Jones, A. T. Blumenau, P. R. Briddon, M. J. Shaw, and S. Öberg, Phil. Mag. **86**, 4757 (2006).
[82] V. Avalos and S. Dannefaer, Diamond Relat. Mater. **14**, 155 (2005).
[83] U. Bangert, R. Barnes, M. H. Gass, A. L. Bleloch, and I. S. Godfrey, J. Phys. Condens. Matter p. 364208 (2009).
[84] R. Jones, L. S. Hounsome, N. Fujita, S. Öberg, and P. R. Briddon, Phys. Status Solidi A **204**, 3059 (2007).

Chapter 3

Theory

3.1 Overview

This Thesis reports data derived from a variety of experimental techniques. However, the bulk the of data results from electron paramagnetic resonance (EPR) experiments which are briefly introduced in Section 1.7. A first glance at diamond-related literature would show EPR in a supporting role to the more frequently used optical techniques. This is in contrast to studies of silicon where magnetic resonance has proved invaluable in the development and exploitation of the material.

The unique nature of each natural diamond hampered the early investigation of the characteristics of diamond. The more widespread use and better control of diamond synthesis has led to a more systematic study of point defects.

EPR is a powerful tool for probing the structure of paramagnetic defects. EPR can reveal details of the defects constituent elements, symmetry and unpaired electron localisation. In addition, EPR is a quantitative technique where the signal intensity is proportional to the concentration of the defect giving rise to it.

With continued improvement in diamond quality, the concentration of many important and common impurities (e.g. nitrogen) have fallen below the detection limits of traditional quantitative techniques such as infrared absorption. Even EPR, a very sensitive technique for paramagnetic defects, is being stretched to its limits, see Chapter 5.

The increased availability of diamond with low defect concentrations may mean a movement away from traditional methods and a heavier reliance upon more sensitive techniques such as EPR and photoluminescence (PL).

3.2 EPR - A historical perspective

In 1922 Otto Stern and Walther Gerlach reported an experiment which passed a beam of silver atoms through a stable magnetic field [1]. They observed that the beam split in two. The resulting theory suggested that the odd number of electrons in each of the silver atoms caused each atom to act as a 'mini bar magnet'. Thus, when the beam passed through the static magnetic field, half of the atoms were deflected in one direction and the other half in the opposite direction. This was the first experimental observation of the electronic Zeeman interaction, the dominant interaction exploited by EPR.

In 1944 the Soviet physicist Yevgeny Zavoisky from Kazan State University reported the first observation of EPR. The resulting paper was published in 1945 [2] and Bloch described this observation in 1946 [3]. Bloch also predicted an alternative parameter space labelled 'rapid passage' (RP) which was observed experimentally by Portis in 1955 [4].

EPR measurements on diamond were first reported by Smith *et al.* in 1959 [5] Smith *et al.* reported the observation of the EPR centre now labelled P2. A further paper, published later that same year, reported the observation of the most prevalent EPR-active defect in diamond, which was labelled P1 and identified as the neutrally charged substitutional nitrogen centre, N_S^0 [6]. Using EPR, additional defects have continued to be observed, named and catalogued. The naming system adopted is as follows: the label's letter indicates the institution where the defect was first observed and the number denotes the chronological order of the discovery. For example, R5 was the fifth unique defect observed at the University of Reading. A review of EPR-active defects in diamond up to 2001 is given by Ammerlaan [7].

For clarity, it should be mentioned that this convention does not hold for optically observed signals and defects. In this case, the defects are labelled either by the energy or wavelength of the zero phonon line (ZPL), or by the method used to create the defect. For example, the label GR1 ('general-radiation') refers to the first defect observed in diamond after irradiation. Caution should be used where the assigned labels clash. For example, the EPR-characterised P2 centre (Poughkeepsie) is the EPR analogue of the optical N3 centre [8] (N for naturally occurring), and should not be confused with the N3 (Novosibirsk) labelled EPR

centre, which is unrelated.

As different parameter spaces for diamond synthesis are investigated and characterisation techniques become increasingly sensitive, the number of catalogued defects continues to grow. This Thesis adds four previously unreported defects, and suggested models to this catalogue. However, given the large number of catalogued defects relatively few have strongly supported models.

3.3 EPR theory

The theory of EPR is well known and is covered in detail elsewhere, for example the text by Weil *et al.* [9]. This Chapter will give a brief overview of EPR discussing the interactions particularly relevant to the experimental work described in later Chapters.

EPR is a spectroscopic technique where microwaves are absorbed by species (or in this case defects), which have one or more unpaired electrons. The basic principle is analogous to that of nuclear magnetic resonance (NMR), but the electron spins are excited rather than the nuclear ones. In order to obtain an EPR signal a strong external magnetic field is applied, orthogonal to the applied microwaves, which acts to split degenerate energy levels. When the energy difference between two energy levels matches the energy of the applied microwaves, absorption occurs and an EPR signal is observed, see Figure 3-1.

EPR exploits the intrinsic quantum nature of electrons and atoms (Stern-Gerlach experiment). Usually, the dominant interaction involved in EPR is the electronic Zeeman interaction, which originates from the interaction between an unpaired electron and an external magnetic field. Classically the energy of the magnetic dipole moment, $\boldsymbol{\mu}$, in an externally applied magnetic field, $\mathbf{B}$, is described by, $\mathbf{U} = -\boldsymbol{\mu} \cdot \mathbf{B}$.

For an unpaired electron the dipole moment, $\boldsymbol{\mu_S}$, is related to the Zeeman splitting constant, g_e, the Bohr magneton[1], μ_B, and the spin, $\mathbf{S}$, by the expression, $\boldsymbol{\mu_S} = -\mu_B g_e \mathbf{S}$.

If it is assumed that $\mathbf{B}$ is parallel to the z-direction, then the part of the

[1] $\mu_B = e\hbar/2m_e$ where, e is the charge on an electron, and m_e the mass of an electron

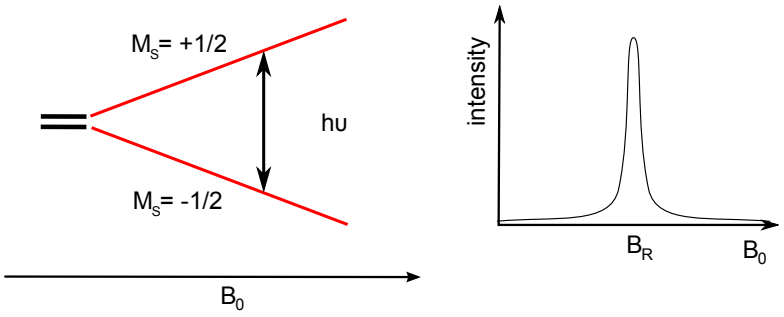

Figure 3-1: To achieve resonance the external magnetic field, B_0, is varied with the microwave frequency held constant. When the energy of the applied microwaves ($h\upsilon$) match that of the gap between the energy levels absorption occurs and a signal is observed.

Hamiltonian which relates to the magnetic perturbation, can be expressed as:

$$\mathscr{H} = \mu_B g_e B S_z \tag{3-1}$$

Hence, for a single unpaired electron, we produce the M_S quantum number from $S_z|\psi\rangle = M_S|\psi\rangle$ with the resulting energy levels at $E_{|\pm\frac{1}{2}\rangle} = \pm\frac{1}{2}\mu_B g_e B$.

EPR exploits the difference in energy levels by the detection of transitions between $M_S = -\frac{1}{2}$ and $M_S = +\frac{1}{2}$. A transition between these levels is generated by the application of microwaves with an energy that matches that of the energy gap between the transitions, hence $h\nu = \mu_B g_e B$.

The energy levels are split by the external magnetic field (Equation 3-1), but in order to observe a transition between the energy levels there must exist an initial population difference between them. Electrons are excited from the lower energy level to the higher one by a microwave photon. To maintain a population difference the excited electrons can relax back but the rate of this relaxation will depend upon the system and the relaxation pathways available.

If this were the only interaction observed by EPR then the technique would not provide much information about the defect. An additional interaction is spin-orbit coupling. In the preceding discussion only the contribution of electron spin to $\boldsymbol{\mu}$ was considered. However, in general the total magnetic moment is the vector sum of the spin, **S**, and orbital angular momentum, **L**.

The spin and orbital angular momenta are coupled. This coupling can be treated as a perturbation and is described by Russell-Saunders coupling. Therefore, there are two contributions to the spin Hamiltonian, one from the electronic

Zeeman interaction (EZ) and the other from the spin orbit coupling (SO), see Equation 3-2.

$$\begin{aligned}\mathscr{H} &= \mathscr{H}_{EZ} + \mathscr{H}_{SO} \\ \mathscr{H} &= \mu_B \mathbf{B} \cdot \left(\hat{\mathbf{L}} + g_e \hat{\mathbf{S}}\right) + \left(\lambda_{\text{so}} \hat{\mathbf{L}} \cdot \hat{\mathbf{S}}\right)\end{aligned} \tag{3-2}$$

The circumflex in Equation 3-2 denotes an operator, $\hat{\mathbf{L}}$ is the ground state orbital angular momentum, $\hat{\mathbf{S}}$ is the effective spin operator for the ground state and λ_{so} is the Russell-Saunders spin-orbit coupling term. Now it is possible to 'mix-in' orbital angular momenta from excited states.

Perturbation theory is invoked to produce the effective spin Hamiltonian as is described in [10]. Therefore, in a system where $S \geq 1$ there are two components, the electronic Zeeman (EZ) and zero field splitting (zfs) interactions.

$$\begin{aligned}\mathscr{H}_{EZ+zfs} &= \mu_B \mathbf{B}^{\mathbf{T}} \cdot \underline{\mathbf{g}} \hat{\mathbf{S}} + \hat{\mathbf{S}}^{\mathbf{T}} \cdot \underline{\mathbf{D}} \hat{\mathbf{S}} \text{ where,} \\ \underline{\mathbf{g}} &= g_e \underline{\mathbf{1}} + 2\lambda_{\text{so}} \underline{\mathbf{\Lambda}} \text{ and } \underline{\mathbf{D}} = \lambda_{\text{so}}^2 \underline{\mathbf{\Lambda}}\end{aligned} \tag{3-3}$$

Where $\underline{\mathbf{g}}$ is a 3×3 matrix and $\underline{\mathbf{\Lambda}}$ is the spin orbit coupling matrix. The superscript $\mathbf{T}$ indicates the transpose.

3.3.1 Zero-field interaction

In the presence of an $S \geq 1$ system and a zero-field interaction, but in the absence of an external magnetic field, the energy levels are split. Considering two coupled electrons, there are four possible spin combinations; a triplet with a symmetric spin combination, each state with a total spin of 1 and $M_S = +1, 0, -1$, and an asymmetric spin combination singlet where the spin is zero, (Figure 3-2). The singlet energy level is significantly different from those of the triplet and is not observed by EPR.

The zero-field splitting term of the Hamiltonian[2] is given by :

$$\mathscr{H}_{zfs} = \hat{\mathbf{S}}^{\mathbf{T}} \cdot \underline{\mathbf{D}} \hat{\mathbf{S}} \tag{3-4}$$

[2] $\underline{\mathbf{D}}$ is made traceless by subtracting the term causing an overall shift in the energy levels. This does not affect the gaps between the energy levels and so there is no affect on the EPR spectrum.

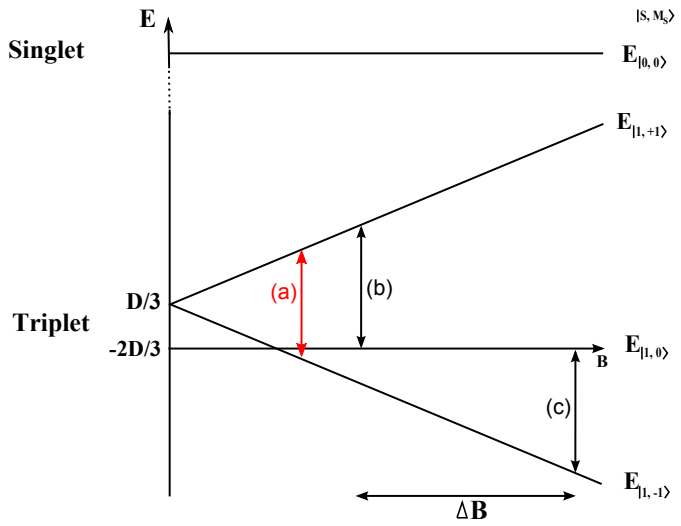

Figure 3-2: Energy levels associated with an $S = 1$ system, displaying a zero field interaction, D. Only those transitions between triplet states result in EPR transitions. The singlet-triplet splitting is assumed to be very large so the spin singlet can be ignored. The transition labelled (a) is a half-field transition and is marked alongside matching energies at (b) low and (c) high, full field transitions. ΔB is the splitting between the high and low field full-field transitions.

Zero field splitting can result from three interactions and remove the degeneracy of the three fold triplet, even at zero-field. They are:

1. The spin-orbit interaction as discussed previously. The contribution from spin-orbit coupling can be determined from Equation 3-3.
2. The exchange interaction, which describes the manifestation of the Coulomb interaction between the two electrons (for $S = 1$) and other magnetic ions. The magnitude of the interaction decreases with separation.
3. Dipole-dipole interaction, see Section 3.3.2.

3.3.2 Dipolar interaction

Dipolar interactions between two electrons in an $S = 1$ system can be described by:

$$\mathscr{H}_{\text{dip}}(\mathbf{r}) = \frac{\mu_0}{4\pi}\left[\frac{\boldsymbol{\mu}_1{}^{\mathbf{T}} \cdot \boldsymbol{\mu}_2}{r^3} - \frac{3(\boldsymbol{\mu}_1{}^{\mathbf{T}} \cdot \mathbf{r})(\boldsymbol{\mu}_2{}^{\mathbf{T}} \cdot \mathbf{r})}{r^5}\right] \tag{3-5}$$

where $\mathbf{r}$ is the inter-electron vector. If $\underline{\mathbf{g}}$ is isotropic, and the magnetic-moment operators are replaced with corresponding spin operators, Equation 3-5 becomes:

$$\mathscr{H}_{\text{dip}} = \left(\frac{\mu_0}{4\pi}\right) g_1 g_2 \mu_B^2 \left[\frac{\hat{\mathbf{S}}_1{}^{\mathbf{T}} \cdot \hat{\mathbf{S}}_2}{r^3} - \frac{3(\hat{\mathbf{S}}_1{}^{\mathbf{T}} \cdot \mathbf{r})(\hat{\mathbf{S}}_2{}^{\mathbf{T}} \cdot \mathbf{r})}{r^5}\right] \tag{3-6}$$

If $g_1 = g_2 = g$ then only two independent parameters are required to describe the zero-field interaction:

$$D = \frac{3}{2} D_z \tag{3-7}$$

$$E = \frac{1}{2}(D_x - D_y) \tag{3-8}$$

By convention D_z is the principal value, where $|D_z| > |D_x| > |D_y|$ (if $D_x = D_y$, $E = 0$).

Equation 3-6 can be re-written as:

$$\mathscr{H}_{\text{dip}} = D\left[{S_z}^2 - \frac{1}{3}S(S+1)\right] + E({S_x}^2 + {S_y}^2) \tag{3-9}$$

where,

$$D = \frac{\mu_0}{4\pi}\ \frac{3}{4} g^2 \mu_B^2 \left\langle \frac{r^2 - 3z^2}{r^5} \right\rangle \text{ and } E = \frac{\mu_0}{4\pi}\ \frac{3}{4} g^2 \mu_B^2 \left\langle \frac{y^2 - x^2}{r^5} \right\rangle \tag{3-10}$$

If **B** is parallel to the z direction and the system has axial symmetry ($E = 0$), then:

$$E_{|M_S\rangle} = g\mu_B B M_S + D\left[M_S^2 - \frac{1}{3}S(S+1)\right] \tag{3-11}$$

Hence for an $S = 1$ system, as shown in Figure 3-2,

$$\begin{aligned} E_{|+1\rangle} &= g\mu_B B + \frac{D}{3} \\ E_{|0\rangle} &= -\frac{2D}{3} \\ E_{|-1\rangle} &= -g\mu_B B + \frac{D}{3} \end{aligned} \tag{3-12}$$

Figure 3-2 shows two $\Delta M_S = \pm 1$ transitions that require the same excitation energy. Therefore, at a single microwave frequency two transitions ((b) and (c)) are possible and will be separated in field by ΔB. Figure 3-2 also shows an additional $\Delta M_S = \pm 2$ transition (a) which has the same excitation energy. The magnetic field applied for transition (a) is approximately half that of the average between the two $\Delta M_S = \pm 1$ transitions, hence such transitions are termed 'half-field' transitions. Third field transitions and above are also possible where $S \geq \frac{3}{2}$.

3.3.3 The spin Hamiltonian

As mentioned, there are interactions between unpaired electrons and the external magnetic field. There are also interactions which involve the nuclei, other unpaired electrons and local magnetic fields. The combination of these interactions are described by the effective spin Hamiltonian ($\mathscr{H}$):

$$\mathscr{H} = \underbrace{\mu_B \mathbf{B}^{\mathbf{T}} \cdot \underline{\mathbf{g}} \hat{\mathbf{S}}}_{\{1\}} + \underbrace{\hat{\mathbf{S}}^{\mathbf{T}} \cdot \underline{\mathbf{D}} \hat{\mathbf{S}}}_{\{2\}} + \sum_j [\underbrace{\hat{\mathbf{S}}^{\mathbf{T}} \cdot \underline{\mathbf{A}}_j \hat{\mathbf{I}}_j}_{\{3\}} - \underbrace{\mu_N g_{N_j} \mathbf{B}^{\mathbf{T}} \cdot \hat{\mathbf{I}}_j}_{\{4\}} + \underbrace{\hat{\mathbf{I}}_j^{\mathbf{T}} \cdot \underline{\mathbf{P}}_j \hat{\mathbf{I}}_j}_{\{5\}}] + \text{higher order terms}, \tag{3-13}$$

where $\hat{\mathbf{S}}$ and $\hat{\mathbf{I}}_j$ are the effective electron spin operator and the nuclear spin operator for the j^{th} nucleus, respectively.

Term {1} in Equation 3-13 parameterises the electronic Zeeman interaction (see Section 3.3). The zero-field interaction term, {2}, describes the spin-spin interaction (see Section 3.3.1. The hyperfine interaction term, {3}, describes the interaction between the unpaired electron and magnetic nuclei (Section 3.3.3.2). The nuclear Zeeman term, {4}, describes the interaction of those magnetic nuclei with the external magnetic field (Section 3.3.3.1). The quadrupole term, {5}, is present only in systems where $I > \frac{1}{2}$ and describes the interaction between the nucleus and local electric fields (Section 3.3.3.3). A brief discussion of each of the remaining three terms will be given in the following sections. For further information texts by Weil *et al.* [9] or Abragam and Bleaney [11] should be consulted.

3.3.3.1 Nuclear Zeeman interaction

The nuclear Zeeman interaction is analogous to the electronic Zeeman interaction, but results from the interaction between the external magnetic field and the magnetic moment of the nucleus involved. The contribution to the spin Hamiltonian is thus given by:

$$\mathscr{H}_{NZ} = -\sum \mu_N g_{N_j} \mathbf{B}^{\mathbf{T}} \cdot \hat{\mathbf{I}}_j \tag{3-14}$$

The magnitude of the nuclear Zeeman interaction is much smaller than the electronic Zeeman interaction, which results in relatively small splittings. The splittings which result from the nuclear Zeeman interaction can be useful for identifying the nuclei involved in a defect. The EPR transitions which would act as a 'finger

print' of the nuclei are to first order 'forbidden' ($\Delta M_S = 1$, $\Delta m_I \neq 0$). However, the probability of such transitions is usually non-zero (see Section 3.3.4) and so they can be used to determine the impurity nuclei as in Chapter 7.

3.3.3.2 Hyperfine interaction

The hyperfine interaction describes the interaction between the spin of an unpaired electron and the spin of a nucleus. Provided that the nuclear spin (I) is non-zero, a hyperfine interaction is present, which if large enough may give rise to hyperfine structure in the spectrum. The hyperfine interaction can provide information regarding a defects structure, symmetry and the localisation of the probability density of the unpaired electron(s).

3.3.3.2.1 Isotropic hyperfine interaction The hyperfine interaction, much as with other components of the effective spin Hamiltonian, can be split into isotropic and anisotropic components. In this case the isotropic component, also known as the Fermi or contact interaction, arises from the nuclear interactions with s-orbital electrons, i.e. those with non-zero electron probability density at the nucleus.

For a system with a single electron, when a strong magnetic field is applied in the z-direction so as to align the electron and nuclear magnetic dipoles, the isotropic hyperfine interaction can be described by:

$$\mathscr{H}_{iso} = \frac{2}{3}\mu_0 g_e \mu_B \, g_N \mu_N \, |\psi(0)|^2 \, S_z I_z = A_0 S_z I_z \tag{3-15}$$

where $\psi(0)$ is the unpaired electron wave-function at the nucleus, ($\psi(0) = 0$ for non s-type orbitals), and A_0 is the isotropic hyperfine coupling constant.

For electron wavefunctions with zero probability density at the nucleus, such as p-orbitals, the anisotropic hyperfine interaction must be considered.

3.3.3.2.2 Anisotropic hyperfine interaction The dipolar interaction (Section 3.3.2) between a nucleus and an electron separated by a vector $\mathbf{r}$ can be expressed as,

$$\mathscr{H}_{\text{dip}} = \frac{\mu_0}{4\pi} g_1 g_2 \mu_B^2 \left[\frac{\hat{\mathbf{S}}_1 \cdot \hat{\mathbf{I}}_2}{r^3} - \frac{3(\hat{\mathbf{S}}_1 \cdot \mathbf{r})(\hat{\mathbf{I}}_2 \cdot \mathbf{r})}{r^5} \right] = \hat{\mathbf{S}}^{\mathbf{T}} \mathbf{T} \cdot \hat{\mathbf{I}} \tag{3-16}$$

where $\mathbf{T}$ is the anisotropic hyperfine matrix.

The full spin Hamiltonian requires contributions from both the isotropic and anisotropic components, hence the spin Hamiltonian term is expressed as $\hat{\mathbf{S}}^{\mathbf{T}} \cdot \underline{\mathbf{A}} \hat{\mathbf{I}}$, where $\underline{\mathbf{A}}$ is the hyperfine parameter expressed as a 3×3 matrix. $\underline{\mathbf{A}} = A_0 1_3 + \underline{\mathbf{T}}$, i.e. the sum of the product of the isotropic component and a 3×3 unity matrix, and the anisotropic 3×3 matrix. A_0 is given simply by the trace of $(\frac{\underline{\mathbf{A}}}{3})$.

Considering an axially symmetric hyperfine system (and isotropic g), where θ is the angle between the unique axis and the external magnetic field, then $\underline{\mathbf{A}}$ can be expressed with respect to the principal axis as $A_\parallel$ and $A_\perp$ such that:

$$A^2(\theta) = A_\parallel^2 \cos^2\theta + A_\perp^2 \sin^2\theta \tag{3-17}$$

or $\underline{\mathbf{A}}$ can be expressed as a matrix:

$$\underline{\mathbf{A}} = \begin{pmatrix} A_\perp & 0 & 0 \\ 0 & A_\perp & 0 \\ 0 & 0 & A_\parallel \end{pmatrix} \tag{3-18}$$

The parallel ($\parallel$) and perpendicular ($\perp$) components can be related directly to the isotropic and anisotropic components of $\underline{\mathbf{A}}$ through the substitution of $\begin{pmatrix} -b & 0 & 0 \\ 0 & -b & 0 \\ 0 & 0 & +2b \end{pmatrix} = \underline{\mathbf{T}}$ into $\underline{\mathbf{A}} = A_0 1_3 + \underline{\mathbf{T}}$. Hence [3], if $A_0 = a$ then,

$$\begin{aligned} a &= \frac{1}{3}(A_\parallel + 2A_\perp) \\ b &= \frac{1}{3}(A_\parallel - A_\perp) \end{aligned} \tag{3-19}$$

3.3.3.3 Quadrupole interaction

The nuclear spin angular momentum is related to the shape of the nucleus with respect to the axis of symmetry. The quadrupole interaction describes the interaction between the electric field gradient and the asymmetric charge distribution on the corresponding nucleus where $I \geq 1$. In general the interaction can be

[3] Since this is the anisotropic part of the expression, the $\underline{\mathbf{T}}$ matrix must be traceless. A restriction placed on the matrix by the system being axial is that the first two diagonal terms must be equal.

represented by:

$$\mathscr{H}_{\mathrm{qp}} = \hat{\mathbf{I}}^{\mathbf{T}} \cdot \underline{\mathbf{P}} \hat{\mathbf{I}} \tag{3-20}$$

where $\underline{\mathbf{P}}$ is the quadrupole tensor. The expression is often given in cartesian coordinates and with respect to a principal axis:

$$\mathscr{H}_{\mathrm{qp}} = P_{\parallel} \left\{ \left[{I_z}^2 - \frac{1}{3} I(I+1) \right] + \frac{\eta}{3} \left({I_x}^2 - {I_y}^2 \right) \right\}, \tag{3-21}$$

where $P_{\parallel} = \frac{3}{2} P_z$ and $\eta = \frac{P_x - P_y}{P_z}$. In the presence of axial symmetry, $\eta = 0$ and

$$P = \frac{e^2 q_{\mathrm{efg}} Q}{4I(2I+1)} \tag{3-22}$$

Where q_{efg} is the electric field gradient at the nucleus (q_{efg} = 0 for s-orbitals). Q is the quadrupole moment, a measure of the nucleus' charge distribution or its departure from a spherical shape. A positive Q indicates an elongated shape along the principal axis. A negative Q indicates a flattened shape [12, 13]. This interaction does not affect the EPR spectrum to first order and is not discussed further in this Thesis.

3.3.4 Transition probabilities

As mentioned previously, the energy to drive a transition between two energy levels is supplied by the application of a time varying magnetic field in the form of microwaves. Hence, $\mathscr{H}_{\mu w} = \mu_B \mathbf{B}_{\mu \mathrm{w}}^{\mathbf{T}} \cdot \underline{\mathbf{g}} \hat{\mathbf{S}}$ describes the perturbation upon the system.

If all the off-diagonal terms in the effective spin Hamiltonian tend to zero, or are small in comparison to the on-diagonal terms, then the EPR transitions occur in accordance with the selection rules ($\Delta M_S = \pm 1$ and $\Delta m_I = 0$) and are labelled as 'allowed'. If the off-diagonal terms cannot be neglected, then the resulting energy levels are shifted, and the spin states are mixed (neither M_S nor m_I are necessarily 'good' quantum numbers). This mixing results in the relaxation of the selection rules such that $\Delta M_S \neq \pm 1$ and $\Delta m_I \neq 0$ transitions can occur. These transitions are labelled as 'forbidden' transitions and are normally significantly less intense than the 'allowed' transitions. However, there are exceptions where intensities can be reversed, see Chapter 7.

3.3.5 Relaxation

Relaxation, when referred to here means is the return, following a perturbation, of the relative populations of the excited and ground states to those which are determined by Boltzmann statistics [9].

EPR can reflect time-dependent processes such as relaxation occurring in a sample. Although not directly exploited in this Thesis, some of the phenomena involved are useful when considering the rapid change in magnetic field over the EPR transitions as well as the interaction of electron spins with each other and their surroundings.

3.3.5.1 The Bloch model

The Bloch equations are a set of coupled differential equations which describe the time dependence of the total spin magnetisation in the presence of a static and an oscillating magnetic field. The Bloch equations are derived and discussed in many standard texts, the specifics of these equations to EPR are described in [9].

The steady state solution to the Bloch equations in a rotating frame are those most commonly referenced in EPR. These solutions are reproduced in Equation 3-23. See [9] for a derivation of these solutions.

$$\begin{aligned} M_{x\phi} &= -M_z^0 \frac{\gamma_e B_1 (\omega_B - \omega)\tau_2^2}{1 + (\omega_B - \omega)^2\tau_2^2 + \gamma_e^2 B_1^2 \tau_1 \tau_2} \\ M_{y\phi} &= +M_z^0 \frac{\gamma_e B_1 \tau_2}{1 + (\omega_B - \omega)^2\tau_2^2 + \gamma_e^2 B_1^2 \tau_1 \tau_2} \\ M_z &= +M_z^0 \frac{1 + (\omega_B - \omega)\tau_2^2}{1 + (\omega_B - \omega)^2\tau_2^2 + \gamma_e^2 B_1^2 \tau_1 \tau_2} \end{aligned} \tag{3-23}$$

where, $\gamma_e = g_e \mu_B / \hbar$ is the electronic gyromagnetic ratio, μ_B is the Bohr magneton and g_e is the unpaired electron g-factor previously discussed in Section 3.3. ω_B is the angular frequency with which the magnetisation vector, M, precesses around the external magnetic field, B_0, i.e. the classic Larmor frequency [14].

τ_1 and τ_2, are the electronic spin-lattice relaxation time and the transverse relaxation time respectively. τ_1 results from the coupling of spins to the lattice and τ_2 is a measure of the spin-spin coherence times. Since spins interact via dipolar coupling, the τ_2 term and the EPR line-width depend upon $1/\tau_2$. High concentrations of paramagnetic defects results in line broadening. From the width

of the line, local defect concentrations can be determined [15]. Both τ_1 and τ_2 are empirical bulk properties which describe the system but reveal nothing about the physical mechanisms behind them [16].

Note that the response of $M_{x\phi}$ is in phase with B_1, whereas $M_{y\phi}$ is 90° out of phase [9]. M_z^0 tends to be large compared with $M_{x\phi}$ and $M_{y\phi}$. For a sufficiently small B_1 the final denominator term (the microwave power saturation term) can be neglected. These solutions are for steady state conditions and therefore are unsuitable for rapid-time resolved experiments such as RP-EPR (see Chapter 5) [9].

It is shown in [9] that the microwave absorption signal is proportional to $M_{y\phi}$. If the denominator term of Equation 3-23 ($\gamma^2 B_1^2 \tau_1 \tau_2$) is significantly less than one (in the absence of microwave power saturation), the form of $M_{y\phi}$ is that of a Lorentzian lineshape, $L = L_{max} \frac{\Gamma^2}{\Gamma^2 + (B - B_0)^2,}$.

In slow passage (SP)-EPR the EPR signal strength is proportional to the square root of the microwave power and so proportional to B_1. This relation holds while the population difference between spin states is presented at the Boltzmann equilibrium value, i.e. in the absence of microwave power saturation.

In solids the τ_1 relaxation time is generally long and so $\gamma^2 B_1^2 \tau_1 \tau_2$ cannot be assumed to be very much less than one and so such samples are prone to microwave power saturation. This is the case for the N_S^0 defect in diamond where microwave power saturation is observed at moderate microwave powers.

The level of microwave power saturation can be described by Equation 3-24. Fitting a range of signal intensities (I_{sat}) from various microwave powers can give an indication of the level of microwave power saturation. From Equation 3-24 the unsaturated intensity (I_{unsat}) can be obtained from the saturated intensity (I_{sat}).

$$I_{sat} = \frac{I_{unsat}}{\left[1 + \gamma^2 B_1^2 \tau_1 \tau_2\right]^{\frac{1}{2}}} \tag{3-24}$$

3.3.6 Rapid passage

RP-EPR is an alternative passage regime where the steady state conditions required for the static solutions to the Bloch equations, of which Equation 3-23 is one, do not hold.

The exact description of RP-EPR theory is complex, and so for a rigorous description the reader is referred to Weger 1960 [17]. In this Chapter we will briefly discuss the technique in sufficient detail to interpret the data presented in Chapter 5.

RP-EPR occurs when the rate of change of B_0 or the modulation field (B_m) is faster than the relaxation rate. Considering both fields:

$$B_z = B_0 + B_m \cos \omega_m t + \int_0^t \frac{\mathrm{d}B_0}{\mathrm{d}t} \mathrm{dt} \tag{3-25}$$

where ω_m is the angular frequency of the modulation field. Differentiating Equation 3-25 gives the rate of change of the applied magnetic field:

$$\frac{\mathrm{d}B_z}{\mathrm{d}t} = B_m \omega_m \sin \omega_m t + \frac{\mathrm{d}B_m}{\mathrm{d}t} \tag{3-26}$$

As has been discussed by Stoner *et al.* [18] and Weger [17], for passage to be considered *rapid* the criterion in Equation 3-27 below must be reached:

$$\frac{B_1}{\frac{dB_0}{dt}\left[\tau_1 \tau_2\right]^{\frac{1}{2}}} < 1 \tag{3-27}$$

That is, the applied magnetic field must sweep through the transition in a time which is short compared to the relaxation time, whereas in SP-EPR the transition is swept through in a time which is long compared to the relaxation time.

3.4 Symmetry

As mentioned previously, one of the strengths of EPR as an analytical technique, is the ability to determine the symmetry of a defect. Consider a single (non-isotropic) paramagnetic defect in a single-crystal diamond. The energy levels resulting from an unpaired electron are affected by the local magnetisation. The local magnetisation is dependent upon the orientation of the defect with respect to the external magnetic field (B_0). Consequently, different magnitudes of splittings between energy levels gives rise to different positions of the transition in magnetic field values at different orientations. Given sufficient spectra at different orientations, the symmetry of the defect can be determined.

In this Thesis, where reference is made to the symmetry of a defect, the Schoenflies notation will be used (Table 3-1); in Figure 3-3 the relevant international equivalent term is given.

Table 3-1: A description of the point group nomenclature (Schoenflies notation) used throughout this Thesis.

Schoenflies notation	Operation
E	None.
C_n	An n-fold rotation about the axis of symmetry.
C_{nv}	An n-fold axis and a mirror plane which contains the principal axis of rotation.
C_{nd}	An n-fold axis and a mirror plane which is perpendicular to the axis of rotation.
S_n	Only an n-fold rotation-reflection axis.
D_n	An n-fold rotation axis and a two fold axis perpendicular to the n-fold axis.
D_{nh}	An n-fold rotation axis and a two fold axis perpendicular to the n-fold axis and a mirror plane perpendicular to the n-fold axis.
D_{nd}	An n-fold rotation axis and a two fold axis perpendicular to the n-fold axis and a mirror plane containing the n-fold axis.
i	Inversion centre in a centre of symmetry.

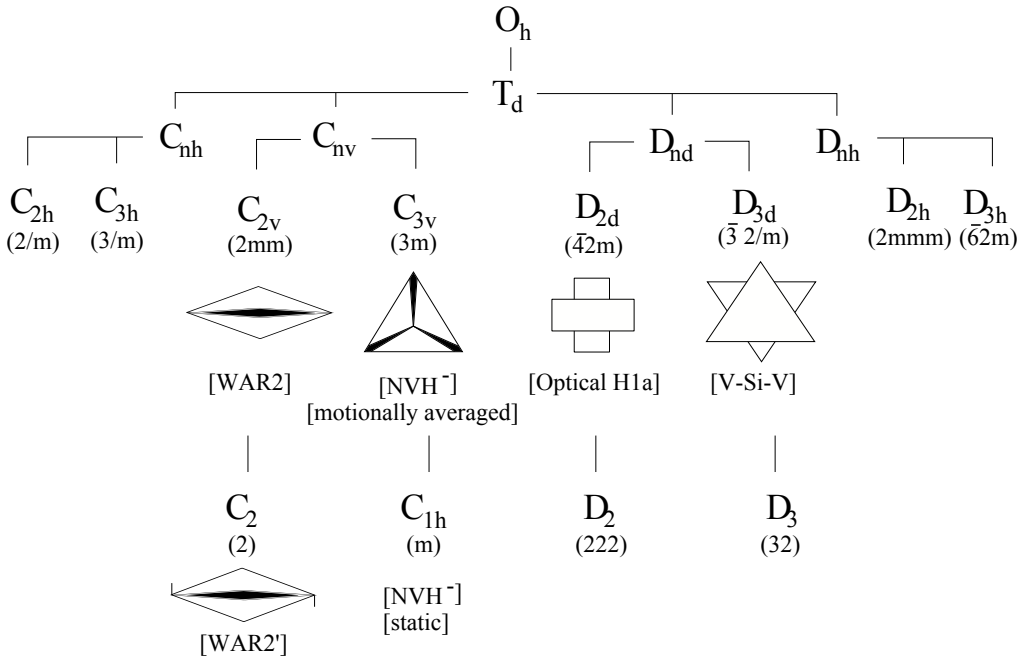

Figure 3-3: The symmetry operations relating to the symmetries of key defects in diamond. The Schoenflies notation is used in the diagram with *international designation* given in round brackets. Examples of defects that exhibit those symmetries are given in square brackets. The symmetry decent of NVH^- [19] and WAR2 (see Chapter 7) are shown. The S_n symmetry group is not shown on this diagram.

The symmetry point group of the diamond lattice is T_d. The number of symmetry elements for T_d symmetry is 24, i.e. there are 24 operations that can be performed on a defect with this symmetry, and there will be no change in the resulting EPR spectrum.

With traditional EPR it is not possible to observe a single defect. Hence, an ensemble of differently oriented defects is observed which populates the sites allowed by its symmetry. This will be discussed here with respect to the N_S^0 defect. N_S^0 has $S = \frac{1}{2}$ and, $I = 1$ (from a ^{14}N nucleus). When the magnetic field is aligned parallel to a $\langle 100 \rangle$ type crystallographic direction the hyperfine interaction of the unpaired electron with the nuclear spin results in a characteristic three line spectrum shown in Figure 3-4(a). The N_S^0 defect has C_{3v} symmetry, the unpaired electron is localised on a nitrogen-carbon anti-bonding orbital which is directed along one of the $\langle 111 \rangle$ crystallographic directions. This unique nitrogen-carbon bond is extended when compared to the bond lengths of the surrounding lattice. This system can be described by four independent sites, i.e. with the unique nitrogen-carbon bond located along each of the four possible $\langle 111 \rangle$ crystallographic directions, as shown in Figure 3-5.

When the crystal is aligned with B_0 parallel to a $\langle 100 \rangle$ crystallographic direction, all four $\langle 111 \rangle$ directions, or possible locations for the unpaired electron, make the same angle with B_0. In this case, the magnitudes of the interaction and so the observed spectra from all sites are thus identical. When the field is aligned parallel to a $\langle 111 \rangle$ crystallographic direction, three of the bonds make the same angle with B_0 and the fourth is parallel to B_0, resulting in the 3:1 ratio seen in Figure 3.4(b).

A roadmap is a collection of spectra obtained when the external magnetic field is rotated in a specific plane. For example the $(1\bar{1}0)$ plane, rotating the crystal 90° from [001] through [111] to [110] is common since it includes all three principle directions.

The symmetry of a defect can be determined from the line intensities observed when the B_0 is parallel to principal crystallographic directions, $[001], [111]$ and $[110]$. The number of sites, and number of transitions that coincide differ between point group symmetries, and from this the symmetry of a defect can be determined.

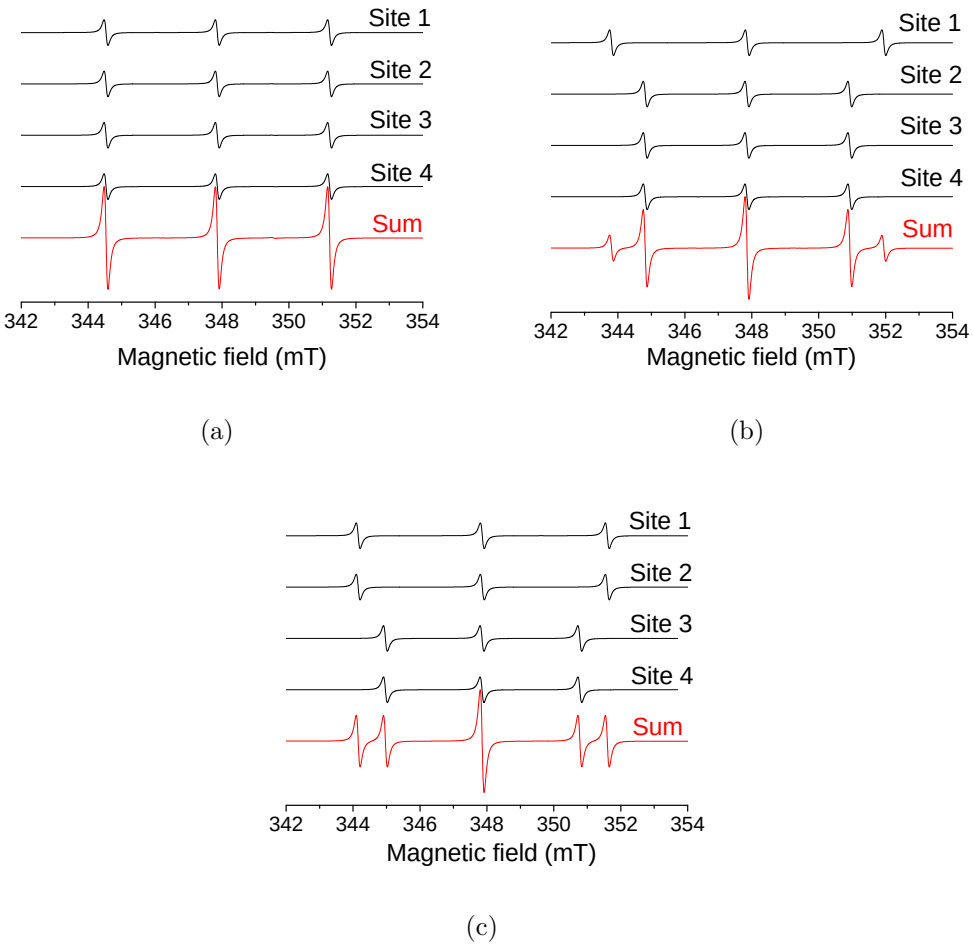

Figure 3-4: The $^{14}N_S^0$ defect simulated at each of the four sites shown in Figure 3-5. The sum of all sites shows the observed signal intensities when the external magnetic field is oriented parallel to the (a) ⟨100⟩, (b) ⟨111⟩ and (c) ⟨110⟩ crystallographic direction. Simulations are at 9.75 GHz with a 0.1 mT line width.

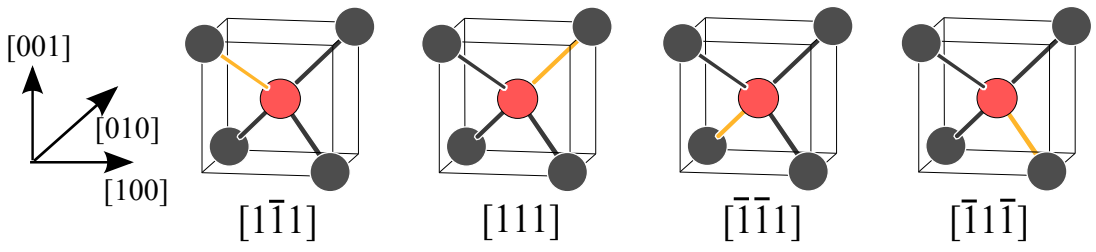

Figure 3-5: The four possible sites the N_S^0 defect can occupy. The central (red when in colour) sphere represents the nitrogen atom and the remaining spheres the nitrogen's nearest carbon neighbours. The lighter (yellow when in colour), elongated bond represents the unique carbon-nitrogen bond.

A table of line intensities and the implied defect symmetries is given by Edmonds [20] (based on the original by Cox, [21]).

The tables given by Edmonds [20] describe the common situation where defects are randomly oriented. However, in this Thesis defects with a preferred alignment to the growth direction are discussed. If there is preferential alignment of defects, certain sites may be significantly under-populated or not populated at all. In the latter case fewer rotation matrices are required to describe the observed spectrum.

3.5 Annealing

In the context of this Thesis, the term annealing refers to the permanent alteration of a defect as a result of thermal treatment. Such alterations occur in samples where the defect concentrations differ from the equilibrium value at the annealing temperature. Defect concentrations can be reduced as a result of:

1. Defects becoming mobile and migrating towards a sink, i.e. a surface, dislocation, vacancy cluster or other defect, with which it then combines.
2. The defect-complex may dissociate to form two separate defects.
3. Defects may combine to form a new complex, e.g. $V + V \rightarrow V_2$.

Defects can also change from being EPR-'observable' (or EPR-'active') to EPR-'silent' in different charge states. The effect of a charge transfer reaction on defect concentrations can be described in the same way as other annealing processes. However, this process is reversible and will usually occur at temperatures lower than those where the defects involved will break-up. To avoid complication, in this Thesis if the heat treatment being applied has a temporary effect caused by charge transfer it will be referred to as *'heat or thermal treatment'*. If the treatment induces irreversible changes, i.e. the formation or break-up of defects it will be referred to as *'annealing'*. From now on, this chapter will discuss annealing behaviour, but identical descriptions are also suitable for charge transfer.

It is important to state that if the reaction requires two stages e.g. a break-up of one defect and formation of another, then the activation energy of the reaction is controlled by the stage that requires the most energy.

3.5.1 First order reaction

A first order reaction is the simplest, but there are assumptions concerning the reaction that must hold in order to assume first order kinetics. These assumptions will be discussed by way of an example where the defect of interest is labelled X in Equation 3-28.

$$[X] + [Y] \rightarrow [XY] \tag{3-28}$$

1. X must be involved in the reaction only once and not involved subsequently.
2. X and Y must be homogeneously distributed throughout the sample and separated by a distance that is smaller than the mean free path of each of the interacting defects[4].
3. The concentration of defect Y must be significantly larger than the concentration of defect X, so that the concentration of Y remains effectively constant.

If these conditions are fulfilled then the solution to a first order reaction is:

$$[X] = [X_0] \exp(-Kt) \tag{3-29}$$

where K is the decay rate and can be expressed as:

$$K = \upsilon_0 \exp\left[\frac{-E}{k_B T}\right] \tag{3-30}$$

where υ_0 and E are the characteristic attempt frequency and activation energy respectively. k_B is the Boltzman constant and T is the treatment temperature. K has units of inverse time.

3.5.2 Second order reaction

If the initial concentration of both X and Y defects (Equation 3-28) is equal then the reaction can be described by second order kinetics. The solution to second

[4]In the case of charge transfer this could involve the conduction or valence band, in which case the distance between defects being smaller than the mean free path is not a requirement. However, if the charge transfer involves only states within the band-gap then the impurities must be sufficiency close for direct electron transfer or quantum mechanical tunnelling between defects (defect band).

order kinetics is given by:

$$[X] = \frac{1}{[X_0]^{-1} + Kt} \tag{3-31}$$

If the concentrations of X and Y differ, but are of similar magnitudes the problem is more complex. Any solutions relevant to specific, more complex, reactions will be discussed in the appropriate chapter of this Thesis.

3.5.3 Experimental methods

Experimentally annealing can be carried out in two ways.

1. *Isochronal annealing* - Each treatment is performed at increasing temperatures, each treatment lasting for the same period of time. From isochronal annealing data, if the decays are assumed to be exponential, then an estimate of K and E can be obtained. The errors involved are typically large but the advantage of such experiments is that the *'characteristic annealing temperature'*, where reactions occur, can easily be determined.
2. *Isothermal annealing* - The temperature of each heat treatment is kept constant and the treatment is carried out over varying lengths of time producing a decay curve at the treatment temperature. If the decay curves are exponential then at each temperature a decay rate, K can be obtained from Equation 3-29 and from this an Arrhenius plot (lnK verses 1/T) can be constructed. From an Arrhenius plot a more accurate activation energy and attempt frequency can be obtained from the gradient and y-intercept respectively.

References

[1] O. Stern and W. Gerlach, Zeitschrift fur Physik **9**, 353 (1922).

[2] E. Zavoisky, J. Phys. USSR **9**, 245 (1945).

[3] F. Bloch, Phys. Rev. **70**, 460 (1946).

[4] A. M. Portis, Phys. Rev. **100**, 1219 (1955).

[5] W. V. Smith, I. L. Gelles, and P. P. Sorokin, Phys. Rev. Lett. **2**, 39 (1959).

[6] W. V. Smith, P. P. Sorokin, I. L. Gelles, and G. J. Lasher, Phys. Rev. **115**, 1546 (1959).

[7] C. A. J. Ammerlaan, *Paramagnetic centers in diamond* (Springer, 2001).

[8] C. D. Clark, R. W. Ditchburn, and H. B. Dyer, Proc. R. Soc. Lond. A. **237**, 75 (1956).

[9] J. A. Weil, J. R. Bolton, and J. E. Wertz, *Electron paramagnetic resonance* (Wiley-Interscience, New York, 1994), 2nd ed.

[10] A. M. Stoneham, *Theory of defects in solids* (Clarendon Press, Oxford, 1975), Chapter 13.

[11] A. Abragam and B. Bleaney, *Electron Paramagnetic Resonance of Transition Ions* (Oxford University Press, 1970).

[12] S. S. M. Wong, *Introductory nuclear physics* (Wiley, 1998).

[13] W. Jevons and A. G. Shenstone, Rep. Prog. Phys. **5**, 210 (1938).

[14] C. P. Slichter, *Principles of magnetic resonance* (Springer-Verlag, 1989).

[15] J. A. van Wyk, E. C. Reynhardt, G. L. High, and I. Kiflawi, J. Phys. D: Appl. Phys. **30**, 1790 (1997).

[16] M. H. Levitt, *Spin dynamics: Basics of nuclear magnetic resonance* (Wiley, 2001).

[17] M. Weger, Bell Syst. Tech. J. **39**, 1013 (1960).

[18] J. W. Stoner, D. Szymanski, S. S. Eaton, R. W. Quine, G. A. Rinard, and G. R. Eaton, J. Magn. Reson. **170**, 127 (2004).

[19] M. J. Shaw, P. R. Briddon, J. P. Goss, M. J. Rayson, A. Kerridge, A. H. Harker, and A. M. Stoneham, Phys. Rev. Lett. **95**, 105502 (2005).

[20] A. M. Edmonds, PhD. Thesis, University of Warwick (2008).

[21] A. Cox, D. Phil. Thesis, University of Oxford (1993).

Chapter 4

Experimental details

The majority of new experimental data contained within this Thesis are a result of EPR experiments. The experimental aspects of EPR have been well described in published texts. For example the EPR spectrometer operation is discussed in detail by Weil, Wertz and Bolton [1] and the individual spectrometer components are well described by Pools [2]. A brief discussion of the experimental set-up is included here, with particular attention paid to non-standard equipment and techniques used.

4.1 The electron paramagnetic resonance spectrometer

There are four essential components to any EPR spectrometer: an external magnetic field generator; a microwave source; a detection system; and a sample resonator. Each component will be discussed in turn.

4.1.1 The external magnetic field

In practice it is easier to sweep the external magnetic field, B_0, than change the frequency of the applied microwaves. The external magnetic field is varied, altering the separation between energy levels, with the microwave frequency locked to the sample resonator (e.g. constant), see Figure 3-1. The magnetic field is commonly generated by an electromagnet, although spectrometers have been constructed with superconducting magnets where fields >2 T are required. All of the spectrometers mentioned here use iron core electromagnets.

The requirements for the external magnetic field are:

1. To be uniform over the sample volume, which in the case of the average

diamond sample is easily achieved. For the Bruker system used here, a field inhomogeneity ($\frac{\Delta B}{B}$) over a cylindrical volume of 10 mm in length and 15 mm diameter, is no larger than 6×10^{-6} at 350 mT. The Varian magnet system has a similar inhomogeneity of 1.4×10^{-5} at 1400 mT over a cylinder 20 mm long and with a 30 mm diameter.

2. The linear sweep rate and range must be reproducible over thousands of repetitions. This is required for averaging the EPR signal over a large number of scans.
3. The magnetic field range must be large enough to encompass full, half and potentially third field transitions.

Given that the magnetic field generated from an iron core electromagnet is not linearly dependent upon the current, and that such a magnet may be subject to hysteresis, an active feedback loop is required to enable a linear, and repeatable field sweep. For this a Hall-probe is used, positioned as close to the sample position as possible, to supply a feedback voltage to the magnetic field controller. It is worth noting that the Hall-probe cannot give an absolute magnetic field reading, rather it reports a change in the field and so must be externally calibrated (usually with a known NMR signal). The temperature stabilised Hall-probe can repeatedly return the field to the same value, this allows repeatable scans over a magnetic field.

The rate of field sweep is generally slow ($\leq$0.1 mTs^{-1}). However, in this Thesis a regime has been investigated where the sweep rate is significantly faster ($\sim$2 mTs^{-1}).

4.1.2 The microwave source

The microwave sources used in EPR spectrometers typically take one of two forms: a Klystron source, or the now more commonly used Gunn diode. All of the spectrometers used in this work use a Gunn diode microwave source. EPR spectrometers operate at different frequencies and are therefore labelled by the microwave frequency, or the 'band' in which they operate. The most widely used frequency band is X-band operating at 8–12 GHz. In this work standard commercial X-band spectrometers were used alongside commercial and 'home-built'

Table 4-1: The frequency bands commonly used in EPR. The most common, X-band and Q-band are emphasised. g_e is the Zeeman splitting constant.

Band	Typical Freq (GHz)	~ Magnetic field for g_e (mT)	~Resonator dimensions (cm)
L	1.5	54	20
S	3.0	110	10
C	6.0	220	5
X	**9.5**	**340**	**3**
K	23	820	1.3
Q	**34**	**1300**	**0.8**
W	94	3400	0.3
D	150	5400	0.2
G	250	9000	0.1

Q-band (27–40 GHz) spectrometers. There are distinct advantages to each operating frequency and the combination of different frequencies can reveal more about the defect under investigation:

1. The absolute spin sensitivity of an EPR spectrometer typically improves with increasing microwave frequency [2]. However, the sensitivity depends on several factors and often the improved sensitivity is not realised. This is due to limitations on the sample volume and microwave power saturation at higher frequencies.
2. Increasing the volume of the resonator (Table 4-2) can make operations more simple, but consistent sample positioning can be difficult. This is a particular problem for quantitative measurements.
3. The higher the microwave frequency, the better the resolving power for defects with similar g-values.
4. Multi-frequency measurements facilitate the identification of field dependent (e.g. Zeeman) and field independent (e.g. hyperfine) terms in the spin Hamiltonian, see Chapter 7.

In commercially available spectrometers, the microwave source is contained within the microwave bridge. The microwave bridge also houses the detector diode, attenuator, reference arm and part of a feedback system to keep the frequency locked to the mode of the resonator (see Figure 4-1). In the case of the 'home-built' Q-band spectrometer, as used in Chapter 8, these components are separate.

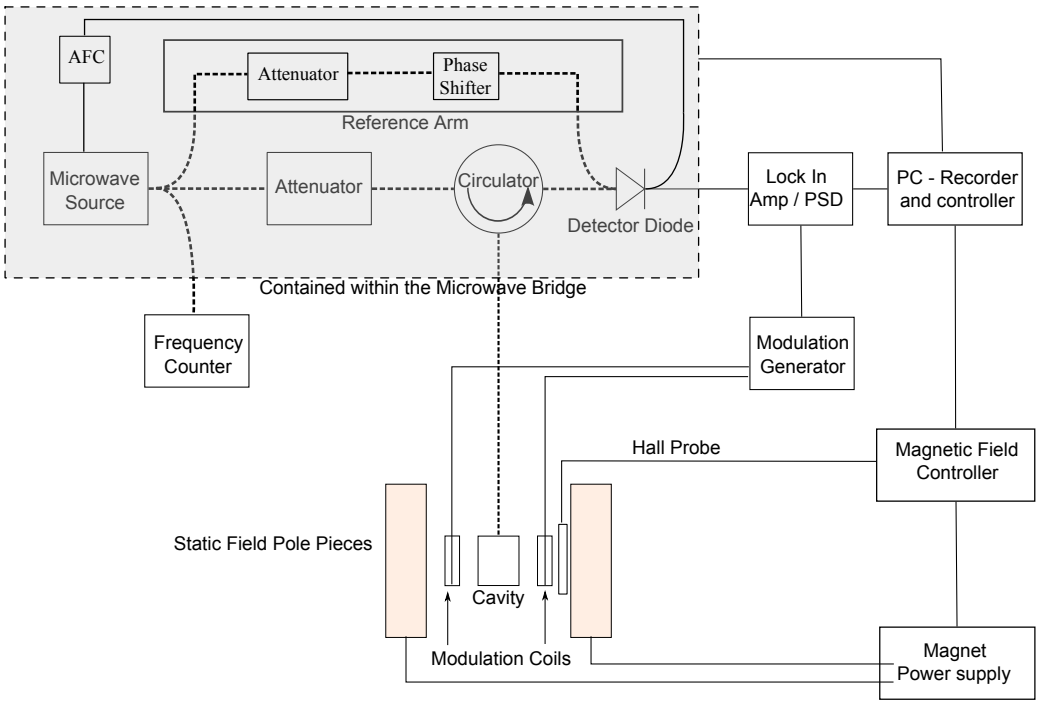

Figure 4-1: Block diagram of the EMX Bruker spectrometer [1, 2], the specifics of which are discussed in Section 4.1.4. The hardware contained within the bridge is marked including the circulator which is used to controls the direction of the microwaves. The path of microwaves is shown by the tight dotted line. Acronyms used are AFC (automated frequency control), and PSD (phase sensitive detection).

4.1.3 Detection of the EPR signal

The sample resonator (cavity in Figure 4-1) is critically coupled to the microwave bridge so that no microwave power is reflected from the resonator. When the spins in the sample are brought into resonance (by changing the magnetic field), the impedance of the resonator/sample system changes, the microwave power is reflected and the EPR signal detected.

An additional, sinusoidally fluctuating magnetic field, parallel to B_0 is applied to enhance sensitivity, the effect of which is described by Figure 4-2. This field modulation is 'transferred' to the microwave signal only at resonance. The amplitude of the microwave signal (modulated at the field modulation frequency) is proportional to the gradient of the absorption lineshape, thus the phase sensitive detection (PSD) signal is a differential absorption lineshape.

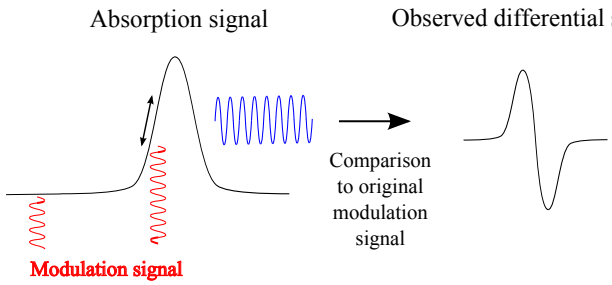

Figure 4-2: Graphical representation of the effect on the resonant microwave absorption signal of a small amplitude field modulation. The resulting first derivative EPR signal, detected with the field modulation and a lock in amplifier is shown on the right hand side.

4.1.3.1 Automatic frequency control (AFC)

The microwaves are frequency modulated (typically at 50-70 KHz). If the microwave frequency drifts off of the precise resonant frequency of the sample resonator, an error signal (at the frequency modulation frequency) is detected. This is used in the automatic frequency control (AFC) feedback loop to correct the microwave frequency back to resonance (see Figure 4-1).

4.1.4 EPR spectrometer detail

The specifications of the EPR spectrometers used here are as follows:

- Bruker EMX and EMX-E systems with transferable microwave bridges. The EMX system is capable of Q-band operation (this has been used in Chapter 7).
- The 'home-made' Q-band spectrometer was initially constructed at the Clarendon Laboratory, Oxford, and is thoroughly discussed by Twitchen [3] and Talbot-Ponsonby [4], modifications made to the acquisition software are discussed by Edmonds [5].
- The X-band bridges produce a maximum power of 200 mW. One bridge attenuates the power to 60 dB and the other to 90 dB, with minimum powers of 200 and 0.2 nW respectively.
- The modulation frequency of the PSD in the commercial Bruker equipment was standardised to 100 kHz, and the home-built system to 115 kHz.
- Cavities were moved between X-band spectrometers for specific experiments.

However, the majority of experiments were carried out with the following experimental set-ups;

1. EMX-E, 90dB, Super high quality cavity (SHQ)
2. EMX, 60dB, High quality cavity (HQ), as well as the High and low temperature cavities (HT, LT) see Table 4-2

4.1.5 Resonant cavities

A resonator is used in EPR to amplify weak absorption signals which would otherwise be impossible to detect. The resonator is typically a resonant cavity, as used here, but it is also possible to use a loop-gap or dielectric resonators [6]. No results are presented here using these resonant structures and so they will be discussed no further.

A resonating cavity can be simply thought of as a metal box with comparable dimensions to the wavelength of the applied microwaves, see Table 4-1. The microwave frequency is locked to the resonant frequency of the sample cavity by the AFC system. The cavity is 'critically coupled', meaning that it is critically matched to the transmission line (waveguide) with no reflected power. Hence, all the microwave energy will either be stored in, or dissipated from, the cavity (e.g. by the heating of the cavity walls through surface currents).

4.1.5.1 Quality factor

The quality or Q-factor is a measure of how much energy is stored in the cavity. The larger the Q-factor the more energy is stored in the resonator and the better the sensitivity. (In the absence of microwave power saturation, see Chapter 3.) Q-factor can be calculated through Equation 4-1 and is calculated in the commercial Bruker software as, $\frac{\upsilon_{res}}{\Delta\upsilon}$. That is, the ratio between the resonant frequency of the mode, υ_{res}, and the full-width half-maximum of the resonant mode, $\Delta\upsilon$.

$$Q = \frac{\text{energy stored per cycle}}{\text{energy dissipated per cycle}} = \frac{\upsilon_{res}}{\Delta\upsilon} \tag{4-1}$$

Table 4-2: Names and descriptions of EPR resonant cavities used in this Thesis.

Name	Referred to	Supplier	part no.	Band	Shape	Mode
Super High Q	(SHQ)	Bruker	ER4122	X	Spherical	TE_{011}
High Q	(HQ)	Bruker	ER4119HS	X	Cylindrical	TE_{011}
Low Temp	(LT)	Bruker	ER4105DR	X	Rectangular	TE_{104}
High Temp	(HT)	*Wroclaw	EX-102	X	Cylindrical	TE_{011}
Q-band	(Q)	Bruker	ER5102QT	Q	Cylindrical	TE_{011} / TE_{012}

*This cavity was custom made, see [3], by The Technical University of Wroclaw, Poland.

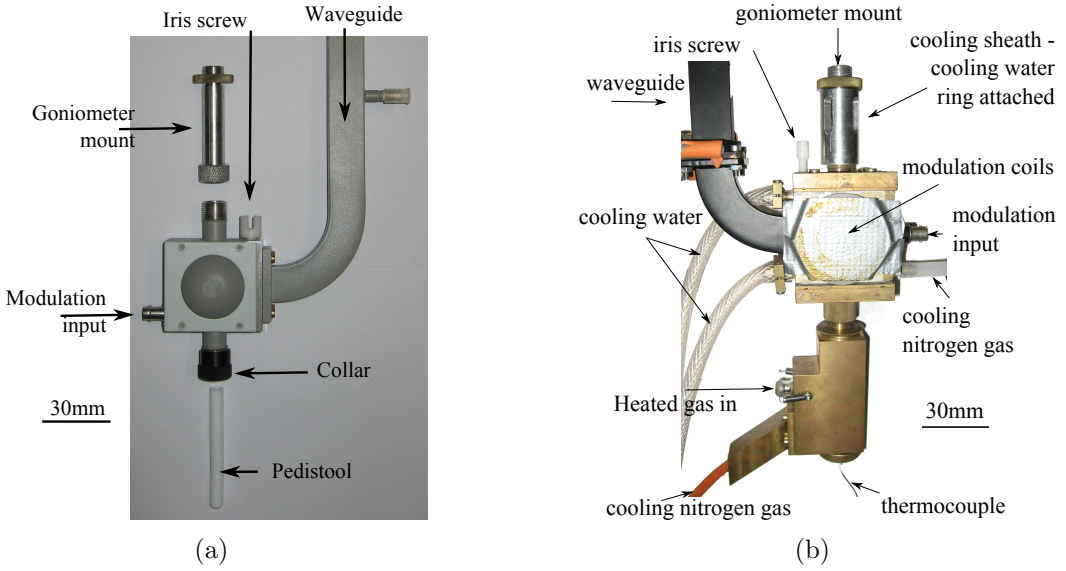

Figure 4-3: Labelled photographs of the (a) super high Q (SHQ) and (b) high temperature (HT) cavities used in this study, see Table 4-2.

4.1.5.2 E and B field components of the microwave radiation

Cavities are carefully designed and constructed to support a standing wave, maximising the magnetic field (B) component and minimising the electric field (E) component of the microwave radiation at the sample. The microwave magnetic field, B_1, is oriented perpendicular to the static Zeeman field. Cavities are built to favour a single mode and are named according to that mode. TM describes a transverse magnetic field mode and TE a transverse electric field mode. Subscripts denote the number of half-wavelengths in the three dimensions that the modes describe. As a result cavities can differ in dimensions but still operate at the same frequency.

Microwaves are transported to the cavity by a waveguide or coaxial cable; the size of the former being dependent upon the frequency band. It is essential that the waveguide and cavity are 'critically coupled' when the spin system is off

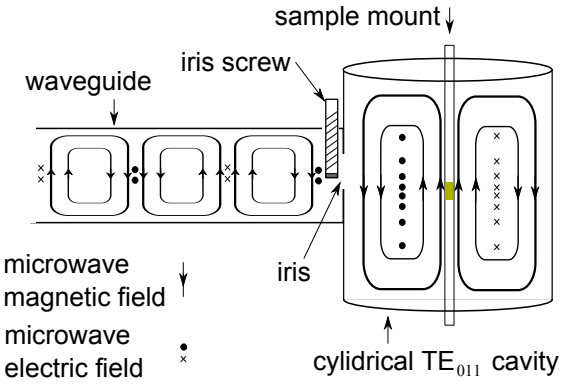

Figure 4-4: A labelled diagram of the magnetic and electric field lines set-up inside a cylindrical TE_{011} resonant cavity. An iris and iris screw are shown, but any affect on the fields is neglected in this figure. Adapted from [2].

resonance. This coupling is achieved through changing the impedance of the iris. In most cases, at X-band, a plastic screw is used with a metal cap, see Figure 4-3 and 4-4.

The sample and sample mounts affect the Q-factor and coupling of the cavity. To reduce these affects, sample mounts are constructed from a low dielectric loss material. Here either PTFE or Rexolite© is used.

4.1.6 Quantitative EPR

The EPR signal strength is dependent upon the number of spins present in the sample, and the number of spins is proportional to the concentration of the paramagnetic defect. Hence, the EPR signal strength is a measure of defect concentration. The number of spins in an unknown sample (s) is compared to a known reference sample (ref). The signal strength is determined by the double integration of the first derivative EPR lineshape, see Figure 4-2. There are a number of factors and experimental parameters which affect the relative signal intensity. These are included in Equation 4-2 [1] which is used to return a defect concentration in the sample of interest [s].

$$\frac{[\mathrm{s}]}{[\mathrm{ref}]} = \frac{I_\mathrm{s}}{I_\mathrm{ref}} \frac{\eta_\mathrm{ref}}{\eta_\mathrm{s}} \frac{Q_\mathrm{ref}}{Q_\mathrm{s}} \frac{\sqrt{(P_{\mu\mathrm{w}})_\mathrm{ref}}}{\sqrt{(P_{\mu\mathrm{w}})_\mathrm{s}}} \frac{M_\mathrm{ref}}{M_\mathrm{s}} \frac{(B_\mathrm{m})_\mathrm{ref}}{(B_\mathrm{m})_\mathrm{s}} \frac{g_\mathrm{ref}^2}{g_\mathrm{s}^2} \frac{S(S+1)_\mathrm{ref}}{S(S+1)_\mathrm{s}} \frac{t_{d\mathrm{ref}}}{t_{d\mathrm{s}}} \frac{G_\mathrm{ref}}{G_\mathrm{s}} \frac{N_\mathrm{ref}}{N_\mathrm{s}}, \qquad (4\text{-}2)$$

Where I denotes the integrated intensity, η is the filling factor (the fraction of the cavity volume occupied by the sample). Q is the quality factor, $P_{\mu\mathrm{w}}$ is the microwave power, M is the sample mass, B_m is the modulation amplitude, g is the defect's g-factor, S is the spin of the system, t_d is the dwell time, G is the receiver gain and N is the number of scans. The square brackets here denote the defect concentration in [s] the sample of interest and [ref] the reference sample.

The integrated intensity is determined by fitting a simulated defect spectrum to the obtained experimental spectrum. This allows the simultaneous fitting of overlapping spectra from different defects and facilitates deconvolution. This fitting method has been shown by Edmonds [5] to be significantly more reproducible than simple integration [7].

The reference sample is selected to be similar to the sample under investigation. The reference sample used in this work is a type Ib single-sector HPHT sample containing 270(30) ppm of single substitutional nitrogen, N_S^0 (determined from FTIR measurements).

In order to reduce the errors in quantitative EPR a uniform microwave magnetic field over the entire sample is necessary. Hence, the consistent positioning of samples is essential for reproducible quantitative measurements.

The detection limit quoted by Bruker for a commercially available X-band spectrometer are $\sim 10^{11}$ spins per mT. These are achieved by using a sample with characteristics that are optimal to achieve a high sensitivity.

Usually for quantitative comparative measurements on paramagnetic defects in single crystal diamond the Zeeman field is applied along the same crystallographic axis. Sample orientation cannot be easily determined when defect concentrations are low. However, experimental data collected here has shown that mis-orientation by ±20° does not adversely influence the measured paramagnetic defect concentration.

4.1.7 Variable temperature EPR

EPR experiments were conducted at temperatures between 4 and 850 K. The high and low temperature EPR systems used here are described by Edmonds [5].

For experiments in which the EPR signal is monitored as a function of treatment temperature, the errors associated with re-positioning the sample after each treatment can be minimised by carrying out the entire experiment in the high temperature cavity.

For the systems studied here no changes in the defect concentrations have been observed as a result of a treatment below 550 K. The highest treatment temperature used in this work was 850 K for a period of 10 minutes. The time the

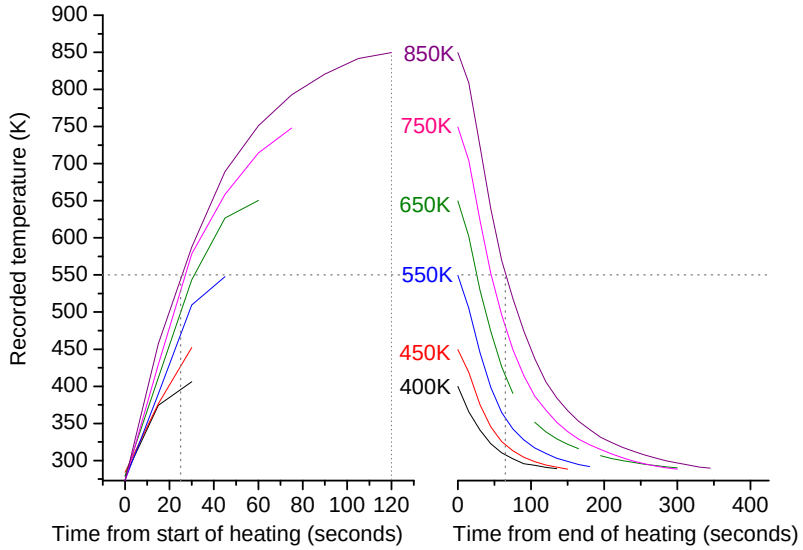

Figure 4-5: Ramp up and down rates of the high temperature cavity over its full working temperature range. 550 K, marks the temperature threshold at which charge transfer processes have been observed.

sample spends between 550 and 850 K during the temperature ramp up and down is ~160 seconds, see Figure 4-5. This is typically ~ $\frac{1}{5}$ of the total treatment time. No allowance has been made for these heating and cooling times, but simulations suggest that this does not introduce significant errors.

There are some limitations with the high temperature system:

(a) Once the sample is inside the cavity it remains there throughout the experiment, which means that complementary optical experiments cannot be carried out.

(b) The sample size is restricted to a maximum of 4 mm in any dimension due to the internal cavity structure.

(c) The high temperature cement (FortaFix Autostic FC6: High temperature Adhesive) used to fix the sample to the quartz mount can produce an EPR signal. Once the cement has been heated to above 700 K an enhanced broad signal around $g = 2$ is observed which is not removed by illumination or cooling. This signal is primarily a problem when quantifying the concentration of NVH^-, since the EPR signature from the cement and NVH^- defect overlap.

(d) Illumination of the samples whilst inside the cavity is possible. However, for a strongly absorbing sample, illumination from one side may be insufficient to uniformly irradiate the entire sample.

4.1.7.1 Optical illumination

Throughout this work, illumination has been provided by a high pressure 200 W Hg-Xe arc lamp. Illumination outside the cavity was done with an unfocused beam for a period of ~5 minutes, where, in each case further illumination had no further effect on defect concentrations. Samples have also been illuminated in-situ using the set up shown in [5]. In this set-up, a collimated 200 W beam is passed through a high pass filter[1] and focused onto a liquid light guide[2], which is held against the protruding end of the quartz rod (sample mount). The sample is mounted on the other end of the rod which has been polished for optimum transmission.

4.2 Annealing

As mentioned in Section 3.5, annealing has been carried out at temperatures where defect concentrations are permanently changed. In this work the 'annealing' has been performed in a tube furnace at atmospheric pressure after the tube has been purged with high purity nitrogen gas. Throughout the anneal, the pressure inside the tube is kept slightly elevated to prevent other gases from entering, so discouraging graphitisation or surface 'frosting'. As an additional precaution, the sample is placed in an alumina boat and covered with sacrificial diamond grit/powder with which any residual oxygen will react (rather than with the diamond surface), see Figure 4-6. Three furnaces were used in this work:

1. Lenton Thermal Designs Ltd. horizontal tube furnace, used for the annealing work presented in Chapter 8 and discussed by Cruddace [7].
2. Elite TSH116/50/180-2416 tube furnace, as shown in Figure 4-6. This furnace displayed a sharper temperature profile resulting from the use of radi-

[1] High pass filters ranged from 2.5-4.5 eV.

[2] A 0.5 m, 5 mm diameter liquid light guide which transmits light of wavelength ~250–750 nm, although the transmission is not consistent across all wavelengths.

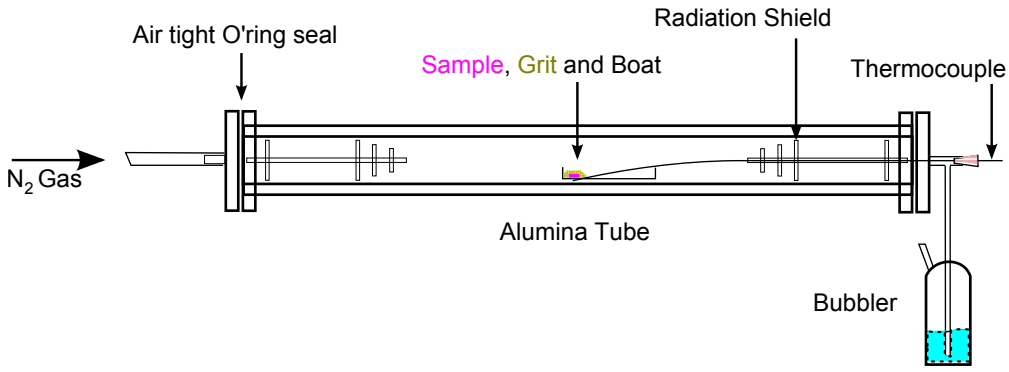

Figure 4-6: Labelled diagram of the 'Elite' tube furnace capable of ~1900 K under vacuum. In this work the furnace has been used with a nitrogen gas flow and bubbler as shown.

ation shields and a shorter temperature stabilisation time.

3. Carbolite-MTF mini tube furnace which uses a quartz rather than alumina tube. The quartz tube which can be ramped at 50 K per minute, but is limited to ~1300 K.

The charge transfer treatments outside of the high temperature cavity were carried out in the dark using the mini tube furnace. Rapid cooling was achieved by submersion of the diamond in deionised water.

Sample preparation following each anneal involved thorough cleaning in sulphuric acid (H_2SO_4) saturated with potassium nitrate and boiled at 523 K for ~10 minutes.

References

[1] J. A. Weil, J. R. Bolton, and J. E. Wertz, *Electron paramagnetic resonance* (Wiley-Interscience, New York, 1994), 2nd ed.
[2] C. P. Poole, *Electron spin resonance* (Dover publications, New York, 1983), 2nd ed.
[3] D. Twitchen, D. Phil. Thesis, University of Oxford (1997).
[4] D. Talbot-Ponsonby, D. Phil. Thesis, University of Oxford (1997).
[5] A. M. Edmonds, PhD. Thesis, University of Warwick (2008).
[6] W. Froncisz and J. S. Hyde, J. Magn. Reson. **47**, 515 (1982).
[7] R. J. Cruddace, PhD. Thesis, University of Warwick (2007).

Chapter 5

Quantitative rapid passage EPR

5.1 Overview

The concentration of defects in high purity single crystal (SC) diamond grown by CVD is below the detection limits of techniques such as infrared absorption. Defect concentrations are now so low that the detection limits for all EPR active defects are being challenged.

Ultra high purity SC-CVD diamond has been synthesised by Element Six Ltd. During growth, particular care has been taken with the substrate preparation, the gas purity and minimising reactor leaks. This work has proved very successful, having grown CVD diamond with undetectable concentrations of paramagnetic neutral single substitutional nitrogen (N_S^0), as studied using quantitative slow passage (SP) EPR. In this high purity diamond, no other point defects have been observed apart from the neutral (NV^0) and negatively (NV^-) charged nitrogen-vacancy centres, which are detected by low temperature photoluminescence (PL) [1]. In high quality, electronic grade diamond the concentration of N_S^0 is significantly greater than the concentration of other defects. Hence, the concentration of N_S^0 is a good indicator of sample purity and the electronic properties of the diamond [2].

In this chapter, the possibility of using rapid passage (RP) EPR techniques to lower the detection limit for N_S^0 in diamond will be discussed. Ultimately, it is hoped that the acquisition time required to assay the concentration of N_S^0 in high purity diamond will be reduced. Thus, making more economical use of EPR spectrometers and making EPR a viable quality control technique for the monitoring of commercially grown diamond.

5.1.1 Historical review

The theory underpinning the observation of magnetic resonance signals was first published by Bloch in 1946 [3]. In his paper, Bloch describes the influence on the magnetisation of modulating the magnetic field. In this paper Bloch produced a mathematical description of RP and SP magnetic resonance. RP-EPR signals were first observed in 1955 by Portis [4] in irradiated LiF. Portis observed a broad resonance resulting from the use of a small modulating magnetic field which was 90° out of phase with the detection phase. Portis explained those observations in terms of Bloch's description of RP magnetic resonance [4].

Microwave power saturation at 'moderate' incident microwave powers is an experimental complication which occurs as a result of long spin-lattice and spin-spin relaxation times (τ_1 and τ_2). For paramagnetic defects in solids, τ_1 and τ_2 are often sufficiently long that microwave power saturation is a problem for SP-EPR. However, for a RP-EPR signal to be observed microwave power saturation is necessary. The quantitative use of RP-EPR has been demonstrated for other materials where microwave power saturation is a problem for quantitative SP-EPR, e.g. Si [5] and SiO_2 [6].

5.1.2 Detection limits

SC-CVD diamond samples (typically $4 \times 4 \times 0.5$ mm) with N_S^0 concentrations below ~1 ppb (2×10^{14} cm^{-3}) present a serious challenge for commercial EPR spectrometers, even though the quoted spin sensitivity is 10^{11} spins per mT. A concentration of ~1 ppb of N_S^0 in a $4 \times 4 \times 0.5$ mm diamond corresponds to ~ 10^{12} spins [7]. The EPR line-width is only 0.02 mT and so on first impression this should be well above the detection limit. However, a commercial EPR spectrometer's sensitivity and its detection limits are dependent upon a number of factors (these are covered in more detail in Chapter 4):

1. The Q or quality factor - (see Section 4.1.5.1.)
2. The filling factor - (see Section 4.1.6.)
3. The signal-to-noise ratio - which is proportional to the square root of the number of accumulations (~ $\sqrt{N}$), however, there is a practical limit on

how beneficial extended averaging can be. Averaging over 5000 scans (i.e. a weekend run) will improve the signal-to-noise ratio by a factor of 70 from that of a single scan (assuming the noise is random). During this work the signal-to-noise ratio has been observed to be proportional to $\sim \sqrt{N}$ for up to 40,000 RP-EPR scans.

4. Microwave power saturation - The signal intensity scales linearly with the square root of the microwave power in the absence of microwave power saturation. Outside this regime, saturation can lead to a significant underestimation of the defect concentrations [8]. This underestimation is a problem for EPR measurements of N_S^0 in diamond and other defects with long relaxation times. This not a problem for the reference samples used when quoting spectrometer sensitivities since those samples do not saturate even at power levels >10 mW.

The SP-EPR detection limit for N_S^0 in a diamond of volume ~0.02 cm^3 with an incident microwave power of 0.2 nW (the maximum attenuation of the system used here) should be ~20 ppb. Increasing the microwave power should, in the absence of microwave power saturation, reduce the detection limit. However, even with an incident power of a few tens of nW microwave power saturation becomes a problem. The detection limit for SP-EPR of 1 ppb has been achieved by fitting data to the microwave power saturation curve, however, this is time consuming and the errors introduced can be large. An alternative technique which is not affected by microwave power saturation is required. In contrast to SP-EPR, with RP-EPR microwave power saturation is not a problem and it will be shown here that an N_S^0 RP-EPR signal can be a quantifiable measure of defect concentration.

5.1.3 Rapid passage

Equation 3-27 must be satisfied in order for the passage through an EPR transition to be described as 'rapid'. In an unsaturated SP-EPR experiment the microwave magnetic field strength, B_1 (see Section 4.1.2), is so small that the spin magnetisation is only slightly perturbed. In RP-EPR, B_1 is large so that the impact is more comparable to that of a pulsed EPR experiment [9]. In RP-EPR, strong passage signals which are out of phase with SP-EPR signals are detected. The

response is typically very sensitive to the field sweep rate (both the external field, B_0, and the field modulation, B_m), as well as τ_1 (spin-lattice relaxation time), τ_2 (spin-spin relaxation time), B_1 and the temperature. However, in this work a set of experimental conditions were used for which the RP-EPR signal is proportional to the concentration of N_S^0 in diamond over three orders of magnitude. The observed RP-EPR transition has an absorption lineshape, rather than the derivative lineshape observed in SP-EPR.

5.1.4 Theoretical description of RP-EPR

Harbridge *et al.* [6] used the Bloch equations (including field modulation) to model the response of a single spin-packet when the magnetic field was swept rapidly through resonance. The simulated spectra were calculated by considering the contribution from a collection of 'spin-packets'. When B_1, B_m and the sweep rate are sufficiently large, the dominant signal is observed 90° out of phase to that which is observed for the detection of a SP-EPR signal. The RP-EPR lineshapes modelled by Harbridge *et al.* [6] have an absorption lineshape, the same shape as those observed by experiment.

For the sweep rate to be considered large it must be sufficiently rapid when compared to the relaxation times. In the case of N_S^0 in diamond at room temperature, the τ_1 and τ_2 relaxation times are of the order 2-3 ms and 7-7000 μs respectively [10, 11].

5.2 Experimental details

A range of samples were studied from two different suppliers (see Table 5-1 and Appendix A): Apollo Diamond and Element Six Ltd. All samples are [100] grown homo-epitaxial plates that vary in mass from 10.9 to 88.5 mg and have N_S^0 concentrations in the range 0.1–1600 ppb. No details of the growth conditions have been made available.

SP-EPR measurements were recorded using a Bruker EMX-E spectrometer in the standard configuration described in Section 4.1.4. All measurements were made at room temperature using a single axis goniometer. The samples were

Table 5-1: Samples used in this Chapter for the quantitative investigation of RP-EPR.

Sample	Mass (mg)	$[N_S^0]$ (ppb)
A	70	130
Q	80	1590
R	89	41
S	56	3.5
T	57	0.6
U	53	0.1
V	51	1.5
W	35	63
X	64	119
Y	52	223
Z	59	228
α	6	456
β	81	503
γ	47	559

aligned such that the external magnetic field was parallel to the [001] crystallographic axis of the sample. Concentrations were determined from SP-EPR by comparison to a reference sample, see Section 4.1.6.

There are certain experimental limitations to be considered when using RP-EPR:

1. A one second delay is required before each RP-EPR scan to allow the magnetic field to stabilise before the next scan starts. Such delays were used in this work and have been accounted for when averaging times are quoted.
2. Even after implementation of precaution (1), the actual magnetic field and the field indicated by the spectrometer do not agree at the start of each scan. This is due to the 'inertia of the magnet system' and hence, the two require time to equalise. The faster the scan the larger the required 'buffer' to each scan before the fields agree.[1] With the conditions used here, the scan should start ~5.0 mT away from the transition of interest.
3. The RP-EPR signal is sensitive to the concentration of other defects in the sample. This is the result of cross-relaxation between defects which can be particularly effective where energy levels are similarly matched. For example, the EPR transitions from the P2 [12] and NVH^- [13] defects are observed at similar magnetic fields (transition energy) to the central $^{14}N_S^0$ transition.

[1] This is particularly important when using RP-EPR to obtain spin Hamiltonian parameters of a new defect, see Chapter 7.

Table 5-2: Optimum RP-EPR conditions determined for two different spectrometer configurations (see Section 4.1.4), compared to typical SP-EPR conditions.

Cavity	Typical SP-EPR conditions SHQ, 90 dB, EMX-E	Typical RP-EPR conditions SHQ, 90 dB, EMX-E	Typical RP-EPR conditions HQ, 90 dB, EMX-E
Modulation Amp. (mT)	0.01–0.1	0.002	0.002
Attenuation (dB)	60	29-30	27
Power (μW)	0.2	200–250	400
$\frac{dB_0}{dt}$ (mTs^{-1})	0.012	1.91	1.91

Hence, a concentration measurement of one defect made by RP-EPR might be affected by the concentration of the other defect. This has not been accounted for in some past literature [14] where the concentration of N_S^0 has been suggested from RP-EPR experiments where P2 is also present.

5.3 Results

As stated, the RP-EPR signal strength is dependent upon B_1, B_m and the sweep rate. These parameters were optimised for the set-ups used here to produce the greatest possible signal-to-noise ratio for the RP-EPR N_S^0 signal. Optimum conditions are given in Table 5-2. Figure 5-1 shows the variation in the signal strength with the microwave power attenuation. Figure 5-1 shows four samples with a three order of magnitude spread in N_S^0 concentrations, from 1590(160) ppb (Sample Q) to 0.6(2) ppb (Sample T), see Table 5-1. Over this range, the peak RP-EPR intensity is attained between microwave power attenuations of 29 and 30 dB. The variation in RP-EPR intensity for each of the four samples between 29 and 30 dB is less than 10%.

Figure 5-2 shows EPR spectra from Sample V (see Table 5-1) which contains 1.5(3) ppb of N_S^0. This concentration has been determined by using conventional SP-EPR at a power which substantially avoids microwave power saturation (69 dB, 25 nW) for ~13.5 hours, over a sweep width of 2.5 mT. This SP-EPR scan resulted in a signal-to-noise ratio[2] of 15:1. The RP-EPR spectrum, also from Sample V, acquired at 0.2 mW (30 dB) for ~19 minutes, over a sweep width of 10 mT resulted

[2]Ratio of the peak-to-peak signal height to the magnitude of a single standard deviation of the noise.

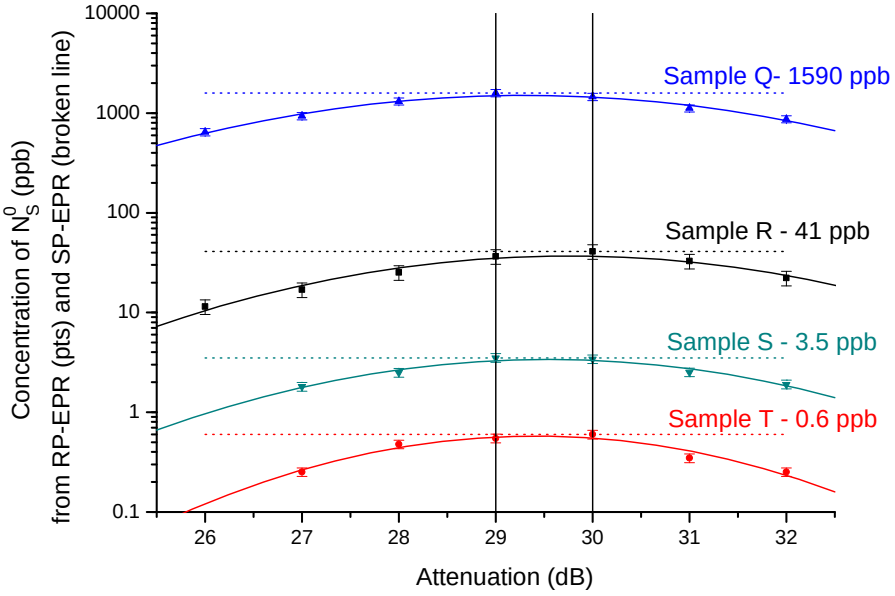

Figure 5-1: The variation in signal strength with microwave power attenuation in the SHQ cavity. The RP-EPR signal intensity (data points) and SP-EPR concentration (broken line) is shown from samples with a range of N_S^0 concentrations (0.6–1590 ppb). The peak intensity of the RP-EPR signal is normalised to the concentration determined by SP-EPR. In each case the peak intensity of the RP-EPR signal is between 29 and 30 dB. Solid curves are given as a guide to the eye only.

in a signal-to-noise ratio[3] of 30:1.

The reproducibility[4] of RP-EPR has been investigated for Sample R and has been shown to be similar to that of SP-EPR.

The HT cavity was used to isochronally heat treat a single sample (Sample A) at increasing temperatures. This reduced the concentration of N_S^0 in sample A from ~130 ppb to ~ 20 ppb, via a charge transfer mechanism, which is discussed in Chapter 6. SP-EPR and RP-EPR measurements were taken after each treatment temperature. This configuration is the optimum with which to assess the quantitative nature of RP-EPR because errors related to sample positioning, and any variation in sample size are eliminated. Figure 5-3 shows a linear relation between the RP-EPR signal strength and the N_S^0 concentration obtained from SP-EPR using the heat treatment method.

[3]Ratio of the peak signal height to the magnitude of a single standard deviation of the noise.

[4]This involves the complete removal and remounting of the sample between experiments.

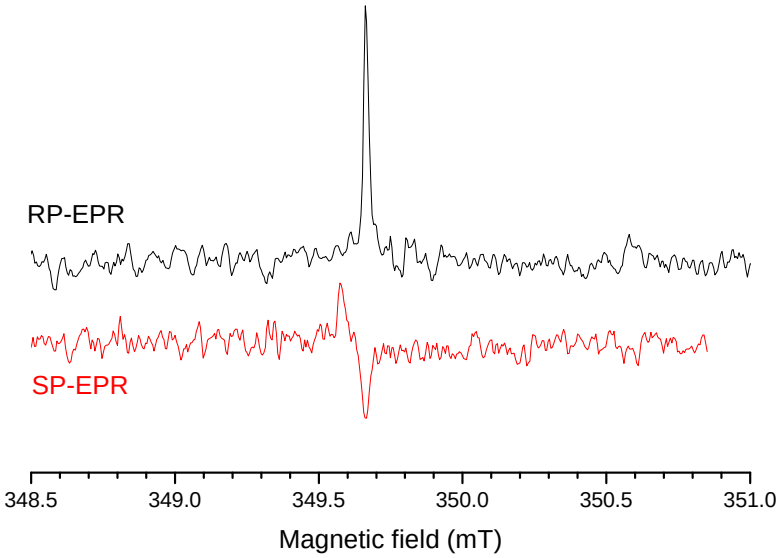

Figure 5-2: EPR spectra obtained from Sample V, (1.5(3) ppb N_S^0). The SP-EPR spectrum (red when in colour) was obtained in ~13.5 hours with 66 dB attenuation and over modulation (0.1 mT) so to avoid microwave power saturation. A signal-to-noise ratio of 15:1 was obtained from this SP-EPR spectrum. The RP-EPR spectra shown is also from Sample V, but obtained in ~19 minutes at 29 dB, with a signal-to-noise ratio of 30:1.

Figure 5-4 shows the integrated intensity of the RP-EPR signal per scan per unit mass (mg) plotted against the concentration of N_S^0 in each sample studied. The N_S^0 concentrations are determined from SP-EPR in the conventional manner.

The data marked with black squares are from the SHQ, 90 dB experimental set-up and the red circles represent the data taken from the high temperature cavity (Figure 5-3). The RP-EPR signal intensities from Figure 5-3 were scaled (using different experimental resonators) so that the two plots overlay.

The concentrations observed in the highest purity diamond samples are below the detection limit of SP-EPR. For example, the N_S^0 defect was not observed in Sample U using SP-EPR but was detected using RP-EPR. Using the RP-EPR intensity for this defect and the gradient (151(7) RP-EPR signal intensity per mg per 40,000 scans per ppb N_S^0) from Figure 5-4 an N_S^0 concentration of 0.10(2) ppb is determined for Sample U.

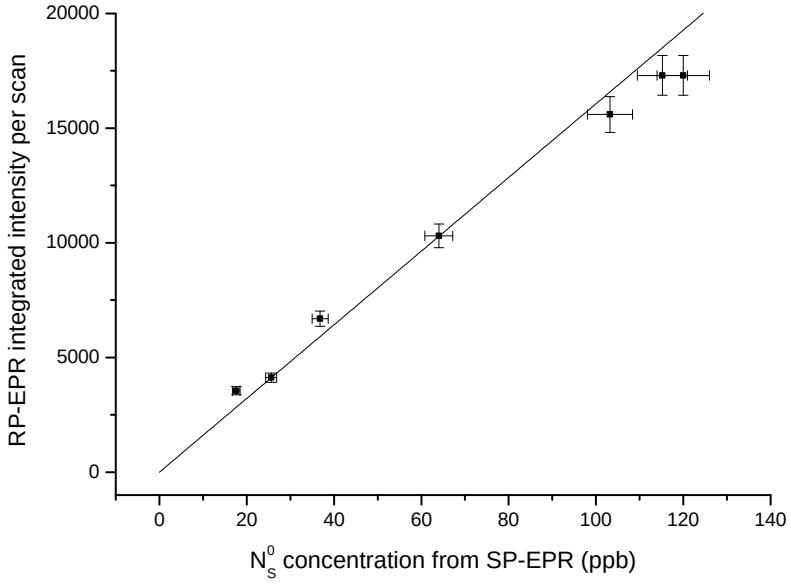

Figure 5-3: The integrated intensities of the N_S^0 spectra from RP-EPR in Sample A following a series of heat treatments in the HT cavity to change the N_S^0 concentration, are plotted against the concentration of N_S^0 determined from SP-EPR in the HT EPR cavity. Error bars in both cases are estimated at 5%.

5.3.0.1 Detection limits

Although possible, it is impractical to accumulate a single spectum for much longer than a weekend, during which ~40,000 RP-EPR scans can be accumulated. Since the N_S^0 EPR spectrum is well characterised and there are no other overlapping spectra it is estimated that a signal-to-noise ratio of 2:1 is required to recognise the defect. With a standard 50 mg diamond sample in the SHQ cavity, after 40,000 scans (Figure 5-5) a signal-to-noise ratio of 2:1 would suggest a concentration of ~0.01 ppb or 10 parts per trillion. This represents a factor of 100 improvement in the detection limit compared with what can be achieved with SP-EPR.

The optimum RP-EPR detection parameters for N_S^0 using the HQ cavity are given in Table 5-2. The HQ cavity exhibits significantly poorer sensitivity than that achieved with the SHQ cavity. The extrapolated N_S^0 detection limit is 0.4 ppb with the HQ EPR cavity under the same conditions (40,000 scans 50 mg sample).

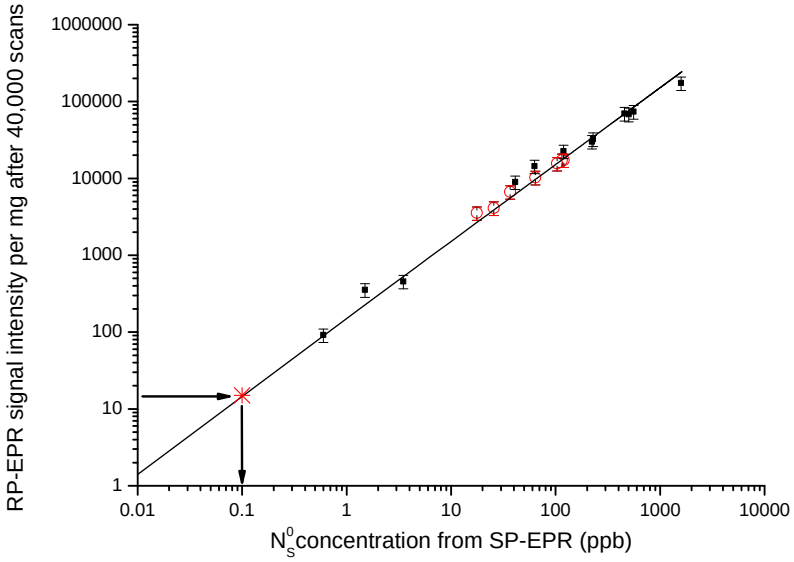

Figure 5-4: The RP-EPR integrated intensity of the N_S^0 signal, from the samples detailed in Table 5-1 plotted against the concentration of N_S^0 determined from SP-EPR. The circles (red when in colour) represent the data overlayed from the HT cavity (Figure 5-3). Sample U (indicated by the star) is positioned by the RP-EPR signal intensity only. The best fit line shown has a gradient of 151(7) RP-EPR signal intensity per mg per 40,000 scans per ppb of N_S^0.

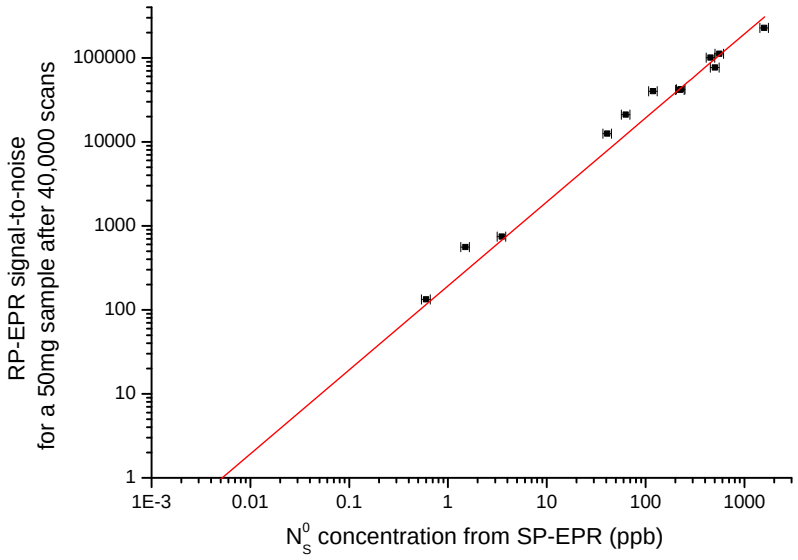

Figure 5-5: The projected variation in signal-to-noise ratio of the RP-EPR N_S^0 signal for a standard sized sample (50 mg), run over a weekend (40,000 scans), in the SHQ cavity plotted against the concentration of N_S^0 determined from SP-EPR (±10%). The fit is constrained through the origin.

5.4 Discussion

For quantitative measurements of the concentration of N_S^0 in CVD diamond, when the N_S^0 concentration is less than ~2 ppm, RP-EPR produces spectra with considerably better signal-to-noise ratios in less time than using conventional SP-EPR. At higher concentrations the spin-spin interactions reduce τ_2 sufficiently that the RP-EPR signal intensity will underestimate the defect concentration. There is some deviation from the linear relation between RP-EPR intensity and N_S^0 concentration at higher concentrations which is consistent with this explanation. Hence, SP-EPR becomes the method of choice to measure higher N_S^0 concentrations.

RP-EPR has been used in the past to study paramagnetic defects in irradiated LiF [6, 15], where the different relaxation rates of different paramagnetic defects have been used to 'disentangle' two overlapping spectra. This effect is used in Chapter 7 to disentangle the WAR2 and H1 spectra.

The RP-EPR signal is dependent upon the local defect concentration and cross-relaxation between defects. N_S^0 is the most abundant defect in the CVD samples studied. The concentration of other paramagnetic defects are sufficiently low that cross relaxation is not a issue. This is particularly significant where EPR transitions from different defects overlap with one another, as described in Section 5.2.

In samples of a typical size (50 mg), concentrations of N_S^0 lower than 0.5 ppb cannot be detected in a SP-EPR experiment. However, here RP-EPR has been used over a concentration range of 0.1–1000 ppb to determine the concentration of N_S^0 in a CVD diamond sample. Assuming that the RP-EPR signal varies linearly with the concentration of N_S^0 below ~1 ppb (see Figure 5-5), it is estimated that the RP-EPR detection limit for N_S^0 in diamond is ~10 ppt, a factor of 100 lower than with SP-EPR. This detection limit is equivalent to ~ 10^{13} spins per mT, still a factor of ~100 worse than that suggested possible by Bruker [7]. This discrepancy can be partially accounted for by the poor filling factor achieved with diamond samples, which are typically a factor of 30 smaller than that of the reference samples used by Bruker [16]. In addition, the applied microwave power for RP-EPR is factor of three lower than that used for the Bruker reference samples [7].

The time saving potential of RP-EPR is demonstrated by Sample U. The N_S^0

concentration has been determined by RP-EPR to be 0.10(2) ppb. To determine this concentration from SP-EPR would have taken longer than 20 days. That is assuming that the spectrometer remains sufficiently stable for such a measurement to be successful.

The detection limits quoted here are the limits of the experimental equipment to detect the paramagnetic N_S^0 defect. There may be other defects in the diamond sample that cause N_S to be present in a diamagnetic state and so remain undetected by EPR. In the absence of an acceptor (e.g. boron) it is reasonable assume that the concentration of N_S^0 is significantly larger than the concentration of N_S^+. Boron is readily incorporated into CVD diamond and because of this great efforts must be taken to exclude it from the growth environment. If such an acceptor is present then EPR will underestimate the total N_S concentration since a fraction will be compensated. In the high purity samples studied here (< 1 ppb N_S^0) the boron content is < 0.3 ppb (< 5×10^{13} cm^{-3}). This upper estimate is derived from the boron detection limit in secondary ion mass spectroscopy (SIMS) experiments [1]. However, alternative traps which have not been quantified may be present, making it difficult to confirm if the assumption that the concentration of N_S^0 is significantly larger than the concentration of N_S^+ is reasonable.

5.5 Conclusions and further work

It has been shown that RP-EPR can be used quantitatively, and that the technique reduces the detection limit for N_S^0 in CVD diamond by a factor of ~100 compared to conventional SP-EPR. The author is unaware of any techniques that are as sensitive for detecting N_S^0 in CVD diamond. This work shows that CVD synthesis can be used to produce SC-CVD diamond samples containing less than 0.1 ppb N_S^0.

In this Chapter the use of RP-EPR to detect N_S^0 is discussed, however, the technique can also be used with other defects with sufficiently long relaxation times, for example the WAR2 defect described in Chapter 7.

The factor of ~100 improvement in the detection limit for N_S^0 in SC-CVD diamond is encouraging but could be further improved by the optimisation of the

modulation frequency.

The currently available high purity SC-CVD diamond samples are relatively small ($4 \times 4 \times 0.5\,\mathrm{mm}$). Larger samples would improve the EPR resonator filling factor. For a 25 mm diameter diamond wafer which is 1 mm thick, it is estimated that a detection limit for N_S^0 of less than 1 ppt is possible. Diamonds of this size are required for some electronic applications (e.g. a single high power diamond switch could be fabricated on a 25 mm wafer), which would benefit from minimal impurity concentrations [2].

RP-EPR appears set to be an important technique for assaying N_S^0 concentrations in CVD diamond.

References

[1] D. Twitchen (2009), private communication.

[2] J. Isberg, J. Hammersberg, E. Johansson, T. Wikstrom, D. J. Twitchen, A. J. Whitehead, S. E. Coe, and G. A. Scarsbrook, Science **297**, 1670 (2002).

[3] F. Bloch, Phys. Rev. **70**, 460 (1946).

[4] A. M. Portis, Phys. Rev. **100**, 1219 (1955).

[5] C. A. J. Ammerlaan and A. van der Wiel, J. Magn. Reson. **21**, 387396 (1976).

[6] J. R. Harbridge, G. A. Rinard, R. W. Quine, S. S. Eaton, and G. R. Eaton, J. Magn. Reson. **156**, 41 (2002).

[7] R. T. Weber, J. Jiang, and D. P. Barr, *EMX user's manual*, manual version 2.0 (Bruker Instruments Inc., 1998), available from Bruker UK Ltd., Banner Lane, Coventry, CV4 9GH, UK.

[8] J. A. Weil, J. R. Bolton, and J. E. Wertz, *Electron paramagnetic resonance* (Wiley-Interscience, New York, 1994), 2nd ed.

[9] C. P. Poole, *Electron spin resonance* (Dover publications, New York, 1983), 2nd ed.

[10] J. A. van Wyk, E. C. Reynhardt, G. L. High, and I. Kiflawi, J. Phys. D: Appl. Phys. **30**, 1790 (1997).

[11] G. Watt, D. Phil. Thesis, University of Oxford (2002).

[12] J. A. van Wyk and J. H. N. Loubser, J. Phys. Condens. Matter **5**, 3019 (1993).

[13] C. Glover, M. E. Newton, P. Martineau, D. J. Twitchen, and J. M. Baker, Phys. Rev. Lett. **90**, 185507 (2003).

[14] I. D. Campbell, J. Magn. Reson. **74**, 155 (1987).

[15] J. S. Hyde, Phys. Rev. **119**, 1483 (1960).

[16] R. J. Cruddace, PhD. Thesis, University of Warwick (2007).

Chapter 6

Charge transfer and trapping in nitrogen doped CVD diamond

6.1 Overview

Diamond exhibits some extreme, and potentially useful properties, which can be affected by impurities or defects in the crystal. Single substitutional nitrogen in the neutral charge state (N_S^0) is a deep donor that has been measured to lie ~1.7 eV below the bottom of the conduction band [1]. Given the wide band-gap of diamond 'mid-gap' defects are common, with the potential for multiple charge states to be simultaneously present, e.g. NV^0 and NV^- [2, 3].

The properties of a defect can change dramatically if the charge state of that defect is altered. Hence, the presence of acceptors and donors in a diamond can significantly alter its electronic properties and colour.

One issue with some brown CVD diamond, is that the concentration of ionised single substitutional nitrogen (N_S^+) is larger than the concentration of negatively charged defects (measured by EPR). This means that for such systems, the dominant electron traps in CVD diamond have not been identified. In Equation 6-1, which describes the transfer of charge from donor to trap, the traps have been labelled X_i^0.

$$N_S^0 + \sum_i X_i^0 \longrightarrow N_S^+ + \sum_i X_i^- \tag{6-1}$$

Techniques currently used for the investigation of charge transfer in diamond include deep-level transient spectroscopy (DLTS) [4, 5], capacitance [4], and thermoluminescence [6, 7] experiments. Variable temperature EPR and optical excitation can be used to quantitatively study the concentration of traps and the

position of those trap levels in the band-gap [8].

The transfer of charge and colour variation observed is a result of thermal treatment and optical excitation, which can be termed:

1. Themo-ionisation / thermo-chromic behaviour, where a reversible change in the charge of a defect, or the colour of the diamond occurs as a result of thermal treatment, either cooling and heating.
2. Photo-ionisation or photo-chromic behaviour, where a reversible change in the charge of a defect, or the colour of the diamond occurs as a result of exposure to light. The illumination can be of various energies (wavelengths) and can result in different charge balances for each illumination energy.

It is important to recognise that illumination does not bring about an equilibrium charge state distribution, but rather a quasi-static charge state distribution. Only after treatment for an infinite period of time at a given temperature, will an equilibrium charge state distribution be attained.

6.1.1 Examples of charge transfer

In addition to being of scientific interest, if the deliberate alteration of a diamond's colour is undetected, the commercial value of a gem diamond could be substantially increased. Therefore, knowledge of such treatments and their disclosure are paramount in the diamond gem industry.

The affect of heat treatment and illumination on both the colour of diamonds and their corresponding defect concentrations were studied. Chameleon diamonds typically change colour from greyish-green to yellow when they are heated at around 200°C and return to their original colour when cooled or illuminated with light of specific wavelengths [9, 10]. Defect concentrations in chameleon diamonds are affected by thermal treatment and illumination, but no single defect has been shown to be responsible for the colour change. One EPR-active defect observed in chameleon diamonds that varies with such treatments is the OK1 (EPR) centre [11], which is temporarily removed by treatment at 800 K [12] and returns after UV illumination.

A range of vacancy-related defects have been generated by the electron irradiation of natural diamond, the concentrations of which show photo/thermal-ionisation behaviour. For example the isolated vacancy can be simultaneously observed in two charge states [13], V^0 (GR1, 741 nm/1.673 eV [14]) and V^- (ND1, 394 nm/3.149(1) eV). The charge transfer process is described in Equations 6-2 [15]. The relative concentrations of V^0 to V^- are dependent upon the concentration of nitrogen donors and the history of the sample.

$$\begin{aligned} \mathrm{GR1}(\mathrm{V}^0) + \mathrm{e}^- &\longrightarrow \mathrm{ND1}(\mathrm{V}^-) \qquad 2.9\,\mathrm{eV} < \text{illumination energy} \lesssim 4\,\mathrm{eV} \\ \mathrm{ND1}(\mathrm{V}^-) + \mathrm{h}^+ &\longrightarrow \mathrm{GR1}(\mathrm{V}^0) \qquad 3.2\,\mathrm{eV} < \text{illumination energy} < 3.5\,\mathrm{eV} \end{aligned} \tag{6-2}$$

A similar relationship between the optical H2 ($[\mathrm{N\text{-}V\text{-}N}]^-$) and H3 ($[\mathrm{N\text{-}V\text{-}N}]^0$) defects was initially suggested by Walker [16]. It was later shown by Mita *et al.*, through photo-ionisation experiments at liquid nitrogen temperatures [17], that the complementary changes in H2 and H3 concentrations match precisely and are described by Equation 6-3. In this case, recovery of the original defect concentrations was observed in a few minutes in the absence of illumination. A dual affect from UV illumination of different wavelengths was observed. This affect was suggested to involves charge transfer via both the conduction and valence bands (see Section 6.1.2).

$$\begin{aligned} \mathrm{H2} + \hbar\omega &\longrightarrow \mathrm{H3} + \mathrm{e}^- \\ \mathrm{e}^- + \mathrm{N}_\mathrm{S}^+ &\longrightarrow \mathrm{N}_\mathrm{S}^0 \end{aligned} \tag{6-3}$$

Nickel centres studied in HPHT-grown diamond [18], specifically NE5, NE6 and NE7 showed photo-ionisation and thermo-ionisation behaviour. Nadolinny *et al.* [19] studied the variation in concentration of the NE5 (EPR-active) defect with illumination wavelength and thermal treatments. The concentration of NE5 was shown to decrease between 200°C and 300°C with an activation energy of ~0.2 eV. From this very low activation energy, Nadolinny *et al.* suggested the defect was a mediating step for electrons or holes, not a final state [19].

An important point made by Nadolinny *et al.* [18] was that charge transfer experiments can corroborate [20] or disprove previously assigned correlations between optical and EPR-active defects. Charge transfer experiments can also

determine if multiple optical transitions result from different defects. (A similar discussion involving the nitrogen-vacancy-hydrogen (NVH) [21–24] complex will be given later in this Chapter.) A summary of charge transfer studies and the affects on defect concentrations in diamond are presented in Table 6-1.

6.1.2 Mechanisms

The transfer of charge between defects can occur directly if the separation between the defects is small and sufficient energy is supplied to overcome any barrier to the transfer. If defect separations are large, then for charge transfer to occur, electronic bands must be involved. Charge transfer commonly occurs through the conduction or valence bands. Alternatively, if defect concentrations are high then charge transfer can occur via defect states. This can occur either through the formation of extended states or by hopping between localised defect states. For a detailed discussion of these transport mechanisms see [30].

The excitation of electrons into the conduction band allows their movement through the lattice and subsequent trapping at a distant defect. The difficultly with this process in diamond is that the dominant donor (N_S^0) lies ~1.7 eV below the conduction band [1], and so a significant initial excitation energy is required to initiate the transfer.

An alternative transfer process is the excitation of an electron from the valence band into a trap. The hole created in the valence band can then move through the lattice and recombine with another electron. This model of charge transfer has been suggested by Dyer *et al.* [26] to be a mechanism which avoids the deep donor level. The activation energy for charge transfer is then dependent upon the position of the trap with respect to the top of the valence band and not the conduction band.

EPR is a bulk technique and so concentration measurements are an average over the entire sample, assuming that defects are homogeneously distributed throughout the lattice. However, this is a simplified picture of a CVD diamond which contains different growth sectors and striations. It has been shown by Martineau *et al.* [31] that the striations observed in CVD diamond are the result of growth on risers and terraces (see Figure 6-1) which may incorporate defects at

Table 6-1: Previously published examples of charge transfer experiments on diamond, adapted from [3]. (H) indicates heat treatment; the specific temperature is given in the Table. (I) indicates illumination treatment; the specific wavelength / energy is given in the Table. ↑ indicates that the result of the treatment was an increase in concentration and ↓ indicates that the result was a decrease.

Defect label	Optical feature (eV)	Defect model	(Treatment) Temp / Energy of treatment	Effect on conc.	Sample Type	Ref. & expt. cond.
GR1	1.673	V^0	(H) 770 K	↑	Electron Irradiated Type I natural	[16, 25–27]
ND1	3.15	V^-	(H) 770 K	↓		
GR1	1.673	V^0	(I) <3.15 eV	↓		
ND1	3.15	V^-	(I) <3.15 eV	↑		
GR1	1.673	V^0	(I) >3.15 eV	↑		
ND1	3.15	V^-	(I) >3.15 eV	↓		
H2	1.267	$[N-V-N]^-$	(I) 2.54 eV	↓	Electron Irradiated Type Ib HPHT synthetic	[17] 77 K
H3	2.463	$[N-V-N]^0$	(I) 2.54 eV	↑		
H2	1.267	$[N-V-N]^-$	(I) 3.40 eV	↑		
H3	2.463	$[N-V-N]^0$	(I) 3.40 eV	↓		
H2	1.267	$[N-V-N]^-$	(I) 2.54 & 3.40 eV	↑		
H3	2.463	$[N-V-N]^0$	(I) 2.54 & 3.40 eV	↓		
H2	1.267	$[N-V-N]^-$	(I) 2.54 & 3.06 eV	↑		
H3	2.463	$[N-V-N]^0$	(I) 2.54 & 3.06 eV	↓		
637 nm	1.945	$[N-V]^-$	(I) 2.8 eV	↓	CVD film, Si substrate	[3] RT
575 nm	2.156	$[N-V]^0$	(I) 2.8 eV	↑		
637 nm	1.945	$[N-V]^-$	(I) 3.7 eV	↑		
575 nm	2.156	$[N-V]^0$	(I) 3.7 eV	↓		
637 nm	1.945	$[N-V]^-$	(H) after 3.40 eV (I) <500°C	↑	HPHT, Ni-Fe catalyst	[28] 80 K
575 nm	2.156	$[N-V]^0$	(H) after 3.40 eV (I) <500°C	↓		
637 nm	1.945	$[N-V]^-$	(H) after 3.40 eV (I) >500°C	↓		
575 nm	2.156	$[N-V]^0$	(H) after 3.40 eV (I) >500°C	↑		
P1(EPR)	1344cm^{-1}	N_S^0	(H) sample dependent	↓	Various	[8, 10, 20]
P1(EPR)	1344cm^{-1}	N_S^0	(I)	↑		
N_S^+	1332cm^{-1}	N_S^+	(H) sample dependent	↑		
N_S^+	1332cm^{-1}	N_S^+	(I)	↓		
OK1(EPR)	-	N & O at next nearest sites [29]	(H) >500°C	↓	Natural Type Ib	[8, 10, 12]
	2.367	Unassigned	(I) <2.1 eV	↑	Natural Type Ib, e irradiated	[13] 77 K
	2.367	Unassigned	(I) <2.9 eV	↓		
	1.979	Unassigned	(I) <2.9 eV	↑		
	1.521	-	Illuminated > 2 eV	↑	Natural Type IIb, e irradiated	[15] 80K
	2.085	Unassigned	Illuminated 2.84 eV or 3.40 eV	↓	HPHT, Ni-Fe catalyst	[28] 80 K
	3.420	Unassigned - V related	Illuminated 2.84 eV or 3.40 eV	↓		
	3.420		(H) after 3.40 eV (I) <500°C	↑		
	3.420		(H) after 3.40 eV (I) >500°C	↑		
	4.325	Unassigned	(H) after 3.40 eV (I) <500°C	↑		
	4.325		(H) after 3.40 eV (I) >500°C	↓		

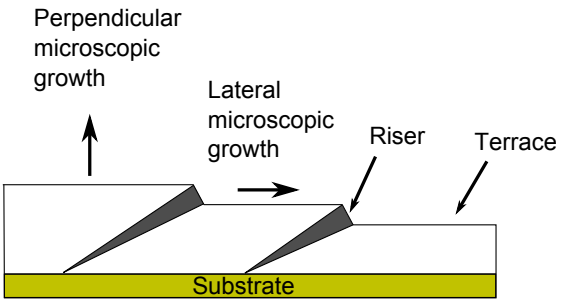

Figure 6-1: Schematic showing the early development of striations in CVD diamond. Shading of the risers and terraces reflects the different defect concentrations. Growth on risers is lateral to the macroscopic growth direction. Figure adapted from [31]

different concentrations. This can result in very inhomogeneous defect distributions.

6.1.3 Chapter aims

The aim of this Chapter is to investigate the transfer of charge between defects in brown single crystal (SC)-CVD diamond in an attempt to answer the following questions:

1. What concentration of uncompensated traps remain in as-grown brown SC-CVD diamond?
2. Where in the band-gap do the energy levels of EPR-active traps, observed in brown SC-CVD diamond lie?
3. Can well-known defects be identified in different charge states?
4. Can any correlations be made between defects observed in FTIR absorption and EPR spectroscopies?

It is important to note that each sample has a unique mix of defects, both donors and acceptors; hence in each sample the amount and rate of charge transfer will vary. Prior work by Twitchen [8] found up to a 75% reduction in the concentration of N_S^0 in one sample as a result of thermal treatment. However, in work on other samples by Nadolinny *et al.* [18], the change reported was much smaller, 15-20%.

6.2 Experimental

Eight SC-CVD diamond samples grown with differing nitrogen doping levels were studied along with one HPHT synthetic type Ib diamond for comparison. The

change in concentration of EPR and IR active defects with isochronal heat treatment (450–850 K) has been investigated. Two methods for isochronal heat treatment were used:

1. Each sample is individually heat treated in-situ with the EPR experiment using the high temperature cavity [22]. Before heat treatment, the sample was directly illuminated for ~5 minutes with a 200 W HgXe arc lamp. The sample was then mounted onto a quartz rod with high temperature cement, loaded into the cavity and further illuminated for ~5 minutes via a liquid light guide and quartz rod. Heat treatment was carried out incrementally at 25 K intervals between 450 K and 850 K for 8 minutes (plus the ramp times as discussed in Section 4.1.7). The sample was kept in the dark throughout the experiment.
2. For EPR / FTIR comparisons, the tube furnaces described in Section 4.2 were used to heat treat the samples. The diamonds were initially illuminated as described above. Heat treatments were carried out incrementally at 50 K intervals between 500 K and 850 K for 10 minutes. After heating, the sample was cooled rapidly to quench the sample and lock defect concentrations. The sample was kept in the dark prior to and during EPR and FTIR absorption spectroscopy.

6.2.1 Samples

The SC-CVD samples (A, C, H, I, J, K, L and M, see Table 6-2) studied have a range of brown colouration and nitrogen concentrations. The single HPHT diamond sample (N) studied for comparison, was grown with a CoFe catalyst and examined in an as-grown state. Defect concentrations, as determined by EPR and FTIR absorption, are given in Table 6-2. In all concentration measurements it is assumed that the defects are homogenously distributed throughout the sample.

Table 6-2: Samples studied in this Chapter. Concentrations are determined by EPR and FTIR absorption after ~5 minute UV illumination. Concentrations for each defect are given in parts per billion (ppb). N_S^+ concentrations are determined using the conversion factor determined by Lawson *et al.* [32] for IR absorption. All other concentrations are determined by EPR and by comparison to a reference sample (see Section 4.1.6). All samples are CVD synthetic stones, apart from Sample N which is a HPHT synthetic type Ia.

Sample	Mass (mg)	Supplier	$[N_S^0]$	[WAR2]	$[V_nH^-]$	$[NV^-]$	$[NVH^-]$	$[N_S^+]$	Figure
A	48	DTC/E6	130	4	1.5	-	-	200(50)	7-2
C	36	DTC/E6	950	5	4	-	25	no data	-
H	70	DTC/E6	510	2	5	0.5	17	250(50)	6-9
I	40	DTC/E6	1680(170)	-	12(2)	13(2)	330(35)	2560(500)	-
J	43	DTC/E6	2570(350)	-	25(3)	18(2)	500(50)	1760(350)	6-9
K	64	DTC/E6	165(17)	1.0(5)	1.0(5)	-	5(2)	no data	-
L	63	DTC/E6	190(19)	1.0(5)	1.0(5)	-	5(2)	no data	-
M	51	Apollo	26(3)	-	0.5(3)	-	0.4(2)	150(30)	-
N	77	DTC/E6	11000	-	-	-	-	<500	-

6.3 Results

6.3.1 Variation in N_S^0

All samples, except Sample N, showed a reduction in the concentration of N_S^0, with heat treatment. Figure 6-2 shows the results of the heat treatment method described in point 1 of Section 6.2. The reduction in the concentration of N_S^0 occurs between 550 K and 700 K, see Figure 6-3. The reduction in the concentration of N_S^0 after 850 K treatment varies from 30% (Sample K) to 99% (Sample C). The HPHT diamond sample (Sample N), has a variation of <2%, across all treatment temperatures.

Given the treatment temperatures, and that the effect is reversible, charge transfer must be responsible for the variation in the concentration of N_S^0 observed. Considering the transfer of electrons from N_S^0 to a collection of neutrally charged traps labelled X_i^0. If $\sum_i X_i^0 = X_T^0$ then Equation 6-1 can be written,

$$N_S^0 + X_T^0 \longrightarrow N_S^+ + X_T^- \tag{6-4}$$

If $[X_T^0] \ll [N_S^0]$, [1] then first order kinetics (see Section 3.5) can be considered, and the change in the concentration of N_S^0 can be described by:

$$\frac{d[N_S^0]}{dt} = -\lambda[N_S^0] \tag{6-5}$$

[1] $[\beta] =$ the concentration of defect β

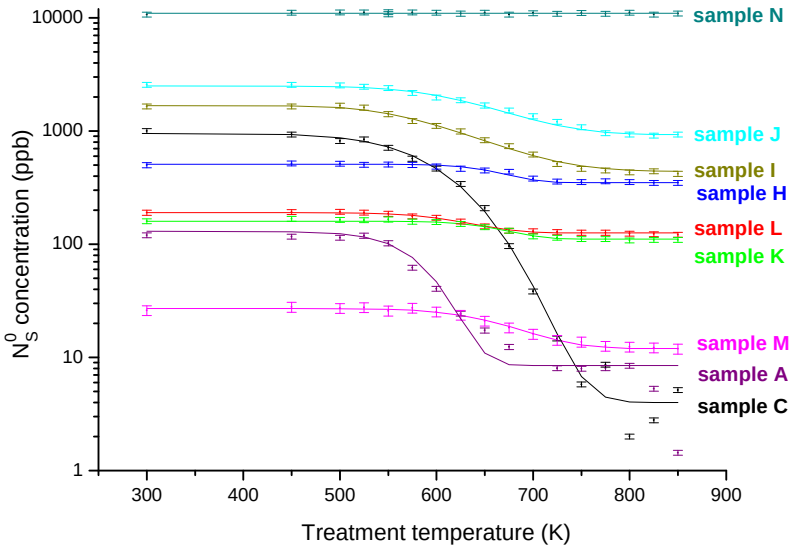

Figure 6-2: Variation in the concentration of N_S^0 with isochronal heat treatment inside the high temperature cavity, see Section 6.2. Fits shown are to first order kinetics (Equation 6-5) with parameters which produce the best fits to the data.

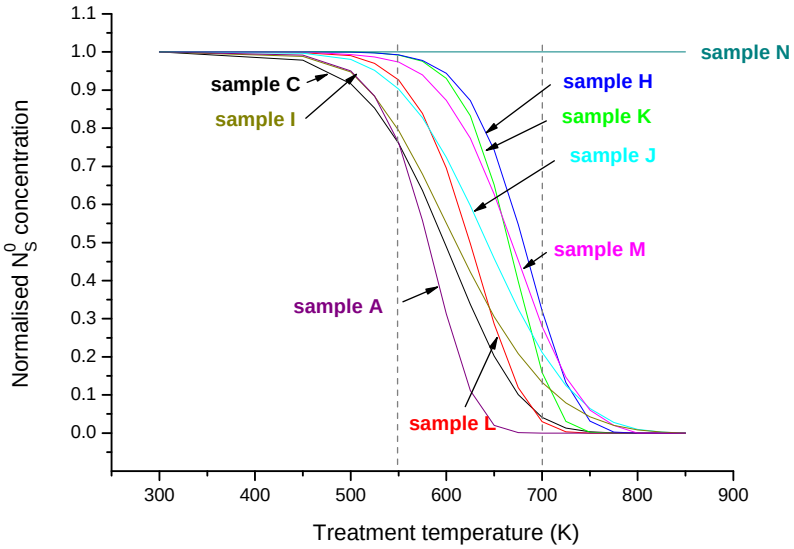

Figure 6-3: The first order kinetics fits shown in Figure 6-2 are normalised here for comparison. (All experimental data points from Figure 6-2 have been removed for clarity.)

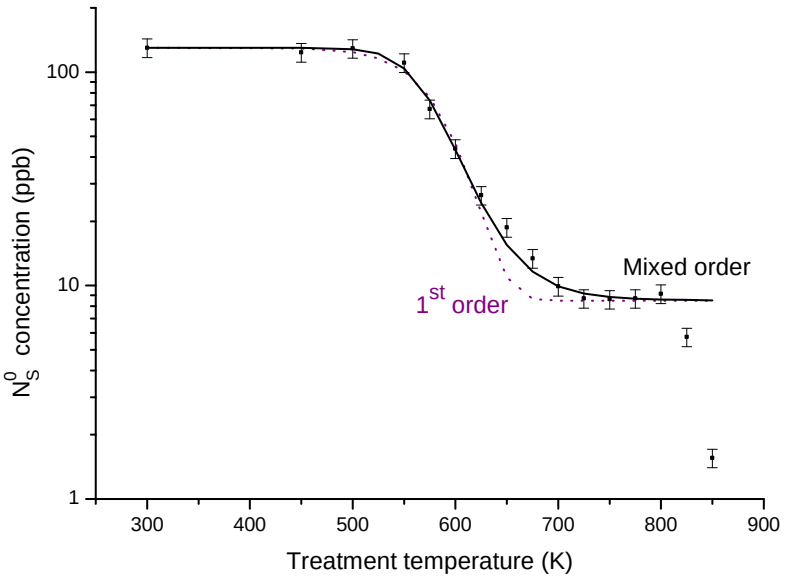

Figure 6-4: Variation in the concentration of N_S^0 in Sample A with isochronal heat treatment inside the high temperature cavity, see Section 6.2. First and mixed order kinetics fits are shown for comparison, first order - dotted (purple when in colour) (Equation 6-5) and mixed order - solid, (Equation 6-11). The secondary fall above 800 K has not been fit (see text).

Fits to each data set with first order decay kinetics are shown in Figure 6-2. In all but one case, the fits adequately describe the data. The exception is Sample A, where the poor fit indicates that first order kinetics do not adequately describe the process.

If $[X_T^0] \lesssim [N_S^0]$, then the concentration of N_S^0 will reduce until all the traps (X_T^0) have been compensated i.e. $[X_T^0] \to 0$. This is indicated by a concentration plateau, e.g. Sample A in Figure 6-4. The variation in the concentration of N_S^0 and X_T^0 are dependent upon one another as shown in Equations 6-6 and 6-7.

$$\frac{d[N_S^0]}{dt} = -\lambda[X_T^0][N_S^0] \tag{6-6}$$

$$\frac{d[X_T^0]}{dt} = \lambda[N_S^0][X_T^0] \tag{6-7}$$

If $[N_S^0]_{t=0} > [X_T^0]_{t=0}$ then the concentration of N_S^0 will not decay to zero as $t \to \infty$ since there are insufficient traps. If it is assumed that Equation 6-1 only goes to the right and $[X_T^0] = [N_S^0] + \alpha$ (where α is a constant unique to the sample)

then substituting into Equation 6-6 gives:

$$\frac{\mathrm{d}[\mathrm{N_S^0}]}{\mathrm{d}t} = -\lambda[\mathrm{N_S^0}][[\mathrm{N_S^0}] + \alpha] \tag{6-8}$$

Defining, $k_1 = \lambda\alpha$ and $k_2 = \lambda$

$$\frac{\mathrm{d}[\mathrm{N_S^0}]}{\mathrm{d}t} = -k_2[\mathrm{N_S^0}]^2 - k_1[\mathrm{N_S^0}] \tag{6-9}$$

The solution is of the form.

$$\frac{1}{[\mathrm{N_S^0}]} = C\exp(-\lambda\alpha t) + \frac{1}{\alpha} \tag{6-10}$$

Applying the boundary conditions, $t = 0$, $[\mathrm{N_S^0}] = [\mathrm{N_S^0}]_0$ and $t \to \infty$, $[\mathrm{N_S^0}] \to \alpha$, leads to:

$$\frac{1}{[\mathrm{N_S^0}]} = \frac{\exp(k_1 t)}{[\mathrm{N_S^0}]_0} + \frac{k_2}{k_1}\left(\exp(k_1 t) - 1\right) \tag{6-11}$$

This is the standard solution for a decay that involves contributions from both first and second order kinetics, which I shall refer to in this Thesis as 'mixed order' kinetics.

Each sample's isochronal data has been fitted to Equation 6-11. Table 6-3 compares the activation energies and fit qualities to those achieved from the first order kinetics fits. In all but Sample A, the fit quality was improved only marginally, if at all. Consequently, the simplest description of the process, involving first order kinetics, will be used in these cases.

In addition, an isothermal annealing study has been carried out on Sample A which produced an activation energy of 1.1(2) eV (see Chapter 7). This value agrees with the 1.2(2) eV determined from the isochronal data (see Table 6-3). Sample A also displays an additional reduction in the concentration of $\mathrm{N_S^0}$ for measurements above 775 K. This decrease has not been fitted since there are only two experimental points.

6.3.2 Variation in $\mathrm{NVH^-}$

In two of the samples studied (see Table 6-3) no $\mathrm{NVH^-}$ could be detected independent of optical or thermal treatments. The remainder of the samples displayed a range of initial concentrations[2], from $0.4(+0.5/-0.2)$ ppb to 500(50) ppb. In six

[2]Such concentrations were obtained with the use of high powers where $\mathrm{NVH^-}$ will not saturate.

Table 6-3: Activation energies (AE) from first and mixed order kinetics fits to isochronal heat treatment experiments carried out in the high temperature cavity. χ^2 values are given for each fit. Initial and final concentrations from the fits are given in parts per billion (ppb) with associated errors of 10% and 15% for the concentration of N_S^0 and NVH^- respectively. The AE determined by isothermal annealing of Sample A is included for comparison in column A_{therm}, (see Chapter 7)

Defect	Sample	A	A_{therm}	C	H	K	L	M	J	I
N_S^0	AE (eV) mixed 1st & 2nd order	1.2(2)	1.1(2)	†	0.9(2)	0.9(2)	0.8(2)	0.8(2)	0.5(1)	0.5(1)
	Normalised χ^2 (fit quality)	13		†	0.3	0.2	0.3	0.8	0.7	1.0
	AE (eV) 1st order	1.0(3)		0.5(1)	0.9(2)	1.1(2)	0.9(2)	0.8(2)	0.5(1)	0.5(1)
	Normalised χ^2 (fit quality)	28		157	0.3	0.2	0.3	1.0	0.4	1.0
	Initial conc. (ppb)	130		950	510	165	190	26	2570	1680
	Final conc. (ppb)	8		4	350	111	126	11	1000	440
	Ratio ΔN_S^0 / initial N_S^0	0.94		1.0	0.31	0.33	0.34	0.58	0.61	0.74
N_S^+	Initial conc. (ppb)	-		-	250(50)	-	-	-	1760(300)	-
	Final conc. (ppb)	-		-	450(80)	-	-	-	4790(500)	-
	Change (ppb)				200				3030	
NVH^-	AE (eV) mixed 1st & 2nd order	-		†	1.2(2)	0.8(2)	†	1(2)	0.5(1)	0.5(1)
	Normalised χ^2 (fit quality)	-		†	3.6	14	†	27	1.0	3.0
	AE (eV) 1st order			†	1.1(2)	1.2(2)	†	1.1(2)	0.7(2)	0.6(1)
	Normalised χ^2 (fit quality)				3.7	24	†	36	1.5	1
	Initial conc. (ppb)	-		†	15	5	5	0.4	500	330
	Final conc. (ppb)	-		†	85	35	25	1.5	1110	830
	Ratio ΔNVH^- / final NVH^-			†	0.82	0.86	0.80	0.73	0.55	0.60
Other	Δ conc. of other defects (ppb)	3		0.3	1.8	0	0	0	124	100
X_1^0	X_1^0 conc. (ppb)	122		946	88	24	44	14	836	640
	Ratio ΔN_S^0 / X_1^0	1		1	0.55	0.44	0.69	0.93	0.53	0.52

† Acceptable fit not achieved

†

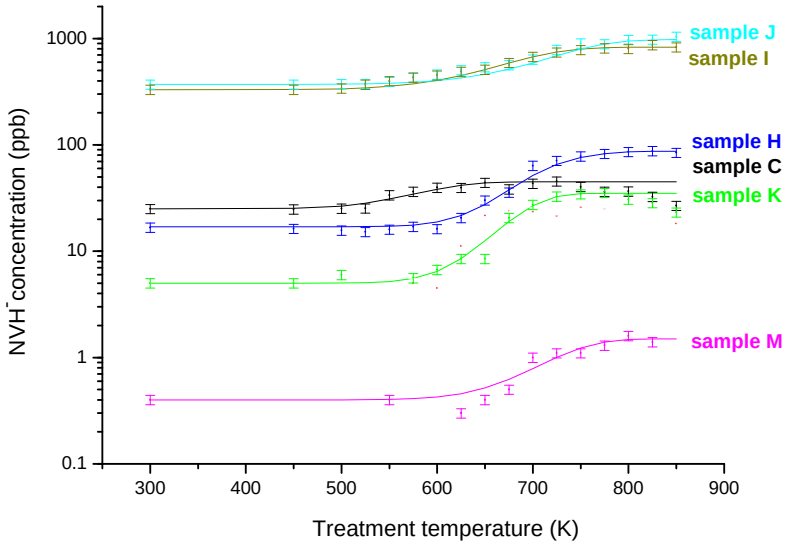

Figure 6-5: Variation in the concentration of NVH^- with isochronal heat treatment inside the high temperature cavity, see Section 6.2. Fits shown are to first order kinetics and activation energies are given in Table 6-3.

samples, the concentration of NVH^- increased with annealing temperature. In two samples (C and K), the concentration of NVH^- reduced at treatment temperatures greater than 775 K (this has not been modelled).

The rise in the concentration of NVH^- in combination with the fall in concentration of N_S^0 could result from processes such as:

$$\begin{aligned} NVH^{-2} + X_T^0 &\longrightarrow NVH^- + X_T^- \\ NVH^0 + N_S^0 &\longrightarrow NVH^- + N_S^+ \end{aligned} \tag{6-12}$$

The first of the processes is perhaps unlikely since it requires double charging of the NVH defect and further unobserved traps to account for this additional charge. Therefore, from here onwards NVH^0 will be considered a trap and one component of the collection of traps labelled X_T^0.

Reconsidering Equations 6-6 and 6-7 and separating NVH^0 from the defects included in X_T^0, $\frac{dN_S^0}{dt}$ is now dependent upon two populations of traps. Again the reverse reactions are considered to be unlikely and so are neglected. Now the situation (Equation 6-13) is much more complicated than the first order model.

$$\frac{d[N_S^0]}{dt} = -\lambda_1[X_T^0][N_S^0] - \lambda_2[NVH^0][N_S^0] \tag{6-13}$$

The concentration of NVH^0, when neglecting the reverse reaction and interactions with multiple other traps, can be modelled by Equation 6-14.

$$\frac{d[NVH^0]}{dt} = -\lambda_2[NVH^0][N_S^0] - \lambda_3[NVH^0][X^-] \tag{6-14}$$

The solution of Equation 6-14 and related equations would be complicated and the data available would be insufficient to produce reliable numerical solutions. For these reasons first order kinetics were used to model the change in concentration, and in each case produce adequate fits to the experimental data, see Figure 6-5.

The activation energies determined for the charge transfer measured in the samples discussed here are $\ll 1.7\,\text{eV}$ (see Table 6-3) and so are dependent upon the position of the trap with respect to the valence band, not the donor. The presence of multiple traps means that activation energies cannot be determined for individual defects unless one trap is dominant in a sample.

Consider Sample A, where the concentration of N_S^0 reduced by 94%. NVH^- is not observed but WAR2 (see Chapter 7) and V_nH^- are present at very low concentrations. In this sample, it appears there is a dominant trap with an activation energy of $1.2(2)\,\text{eV}$ (from isochronal annealing) which will be labelled X_1^0. In the other samples it is assumed that X_1^0 and NVH^0 are both present, along with a small concentration of other traps. X_1^0 and NVH^0 are common traps in CVD diamond and so for future descriptions are excluded from X_T^0.

In all of the SC-CVD samples studied, $\Delta[N_S^0] > \Delta[NVH^-]$ (see Table 6-3). The discrepancy in concentration change is not accounted for by the changes in other observed EPR active defects. This implies that an unobserved trap is present in each case. Here this defect is labelled X_1^0.

6.3.3 Other contributing defects

Defects which have maximum concentrations that are small when compared to $\Delta[N_S^0]$, are labelled here as 'other contributing defects'. These defects take part in the transfer of charge and each has an independent relationship with the donor, N_S^0.

To accurately describe the charge transfer from 'another contributing defect' the transfer should be considered with respect to each of the other defects. Mod-

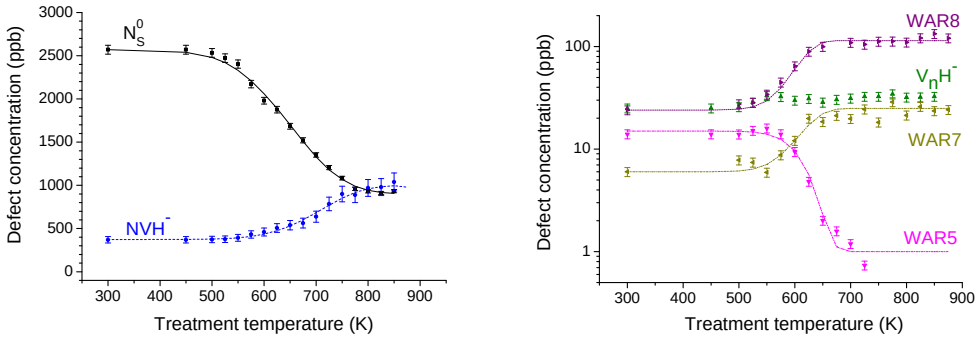

(a) (b)

Figure 6-6: Variation in the concentration of (a) N_S^0 and NVH^- and (b) WAR8, WAR7, WAR5 and V_nH^- in Sample J with isochronal heat treatment inside the high temperature cavity, see Section 6.2. Fits shown are to first order kinetics with activation energies of (a) 0.5(2) (N_S^0) and 0.7(2) eV (NVH^-) (b) 1.2(2) (WAR5), 1.1(2) (WAR7), 1.1(2) eV (WAR8) and no change (V_nH^-).

elling the change in concentration of the defect of interest would require an expression with a different term for each other defect in the sample. Each term would have a separate constant, λ_x. Considering the experimental data collected such an analysis would require too many variables and because of this simple first order kinetics were used.

The changes in concentrations of other contributing defects, WAR5, 7 and 8 (Chapter 9 and [33]), have been fitted in Figure 6.6(b) with activation energies of 1.2(2), 1.1(2) and 1.1(2) eV respectively. WAR2 and V_nH^- and the associated activation energies are discussed in Chapter 7.

6.3.4 Illumination

Illumination of all samples following heat treatment with the HgXe 200 W arc lamp (as described in Section 4.1.7.1) resulted in the return of all defect concentrations to pre-heat treatment levels.

More detailed illumination studies were conducted on Sample A. The sample was treated at 650 K for 15 minutes (plus the ramp times discussed in Section 4.1.7) inside the high temperature cavity. The sample was then illuminated by the 200 W HgXe arc lamp via a liquid light guide and quartz rod. The rate of recovery of the concentration of WAR2 and N_S^0 was monitored.

Table 6-4: The concentration of N_S^0 determined from the 270 nm absorption peak (ppb) and the relative intensities of the 360 and 520 nm absorption bands resulting from the UV-Vis optical absorption spectrum from Sample H. Spectra were obtained under three conditions, before treatment, after heating and after illumination. Data has been supplied by Dr. R. U. A Khan of the DTC research centre.

Peak / band	Units	Before treatment	After heating (798 K)	After illumination (UV)
270 nm	(ppb)	500	300	650
360 nm	(cm^{-1})	0.4	0.2	0.5
520 nm	(cm^{-1})	0.3	0.1	0.3

The wavelength dependence of the recovery of the defect concentrations were investigated using 'high-pass' glass filters. Figures 6.7(a) and (b) show the recovery of the concentration of N_S^0 and WAR2 when illuminated with light of wavelength longer than the stated cut off. The increase in signal strength is rapid with unfiltered illumination. The lower the maximum illumination energy the less complete the signal recovery and the longer that recovery takes. Figure 6.7(a) and 6.7(b) show the total recovery with the maximum incident photon energy. Figure 6.7(c) compares the recovery of the concentration of WAR2 and N_S^0 with the maximum incident photon energy.

6.3.5 Thermo-chromic and visual variations

Thermoluminescence and ultra-violet visible (UV-Vis) absorption measurements have been carried out at the DTC Research Centre by Dr. R. U. A Khan, the results of which are summarised here and discussed in more detail in reference [34].

Sample H was examined by UV-Vis absorption spectroscopy after illumination with a UV lamp and heating to 798 K. Before each measurement the sample was illuminated with UV light for 30 minutes and then kept in the dark for the duration of the experiment. Changes in defect concentrations are noted in Table 6-4. The variation in the 270 nm band is consistent with the variation in the concentration of N_S^0 observed by EPR. The 360 nm and 520 nm bands both decreased in intensity with heat treatment and increased with illumination.

Samples A, C, H and J were investigated by thermoluminescence spectroscopy

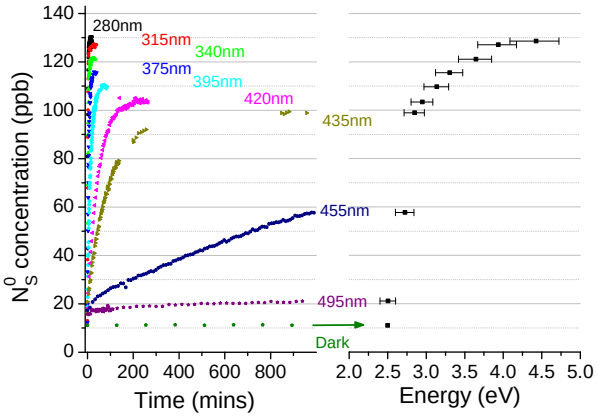

(a)

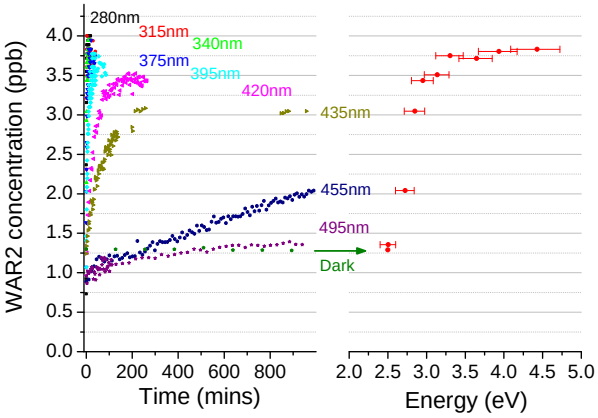

(b)

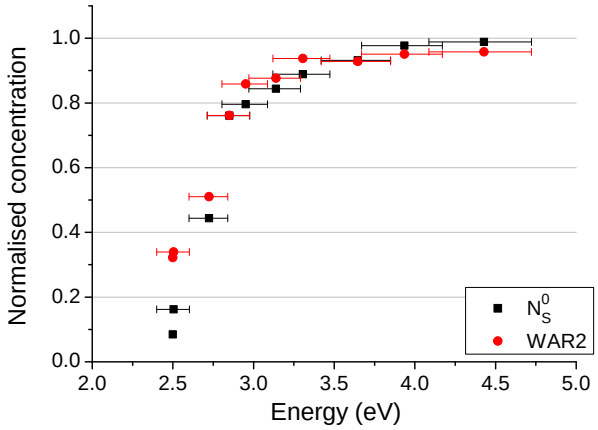

(c)

Figure 6-7: The recovery in the concentration of (a) N_S^0 and (b) WAR2 in Sample A with differing high pass illumination energies (after 650 K heat treatment, see text). The signal recovery against maximum illumination energy after the maximum exposure time is shown to the right hand side of Figures (a) and (b). Figure (c) shows the normalisation of the recoveries of N_S^0 (black squares) and WAR2 (red circles, when in colour) concentrations for comparison.

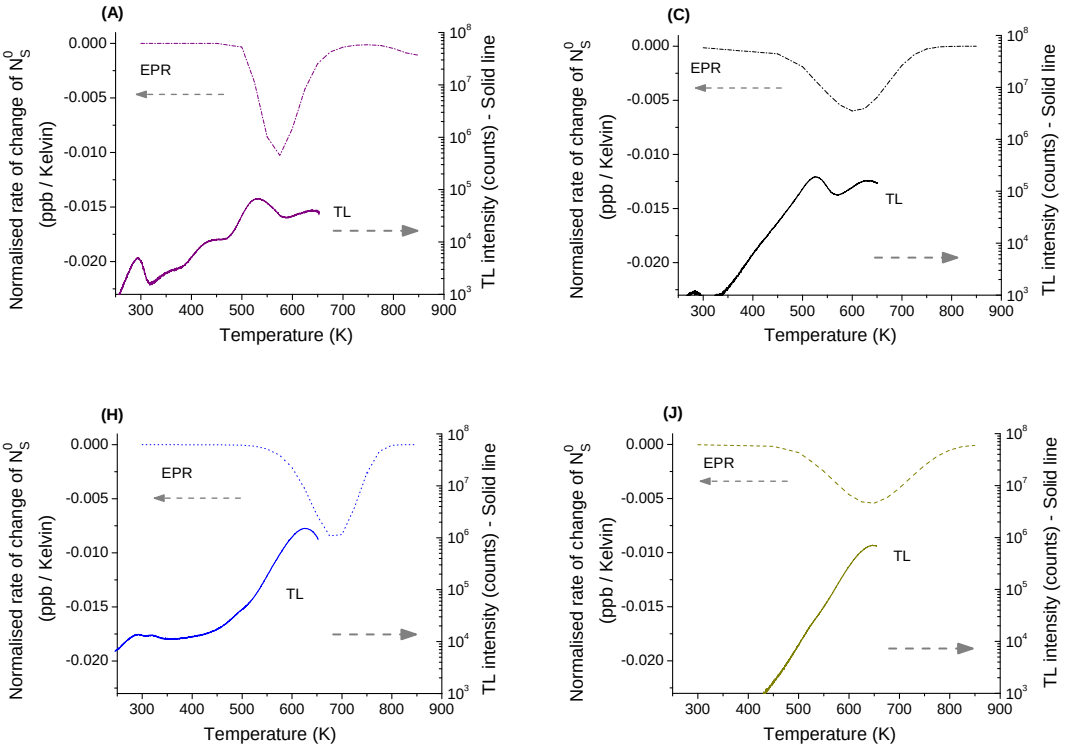

Figure 6-8: Thermoluminescence glow curves of samples, A, C, H and J taken between room temperature and 673 K, plotted underneath (solid), the y-axis being to the right hand side of each plot. Data is compared to the derivative of the fits to the change in the concentration of N_S^0 with isochronal heat treatment shown in Figure 6-2. These are plotted above (broken) and the y-axis is on the left hand side of each plot.

as shown by the lower experimental plots in Figures 6-8.

Samples H and J, which show high concentrations of NVH^-, show a feature at ~650 K and Sample J shows some evidence of a feature at 560 K. This feature is much stronger in samples A and C where concentrations of NVH^- are small or undetectable. Therefore, any changes in concentration in Sample A and C could be assigned to defect X_1^0. In samples A and C the 650 K peak is reduced.

The upper lines in Figures 6-8 are the differentiated fits to the changes in concentration of N_S^0 from isochronal treatment (Figure 6-2). Sample A and H show more rapid changes in concentration at low and higher temperatures respectively. Samples C and J show broader differentials; this is indicative of a less rapid change in the concentration of N_S^0.

Upon heat treatment, the colour of samples H and J were changed significantly. The original colouration was restored after illumination. The colour change of

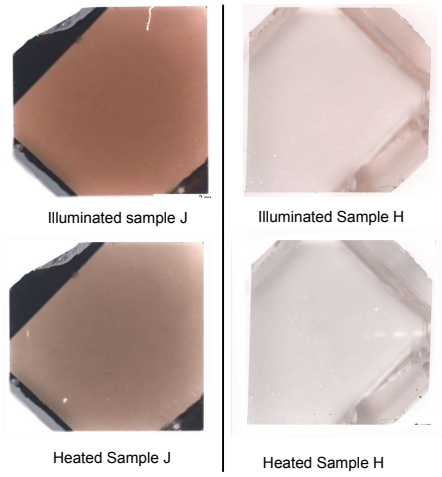

Figure 6-9: Images taken at room temperature of samples H and J after illumination (40 minutes) and after heat treatment (798 K).

samples H and J are shown in Figure 6-9. The results of heat treatment show a non-permanent 'improvement', or lightening of the sample's colour. Sample H was almost colourless before heat treatment and pink after UV illumination. Sample J became redder and browner following UV illumination[3]. In the case of near colourless sample's no 'by-eye' change was observed.

6.3.6 The 3123 cm^{-1} absorption line and the NVH defect

After heat treatment at 850 K the FTIR absorption spectrum from Sample J displayed no observable 3123 cm^{-1} absorption line. However, after illumination the maximum signal was observed, see Figure 6-10(ii).

Since in Sample H no other EPR-active defects of significant concentration were present, it was used to investigate the change in the intensity of the 3123 cm^{-1} absorption line with isochronal heat treatment . The sample path length has been accounted for in the usual way [35] and because of the uniform colouration of the sample (see Figure 6-9), a 2 mm aperture was used for increased throughput.

The width of the 3123 cm^{-1} absorption peak was not observed to vary with heat treatment. The absorption strength fell with increasing treatment temperature, as shown in Figure 6-11. An inverse linear relation between the 3123 cm^{-1} integrated absorption and the change in the concentration of NVH^- (as determined by EPR), is shown in Figure 6-12.

The gradient of the line shown in Figure 6-12 suggests there is a correlation between the change in the concentration of NVH^- and the intensity ($I_{3123cm^{-1}}$),

[3]Other samples have also shown changes in colour but photographs are not available.

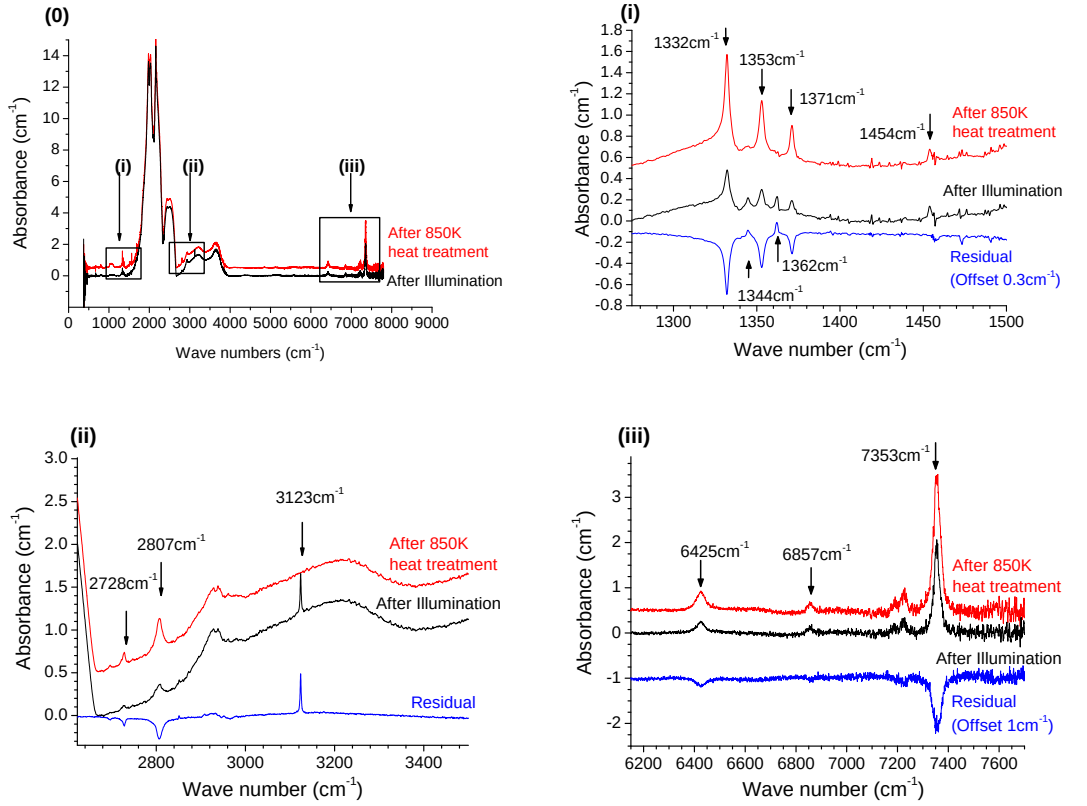

Figure 6-10: FTIR absorption spectra of Sample J, after heat treatment at 850 K (red when in colour), offset by 0.5 cm^{-1}, and after illumination with a HgXe 200 W arc lamp (black). The boxed areas in Figure (0) are magnified in Figures (i),(ii) and (iii). Differences between the spectra are shown (blue when in colour, labelled residual), with an offset in the figures of 0.2 cm^{-1} and 1 cm^{-1} in Figures (i) and (iii) respectively.

of the 3123 cm^{-1} absorption line. If it is assumed that $\Delta[NVH^-] = -\Delta[NVH^0]$ and that the only contributor to the 3123 cm^{-1} line is the NVH^0 defect, then the correlation between the concentration of NVH^0 and the 3123 cm^{-1} absorption peak ($A_{3123cm^{-1}}$) is given by Equation 6-15.

$$\begin{aligned} NVH^0_{ppb} &= 330(30) \times I_{3123cm^{-1}}(cm^{-2}) \\ NVH^0_{ppb} &= 1220(120) \times A_{3123cm^{-1}}(cm^{-1}) \end{aligned} \tag{6-15}$$

Figure 6-13 shows the relation from Equation 6-15 placed on a log scale. The axes are switched compared to Figure 6-12 and the now y-axis inverted to display $[NVH^0]$. The small, black data points are those from Sample H (Figure 6-12), the larger square red point results from Sample J. This latter point has not been used in the linear fit, but the point lies on the fit within error.

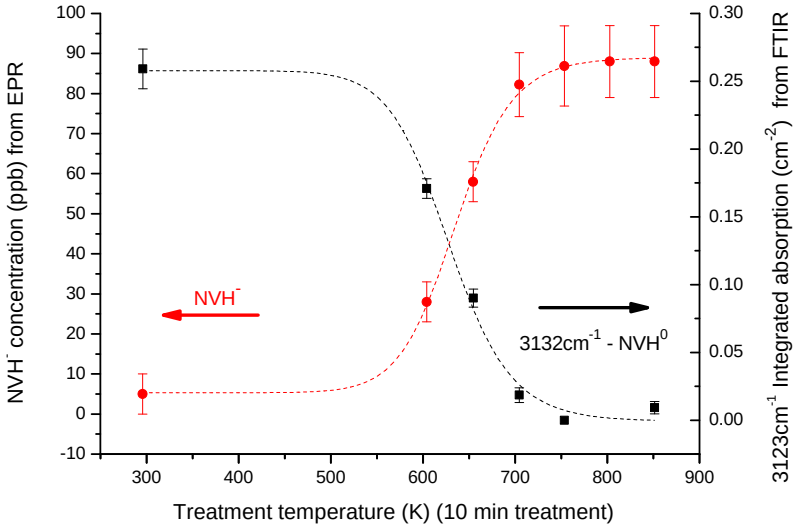

Figure 6-11: Variation in the concentration of NVH^- from EPR, and the integrated absorption of the 3123 cm^{-1} line in Sample H, with isochronal heat treatment using the furnace method (see Section 6.2). Curves are provided as a guide to the eye only.

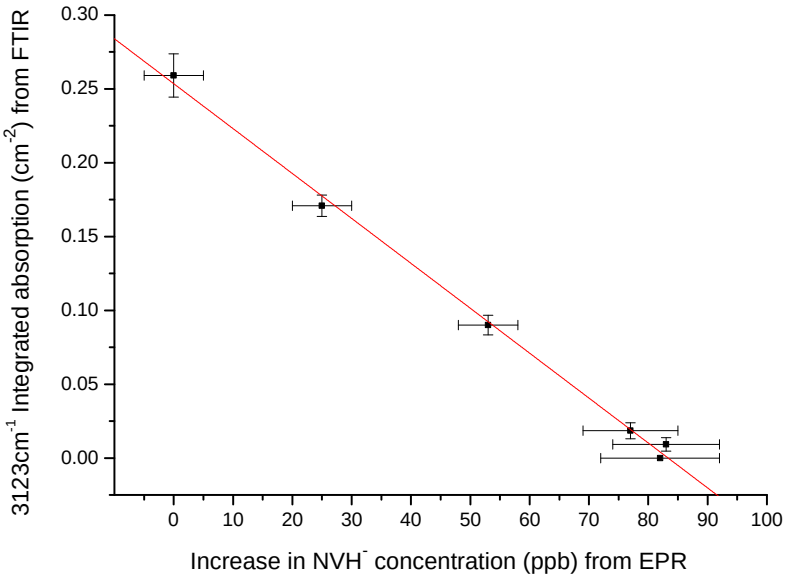

Figure 6-12: The 3123 cm^{-1} integrated absorption as determined by FTIR absorption versus the change in concentration of NVH^- as determined by EPR in Sample H. The linear fit shown yields a gradient of -0.0030(2) and y-intercept at 0.25(1).

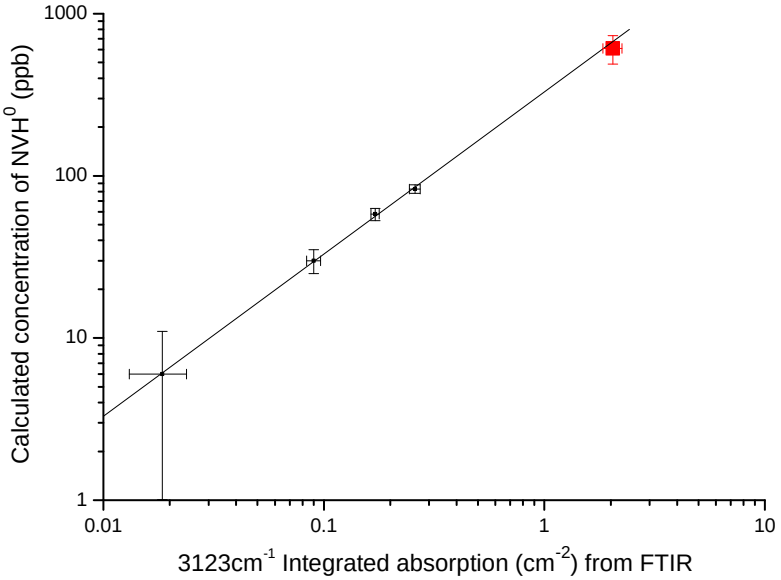

Figure 6-13: The concentration of NVH^0 (EPR) verses the integrated intensity of the 3123 cm^{-1} absorption line (FTIR). The linear fit displayed uses the gradient determined from Figure 6-12, (0.0030(2) cm^{-2} ppb^{-1}). Four of the points shown on Figure 6-12 are plotted here (black). (Those points have been selected where there is a measurable change in the concentration of NVH^0.) The square point (red when in colour) represents Sample J. This point has not been used in the fit but agrees to within error.

6.3.7 Additional IR features

Other IR absorption lines were observed to vary with heat treatment. The 7354 cm^{-1} absorption line, see Figure 6-14, increased in absorption from 1.8 to 7.0 cm^{-2} with heat treatments between 600 and 850 K. Other absorption lines 6857 and 6426 cm^{-1} in Sample J showed enhancement with heat treatment, see Figure 6-10(iii), but the variation of those line intensities observed in Sample H (Figure 6-14) was insufficient to accurately distinguish. The enhancements of the 7354 cm^{-1} (1360 nm) line were also recorded using UV-vis absorption spectroscopy [36].

Time constraints did not permit the detailed study of the changes in the absorption lines at 2807 and 2728 cm^{-1} observed during heat treatments. However, these should be studied further as potential candidates for the optical analogue of the NVH^- defect.

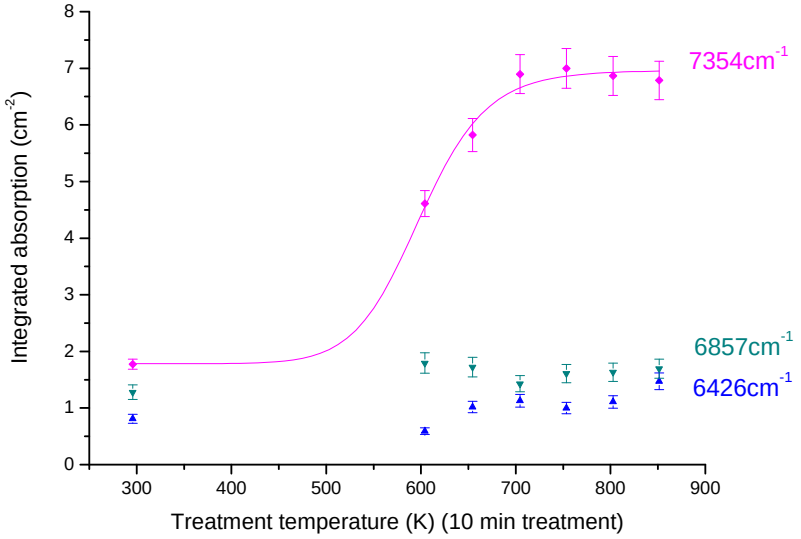

Figure 6-14: Variation in the concentration of integrated intensity of 7354, 6857 and 6426 cm^{-1} absorption lines in Sample H, with isochronal heat treatment using the furnace method (see Section 6.2). The curves is provided as a guide to the eye only.

6.4 Discussion

In those nitrogen doped SC-CVD samples studied, the concentration of N_S^0 decreased with heat treatment (≤850 K). This affect is reversed by UV illumination at room temperature. Thus, this is not the result of a permanent change to the defect, but a transfer of charge as described by Equation 6-1. FTIR absorption data is consistent with this interpretation, see Figure 6-10.

The activation energies for charge transfer observed here (see Table 6-3) are insufficient to overcome the ionisation energy of N_S^0 (1.7 eV [1]), hence the transfer of charge must occur through the valence band. This means that the activation energies determined indicate the position of the traps with respect to the top of the valence band.

Two traps common to CVD diamond have been identified, X_1^0 and NVH^0, the former through a discrepancy in charge balance and the latter through changes in the concentration of NVH^-. In the CVD diamonds studied, X_1^0 must account for 50–100% of the change in the concentration of N_S^0. In Sample A, the X_1^0 trap accounts for a large percentage of the change in the concentration of N_S^0.

This suggests that the activation energy determined indicates the position of X_1^0 (1.2(2) eV) with respect to the top of the valence band. Similarly, the activation energy determined from the increase in concentration of NVH^- suggests that the trap, NVH^0, lies 1.1(2) eV from the top of the valence band.

Those samples with higher overall defect concentrations (samples I and J) have shown significantly lower activation energies (0.5(2) eV) for the change in concentration of N_S^0 and NVH^-. In the case of N_S^0 the defect concentrations are approaching that where defect bands may be formed, ~ $10^{17}\,cm^{-3}$ (1 ppm) [37, 38] potentially affecting the activation energy. The concentration of NVH^0 is significantly lower, but inhomogeneous defect distribution can lead to higher local concentrations where defect bands could exist. Alternatively this could be the result of another trap (X_2^0) which occurs in the higher concentration samples and lies 0.5 eV from the valence band. It is also possible that additional contributing defects may have an affect upon the activation energies. Such affects have been reported by Lagrange *et al.* [38] in diamond and Lee *et al.* in silicon [39].

Four of the samples have been studied using TL spectroscopy. A TL peak indicates the activation energy of carriers from their trapped states. The same process is suggested to be responsible for both the TL peaks and the charge transfer observed by EPR and optical absorption spectroscopy because the temperatures observed are similar.

In samples A and C, the defect X_1 accounts for ~100% of the change in the concentration of N_S^0 and both display a TL peak at ~550 K. Whereas in samples where NVH^0 is present in significant concentrations the peak is severely lessened or not present at all. The defect labelled X_1 may be responsible for the ~550 K feature and the presence of NVH^- may act to broaden or reduce the intensity of it.

In the CVD diamonds studied, UV illumination at room temperature returned all observable defect concentrations to pre-heat treatment levels. It is suggested that this occurs through charge transfer from the traps X_1^- or NVH^- to N_S^+ via the conduction band (see Figure 6-16). Figure 6-7 shows that the return in the concentration of N_S^0 is spread over a range of energies. This implies that the defect, or defects, (X_1 or X_T) have a spread of levels between 2.5 and 4 eV below

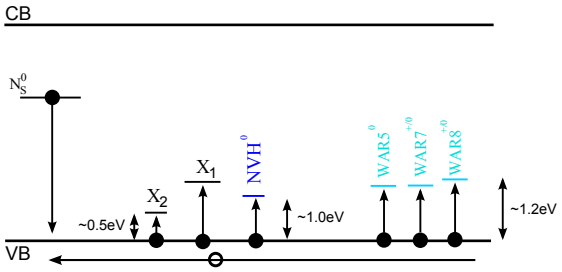

Figure 6-15: Model suggested for the change in concentration of traps, X_2, X_1, NVH^-, $WAR5^0$, $WAR7^{0/-}$ and $WAR8^{0/-}$ as a result of thermal treatment. The defects are shown to lie 0.5 eV, 1.2 eV, 1.0 eV, 1.1 eV, 1.1 eV and 1.2 eV from the top of the valence band respectively.

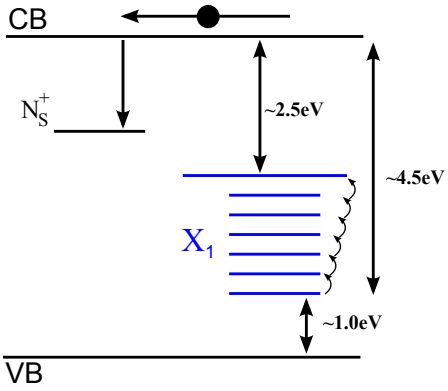

Figure 6-16: Model for the photo-excitation of charge from the extended defect, X_1, to N_S^+ at room temperature, restoring the pre-heat treatment concentrations.

the bottom of the conduction band. This is a large portion of the band-gap and if a single defect type is responsible it might be expected to be extended in nature.

A potential candidate for X_1 is the vacancy cluster. A vacancy cluster would be expected to accept charge, and so might be expected to be EPR-active in one charge state. However, such a defect would occupy the already crowded central $g = 2$ region of the EPR spectrum. The size of the defect might also cause the lines to be broadened to a few mT, meaning that any changes would go undetected. Another potential candidate for X_1 are dislocation boundaries which are commonly but not uniquely found in CVD diamond [31].

The colour variation observed 'by eye' correlates with the changes in the absorption bands (see Table 6-4). In this work an absorption ramp as discussed by Jones [40] has been observed alongside bands at 360 and 520 nm, which decreases in intensity with heat treatment. Any of these bands, or most probably a combination of them, could be responsible for the variations in colour. These bands or the aforementioned ramp, for which vacancy clusters have been suggested responsible [40], could also be optical analogues of the extended X^0 defect.

The changes in concentration of N_S^0 (Table 6-4) derived from measurements of the 270 nm band [41] agree well with those determined by EPR.

6.4.1 Other contributing defects

Changes in a defect concentration can indicate its charge state. Here it is assumed that N_S^0 is the dominant donor and that the concentration of N_S^0 is much larger than the concentration of all other defects, because of this the position of defects in the band-gap were determined as follows; WAR5 (Chapter 9) decreased in concentration with heat treatment, (Figure 6.6(b)), whilst WAR7 and WAR8 both increased in concentration. The activation energies are below 1.7 eV, suggesting that the defect is a trap. The concentration of WAR5 reduces with heat treatment and at higher temperatures, when the energy available is greater than 1.7 eV and electrons could be excited into the conduction band, the WAR5 signal does not recover. It is assumed that the decrease in concentration at 1.2 eV cannot be the result of WAR5 donating electrons because it would be expected to re-trap electrons at higher temperatures, as is observed for WAR2 in Chapter 7, which it does not. For that reason it is suggested that the WAR5 defect is accepting an electron, becoming more negative and so diamagnetic, thus the EPR-active WAR5 defect is positive or neutrally charged. This is consistent with the defect model suggested in Chapter 9. The same argument can be made to explain the increase in concentration of the WAR7 and WAR8 EPR defects and the defects responsible for the 7554 cm^{-1}, 6857 cm^{-1} and 6426 cm^{-1} IR absorption lines. The defect concentration does not decrease at higher temperatures and so the defect must be more negative in its EPR-active state, see Figure 6-15.

6.4.2 The 3123 cm^{-1} absorption line

Previous work (see Section 2.4.2) [22, 24] has noted a correlation between the concentration of NVH^- and the intensity of the 3123 cm^{-1} absorption line. It has also been shown that the symmetries of the 3123 cm^{-1} absorption line [24] is consistent with the dynamic NVH model [22]. In this work the concentration of NVH^0 has been shown to correlate with the 3123 cm^{-1} absorption line (Equations 6-15). However, this is consistent with the previous observations.

The equivalent mode of the NVH^- defect is yet to be identified. Theoretical calculations by Goss *et al.* [42], suggest that the NVH^- carbon-hydrogen stretch mode might be higher in wave number[4]. However there is no evidence of a line in the predicted range; this may be because the line is very broad, or that the difference in mode frequencies is larger than predicted by this calculation.

The $7354\,cm^{-1}$ (1360 nm) line intensity and the concentration of NVH^-, as determined by EPR, vary in approximately the same temperature range and the fractional changes are similar. Nevertheless, when the absorption spectrum of Sample J is recorded with light which is linearly polarized either parallel or perpendicular to the direction of growth ([001]) preferential alignment with the growth direction is observed [43]. The NVH^- defect[5] shows no such preferential alignment[6] in the samples studied and so the $7354\,cm^{-1}$ line cannot be the optical analogue of the NVH^- defect.

6.5 Conclusion

The affect of heat treatment and illumination on nitrogen doped SC-CVD diamond has been investigated. Heat treatment has been shown to drive charge transfer, via the valence band. This should be confirmed with Hall measurements to allow comparison to the Photocurrent measurements carried out on similar samples by M. Nesladek *et al.* [36], who have independently suggested a model which involves a defect with a ~1 eV activation energy [36]. The defect X_1 reported in this Thesis is suggested to lie 1.2(2) eV above the top of the valence band, but illumination studies suggest further energy levels extend into the band-gap. The defect X_1 appears to be an extended defect which is unique to CVD diamond. It is suggested that the X_1 defect could be vacancy clusters or dislocations. Further work is required to observe the X_1 defect directly by EPR.

Analysis of these experiments has resulted in suggested charge states of newly

[4] NVH^- and NVH^0 were calculated to have local vibrational modes at ~ $2827\,cm^{-1}$ and ~ $2679\,cm^{-1}$ respectively

[5] Motionally averaged trigonal symmetry

[6] Any trigonal defect grown on a [001] sample would not be expected to show such preferential alignment since all [111] bonds make the same angle with the growth surface, hence there will be no preferential orientation.

reported EPR-active defects WAR2^0 (see Chapter 7), WAR5^0 (see Chapter 9, WAR7$^{0/-}$ and WAR8$^{0/-}$ and positions of these defects within in the band-gap. Specifically, NVH^0 is suggested to lie 1.0(2) eV from the top of the valence band.

The 3123 cm^{-1} absorption line has been shown to arise from the neutral charge state of the NVH defect. No evidence of optical absorption at the NVH$^-$ centre has been observed.

Implications of this work are two-fold. Firstly, monitoring the concentration of traps could lead to improvements in the quality of CVD diamond, ultimately improving electronic diamond devices. Secondly, from a gemological perspective, the variation in colour observed is significant on grading scales. Diamonds might be subjected to comparable conditions as used here in grading laboratories, during polishing or setting in jewelery, hence these conditions must be accounted for. For example, the 'Diamond View' equipment uses UV illumination.

References

[1] R. G. Farrer, Solid State Commun. **7**, 685 (1969).

[2] Y. Mita, Phys. Rev. B **53**, 11360 (1996).

[3] K. Iakoubovskii, G. J. Adriaenssens, and M. Nesladek, J. Phys. Condens. Matter **12**, 189 (2000).

[4] C. E. Nebel, R. Zeisel, and M. Stutzmann, Phys. Status Solidi A **174**, 117 (1999).

[5] D. V. Lang, J. Appl. Phys. **45**, 3023 (1974).

[6] E. Vittone, C. Manfredotti, F. Fizzotti, A. L. Giudice, P. Polesello, and V. Ralchenko, Diamond Relat. Mater. **8**, 1234 (1999).

[7] C. Descamps, D. Tromson, M. Guerrero, C. Mer, E. Rzepka, M. Nesladek, and P. Bergonzo, Diamond Relat. Mater. **15**, 833 (2006).

[8] D. Twitchen, D. Phil. Thesis, University of Oxford (1997).

[9] E. Fritsch, L. Massi, G. Rossman, T. Hainschwang, S. Jobic, and R. Dessapt, Diamond Relat. Mater. **16**, 401 (2007).

[10] J. A. van Wyk, J. H. N. Loubser, M. E. Newton, and J. M. Baker, J. Phys. Condens. Matter **4**, 2651 (1992).

[11] P. E. Klingsporn, M. D. Bell, and W. J. Leivo, J. Appl. Phys. **41**, 2977 (1970).

[12] G. J. Hill, J. A. van Wyk, and M. J. R. Hoch, Radiat. Eff. Defect. Solid. **156**, 221 (2001).

[13] A. T. Collins and S. Rafique, Proc. R. Soc. Lond. A. **367**, 81 (1979).

[14] G. Davies, Rep. Prog. Phys. **44**, 787 (1981).

[15] K. P. O'Donnell, J. Phys. C: Solid State Phys. **13**, L363 (1980).

[16] J. Walker, Rep. Prog. Phys. **42**, 1605 (1979).

[17] Y. Mita, Y. Nisida, K. Suito, A. Onodera, and S. Yazu, J. Phys. Condens. Matter **2**, 8567 (1990).

[18] V. Nadolinny, A. Yelisseyev, O. Yurjeva, A. Hofstaetter, B. Meyer, and B. Feigelson, Diamond Relat. Mater. **7**, 1558 (1998).

[19] V. Nadolinny and A. Yelisseyev, Diamond Relat. Mater. **3**, 17 (1994).

[20] V. Nadolinny, A. Eliseev, and O. Yurieva, J. Struct. Chem. **35**, 817 (1994).

[21] C. Glover, M. E. Newton, P. Martineau, D. J. Twitchen, and J. M. Baker, Phys. Rev. Lett. **90**, 185507 (2003).

[22] A. M. Edmonds, PhD. Thesis, University of Warwick (2008).

[23] M. J. Shaw, P. R. Briddon, J. P. Goss, M. J. Rayson, A. Kerridge, A. H. Harker, and A. M. Stoneham, Phys. Rev. Lett. **95**, 105502 (2005).

[24] R. J. Cruddace, PhD. Thesis, University of Warwick (2007).

[25] G. Davies, Chem. Phys. Carbon **13**, 1 (1977).

[26] H. B. Dyer and L. du Preez, J. Chem. Phys. **42**, 1898 (1965).

[27] H. B. Dyer and L. du Preez, in *Science and technology of industrial diamonds; proceedings of the International Industrial Conference, Oxford*, edited by J. Burls (1967).

[28] I. N. Kupriyanov, V. A. Gusev, Y. N. Pal'yanov, and Y. M. Borzdov, J. Phys. Condens. Matter **12**, 7843 (2000).

[29] M. E. Newton and J. M. Baker, J. Phys. Condens. Matter **1**, 10549 (1989).

[30] B. I. Shklovskii and A. L. Efros, *Electronic properties of doped semiconductors* (Springer, 1984).

[31] P. M. Martineau, S. C. Lawson, A. J. Taylor, S. J. Quinn, D. J. F. Evans, and M. J. Crowder, Gems. Gemmol. **40**, 2 (2004).

[32] S. C. Lawson, D. Fisher, D. C. Hunt, and M. E. Newton, J. Phys. Condens. Matter

10, 6171 (1998).

[33] B. L. Cann, S. Felton, M. E. Newton, J. M. Baker, P. M. Martineau, R. U. A. Khan, and D. J. Twitchen, *WAR6, 7 and 8: Three new point defects in CVD diamond*, The 59th Diamond Conference, Oxford, poster presentation (2008).

[34] R. U. A. Khan, P. Martineau, B. L. Cann, M. E. Newton, and D. J. Twitchen, J. Phys. C Solid State **21**, 364214 (2009).

[35] E. D. Palik, *The handbook of optical constants* (Academic Press, 1985).

[36] P. M. Martineau (2009), private communication.

[37] G. L. Pearson and J. Bardeen, Phys. Rev. **75**, 865 (1949).

[38] J. P. Lagrange, A. Deneuville, and E. Gheeraert, Diamond Relat. Mater. **7**, 1390 (1998).

[39] T. F. Lee and T. C. McGill, J. Appl. Phys. **46**, 373 (1975).

[40] R. Jones, Diamond Relat. Mater. **18**, 820 (2009).

[41] R. M. Chrenko, H. M. Strong, and R. E. Tuft, Phil. Mag. **23**, 313 (1971).

[42] J. P. Goss, P. R. Briddon, R. Jones, and S. Sque, J. Phys. Condens. Matter **15**, S2903 (2003).

[43] U. F. S. D'Haenens Johansson (2009), private communication.

Chapter 7

A preferentially aligned defect in CVD diamond

7.1 Overview

The type and concentration of point defects in synthetic CVD diamond depends upon the growth conditions and post-growth treatments, such as annealing or irradiation. Increased understanding of defects and their formation could provide information about the CVD growth process; which could in turn allow better control of their incorporation.

7.1.1 Hydrogen in diamond

Hydrogen is found in natural diamond [1–3], annealed HPHT-grown diamond [4, 5] and CVD grown diamond [6, 7]. The presence of hydrogen can have a significant affect on the electrical and optical properties of all semiconductors. Hence, it is essential to understand the affect of hydrogen on the exploitable properties of diamond if the material is to be developed for electronic applications. Section 2.4 further discusses hydrogen in diamond and specific point defects which contain hydrogen.

7.1.2 CVD Diamond growth

Homoepitaxial CVD diamond growth has been achieved on surfaces with different crystallographic orientations. However, the majority of high purity single-crystal (SC)-CVD diamond is grown on {100} oriented substrates, where the numbers of defects such as growth hillocks and penetration twins [8] are minimised, so producing the smoothest possible surface.

Although macroscopic modelling of CVD growth has successfully predicted growth rates [9], there is still considerable confusion concerning the microscopic mechanisms of CVD diamond growth, particularly in the [100] direction [10–13].

There also exists a third description of diamond growth suggested by Martineau *et al.* [14], which lies between the microscopic and macroscopic models. The Martineau model explains the striations often observed in CVD diamond (see Figure 6-1).

7.1.2.1 Mono-hydride dimer model

A plausible surface reconstruction model for {001} diamond growth is the mono-hydride dimer surface reconstruction model. This model is discussed in detail by Thoms and Butler [12] and summarised here. In a hydrogen-rich CVD diamond growth environment hydrogen acts to terminate the growth surface. Figure 7.1(a) shows an example of this surface, where the hydrogen-hydrogen repulsion is alleviated by the distortion of the lattice and the formation of carbon-carbon (dimer) bonds. To minimise the energy involved in the distortion the carbon–carbon dimers occur in rows (Figure 7.1(b)) [12]. It has been suggested [15] that these rows formed in a zipper type process which moves in a ⟨110⟩ direction. In such a structure all bonds are compensated, but the hydrogen atoms are sufficiently separated so as not cause excessive strain [16]. Recent experimental and theoretical work regarding this structure, and diamond growth upon it, is reviewed by Butler *et al.* [17].

This dimer mechanism has been suggested as the initial stage of growth on a (100) diamond surface [18]. A new diamond layer might begin with the nucleation of a single carbon atom at the dimer bond. In the case of methyl based environments, the nucleation of this carbon atom results from the surface interaction with a methyl radical [19–22].

7.1.3 Preferentially aligned defects in diamond

Preferentially aligned point defects show a non-equal distribution over crystallographically equivalent orientations. Such defects have been observed in natural diamond (e.g. N4 [23] and W4 [24]), where it has been presumed that the prefer-

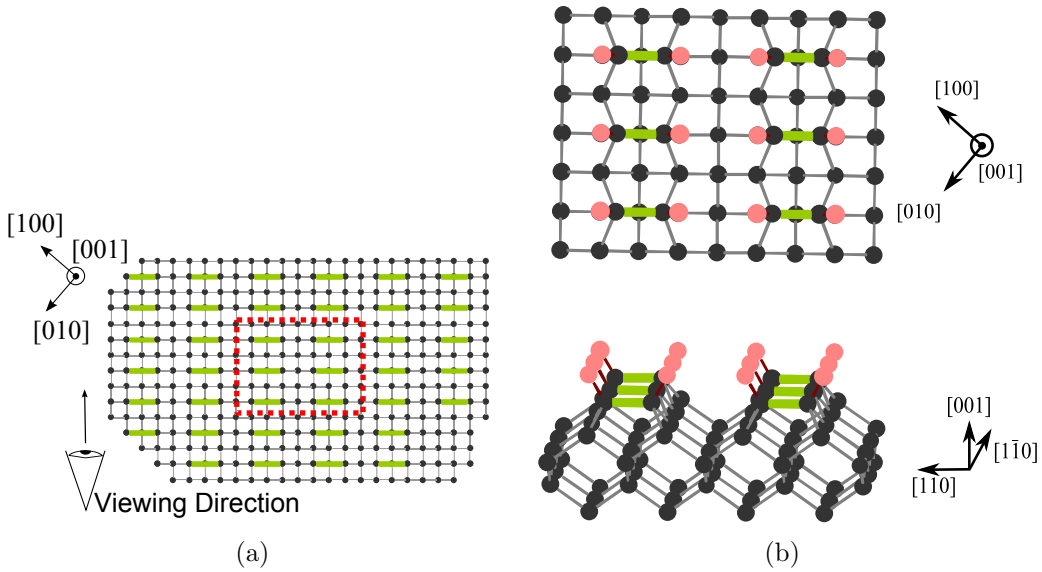

Figure 7-1: A calotte model of a (001) mono-hydride reconstructed surface, where each track of dimer bonds extends without interruption. Hydrogen atoms are lightly shaded (red when in colour), carbon atoms black and dimer bonds are thick and lightly shaded (green when in colour). (a) shows a large surface but no hydrogen atoms nor displacement of carbon atoms. The viewing direction illustrated in (a) is related to (b) and the red dotted box indicates the limit of (b). In (b) dimers, hydrogen atoms and their displacements and the affect on the near surface lattice is shown. Two perspectives are shown in (b); [001] above and close to [1$\bar{1}$0] below.

ential distribution is the result of plastic deformation [25].

Preferential alignment is also observed in both HPHT and CVD synthetic diamond. An example of a preferentially aligned defect in HPHT synthetic diamond is the 2.463 eV [26], H3 defect, which comprises of a pair of substitutional nitrogen atoms separated by a lattice vacancy $(N_s - V - N_s)^0$. This defect has been shown to align exclusively with the [100] growth direction in as-grown HPHT diamond [26]. A model to explain this preferential alignment has been suggested by Dodge [27]. Recently, in diamond grown by CVD, preferentially aligned defects have been reported by Edmonds [28] and D'Haenens-Johansson [29].

For growth on ⟨001⟩ oriented substrates defects with, for example D_{2d} or C_{2v} symmetry, might be expected to show preferential alignment, whereas those with trigonal symmetry (e.g. C_{3v} or D_{3d}) would not. This is because each bond in a defect with this symmetry would present the same angle to each of the {001}-type crystallographic growth planes. However, preferential alignment of the latter could occur for growth on {110} oriented substrates.

Preferentially aligned defects have also been observed in CVD diamond through cathodoluminescence (CL) [30]. Charles [30] observed three ZPLs at 496.8 nm, 496.8 and 562.5 nm with preferential alignment. The first line is thought to be nitrogen related, but the latter two are more likely to be hydrogen related. The latter lines have shown C_{2v} and C_{2v} or C_{1h} (undetermined by experiment) symmetries respectively, and both show high stress-splitting rates, which implies the involvement of vacancies. Suggested models are [V-X-V] and [V-X-V-Y], respectively where X and Y are non-nitrogen impurities [30].

7.2 Experimental details

7.2.1 CVD growth conditions

Eight free-standing SC-CVD diamonds grown on {100} substrates from three independent suppliers were investigated:

1. One sample from IMOMEC (Institute for Materials Research in Micro Electronics - Hasselt University, Diepenbeek, Belgium). This sample was a 2.5 mm square plate ~0.5 mm thick, grown in a ASTeX1 system, at 973–1023 K and 180 Torr, for a duration of 163 hours in an H_2 atmosphere with 10% methane [31].
2. One sample from LIMHP (Laboratoire d'Ingénierie des Matériaux et des Hautes Pressions - Université Paris, France). This sample was grown in a pulsed microwave CVD mode with a gas source composition of 7% methane in a H_2 atmosphere with 6 ppm nitrogen at 1073–1123°C [32]. This sample was ~ $4 \times 4 \times 1$ mm subsequently cut into ten approximately equally sized blocks, two of which were used here for annealing studies.
3. Six samples from Element Six Ltd. (E6). No specific growth conditions for these samples have been made available, although general conditions have been discussed by Isberg *et al.* [33].

Defect concentrations determined by EPR are given in Table A-1.

Table 7-1: Defect concentrations in samples from three different suppliers which contain varying concentrations of the WAR2 defect. All concentrations are given in ppb and with an associated 10% error. (See Chapter 2 for details of the defects.)

Sample	Mass / (mg)	Supplier	$[N_S^0]$	[WAR2]	$[V_nH^-]$	$[NV^-]$	$[NVH^-]$	Figure
A	48	DTC/E6	130	4	1.5	-	-	7-2
B	14	IMOMEC	-	~2	-	-	-	7-3
C	36	DTC/E6	265	5	4	-	25	-
D	9	LIMHP	250	1	1	-	-	7-4
E	80	DTC/E6	160	0.5	1	-	-	-
F	146	DTC/E6	230	9	5	5	75	-
G	52	DTC/E6	130	0.3	1	-	-	-
H	70	DTC/E6	560	2	5	0.5	50	-

7.2.2 Experimental apparatus

EPR measurements were made using the apparatus outlined in Chapter 4. At X-band the SHQ and HQ cavities are used alongside the commercial Q-band spectrometer, see Section 4.1.5. EPR measurements were made using both SP-EPR and RP-EPR regimes, see Chapter 5. Measurements were also made at low temperatures (10-100 K).

Photoluminescence (PL) measurements at liquid nitrogen temperatures have been recorded at the DTC Research Centre using a Labram HR PL spectrometer with excitation at 325, 458, 488, 514, 660 and 785 nm.

Annealing work has been carried out using the Elite Thermal Designs tube furnace which is described in Section 4.2.

7.3 Results

7.3.1 Samples and defect concentrations

Samples obtained from E6 and LIMHP (Table A-1) contained neutral single substitutional nitrogen (N_S^0) in concentrations of 20–300 ppb. Those from IMOMEC showed no detectable N_S^0 in SP-EPR or RP-EPR [34]. However, in SP-EPR the spectrum is dominated by the H1 signal [35].

In tens of [001] grown CVD diamonds, including those detailed in Table A-1 an additional unreported defect of $S = \frac{1}{2}$ has been detected using EPR, and is labelled WAR2. The concentration of WAR2 is 1–2 orders of magnitude lower

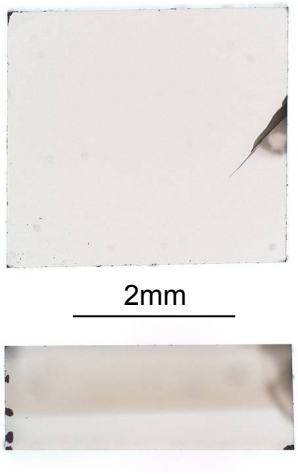

Figure 7-2: Photograph of Sample A, a SC-CVD diamond with two growth phases. A darker brown region and a lighter region can be distinguished by eye.

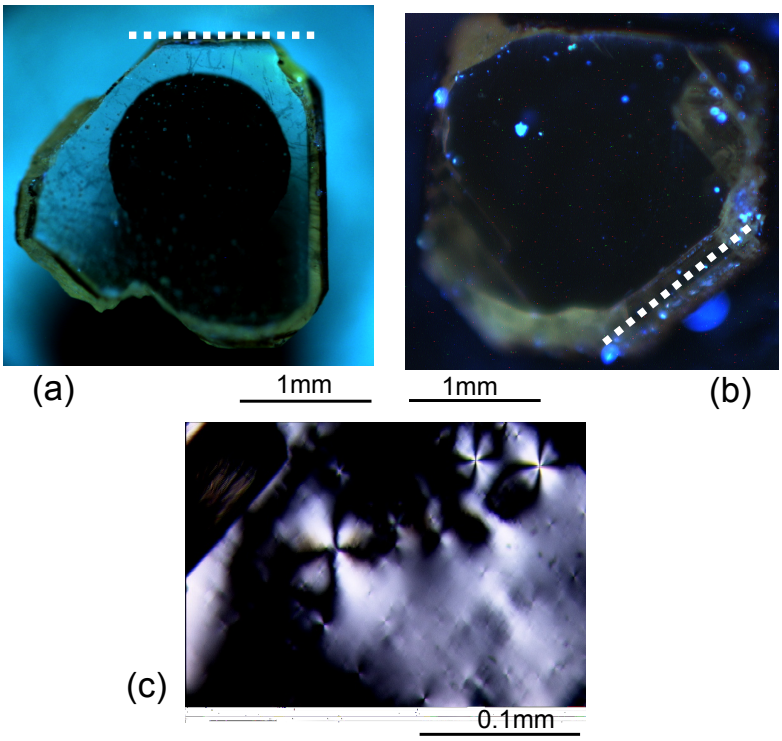

Figure 7-3: Images of Sample B. (a) is a picture of Sample B under optical illumination within a 'Diamond View' experiment and (b) is an image from a 'Diamond View' system. (The same edge is highlighted in both figures.) (c) shows the image through cross polarisers and an optical microscope, this indicates significant strain in the diamond.

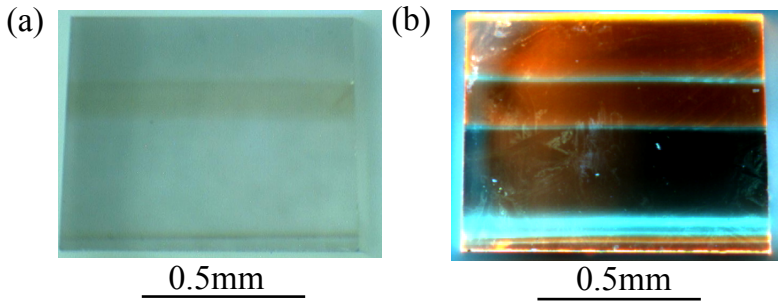

Figure 7-4: Sample D, a single crystal sample which shows three growth phases. (a) shows the sample under optical illumination and (b) is an image from a 'Diamond View' system.

than that of N_S^0. This means that the WAR2 lines are of comparable magnitude to the ^{13}C satellites from N_S^0.

Sample B showed a strong H1 signal but the concentration of N_S^0 was below the X-band EPR detection limit. However, the sample contains a significant concentration of the H1 defect which has a strong EPR signal around $g = 2.00$ which can obscure other defects. The H1 defect is hydrogen-related and is found in high concentrations at grain boundaries [36]. The WAR2 defect in Sample B is obscured in SP-EPR by the H1 defect but the difference in relaxation rates between the WAR2 and H1 defects means that in RP-EPR the defects can be disentangled as shown in Figure 7-5. Hence, the concentration of WAR2 is determined from the non-conventional RP-EPR technique described in Chapter 5, (see Table A-1).

Sample D is the only sample from LIMHP, analysed by the Warwick group, to show the WAR2 defect. This sample contains a brown stripe through the sample in a {001} plane (Figure 7-4), which was grown-in when the CVD growth was interrupted. From measurements on the nine samples which contain the WAR2 defect, in the concentration range 1–9 ppb, no correlation with any other EPR-active defect has been observed (see Table A-1).

7.3.2 EPR - WAR2 characterisation

Using samples A and B, where the ratio of the concentration of WAR2 to that of N_S^0 is relatively high, the EPR transitions of the WAR2 defect were mapped as a function of orientation of the external magnetic field (B_0). The WAR2 lines are thus are distinguishable from the ^{13}C satellites of the N_S^0 EPR spectrum.

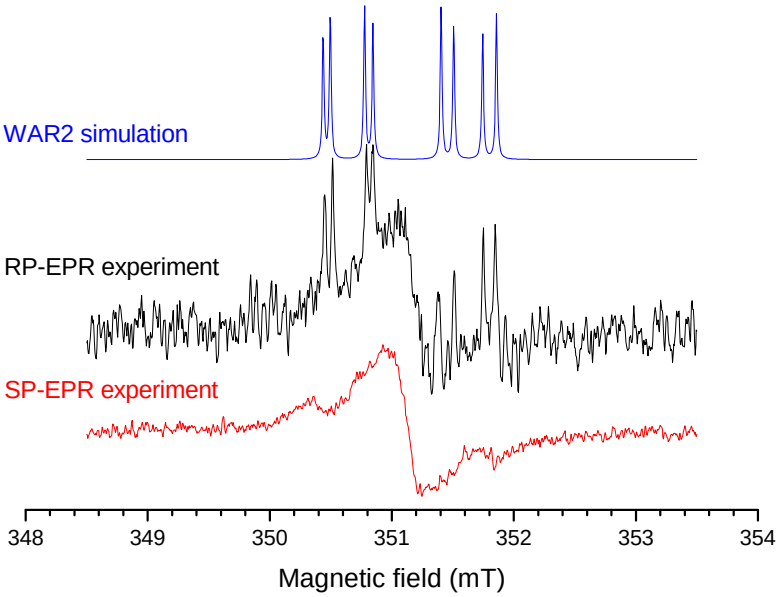

Figure 7-5: The SP-EPR spectrum scan (red when in colour) of Sample B, acquired over ~17 hours at 60 dB, shows a strong H1 [35] signal. The RP-EPR spectrum scan (middle spectrum) of Sample B, acquired over ~14.5 hours at 30 dB, shows additional signals which are labelled the WAR2 defect. The WAR2 defect is simulated (blue when in colour) using the spin Hamiltonian parameters given in Table 7-2.

Figure 7-6: A cartoon of a [001] grown sample showing the roadmap planes of rotation. (a) the rotation of the external magnetic field from [100] to [010] in the (001) plane, (Figures 7.7(a) and 7-8), and (b) the rotation of the external magnetic field from [001] to [100] in the (100) plane (Figure 7.7(b)).

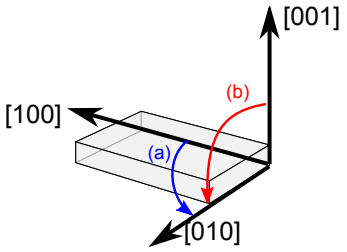

X-band roadmaps were produced by recording spectra with the external magnetic field applied at 5° intervals in a {001} plane as shown in Figure 7-6 labelled (a) (remaining in the growth plane). The resulting roadmap, which is shown in Figure 7.7(a) repeats every 90°. A roadmap in the {100} plane is depicted in Figure 7-6 labelled (b) (involving the growth direction). The resulting roadmap repeats every 180°, as shown in Figure 7.7(b). Q-band spectra were obtained at 10° intervals in the {001} plane, as shown in Figure 7-8.

Crystal alignment with respect to the external magnetic field has been confirmed by comparing it to a simulated N_S^0 roadmap [37]. All of the transitions of interest are observed around $g \approx 2.00$ within a 2 mT range at X-band and within a 4 mT range at Q-band.

The simulated fits to the WAR2 spectra and peak positions are produced using the parameters which provide the best fit to the roadmaps and spectra shown. The parameters are determined by a least squares fit of the experimental EPR transition positions to the spin Hamiltonian:

$$\mathscr{H} = \mu_B \mathbf{B^T} \cdot \underline{\mathbf{g}} \hat{\mathbf{S}} + \hat{\mathbf{S}}^{\mathbf{T}} \cdot \underline{\mathbf{A}}_j \hat{\mathbf{I}}_j - \mu_N g_{N_j} \mathbf{B^T} \cdot \hat{\mathbf{I}}_j \tag{7-1}$$

where $S = \frac{1}{2}$ and $I = \frac{1}{2}$ (from a single hydrogen atom). The symmetry of the WAR2 defect has been simulated as C_{2v} in Figures 7-7 and 7-8 and subsequently with C_2 symmetry in Figures 7-11 and 7-12. The spin Hamiltonian parameters are given in Table 7-2.

The EPR spectra recorded with $B_0 \parallel [100]$ and $B_0 \parallel [010]$ are identical (see Figure 7.7(a)), but with $B_0 \parallel [001]$ (the growth direction) a different spectrum is observed (Figure 7.7(b)).

The EPR spectrum becomes complicated when the external magnetic field is close to a ⟨110⟩ crystallographic direction (in the growth plane), where the transitions coincide. This is due to the hyperfine and nuclear Zeeman interactions are of similar magnitudes at X-band magnetic fields (Figure 7-9).

The Q-band spectra show a larger separation between the transitions, which resulting in a simpler roadmap. The magnitude of the outermost observed splitting is approximately twice the proton NMR frequency (the arrow in Figure 7-8) indicating the involvement of a single hydrogen nucleus (i.e. these are electron-proton double spin flip transitions).

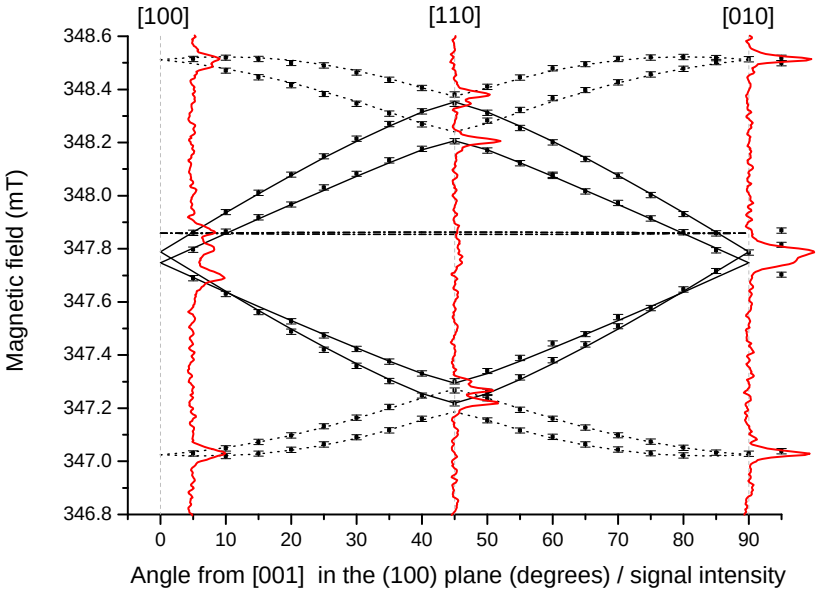

(a)

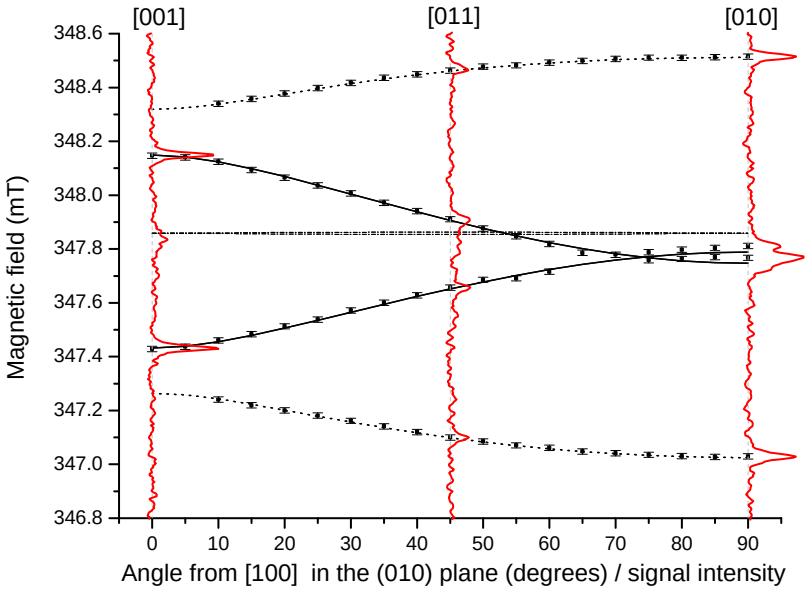

(b)

Figure 7-7: Roadmaps and experimental EPR spectra recorded from Sample B at X-band frequencies in (a) (001) and (b) (100) crystallographic planes with the microwave frequency corrected to 9.752 GHz. WAR2 line positions are marked with appropriate error bars and simulated EPR line positions are marked by lines. The allowed EPR transitions ($\triangle M_S = 1$) are shown by solid lines, and the forbidden EPR transitions by broken lines. The spin Hamiltonian parameters used for the simulation are given in Table 7-2. Simulation of the central N_S^0 transition is shown by a dot-dash line. Experimental RP-EPR spectra are shown vertically (red when in colour).

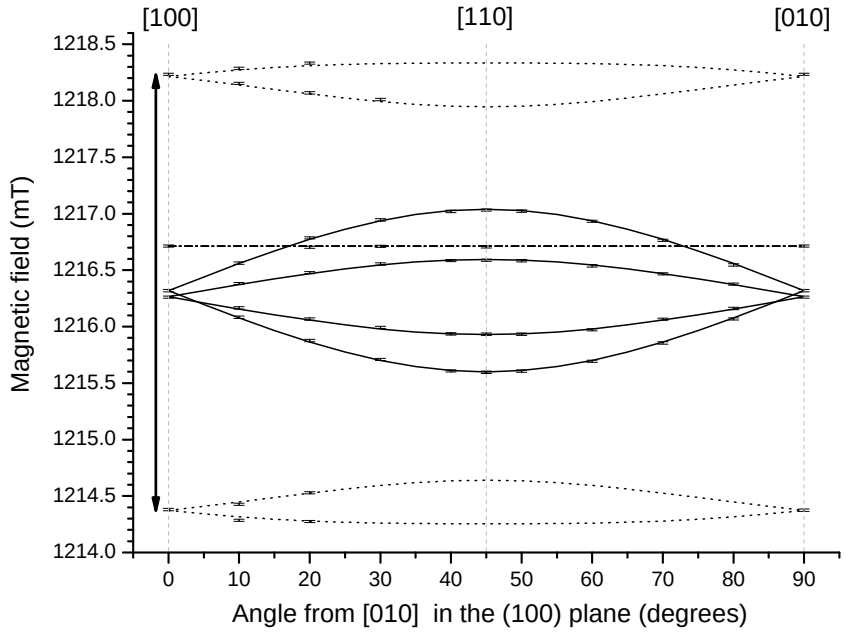

Figure 7-8: (001) roadmap with peak positions determined from Sample B at with the microwave frequency corrected to 35 GHz. WAR2 line positions are marked with appropriate error bars and the simulated EPR line positions are marked by lines. The allowed EPR transitions ($\triangle M_S$ = 1) are shown by solid lines, and the forbidden EPR transitions by broken lines. The spin Hamiltonian parameters used for the simulation are given in Table 7-2. Simulation of the central N_S^0 EPR transition is shown by a dot-dash line.

The angular variation observed in the roadmaps indicates that the defect has C_{2v} symmetry. To account for the preferential alignment only two of the possible six sites usually associated with C_{2v} symmetry are required, i.e. those with the axis of symmetry along [001] (the growth direction).

7.3.3 EPR high resolution

In the majority of samples where the WAR2 defect is present, the concentration of N_S^0 is significantly larger than the concentration of WAR2, or, as in the case of Sample B, there are other complications. This makes detailed study of the WAR2 defect difficult.

To improve the ability to observe the WAR2 defect the following routes were taken:

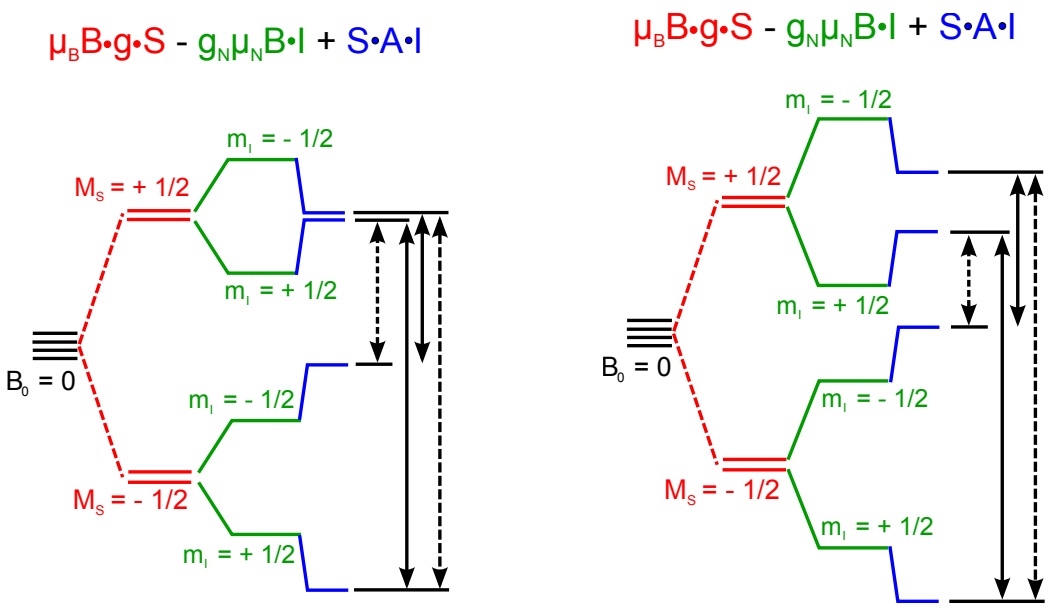

(a) (b)

Figure 7-9: Cartoon energy level diagram showing the affect that comparable magnitudes of nuclear Zeeman and hyperfine interactions can have on the WAR2 energy levels at X-band. (a) shows the energy levels at X-band where $|g_N \mu_N B_0| \sim \frac{A}{2}$ and (b) at Q-band where $|g_N \mu_N B_0| > \frac{A}{2}$. The energy gaps between levels are proportional to the magnetic field at which the transition is observed, hence at X-band transitions are observed at very similar fields. Note the cartoons are not to scale and that the electronic Zeeman interaction is significantly larger than the nuclear Zeeman interaction.

1. Charge transfer - As shown in Chapter 6 the heat treatment of CVD diamond can result in a temporary reduction in the concentration of N_S^0. In the case of Sample A the concentration of N_S^0 was reduced from 130(13) to ~1 ppb after a 850 K treatment, whereas the concentration of WAR2 was only reduced from 4.0(5) to 2.9(5) ppb. As a result the observed spectra was substantially altered.
2. Frequency drift - Although the microwave frequency is locked to the sample resonator, the microwave frequency will vary during signal averaging due to external factors, for example laboratory temperature variation. By correcting for this frequency drift prior to averaging the spectra, splittings of 0.01 mT can be resolved which were previously broadened beyond detection.

Splittings were now observed which could not be the result of misalignment

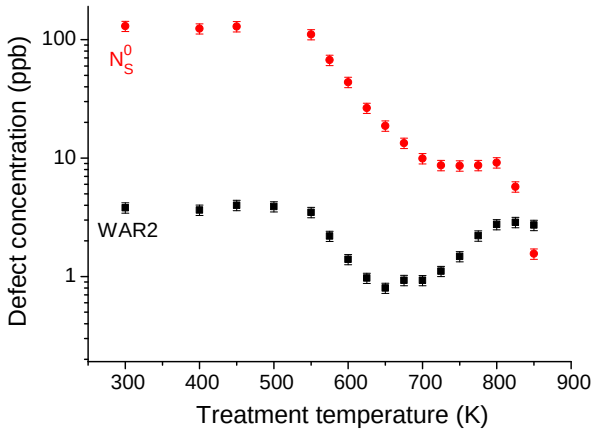

Figure 7-10: Variation in concentration of N_S^0 and WAR2 in Sample A as a result of isochronal heat treatment inside the high temperature cavity. See Section 6.2.

Table 7-2: The best fit spin Hamiltonian parameters determined for WAR2 at room temperature. Electronic Zeeman (**g**) and hyperfine interactions (**A**) and their directions are given. θ is defined as the angle from the crystallographic [001] direction and φ is the angle from [100] measured towards [010] in the (100) plane. The g-factor is given relative to that of N_S^0 which is assumed isotropic with a value of $g = 2.0024$. $[hkl]$ is given for the C_{2v} symmetry and is approximate for the C_2 symmetry. Figure 7-13 describes the spin Hamiltonian parameters pictorially.

	C_{2v}				C_2					
[hkl]	θ (°)	ϕ (°)	**g**	**A** (MHz)	θ (°)	ϕ (°)	**g**	θ (°)	ϕ (°)	**A** (MHz)
[001]	0	90	2.0030(1)	∓20.1(1)	0	90	2.0030(1)	0	90	∓20.1(1)
[110]	90	45	2.0028(1)	±30.9(1)	90	46.1(1)	2.0028(1)	90	44.6(1)	±30.9(1)
[1$\bar{1}$0]	90	315	2.0034(1)	∓27.7(1)	90	316.1(1)	2.0034(1)	90	314.6(1)	∓27.9(1)

since the number of lines allowed by the defect's symmetry is constrained[1] to 8. This splitting indicates the defects symmetry is lower, C_2 not C_{2v}, but the defects preferential alignment is conserved. For C_{2v} the principle components of the Zeeman and hyperfine interactions of the spin Hamiltonian are oriented along [001], [110] and [1$\bar{1}$0]. To account for the splitting, it is necessary to rotate the electronic Zeeman and hyperfine interactions about [001] by approximately one degree in opposing directions as shown in Figure 7-13. The degree of rotation has been determined by a least squares fit to the data from Figure 7-11, constraining the symmetry to C_2. The fit quality is improved by this lowering of symmetry (Figure 7-12) and the C_2 symmetry simulations predict the observed line broadening caused by unresolved splittings.

[1] As shown in Figure 7-9 there are four different transitions associated with each site and in the case of the preferentially oriented C_{2v} structure there are two sites.

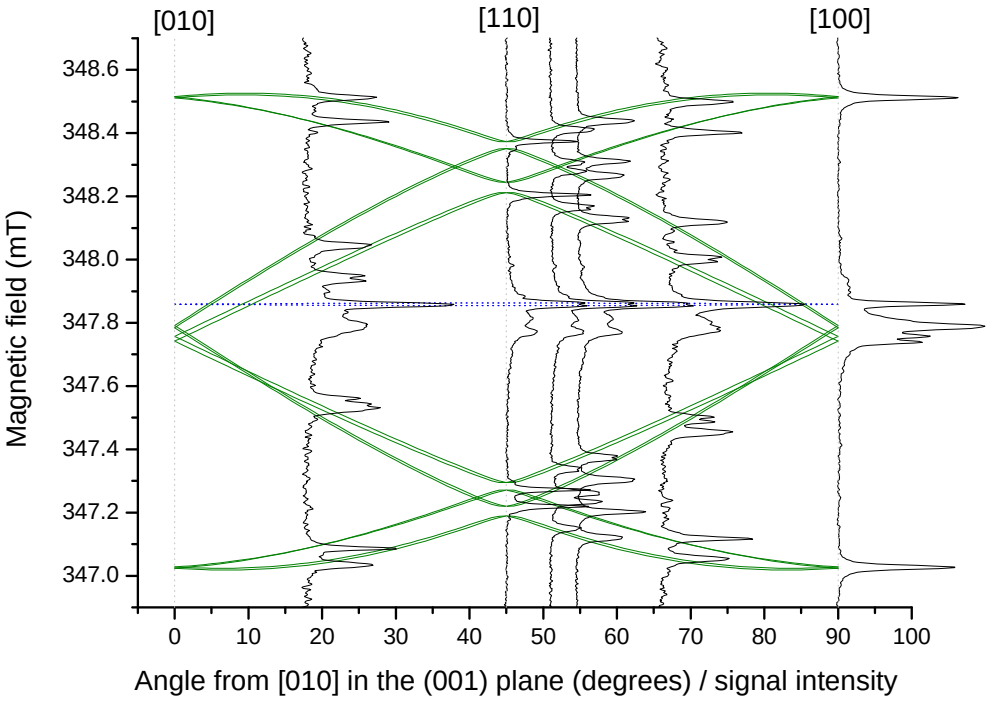

Figure 7-11: Experimental EPR spectra from Sample A after heat treatment at 850 K shown vertically. The simulated WAR2 roadmaps (9.75 GHz) are shown by solid (green when in colour) lines modelled with C_2 symmetry using the spin Hamiltonian parameters given in Table 7-2. The central N_S^0 transition is shown by the dotted line (blue when in colour). The line broadening and splittings are well explained by the C_2 symmetry model.

7.3.4 High temperature annealing

Sample B and two of the portions of the original sample, from which Sample C is a part, were isothermally annealed (each at a different temperature). Periodically the anneal was interrupted, and the sample was cooled to room temperature and illuminated with UV light (to maximise the remaining WAR2 defect concentration). The WAR2 concentration was then measured. The solid lines in Figure 7.14(a) show the best fit to first order kinetics at three temperatures. The activation energy determined from the resulting Arrhenius plot (Figure 7.14(b)) is 4.2(1) eV with a characteristic time of $8(9) \times 10^{-13}$ s. No change in the preferential alignment was noticed with annealing or heat treatment, an no other complementary changes in other defect concentrations were observed.

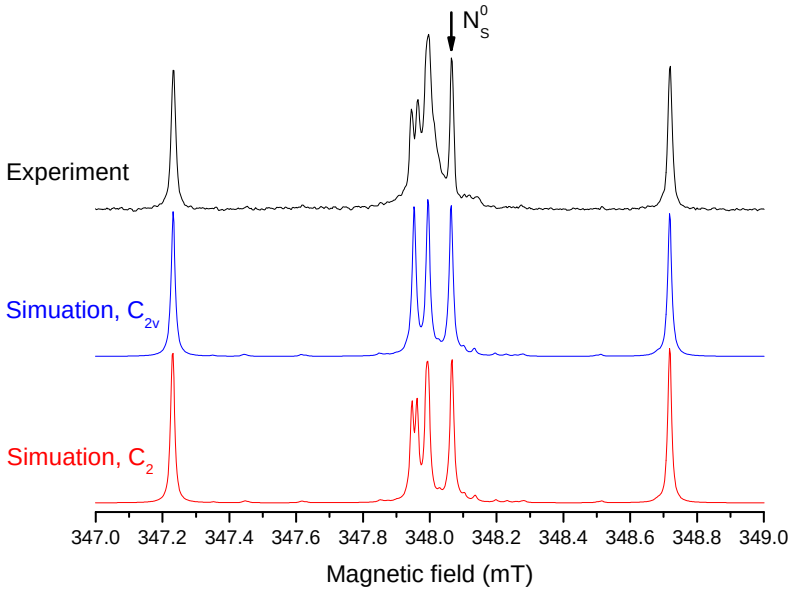

Figure 7-12: The experimental EPR spectrum from Sample A after heat treatment to 850 K with the external magnetic field aligned parallel to [100]. The N_S^0 and WAR2 spectra are simulated using the best fit spin Hamiltonian parameters of WAR2 (Table 7-2) with C_{2v} and C_2 symmetry.

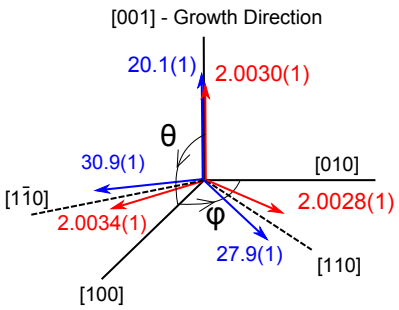

Figure 7-13: Cartoon describing the hyperfine and electronic Zeeman interactions in Table 7-2, where the WAR2 defect has C_2 symmetry.

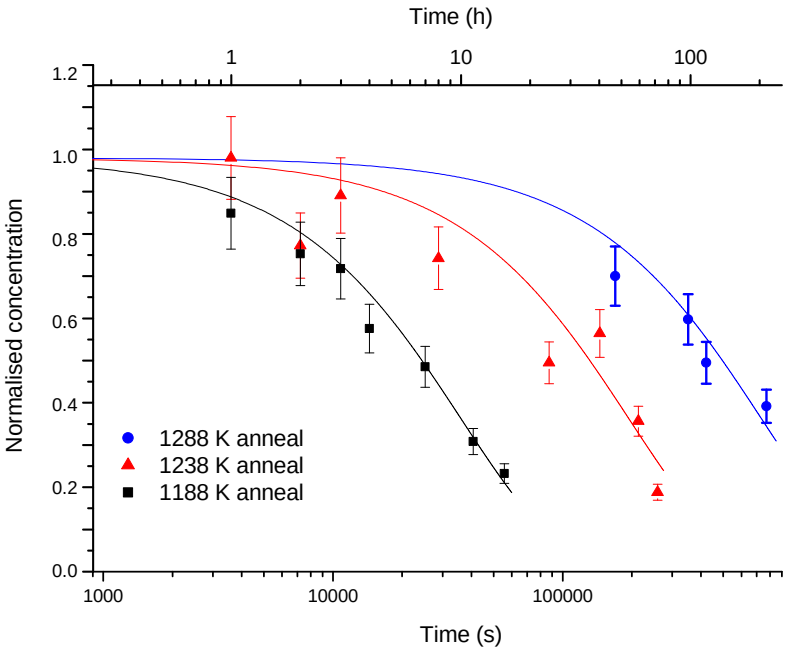

(a)

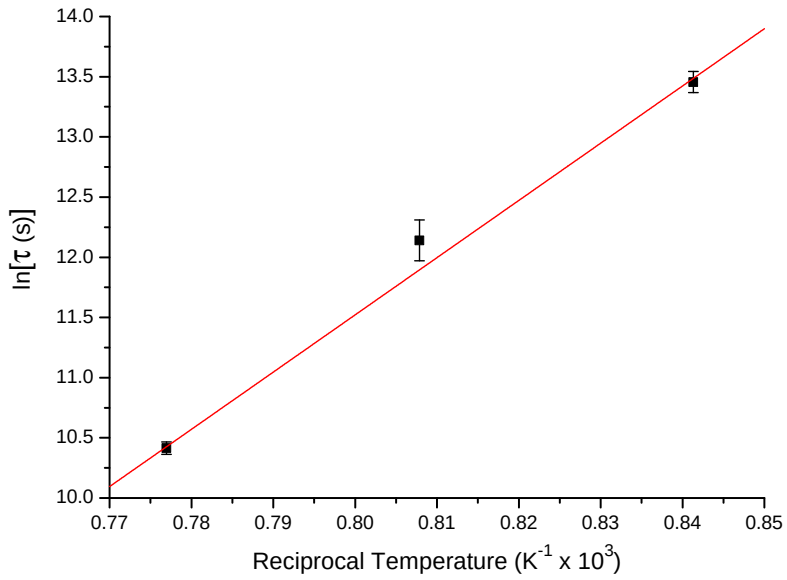

(b)

Figure 7-14: (a) Isothermal annealing decay curves of the concentration of the WAR2 defect in Sample B and two sister portions of Sample D at 1288, 1238 and 1188 K. Initial WAR2 concentrations were ~1 ppb. (b) shows the Arrhenius plot generated from the fits to data shown in (a). The best fit line gives an activation energy of 4.2(1) eV and a characteristic time of $8(9) \times 10^{-13}$ seconds.

7.3.5 Heat treatment

The effect of heat-treatment at 400–850 K on defect concentrations in samples A, B, C and H were investigated. Any observed variation in defect concentrations with heat treatment (below the defect annealing temperature) could be completely reversed by UV illumination. Variation in defect concentrations were observed for treatment temperatures equal to or above 550 K. For the purposes of this discussion the 550–850 K range has been broken up into regions (see Figure 7-15): Region 1 (550–700 K) where the activation energies are ~1 eV, Region 2 (700–800 K) where the activation energies are ~1.5 eV and Region 3 (>800 K) where activation energies are $\gtrsim$1.7 eV.

7.3.5.1 Sample A

The concentration of N_S^0 (Figure 7-15), WAR2 and V_nH^- observed in Sample A all varied with treatment temperature. Isochronal heat treatment resulted in the reduction in the concentration of N_S^0 in Region 1. This reduction was fitted to a 'mixed first and second order' expression derived in Section 6.3.1 (Equation 6-11), this resulted in an activation energy of 1.2(2) eV.

Isothermal heat treatment was also carried out on Sample A at seven temperatures in the temperature regions 1 and 2. An example of the thermal heat treatment on the concentration of N_S^0 in Sample A is shown in Figure 7.16(a). The reduction in the concentration of N_S^0 was fitted to a bi-exponential decay (two separate first order decays) and for comparison to the 'mixed order' expression given by Equation 6-11. The fits achieved to the experimental data by both expressions are of comparable quality, see the residuals plotted in Figure 7.16(a). Figure 7.16(b) shows the Arrhenius plot resulting from the 'mixed order' fits over the seven experimental temperatures. An activation energy of 1.1(2) eV was determined from these 'mixed order' fits. This activation energy was similar to those determined from the bi-exponential fits where the Arrhenius plots determined activation energies of 1.2(1) eV and 1.3(2) eV. These values are in agreement with the activation energy determined by isochronal annealing.

The second reduction in the concentration of N_S^0, which occurred in temperature Region 3 (see Figure 7-15) has not been fitted because of the excessive

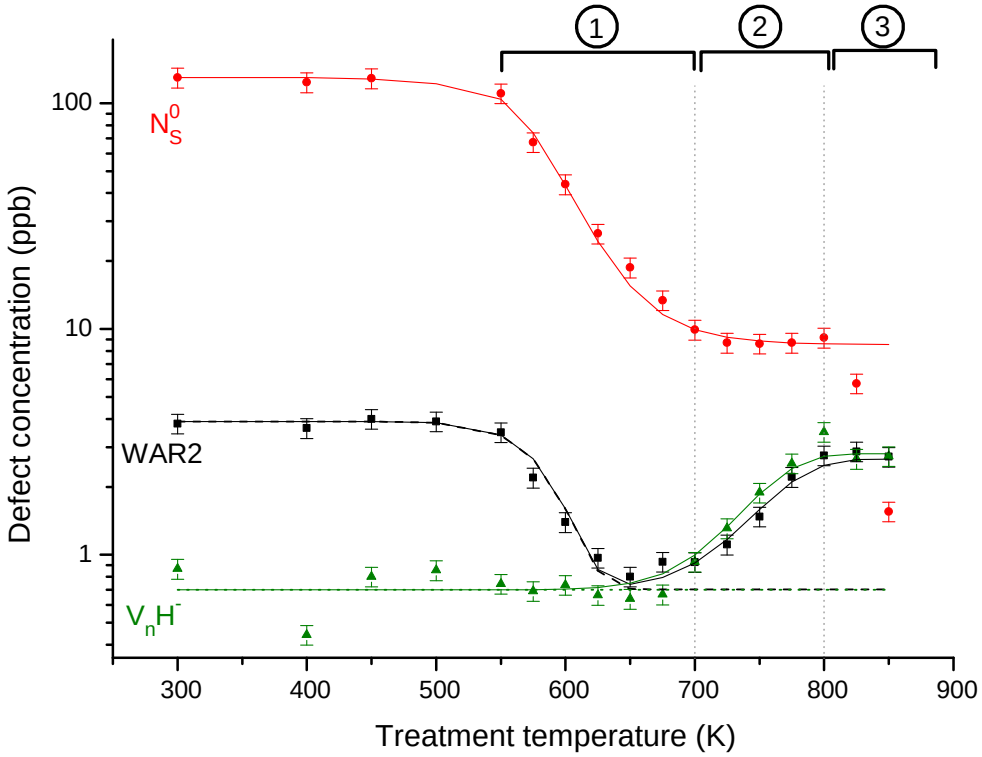

Figure 7-15: Variation in the EPR-active defect concentrations observed in Sample A with isochronal heat treatment between 400 and 850 K with the sample kept in the dark. The mixed order fit to the change in the concentration of N_S^0 gives an activation energy of 1.2(2) eV. Activation energies of 1.2(2) eV to the decay, and 1.5(2) eV to the recovery (first order) are determined from fits to the variation in concentration of WAR2. An activation energy of 1.5(2) eV is fit to the increase in concentration of V_nH^- (first order). The dotted line (green when in colour) indicates the initial concentration of V_nH^- and the dashed line is the fit to the reduction in the concentration of WAR2 to a plateau. For analysis the treatment temperature is split into three treatment temperature regions as displayed.

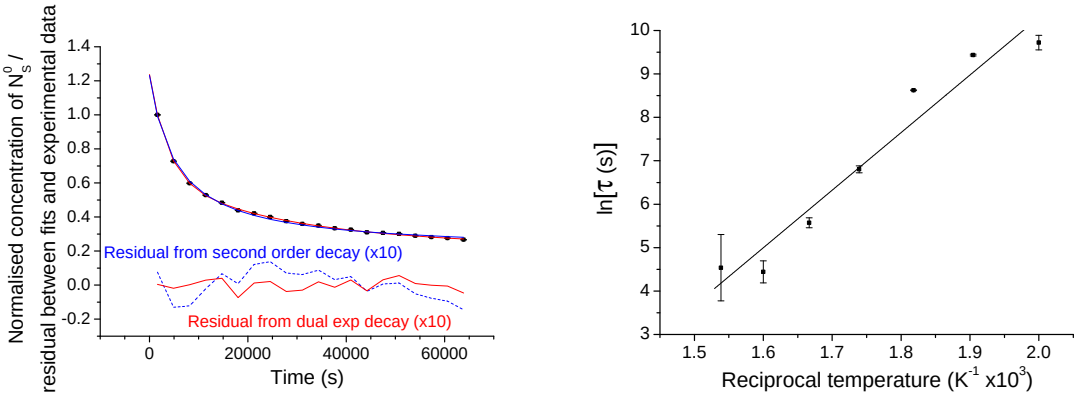

(a) (b)

Figure 7-16: (a) shows an isothermal annealing curve showing the reduction in concentration of N_S^0 when Sample A was heat treated in the dark at 550 K. Two fits are shown, a bi-exponential (both first order decays) (fit line in red when in colour) and a single exponential (mixed order decay) (fit line in blue when in colour). The residual between the experimental data and the fits are also shown but multiplied by 10 so to fit onto the same scale. The residual from the second order decay fit is shown by a dashed line (blue when in colour) and the residual from the first order decay by a solid line (red when in colour). (b) shows the Arrhenius plot for the decay of N_S^0 in Sample A over seven heat treatment temperatures. τ is determined from a single mixed order decay. The resulting activation energy is 1.1(2) eV with a characteristic time of $1(2)\times10^{-7}$ seconds.

weighting that would be placed on a single experimental data point. However, the region is consistent with processes characterised with an activation energy of ~1.7–2 eV.

The initial reduction in the concentration of the WAR2 defect (in temperature Region 1) had the same activation energy, to within error, as the reduction in N_S^0. The activation energy, as determined from isochronal annealing, is 1.2(2) eV, see Figure 7-15. (This reduction in concentration has been modelled as a decrease to a plateau at 0.8 ppb.) The activation energy as determined by isothermal annealing (1.0(2) eV) agrees to within error with that which was determined from isochronal annealing.

A recovery in the concentration of the WAR2 defect, as well as a change in the concentration of V_nH^- occurred in temperature Region 2, (see Figure 7-15). Both of these changes in concentration were fitted as a first order process, and both with an activation energy of 1.5(2) eV. The concentration of the WAR2 defect was

modelled to increase from zero[2] and the concentration of V_nH^- from an initial plateau of 0.18 ppb.

UV illumination of Sample A resulted in the recovery of the defect concentrations to those observed prior to heat treatment.

7.3.5.2 Sample C

Isochronal annealing was also performed on Sample C. For this sample, fits to the change in N_S^0 with temperature were better when using first order kinetics rather than 'mixed order' kinetics (see Chapter 6). First order kinetics fits give an activation energy of 0.5(1) eV (see Figure 7-17).

In temperature Region 1 the reduction in the concentration of the WAR2 defect in Sample C was fitted to first order kinetics and gave an activation energy of 1.0 eV (see Figure 7-17). The concentration of the WAR2 defect recovered in temperature Region 2 with an activation energy of 1.5 eV (first order kinetics). The concentration of V_nH^- also increased in temperature Region 2 and was fitted to the same activation energy of 1.5 eV (first order kinetics) see Figure 7-17.

7.3.5.3 Samples B and H

For Sample B no change in the concentration of N_S^0 or the WAR2 defect was detected when the sample was isochronally heat treated up to 850 K or illuminated with UV light.

For Sample H the concentration of the WAR2 defect was initially close to the detection limit. When the sample was isochronally heat treated the concentration of the WAR2 defect fell to below the detection limit, with an activation energy of 1.2(2) eV (first order kinetics). No recovery in the concentration of the WAR2 defect was detected with higher treatment temperatures as was observed in samples A and C. The concentration V_nH^- also increased in Sample H with an activation

[2]A good fit to the variation in the concentration of WAR2 with heat treatment cannot be obtained by summing two fits which model the reduction in the concentration of WAR2 to zero and the increase in the concentration of WAR2 from zero. Therefore, either the loss in concentration is to a plateau, as suggested here, or the subsequent increase in concentration starts from a non-zero value.

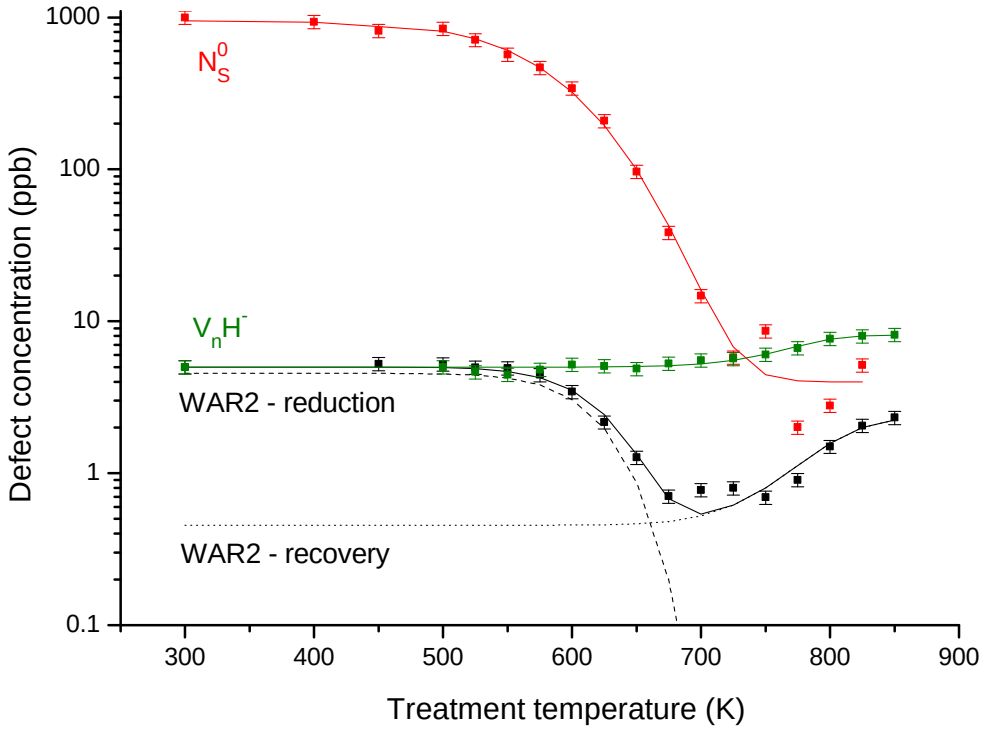

Figure 7-17: Experimental data from Sample C. The change in the concentration of N_S^0 is fitted to a first order decay with an activation energy of 0.5(2) eV (red when in colour). The reduction in the concentration of the WAR2 defect is fitted to first order kinetics with an activation energy of 1.2(2) eV (dashed line). The recovery in concentration of the WAR2 defect is fitted to first order kinetics with an activation energy of 1.5(2) eV (dotted line) and the sum of reduction and recovery is shown by a solid line. The increase in the concentration of V_nH^- is also fitted to first order kinetics with an activation energy of 1.5(2) eV (green when in colour).

energy of 1.3(3) eV (first order kinetics). UV illumination of Sample B resulted in the recovery of the defect concentrations to those observed prior to heat treatment.

7.3.6 Supporting data

Photoluminescence measurements made at liquid nitrogen temperatures (at the DTC Research Centre) on samples containing a range of different concentrations of the WAR2 defect, did not reveal an optical analogue.

Micro-twinning has been reported to be more prevalent in samples that contain the WAR2 defect than samples of similar overall defect concentrations that do not [38]. However, the volume of the twinned regions were not sufficiently large for them to be identified by EPR.

7.4 Discussion

The WAR2 defect is a paramagnetic defect with $S = \frac{1}{2}$ and which incorporates a single proton. The WAR2 defect is preferentially aligned with respect to the [001] growth direction. In all samples the defect has been observed in, the defect has displayed 100% preferential incorporation. However, due to the signal to noise level the highest preferential incorporation ratio determined is 200:1 (Sample A). This means that the likelihood of having the C_2 axis of the defect parallel to [001] (the growth direction) is at least 200 times more likely than it is to be perpendicular to it. To date, the WAR2 defect has only been observed in samples which are homoepitaxially grown on {001} oriented substrates.

The preferential alignment of the WAR2 defect is still observed after heat treatment at 1288 K and no reorientation is observed before the defect anneals out. The 4.2(1) eV activation energy associated with the permanent removal of the WAR2 defect is similar to the activation energy for the break-up of V_nH^- [39–41] which was experimentally determined by Cruddace [42] as 4.3(2) eV. This value is close to the bond disassociation energy value for carbon-hydrogen bonds of 4.3 eV (~420 $kJmol^{-1}$) [43].

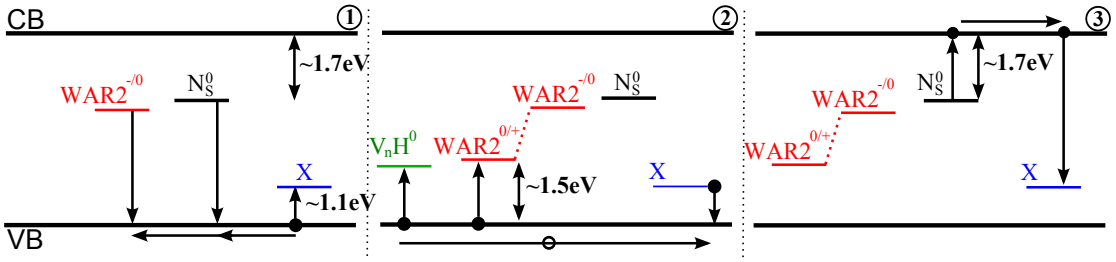

Figure 7-18: Cartoon depiction of the band-gap and the positions of defects within it. The charge transfer processes suggested by the model are shown in separate diagrams for each of the treatment temperature regions 1, 2 and 3, as marked.

7.4.1 Charge state

Although charge transfer is discussed in Chapter 6 it is necessary to mention it here in order to consider the charge state of the WAR2 defect.

The variations in defect concentrations in Sample A when it is heat treated or illuminated with UV light will be discussed in detail below using the temperature regions outlined in Figure 7-10. The behaviour of the WAR2 defect and other EPR-active defects in samples B, C and H are discussed in light of this model.

7.4.1.1 Temperature Region 1 in Sample A

The most abundant EPR-active defect in Sample A is the N_S^0 defect. When Sample A is heat treated in the dark between 550 and 850 K the concentration of N_S^0 decreases with an activation energy of 1.1(2) eV. The donor level of the N_S^0 defect is known to lie 1.7 eV below the conduction band, which is too deep to be responsible for this change. This implies that this charge transfer does not involve the conduction band, but instead the capture of holes by N_S^0 (see Equation 7-2). Such holes are produced by thermal excitation of electrons from the valence band to a low lying trap labelled X.

The reduction in the concentration of the WAR2 defect in Sample A with isochronal heat treatment in the dark between 400 and 850 K (see Figure 7-15), has a comparable activation energy (1.0(2) eV) to the decrease in the concentration of N_S^0, when treated under the same conditions. It is suggested that this similarity is due to the same charge transfer process, i.e. the capture of holes by the WAR2 defect. This means that the WAR2 defect becomes more positive, and if double

charging on the defect is considered unlikely[3], then this suggests the EPR-active charge state of the WAR2 defect is negative or neutral ($WAR2^{-/0}$). The charge transfer process can be described by Equation 7-2.

$$\begin{aligned} N_S^0 + X^0 &\longrightarrow N_S^+ + X^- \\ WAR2^{-/0} + X^0 &\longrightarrow WAR2^{0/+} + X^- \end{aligned} \tag{7-2}$$

It is suggested that $WAR2^{-/0}$ lies more than 1.0 eV below the conduction band and that charge transfer occurs via the valence band.

7.4.1.2 Temperature Region 2 in Sample A

The concentration of N_S^0 and WAR2 in Sample A reaches a plateau in temperature Region 2, this suggests that the trap X is fully compensated. The concentration of WAR2 recovers, with the same activation energy as the increase in the concentration of V_nH^- (see Figure 7-15).

Discounting the possibility of a doubly charged defect, both the $WAR2^{0/+}$ defect and V_nH^0 must accept an electron in order to become EPR-active. There is no correlating fall in N_S^0 which suggests that the electrons must be thermally excited from the valence band. This would leave holes in the valence band which will subsequently recombine with another defect, perhaps defect X. If this recombination results in another meta-stable 'equilibrium', then this would explain why the concentration of the EPR active, $WAR2^{-/0}$, defect does not fully recover (see Figure 7-18).

The position of $WAR2^{-/0}$ with respect to the valence band is uncertain because the experimentally determined activation energy gives the energy required to thermally excite an electron into the trap X from the valence band (see Figure 7-18).

7.4.1.3 Temperature Region 3 in Sample A

In temperature Region 3 when Sample A is heat treated in the dark between 750 and 850 K the concentration of N_S^0 reduces further. The reduction in concentration

[3]This may be explained by the repulsive forces that would be experienced by the charges over the small region of a single point defect

has not been fitted, but the temperatures involved are consistent with an activation energy of ≥1.7 eV. Such energies are sufficient to excite the electrons from the nitrogen donor into the conduction band, therefore it is suggested that the charge transfer occurs via the conduction band, see Figure 7-18.

7.4.1.4 Dual sector model - inhomogeneous distribution of defects

The variation in the concentration of V_nH^- does not fit well to the charge transfer model proposed. Specifically, how could the concentration of V_nH^- increase with heat treatment in temperature Region 2, but not reduce in concentration with heat treatment in temperature Region 1?

One explanation for this behaviour is that the EPR active defects observed are not homogenously distributed throughout the sample. For example, in Sample A the optical inhomogeneities suggest two distinct sectors, which could be treated independently, see Figure 7-2. This is consistent with the comparable fit quality achieved to the isothermal heat treatment data by the 'mixed order' decay and bi-exponential (first order) fits.

Assuming that the optical inhomogeneities reflect the defect concentrations the sample will be considered as two distinct sectors:

1. Sector one contains a high concentration of the X defect, sufficient for the concentration of N_S^0 and WAR2 to be reduced to zero. There is no detectable V_nH^- in this sector. See Figure 7-19(i).
2. In sector two there is little or no defect X, thus defect concentrations are unaffected by low activation energies and charge transfer can only occur at higher temperatures (see Figure 7-19(ii)).

The summation of the defect concentrations in both sectors can explain the observations from Sample A. As a result it is suggested that $WAR2^{0/+}$ lies ~1.5 eV above the valence band.

7.4.1.5 Samples B, C and H

The behaviour of Sample C fits with the suggested model and with the comparable activation energies. Given the unstable concentration of N_S^0 it is possible that N_S^0

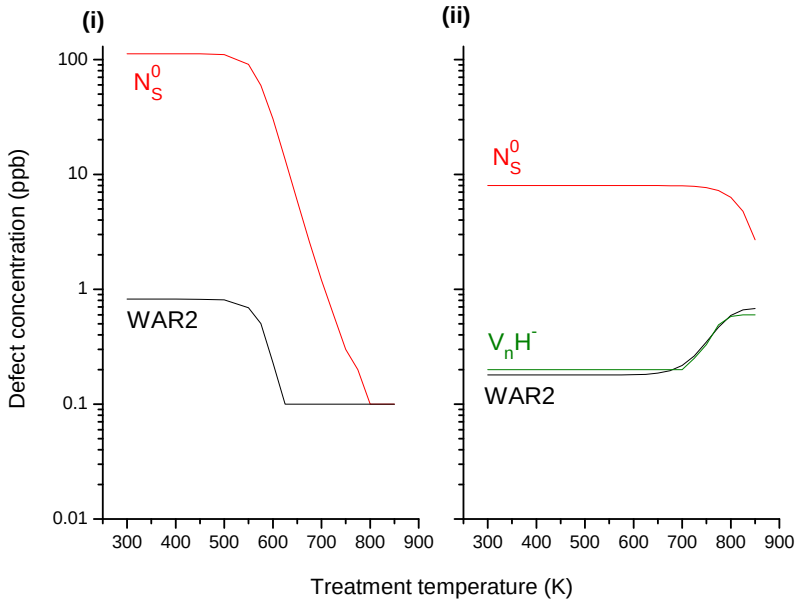

Figure 7-19: Simulated defect concentrations in two separate sectors of Sample A (see text) which could account for the observed behaviour of defect concentrations in Sample A with isochronal heat treatment between 400 and 850 K. Sector (i) has a high concentration of the defect X, (note that any concentration <0.1 ppb has been rounded to 0.1 ppb so it is observable on the log scale). Sector (ii) has little or no X.

is involved in the observed increase in V_nH^- and WAR2 in temperatures Region 2.

Sample B showed no variation in the concentrations of the paramagnetic defects with heat treatment or UV illumination. This can be explained by the lack of N_S^0, as any traps have already been compensated, meaning that any charge excited from WAR2 is not captured.

Sample H contains a concentration of WAR2 close to the detection limit.The activation energy for the change in the concentration of WAR2 is similar to that discussed for other samples (1.2 eV), but in this case the WAR2 signal does not recover in temperature Region 2. This could mean that the trap causing the reduction in the concentration of the WAR2 defect is different to that causing the secondary increase in concentration and in Sample H this second defect is not present.

7.5 Proposed model for WAR2: (V-(CH)-V)^0

The requirements for a model to describe the WAR2 EPR defect are as follows:

1. The defect has a small proton hyperfine interaction,
2. The electron probability density is localised on carbon atoms with little localisation on the proton. This is determined by the application of Equation 3-19 to the hyperfine parameters in Table 7-2.
3. The defect must have a process by which it can be preferentially aligned with the direction of growth.
4. The defect must have C_2 symmetry but very only a small distortion from C_{2v}.

A model which describes the EPR observations of the WAR2 defect is the $(V-(CH)-V)^0$ structure, this is pictorially described in Figure 7-20. A hydrogen atom is bonded to a carbon atom which bonds with two other carbons (sp_2 configuration). This carbon-hydrogen unit is flanked by two vacancies in a {110} type plane. In this structure there are seven dangling orbitals (see Figure 7-20), one π-orbital on the unique carbon and six on the carbons which surround the vacancies. In the neutral charge state seven electrons must be accommodated in the linear combination of orbitals produced from the dangling orbitals.

The defect is thus left in a neutral charge state with one unpaired electron and $S = \frac{1}{2}$, in agreement with EPR and charge transfer data.

The unreconstructed (V-(CH)-V)^0 structure would have C_{2v} symmetry, see Figure 7-20. Extended bonds between bonds (b) and (c) as well as (e) and (f) could occur (Figure 7-21(i)). It is possible that the remaining dangling bond from each vacancy might reconstruct to form an extended bond with the π-orbital on the unique carbon, ((a) and (d) in Figure 7-21(ii)). This reconstruction would retain C_{2v} symmetry. Given the observed preferential alignment observed, the defect will only populate two of the possible six sites for C_{2v} symmetry.

In an alternative reconstruction, one could envisage extended bonds being formed between (a) and (b), (f) and (d) as well as an extended bond between (c), the π-orbital on the unique carbon and (e). Such a reconstruction would lower the symmetry from C_{2v} to C_2. The hyperfine and electronic Zeeman interactions would

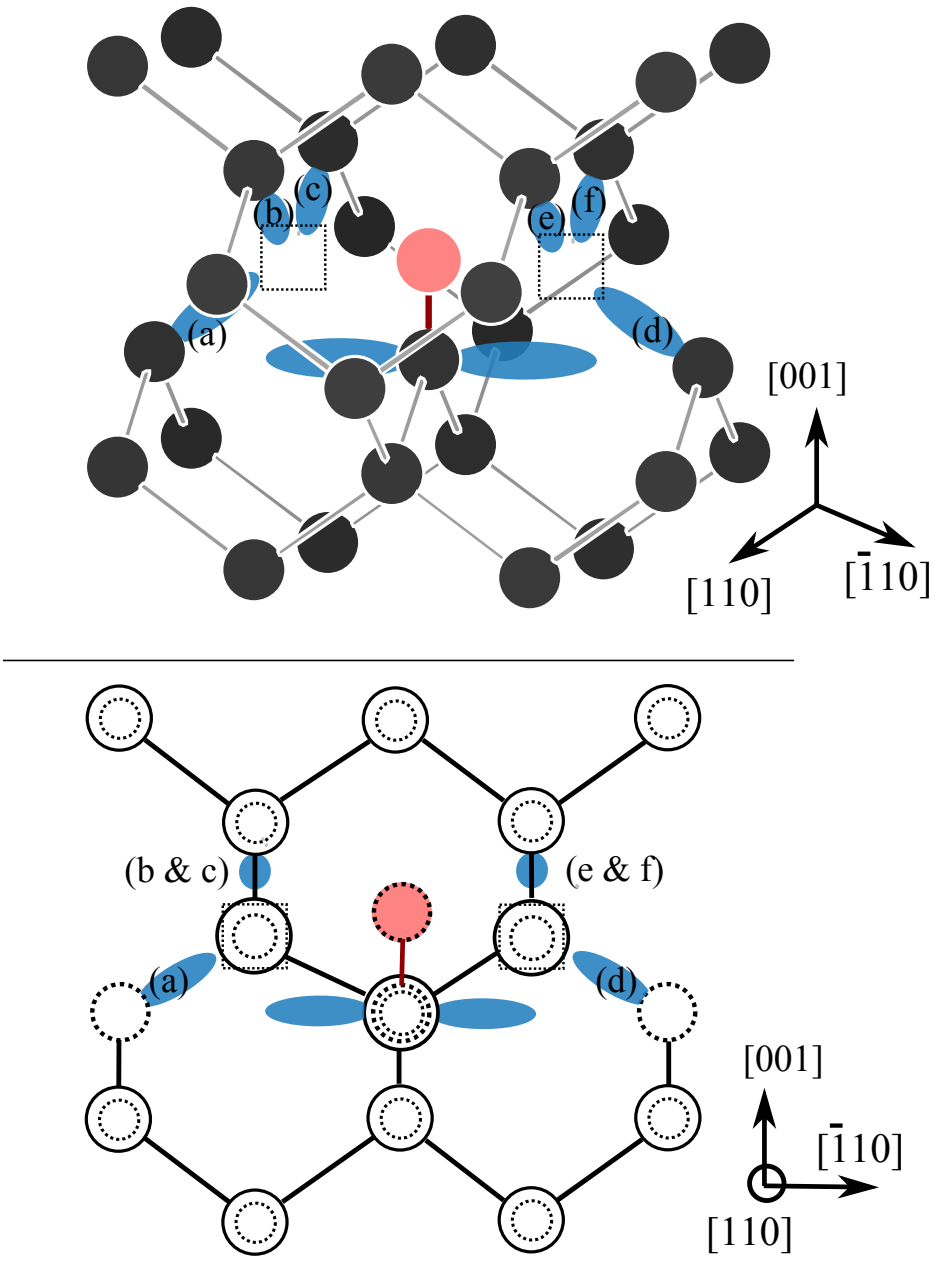

Figure 7-20: A suggested model for the WAR2 defect shown in three and two dimensions. Vacancies are represented by dotted squares, hydrogen by the central shaded sphere (red when in colour) and the carbon lattice by dark spheres. Dangling orbitals are shaded (blue when in colour) with the π-orbital on the unique carbon being constrained within the same (110) plane as the vacancies. The model is not distorted and has C_{2v} symmetry (see text for further details). Dangling orbitals not located on the unique carbon are labelled (a)–(f).

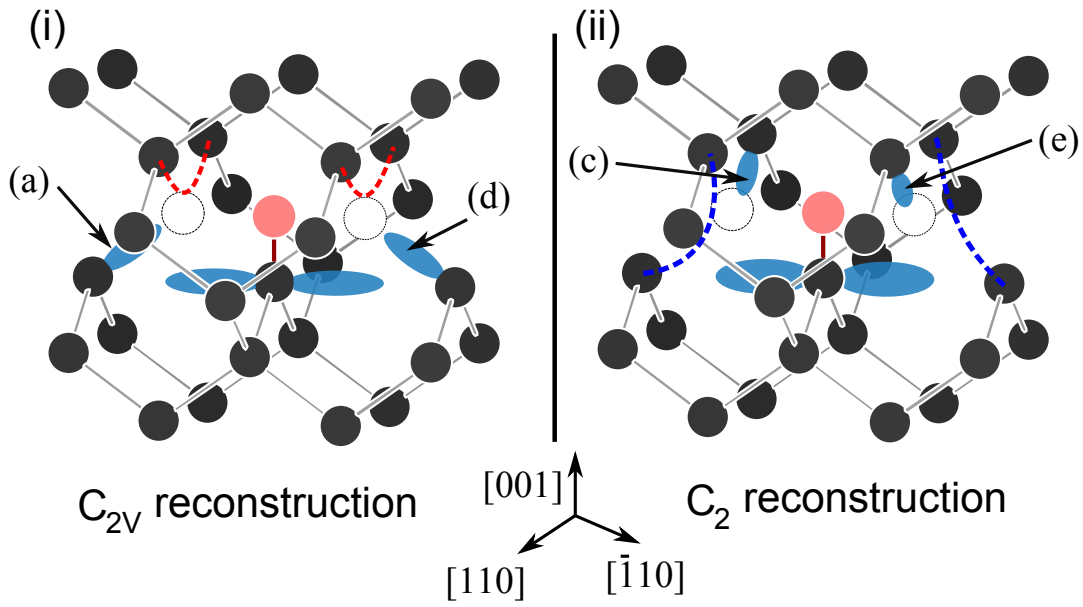

Figure 7-21: A suggested model for the WAR2 defect. Vacancies are represented by dotted squares, hydrogen by the central shaded sphere (red when in colour) and the carbon lattice by dark spheres. Dangling orbitals are shaded (blue when in colour) with the π-orbital on the unique carbon being constrained within the same (110) plane as the vacancies. Figure (i) describes a reconstructed model with C_{2v} symmetry where dangling orbitals (b) and (c) form extended bonds as do orbitals (e) and (f). (ii) describes an alternative reconstruction model with C_2 symmetry where extended bonds are formed between (a) and (b), (f) and (d) as well as (c), the π-orbital on the unique carbon and (e).

be twisted slightly out of the {110} plane as observed experimentally, see Table 7-2. For C_2 symmetry twelve sites would be expected but with the preferential alignment only four would be observed. One of the four is shown in Figure 7-21(ii). The second involves the same location but the opposite reconstruction ((b) and (f) now forming the extended π-orbital). The remaining two sites can be visualised through a 90° rotation about the principal axis [001] and translation to the next growth layer.

By using EPR it is not possible to determine whether the carbon-hydrogen bond is directed towards or away from the crystal growth surface. However, possible growth mechanisms of the models suggest it is directed towards the growth surface.

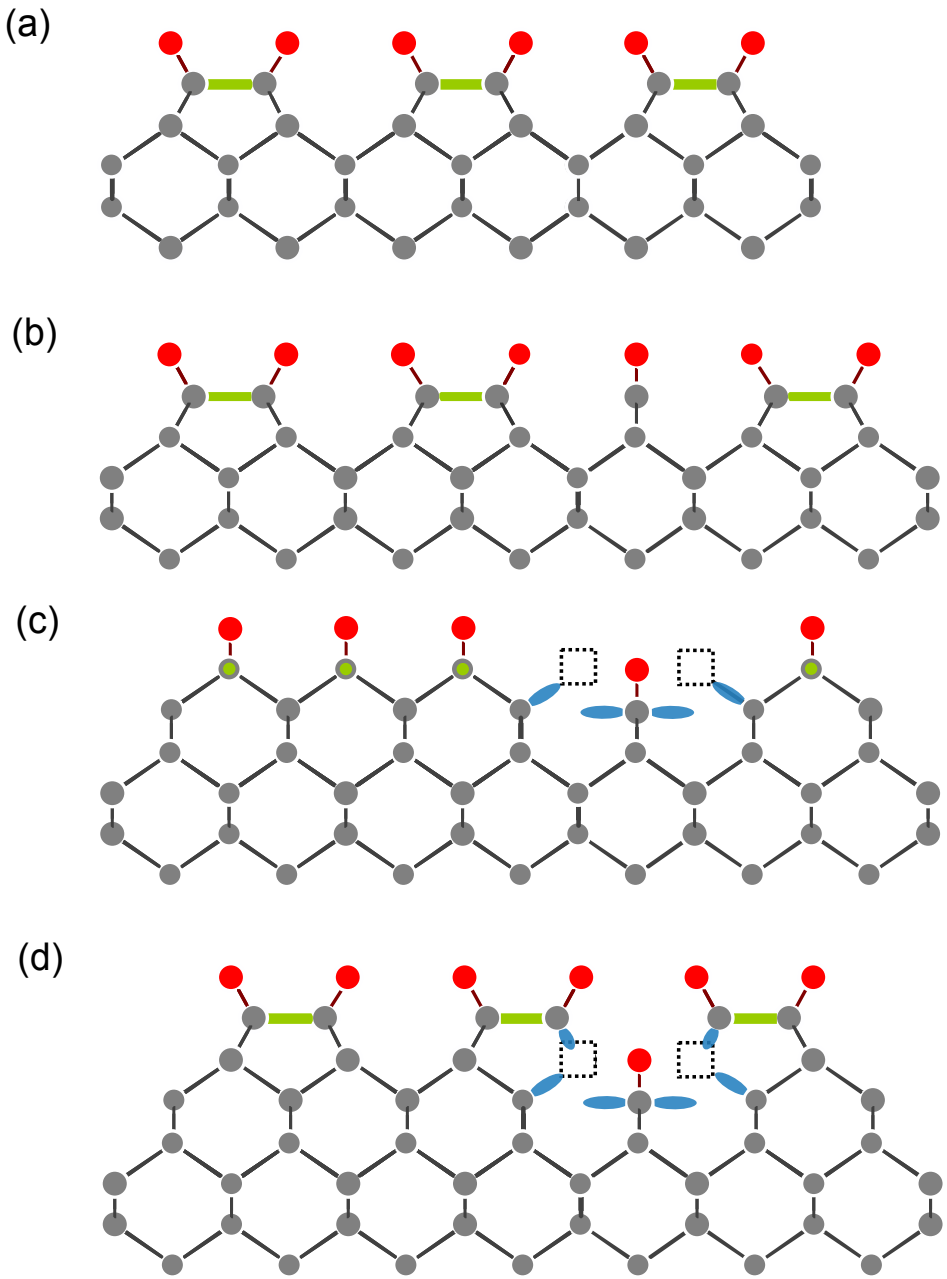

Figure 7-22: A [1$\bar{1}$0] cross section through a [001] growing surface. (a) shows a (001) mono-hydride reconstructed surface. The darkened circles (red when in colour) on the upper surface in each Figure represent hydrogen atoms, the lighter grey circles represent carbon atoms. Dimers are represented as thick (green when in colour) bonds and as in (c) as outlined circles. (b) shows a (001) mono-hydride reconstructed surface containing a surface error which could be the beginnings of the (V – (CH) – V) defect. (c) shows the next layer of growth on top of Figure (b). The final positions of the vacancies in the (V – (CH) – V) defect are shown by the dotted squares and the dangling orbitals as (blue when in colour) lobes. (d) shows the next layer on (c) that might occur if a carbon atom is deposited above the vacancies but do not fill them.

7.5.1 Potential incorporation mechanism

The mono-hydride dimer model has been discussed in Section 7.1.2.1. If carbon atoms dimer-pair as in Figure 7-22(b) as opposed to Figure 7-22(a) then a lone carbon-hydrogen bond, perpendicular to the growth surface, will remain. Such a structure may occur if two mismatched 'zippers' [15] come together from opposing directions. In the next growth layer, Figure 7-22(c) the surface dimer bonds will be rotated by 90° to those formed on the initial growth layer. The positions of the vacancies in the (V-(CH)-V)^0 defect are shown in Figure 7-22(c). Figure 7-22(d) shows the following layer where the defect is being grown over.

Considering the new layer in Figure 7-22(d), the incorporation of a carbon above the (V-(CH)-V) structure is potentially less likely than incorporation on the remaining surface. On an atomic scale the rate of growth is rapid[4]. However, the defect burial may be affected by the probability of deposition at specific sites, and so may affect those structures formed. In this case the probability of population of the sites surrounding the lone carbon-hydrogen bond might be reduced, meaning that diamond would be less likely to grow above the defect and a 'growth pit' might develop. Such a pit would present {111} faces, on which twinned material could grow. This agrees with the observation that micro-twinning is more prominent in samples where WAR2 is present [38].

If the structure in Figure 7-22(b) is stable on the diamond surface, and is subsequently buried it might produce the (V-(CH)-V) defect, Figure 7-20. Alternatively it may be more energetically favourable for the defect to reconstruct to a VH structure (Figure 10.2(b)) with one of the vacancies migrating away from the defect. Or to V_2H structure (Figure 2.5(b)) which requires one of the vacancies and the unique carbon to exchange positions.

The WAR2 defect has been observed in tens of samples but at low concentrations (0.1-10 ppb) are too high to result from a defect on an external surface. However, the low concentration suggests that one or more of the steps involved in its formation is unlikely. The defect's presence might be an indication of the growth conditions, for example faster growth rates or lower temperatures, where growth errors have not been corrected.

[4]Even a modest ~ 1 μm/h is the equivalent of ~3 atomic layers per second.

7.5.2 The stability of (V-(CH)-V)^0

Dr. J. Goss has modelled, by density functional theory (DFT) calculations, the structure shown in Figure 7-20. The (V-(CH)-V)^0 model describes the experimental EPR spectra, but a barrier of only ~1.2 eV has been calculated for the defect to relax into the V_2H structure [41]. Such a recombination energy would leave the structure unstable at moderate growth temperatures. A potential explanation for the discrepancy could be the small lowering in symmetry; this distortion may perhaps act to stabilise the structure. However, this would be a large stabilisation energy to acquire from such a small deviation and this stabilisation is not predicted by the DFT calculations. Multiple hydrogen atoms might also act to stabilise the defect, although a single hydrogen atom fits with the observed EPR data (Figure 7-8).

DFT calculations have also suggested that a low, ~0.3 eV barrier exists to what has been termed a 'flip-flop' mechanism. This involves the hydrogen hopping between the vacancy sites, with the unique carbon recombining with the carbon adjacent to it in the {110} plane bordering the opposing vacancy. If this structure were static it would have C_1 symmetry, not the symmetry observed by EPR. Thus, if the defect is 'flip-flopping' then it must be on a time scale faster than the EPR sampling frequency, resulting in the observation of a pseudo C_{2v}. EPR at low temperatures (~10 K) has shown no freezing in or slowing of any 'flip-flop' mechanism, however, given the calculated activation energy this might be expected.

7.6 Conclusion

An $S = \frac{1}{2}$ defect has been observed by EPR which has been shown to involve a single hydrogen nucleus and has been labelled WAR2. The defect is commonly observed in {001} grown CVD diamond at sub 10 ppb levels. A model of the defect, (V-(CH)-V)^0, and its production route has been suggested. The proposed model is consistent with the defects constituent atoms, the defect's symmetry, preferential alignment, charge state, common occurrence at low concentrations and the elevated level of twinning. Nevertheless, DFT calculations suggest the

proposed structure to be unstable at growth temperatures. The DFT calculations also predict that the carbon-hydrogen bond would 'flip-flop', something that has not been observed between 10 and 300 K.

There is no reason why this modelled defect structure should not be detected optically, but detection would be made more difficult by the low concentrations.

7.7 Further work

1. To date no optical analogue of the WAR2 defect has been observed. Potential similarities exist between defects observed using CL [30]. CL studies should be completed on the samples studied here to asses any correlations.
2. If samples were available with higher concentrations then the ^{13}C hyperfine structure should be investigated. Also, it would be interesting to look for any preferentially aligned components in samples after the WAR2 defect has been annealed out. Theoretical predictions suggest that the model proposed here should relax to the V_2H structure, but the experimental activation energy and that experimentally determined for V_nH^- [42] (where n=2) are similar.
3. To date it has not been possible to see the high resolution splittings at elevated temperatures. Investigation of this splitting at extreme temperatures may further help to model this defect.

References

[1] P. R. W. Hudson and I. S. T. Tsong, J. Mater. Sci. **12**, 2389 (1977).

[2] R. M. Chrenko, R. S. McDonald, and K. A. Darrow, Nature **213**, 474 (1967).

[3] W. A. Runciman and T. Carter, Solid State Commun. **9**, 315 (1971).

[4] F. De Weerdt and I. N. Kupriyanov, Diamond Relat. Mater. **11**, 714 (2002).

[5] I. Kiflawi, D. Fisher, H. Kanda, and G. Sittas, Diamond Relat. Mater. **5**, 1516 (1996).

[6] G. Janssen, W. Vollenberg, L. J. Giling, W. J. P. van Enckevort, J. J. D. Schamine, and M. Seal, Surf. Coat. Tech. **47**, 113 (1991).

[7] G. Janssen, W. J. P. van Enckevort, J. J. D. Schamine, W. Vollenberg, L. J. Giling, and M. Seal, J. Cryst. Growth **104**, 752 (1990).

[8] C. Findeling-Dufour, A. Vignes, and A. Gicquel, Diamond Relat. Mater. **4**, 429 (1995).

[9] C. Wild, R. Kohl, N. Herres, W. Muller-Sebert, and P. Koidl, Diamond Relat. Mater. **3**, 373 (1994).

[10] T. Frauenheim, U. Stephan, P. Blaudeck, D. Porezag, G. Busmann, H, W. Zimmermann-Edling, and S. Lauer, Phys. Rev. B **48**, 18189 (1993).

[11] L. F. Sutcu, C. J. Chu, M. S. Thompson, R. H. Hauge, J. L. Margrave, and M. P. D'Evelyn, J. Appl. Phys. **71**, 5930 (1992).

[12] B. D. Thoms and J. E. Butler, Surf. Sci. **328**, 291 (1995).

[13] J. B. Marsh and H. E. Farnsworth, Surf. Sci. **1**, 3 (1964).

[14] P. M. Martineau, S. C. Lawson, A. J. Taylor, S. J. Quinn, D. J. F. Evans, and M. J. Crowder, Gems. Gemmol. **40**, 2 (2004).

[15] D. G. Goodwin and J. E. Butler, in *Handbook of Industrial Diamonds and Diamond Films*, edited by M. A. Prelas, G. Popovici, and L. K. Bigelow (Marcel Dekker, New York, 1998), pp. 527–581.

[16] G. Celii, F and E. Butler, J, Annu. Rev. Phys. Chem. **42**, 643 (1991).

[17] J. E. Butler, Y. A. Mankelevich, A. Cheesman, J. Ma, and M. N. R. Ashfold, J. Phys. Condens. Matter **21**, 364201 (2009).

[18] S. J. Harris and D. G. Goodwin, J. Phys. Chem. **97**, 23 (1993).

[19] H. Tamura, H. Zhou, Y. Hirano, S. Takami, M. Kubo, R. V. Belosludov, A. Miyamoto, A. Imamura, M. N. Gamo, and T. Ando, Phys. Rev. B **62**, 16995 (2000).

[20] M. Kaukonen, P. K. Sitch, G. Jungnickel, R. M. Nieminen, S. Pykk, D. Porezag, and T. Frauenheim, Phys. Rev. B **57**, 9965 (1998).

[21] J. K. Kang and C. B. Musgrave, J. Chem. Phys. **113**, 7582 (2000).

[22] C. C. Battaile, D. J. Srolovitz, I. I. Oleinik, D. G. Pettifor, A. P. Sutton, S. J. Harris, and J. E. Butler, J. Chem. Phys. **111**, 4291 (1999).

[23] C. M. Welbourn, Solid State Commun. **26**, 255 (1978).

[24] J. H. N. Loubser and A. C. J. Wright, J. Phys. D: Appl. Phys. p. 1129 (1973).

[25] M. E. Newton and J. M. Baker, J. Phys. Condens. Matter **3**, 3605 (1991).

[26] A. T. Collins, Diamond Relat. Mater. **1**, 457 (1992).

[27] C. Dodge, Ph.D. thesis, University of Reading (1986).

[28] A. M. Edmonds, PhD. Thesis, University of Warwick (2008).

[29] U. F. S. D'Haenens-Johansson, A. M. Edmonds, M. E. Newton, P. M. Martineau, R. U. A. Khan, D. J. Twitchen, and S. D. Williams, *Preferential alignment of silicon-related defects in CVD diamond*, The 59$^{\text{th}}$ Diamond Conference, Oxford, oral presentation (2008).

[30] D. Charles, PhD. Thesis, King's College London (2008).
[31] G. Bogdan, M. Nesldek, J. D'Haen, J. Maes, V. V. Moshchalkov, K. Haenen, and M. D'Olieslaeger, Phys. Status Solidi A **202**, 2066 (2005).
[32] J. Achard, A. Tallaire, R. Sussmann, F. Silva, and A. Gicquel, J. Cryst. Growth **284**, 396 (2005).
[33] J. Isberg, J. Hammersberg, E. Johansson, T. Wikstrom, D. J. Twitchen, A. J. Whitehead, S. E. Coe, and G. A. Scarsbrook, Science **297**, 1670 (2002).
[34] A. M. Portis, Phys. Rev. **100**, 1219 (1955).
[35] X. Zhou, G. D. Watkins, K. M. M. Rutledge, R. P. Messmer, and S. Chawla, Phys. Rev. B **54**, 7881 (1996).
[36] D. F. Talbot-Ponsonby, M. E. Newton, J. M. Baker, G. A. Scarsbrook, R. S. Sussmann, A. J. Whitehead, and S. Pfenninger, Phys. Rev. B **57**, 2264 (1998).
[37] A. Cox, D. Phil. Thesis, University of Oxford (1993).
[38] D. Twitchen (2009), private communication.
[39] K. Iakoubovskii and A. Stesmans, Phys. Rev. B **66**, 195207 (2002).
[40] C. Glover, M. E. Newton, P. M. Martineau, S. Quinn, and D. J. Twitchen, Phys. Rev. Lett. **92**, 135502 (2004).
[41] M. J. Shaw, P. R. Briddon, J. P. Goss, M. J. Rayson, A. Kerridge, A. H. Harker, and A. M. Stoneham, Phys. Rev. Lett. **95**, 105502 (2005).
[42] R. J. Cruddace, PhD. Thesis, University of Warwick (2007).
[43] D. R. Lide, *CRC handbook of chemistry and physics* (CRC Press, Boca Raton, FL, USA, 2006), 87th ed.

Chapter 8

Nitrogen Interstitial

8.1 Overview

Nitrogen is the most common impurity in diamond and forms the basis for the materials classification which is outlined in Section 1.4.1 [1].

Vacancies (V) and carbon self-interstitials (I) are generated in diamond when the material is irradiated with particles or photons which have sufficient energy to displace a carbon atom from its position in the lattice. Vacancies and self-interstitials are primary irradiation defects and have been studied in detail. Some secondary irradiation defects such as the NV^- centre have also received detailed scrutiny, see Section 2.3.2.

Neutral and negatively charged vacancies have been studied by optical techniques [2–6] and EPR [7, 8]. An activation energy for the migration of vacancies has been determined by Davies *et al.* [9] to be 2.2 eV. Di-vacancies have been observed in diamonds that have been irradiated and subsequently annealed to 1100 K [10]. There is currently no evidence to suggest that excitation enhances vacancy migration [11].

The $\langle 001 \rangle$ split self interstitial (I_{001}) is the lowest energy configuration interstitial [12] and has been observed by both optical [13] and EPR spectroscopy [11]. It has been shown that irradiation with 1-2 MeV electrons at 100 K produces comparable numbers of vacancies and interstitials [11]. However, this is not the case at higher irradiation temperatures. A study of this behaviour has determined an activation energy of ~0.3 eV [14] for the migration of interstitials under electron bean excitation, this mobile form of the self interstitial has been labelled I^*.

Di-interstitials have been observed after room temperature irradiation [15], despite the activation energy for the migration of I^0_{001} (which has been determined to be 1.6 eV [14, 16]) being too high for migration at room temperature. The

observation of this apparent 'enhanced mobility' accounts for the discrepancy in activation energy and temperature. This could be due to a specific charge state being more mobile, for example I^{-}_{001} (the negative charge state), or as a result of some excitation of the neutral charge state, I^{0}_{001}, resulting in the observed ~0.3 eV activation energy [14].

Vacancies and interstitials can migrate and aggregate to form larger defects or complexes, e.g. di-vacancies, di-interstitials, vacancy chains, etc. Chains of vacancies have been suggested to be responsible for certain EPR-active defects; from three in a chain (the R8 defect), to six or seven (the R11 defect) see [17] for a review. Vacancy clusters can also form and are observed by PAS [18, 19]. Groups of two and three interstitials have been observed by EPR [20] and theoretical calculations have suggested a group of four interstitials would form a stable structure [12]. Further aggregation of interstitials is believed to produce extended defects called platelets [21].

Impurities (in this case nitrogen), vacancies and interstitial are the building blocks of further, more complicated defects. The interaction between vacancies and the nitrogen impurity has been well studied. The stationary substitutional nitrogen (N_S) readily captures mobile vacancies when the sample is annealed at ~900 K [9]. This forms both negative and neutrally charged nitrogen-vacancy defects as shown in Equations 8-1.

$$\begin{aligned} N^{0}_{S} + V^{0} &\rightarrow NV^{0} \\ NV^{0} + N^{0}_{S} &\rightarrow NV^{-} + N^{+}_{S} \end{aligned} \tag{8-1}$$

The nitrogen-vacancy centre anneals out at ~1800 K, a process which contributes to the aggregation of nitrogen to form A-centres [22]. Vacancies are also trapped directly by A-centres to form [N-V-N] centres [9], both in the neutral (H3) and negative (H2) charge states [23].

The subject of this Chapter is the interaction of interstitials with nitrogen centres, which is less well studied and understood than the interaction of nitrogen with vacancies. It has been shown that di-interstitials (the EPR-active R1 centre [15]) are not produced in nitrogen-doped diamond when the concentration of N_S is much larger than the number of interstitials [14]. However, the production of I_{001} is unaffected by the presence of N_S [14]. It is postulated here that once mobile

the I_{001} can be caught by N_S, and the nitrogen will take up position at one end of the interstitial 'dumbbell', as shown in Figure 8-1(c) and (d). This product will be labelled the nitrogen-interstitial, N_I.

In the neutrally charged nitrogen-interstitial model (N_I^0) the two central atoms are sp_2 bonded, each with a non-bonding π-orbital oriented [011] and [1$\bar{1}$0], this is normal to the sp_2 bond. The unique carbon and nitrogen atoms lie on the same [100] axis which passes through the substitutional site. Figure 8-1(a) and (b) show the undistorted lattice in two and three dimensions; (c) and (d) show the lattice including this defect in two and three dimensions.

The N_I^0 and I_{001}^0 defects have similar structures. The I_{001}^0 defect has one electron accommodated in each π-orbital, and a low lying $S = 1$ excited state (observed by EPR). In the N_I^0 defect two electrons are accommodated in the π-orbital which is centred on the nitrogen, leaving a single unpaired electron in the π-orbital centred on the unique carbon atom, see Figure 8-1(c) and (d).

It has been suggested by Goss *et al.* [24] that the N_I defect would be more likely to migrate as a unit than dissociate. Goss *et al.* [24] also suggested that the migration energy for the negatively charged nitrogen-interstitial (N_I^-) would be significantly lower than that of the neutral charge state (N_I^0) [24].

The capture of I_{001} by N_I would produce a R1 like di-interstitial with one of the three-fold coordinated carbon atoms being replaced by a nitrogen ([N_I–I_{001}]). The [N_I–I_{001}]^0 defect would have C_{1h} symmetry with the {110} mirror plane containing two adjacent interstitials. The π-orbital, centred on the nitrogen atom, is normal to the plane of symmetry and contains two electrons. The π-orbital, centred on the unique carbon, is again normal to the plane of symmetry, but contains a single unpaired electron. Therefore, in its neutral charge state, [N_I–I_{001}]^0 would have a spin of $S = \frac{1}{2}$. The defect structure is similar to the R1 defect but with the inclusion of a nitrogen atom [25]. The structural relaxation suggested in Figure 8-2(c) and (d) is similar to that predicted for the R1 defect [25].

An alternative nitrogen aggregation route to [N_I–I_{001}] is the capture of N_I by N_S. This would produce the N_{2I} defect where both 'dumbbell' atoms of the interstitial are replaced by nitrogen atoms[1]. Goss *et al.* [24] proposed that this

[1]This is not the only process that could form this defect. It was initially postulated by Goss

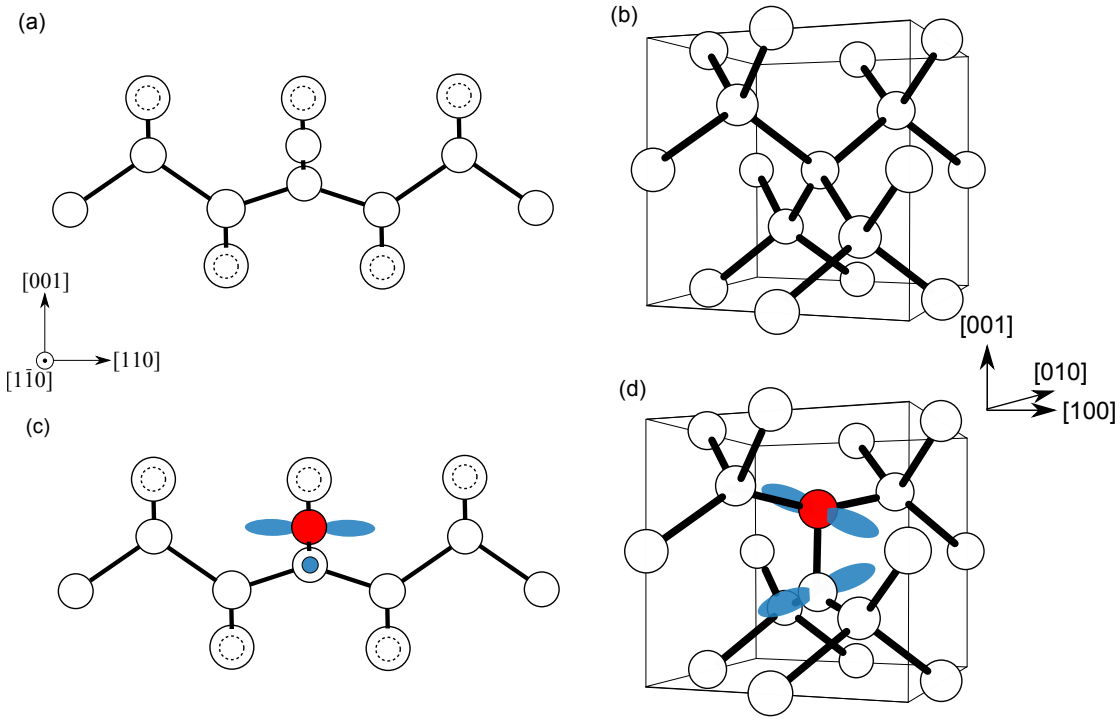

Figure 8-1: (a) and (b) show an undistorted diamond lattice, (a) viewed in the [1$\bar{1}$0] crystallographic direction. The larger circles in (a) and (c) represent those atoms in the foreground, the smaller dotted circles represent those in the plane behind when viewed in this direction. (b) shows the lattice in three dimensions. (c) and (d) show a ⟨001⟩–nitrogen-split interstitial (N_I) the nitrogen atom is darkened (red when in colour). Two π-orbitals are shown in (c), perpendicular and parallel to the plane of the paper (the former is designated by a filled (blue when in colour) circle) in which the unpaired electron is localised. (d) shows the N_I defect in three dimensions in the same format as used by Goss *et al.* [12]

.

defect was responsible for the H1a local vibrational mode [26]. In this neutral charge state, both N_I and [N_I–I_{001}] defects would be paramagnetic and if are not obscured by other defects should be observable by EPR. The structures of both defects are shown in Figures 8-1(c) and (d) and Figures 8-2(c) and (d) and are the subject of this Chapter.

It is important to consider the differences in nitrogen incorporation in different growth sectors within an HPHT synthetic diamond. Typically the {111} sector contains the highest concentration of nitrogen [27]. Burns *et al.* [27] showed that the {111}, {100}, {113} and {110} growth sectors of a HPHT synthetic diamond

et al. [24] that this defect could be formed through the capture of a mobile I_{001} defect by an A-centre.

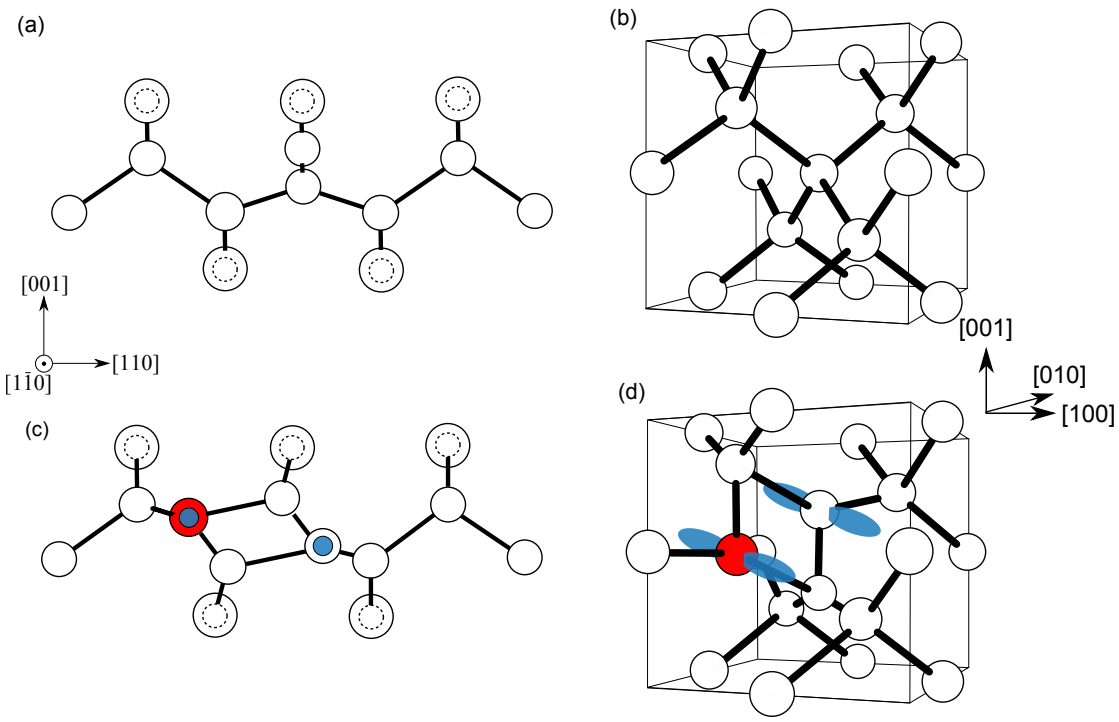

Figure 8-2: (a) and (b) show an undistorted diamond lattice, (a) viewed in the [1$\bar{1}$0] crystallographic direction. The larger circles in (a) and (c) represent those atoms in the foreground, the smaller dotted circles represent those in the plane behind when viewed in this direction. (b) shows the lattice in three dimensions. (c) and (d) show a nitrogen di-interstitial (N_I-I_{001}). (c) has the same projection as used by Twitchen *et al.* [15] to describe the R1 defect. Two π-orbitals are shown, perpendicular to the plane of the paper (designated by a filled (blue when in colour) circle). The unpaired electron is localised in that orbital on the unique carbon atom. The nitrogen atom is shown darkened (red when in colour). The relaxation of the lattice shown is the same relaxation as suggested in [15] for the R1 defect.

contained 100 ppm, 50 ppm, 10 ppm and 1 ppm respectively. Therefore, it is important to note that after irradiation, the ratio of nitrogen concentration to interstitial concentration will vary depending upon the initial nitrogen concentration in the growth sector. Different growth sectors will be observed where[2] $[N_S^0] > [I_{001}]$,[V] and where $[N_S^0] < [I_{001}]$,[V]. It would be expected that in the former sector, negatively charged defects are likely to be formed (since donation from N_S^0 is likely), and in the latter defects that are neutrally charged will be the most common. Relating this to the N_I and [N_I-I_{001}] defects, it is the neutral ones that will be EPR-active and might be expected to be formed in regions with a low nitrogen

[2] $[\alpha]$ = the concentration of defect α.

concentration. Furthermore, the different charge states of N_I are predicted to have different migration energies, thus variations between sectors may be enhanced by annealing.

8.2 Experimental

The detection of paramagnetic defects with S=$\frac{1}{2}$ and small Zeeman and hyperfine splittings, in nitrogen doped diamond is challenging because the central EPR transition from the ubiquitous $^{14}N_S^0$ defect dominates the spectral region close to $g \approx 2.00$, where many common defects are predicted to lie. Removing nitrogen from the diamond synthesis source material would allow the growth of nitrogen free diamond. This would remove the $^{14}N_S^0$ defect but would not facilitate the study of other nitrogen related defects. The solution to this problem is to dope the diamond exclusively with ^{15}N. The $^{15}N_S^0$ defect with $S = \frac{1}{2}$ has no EPR transition in the $g \approx 2.00$ spectral region. Therefore, allowing the study of other potentially nitrogen related defects.

Sample P (see Table 8-1), is a synthetic mixed type IaA/Ib diamond that was grown using a modified high pressure high temperature (HPHT) synthesis method [28, 29]. This produced a type Ib diamond with an average N_S^0 concentration of 150 ppm, but more than 95% of the nitrogen in the sample was ^{15}N. The sample was subsequently HPHT treated at 2300 K and 6.5 GPa to aggregate some of the nitrogen.

Since the concentration of nitrogen varies between different growth sectors, the fraction of the N_S^0 defects which will have aggregated into A-centres upon annealing also vary. Considering the aggregation of nitrogen to A-centres, and using the activation energy and rate constant determined for the aggregation of N_S^0 to A-centres [30, 31], for sectors (e.g. $\langle 110 \rangle$) containing 1 ppm of N_S^0, 1% of the N_S^0 defects will have aggregated to form A-centres. Whereas, in sectors containing ~150 ppm of N_S^0, ~80% of the N_S^0 will have aggregated to form A-centres. After HPHT treatment the average A-centre and N_S^0 concentration (over the whole sample) was ~60 ppm and ~30 ppm respectively.

Following HPHT annealing, Sample P was irradiated at room temperature with

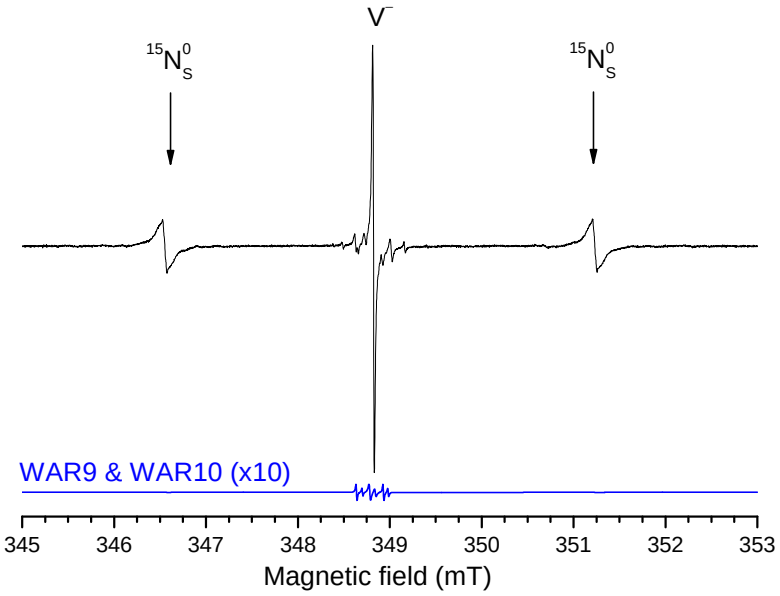

Figure 8-3: Experimental EPR spectrum obtained from Sample P after irradiation (1.5 MeV electrons to a dose of 4×10^{17}electrons/cm^2), the external magnetic field aligned parallel to a ⟨001⟩ crystallographic direction. Note the large signal, with ^{13}C satellites, in the middle of the spectrum which results from the negatively charged vacancies present in the sample post-irradiation (a concentration of ~1 ppm). For comparison, a simulated spectrum of the two new defects (blue line when in colour) is shown below the experimental spectrum, at approximately ten times the signal intensity expected from the concentration detected post-annealing.

1.5 MeV electrons to a dose of 4×10^{17} electrons/cm^2. This dose is predicted to generate vacancies in both neutral and negative charge states with a total concentration of ~3 ppm [11]. The average concentration of negatively charged isolated vacancies (V^-) was determined from EPR (Figure 8-3) to be ~1 ppm, consistent with that predicted by the irradiation dose [11]. The sample was subsequently annealed for 4 hours at 1100 K.

The Bruker EMX-E X-band spectrometer with a 60 dB bridge and the home-built Q-band spectrometer [32] were used in this work.

Photoluminescence (PL) spectra were obtained at 4 K with 514 nm excitation using an Oxford Instruments continuous flow LHe Microstat and Renishaw Raman Invia microscope system. Mid and near infra-red (M/NIR) absorption spectra were recorded at room temperature using a PerkinElmer Spectrum GX,

and PerkinElmer beam condenser.

After irradiation the sample was annealed at temperatures between 1200 and 1500 K using the Lenton Thermal Designs Furnace described in Section 4.2.

8.3 Results

8.3.1 EPR measurements

From the EPR spectra presented in Figure 8-4(a) it was determined that greater than 95% of the N_S^0 observed in Sample P was $^{15}N_S^0$.

In Figure 8-4(b) the $^{15}N_S^0$ EPR spectrum is shown to be composed from components with two different lineshapes. This is consistent with the sample containing multiple growth sectors, with each sector containing different nitrogen concentrations. This is because for N_S^0 concentrations $\gtrsim$10 ppm the EPR line-width indicates the local N_S^0 concentration [33]. The experimental spectrum could be reproduced satisfactorily, assuming that the sample contained predominantly two types of growth sectors with ~11 ppm and ~80 ppm of N_S^0. Minor sectors which contain lower concentrations of N_S^0 would not contribute significantly to the overall N_S^0 EPR spectrum.

Distinct sectors are apparent in the sample's colouration, purple at each edge and yellow in the centre (Figure 8-5). The variation in the concentration of N_S^0 between different sectors can be enhanced by irradiation and annealing. For example, pre-irradiation, a {110} sector might contain as little as 1 ppm N_S^0 and the irradiation process introduces ~3 ppm of vacancies, such that $[V] > [N_S]$. In such a situation, it is expected that N_S^0 would donate charge to V^0, leaving the majority of the N_S defects in a positive charge state and diamagnetic (EPR-silent). EPR spectra in Figures 8-3 and 8-4 were recorded before and after irradiation respectively. A marked decrease in the N_S^0 EPR spectra with a narrow line-width (low concentration linewidth) is obvious between Figures 8-3 and 8-4, which supports the previous prediction.

The defects of interest here are observed around the central $g \approx 2.00$ region. From Figure 8-3, it is obvious that no such defect could be observed with a strong V^- EPR signal present [7]. Hence, Sample P has been annealed for 4 hours at

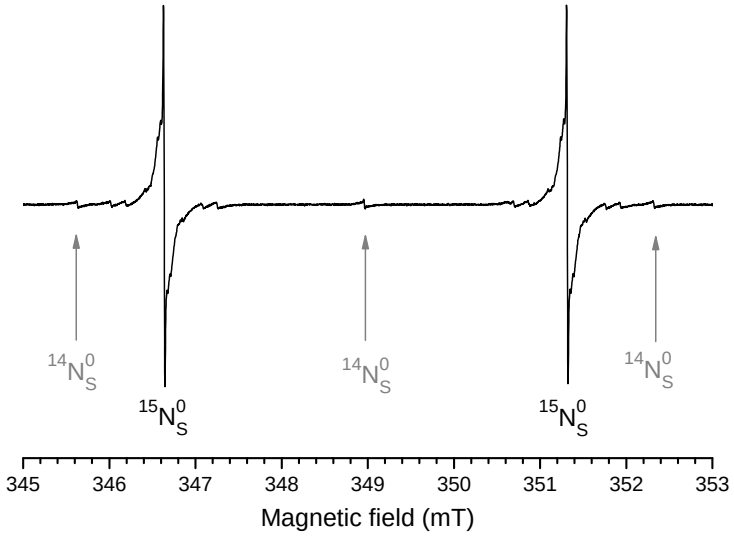

(a)

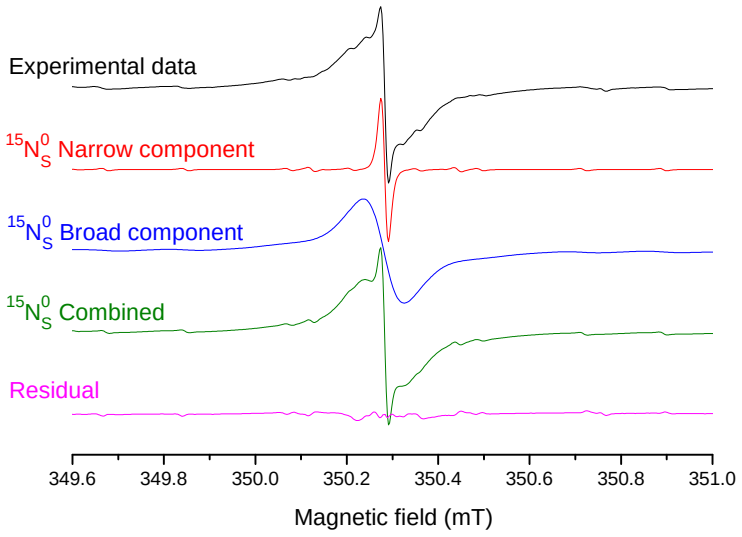

(b)

Figure 8-4: Experimental EPR spectra of Sample P over the $^{15}N_S^0$ and $^{14}N_S^0$ spectral regions after the initial HPHT annealing, but before irradiation. The external magnetic field is aligned parallel to a ⟨001⟩ crystallographic direction. (a) shows the full acquired spectrum, and (b) shows the experimental spectrum over the high field $^{15}N_S^0$ peak. (Note the experimental spectra in (a) and (b) are recorded at slightly different microwave frequencies.) The defect is simulated with both a broad and narrow line-width component. Note that the narrow component of the N_S^0 EPR spectrum is significantly stronger here (before irradiation) when compared to Figure 8-3. This is attributed to almost complete charge transfer from N_S to vacancies in the low nitrogen sectors, see text for details.

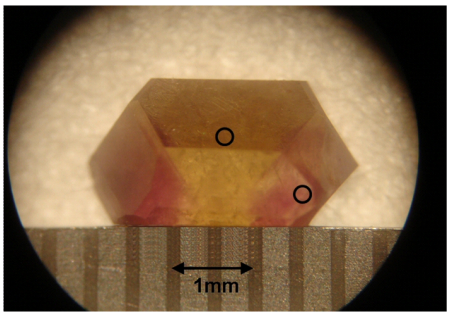

Figure 8-5: Photograph of Sample P, after irradiation and annealing at 1100 K. Three distinct sectors of the sample are discernable by eye, two ends pink/purple and the central yellow sector. The circled areas are those points used for PL measurements.

Table 8-1: Concentrations, given in ppm, of defects observed in Sample P. Concentrations quoted assume that defects are homogenously distributed throughout the sample.

Sample	NV^-	$[^{15}N_S^0]$	$[^{14}N_S^0]$	[WAR9]	[WAR10]
P	0.6(1)	20(2)	0.72(7)	0.10(1)	0.10(1)

1100 K, creating secondary irradiation defects, [9] and removing the V^- EPR spectrum. After annealing, a small central ^{14}N line around $g \approx 2.00$ and some additional defects are observed.

Figure 8-6 shows the EPR spectra recorded in the $g \approx 2.00$ spectral region with the external magnetic field applied parallel to the $\langle 001 \rangle$ crystallographic direction after a 1100 K anneal. The majority of $^{14}N_S^0$ has been replaced by $^{15}N_S^0$ through isotopic enrichment, however, 0.72(2) ppm remains leaving a residual central lineshape in the region of interest. The central line from the $^{14}N_S^0$ spectrum can be accounted for as shown in Figure 8-6 by fitting the $^{14}N_S^0$ spectra to the outer ($m_I = \pm 1$) transitions.

The EPR line positions are more easily discernable following the differentiation of the experimental spectra, see Figure 8.7(a).

EPR measurements around the $g \approx 2.00$ region have revealed two previously unreported defects labelled WAR9 and WAR10. In both cases, the EPR line-width is 0.02 mT showing that these defects are found in regions with a low concentration of the defects (e.g. N_S^0).

X-band roadmaps were produced (Figure 8.7(a)) and peak positions determined (Figure 8.7(b)) by recording spectra with the external magnetic field applied at 5° intervals in a $\{\bar{1}10\}$ crystallographic plane. In both cases the crystal alignment with the external magnetic field has been confirmed by comparison to wider scans which were compared to simulated $^{15}N_S^0$ spectra. The $^{15}N_S^0$ EPR and

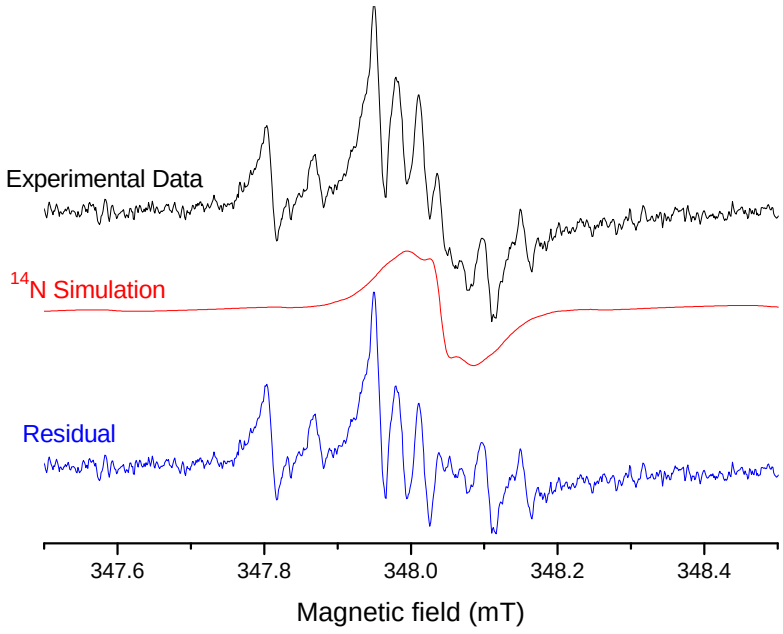

Figure 8-6: Experimental EPR spectrum over the $g \approx 2.00$ region after the sample has been irradiated and annealed at 1100 K. The external magnetic field is aligned parallel to the ⟨001⟩ crystallographic direction. A combined simulation (red when in colour) is shown for the $^{14}N_S^0$ defect with two line widths (see text). The residual spectra resulting from the subtraction of the $^{14}N_S^0$ simulation is shown below it (blue when in colour).

central $^{14}N_S^0$ peaks are used as an internal frequency calibration.

The fits to the peak positions (Figure 8.7(b)) are produced using the best fit parameters given in Table 8-2 and the spin Hamiltonian:

$$\mathscr{H} = \mu_B \mathbf{B^T} \cdot \underline{\mathbf{g}} \hat{\mathbf{S}} + \hat{\mathbf{S}}^{\mathbf{T}} \cdot \underline{\mathbf{A}}_j \hat{\mathbf{I}}_j - \mu_N g_{N_j} \mathbf{B^T} \cdot \hat{\mathbf{I}}_j \tag{8-2}$$

where $S = \frac{1}{2}$ and $I = \frac{1}{2}$ ($^{15}N_S^0$). The WAR9 defect has C_{2v} symmetry and the WAR10 defect has C_{1h} symmetry.

The electronic Zeeman interaction of both defects is the same to within error, but the hyperfine interactions are significantly different. The WAR9 defect has a close to isotropic hyperfine interaction (a variation of 0.4 MHz in ~8 MHz), whereas the hyperfine interaction for WAR10 is small and anisotropic, see Table 8-2.

The spin Hamiltonian parameters for WAR9 and WAR10 accurately reproduce the experimental EPR peak positions and intensities, as shown in Figure 8.7(b) and 8-8. In Figure 8.8(b), WAR9, WAR10 and $^{14}N_S^0$ EPR transitions are simulated

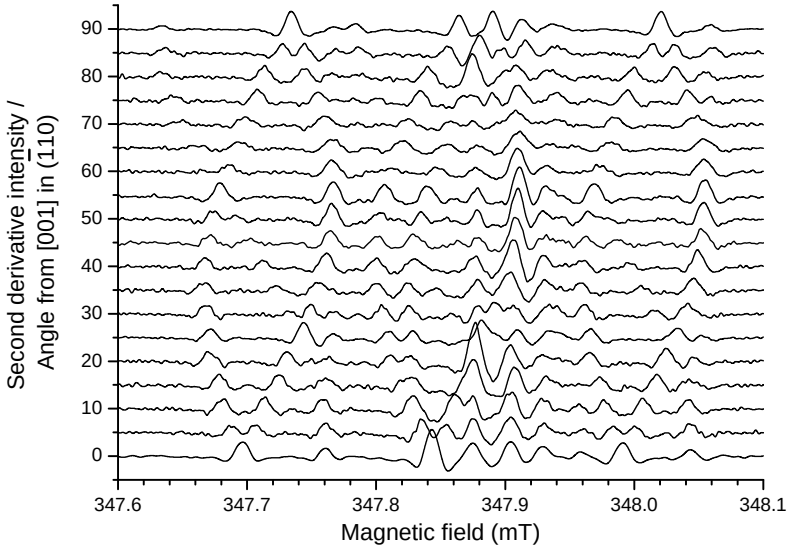

(a)

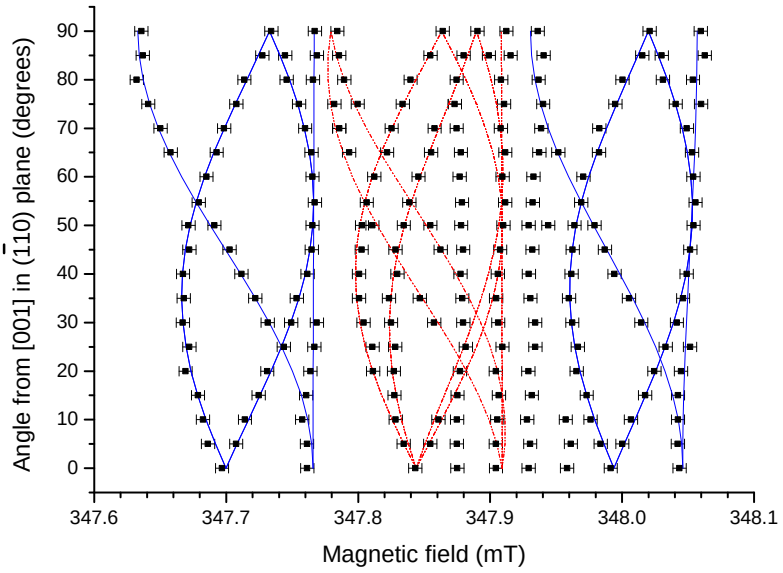

(b)

Figure 8-7: X-band EPR (a) differentiated experimental spectra and (b) line positions for different orientations of the applied magnetic field in the crystallographic $(1\bar{1}0)$ plane, with the microwave frequency corrected to 9.752 GHz. In Figure (b) the points represent experimental peak positions and the lines represent simulated peak positions of the WAR9 defect (solid line, blue when in colour) and WAR10 defect (dot-dashed line, red when in colour). These simulations are made using the fitted parameters given in Table 8-2. The peak, unaccounted for at the consistent field position, ~347.93 mT, is due to $^{14}N_S^0$ from the low concentration region. The other stationary line at ~347.87 mT remains unaccounted for.

Table 8-2: The spin Hamiltonian parameters for the two new ^{15}N containing defects. Electronic Zeeman (**g**) and hyperfine interactions (**A**) and their directions are given. θ is defined as the angle from the crystallographic [001] direction and φ is the angle from [100] measured towards [010] in the (100) plane.

Defect	$\mathbf{g}_1$	$\mathbf{g}_2$	$\mathbf{g}_3$
WAR9	2.00343(10) ∥ [90°, 45°]	2.00272(10) ∥ [180°, 45°]	2.00268(10) ∥ [90°, 315°]
WAR10	2.00344(10) ∥ [90.1(2)°, 45.0(2)°]	2.00272(10) ∥ [179.9(2)°, 45.0(2)°]	2.00269(10) ∥ [90°, 315°]
	$\mathbf{A}_1$ **/ MHz**	$\mathbf{A}_2$ **/ MHz**	$\mathbf{A}_3$ **/ MHz**
WAR9	8.30(5) ∥ [90°, 45°]	7.85(5) ∥ [180°, 45°]	8.17(5) ∥ [90°, 315°]
WAR10	1.00(4) ∥ [44.8(3)°, 45.0(7)°]	-1.01(4) ∥ [134.8(3)°, 45.0(7)°]	0.00(4) ∥ [90°, 315°]

with the magnetic field aligned parallel to [001], [111] and [110] crystallographic directions.

Q-band spectra were obtained in the $(\bar{1}10)$ crystallographic plane of rotation. Spectra are presented with the external magnetic field aligned parallel to [001], [111] and [110] crystallographic directions as well as two additional orientations in between, (Figure 8-9). Experimental, second derivative EPR spectra and peak position roadmaps (corrected to 35 GHz) are shown in Figure 8-9.

No change was observed in either of the WAR9 or the WAR10 spectra as the temperature was decreased to 10 K.

8.3.1.1 Optical

PL spectra from Sample P were obtained at 4 K at two different points on the sample, see Figure 8-5. Sample P contains NV^- and NV^0 centres (637 nm and 575 nm respectively) in both of the differently coloured sectors. MIR and NIR absorption spectra, through the whole sample, taken at 4 K and room temperature, have shown absorption peaks related to the H1a [35, 36], H1b [37], and H2 [38] optical centres.

No change in colouration was observed when Sample P was isochronally annealed for 1 hour in 100 K increments between 1173 K and 1573 K. No change in the concentrations of the WAR9 and WAR10 defects were observed outside of the ~15% error which was realistically assigned. The ratio of concentrations, i.e. [WAR9]:[WAR10] remained constant to within <10%.

Room temperature MIR absorption was performed after each anneal. The

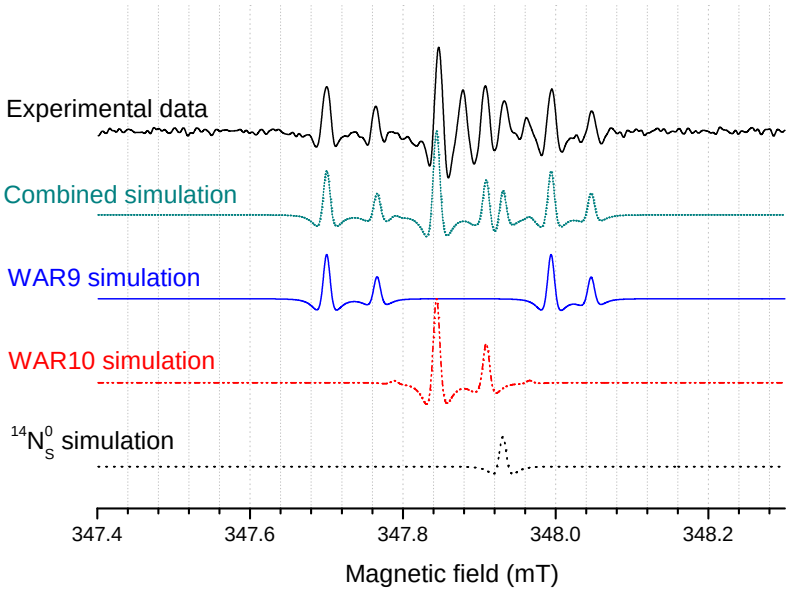

(a)

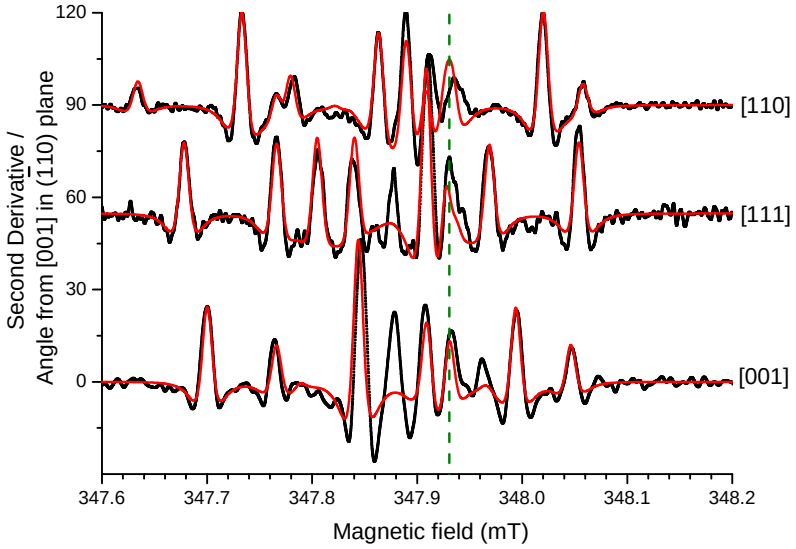

(b)

Figure 8-8: X-band second derivative experimental (thick black line) and simulated spectra at 9.752 GHz. Figure (a) shows the EPR spectra with the magnetic field applied parallel to a ⟨001⟩ crystallographic direction. Simulations for the WAR9, WAR10 and $^{14}N_S^0$ defects are shown independently and combined above (green when in colour). The $^{14}N_S^0$ line is used as a g-marker and the electronic Zeeman parameters from Table 8-2 are referenced to the g-value 2.0024 of N_S^0 [34]. Figure (b) shows the experimental data (black) and sum of all the simulated spectra shown in Figure (a) (red when in colour) with the external magnetic field applied parallel to ⟨001⟩, ⟨111⟩ and ⟨110⟩ crystallographic directions. The dotted vertical line shows the position of the central $^{14}N_S^0$ peak.

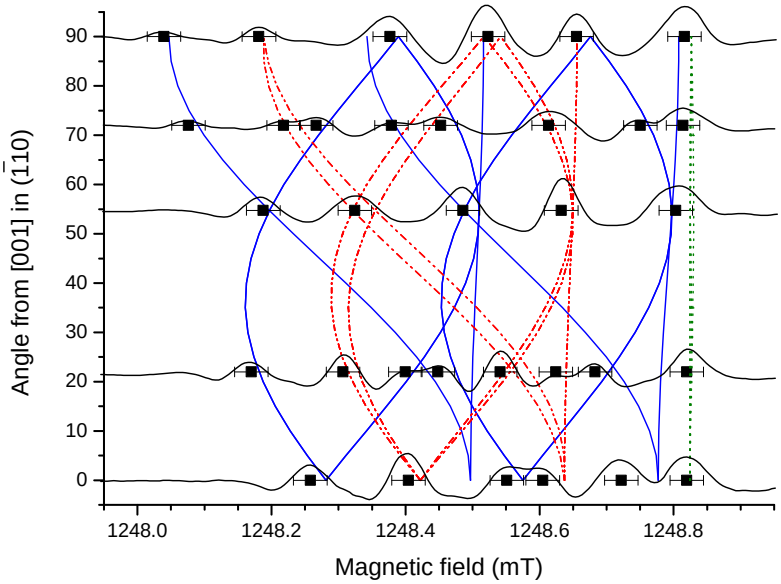

Figure 8-9: Q-band second derivative experimental EPR spectra and line positions for different orientations of the applied magnetic field in the crystallographic (1$\bar{1}$0) plane at a microwave frequency of 35 GHz. Peak positions are marked by points and the lines show simulated peak positions for WAR9 as solid lines (blue when in colour) and WAR10 as dashed lines (red when in colour) using the fitted parameters from Table 8-2. The dotted line (green when in colour) shows the position of the central $^{14}N_S^0$ peak which used as a g-marker. The electronic Zeeman parameters from Table 8-2 are referenced to the g-value (2.0024) of N_S^0 [34].

variation in the H1a and H1b peaks observed was in agreement with previously reported works [39, 40].

8.4 Discussion

In this work, two previously unreported defects, labelled WAR9 and WAR10, with C_{2v} and C_{1h} symmetry respectively were observed in EPR measurements on electron-irradiated and annealed diamond. Both defects have $S = \frac{1}{2}$, and contained one nitrogen atom each. Such defects have not previously been observed as a result of overlap with the central $^{14}N_S^0$ EPR transition; this was overcome here by the use of isotopic enrichment of the source material with ^{15}N.

The doping of the growth material with ^{15}N has produced samples with >95% ^{15}N. As a result the central $g \approx 2.00$ region was left relatively clear for study by

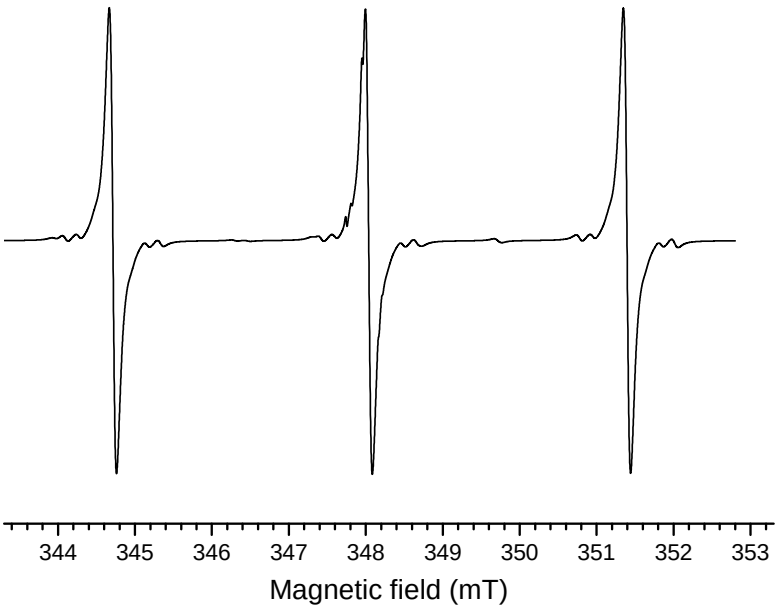

Figure 8-10: A simulated X-band first derivative EPR spectrum with the magnetic field applied parallel to a ⟨001⟩ crystallographic direction showing $^{14}N_S^0$ overlapping with ^{14}N versions of WAR9 and WAR10. WAR9 and WAR10 defects are simulated with the ^{15}N hyperfine interaction (multiplied by the ratio of the nuclear Zeeman values for ^{14}N and ^{15}N [41]). The quadrupole interaction is set to zero. The relative concentrations of WAR9 and WAR10 to $^{14}N_S^0$ in this Figure is consistent with the ratio of WAR9 and WAR10 to the concentration of $^{15}N_S^0$ observed in Sample P. The WAR9 and WAR10 spectra are just discernable in this simulated spectra around 348 mT.

EPR, but with a high nitrogen concentration. If the WAR9 and WAR10 defects were present in diamonds doped with ^{14}N rather than ^{15}N, in similar concentrations to Sample P, the EPR transitions of WAR9 and WAR10 would have been masked by the central $^{14}N_S^0$ transition. Figure 8-10 shows simulated $^{14}N_S^0$, WAR9 and WAR10 spectra with all the same concentrations observed in Sample P but with a ^{14}N impurity atom[3] rather than ^{15}N. From this simulation it is almost impossible to distinguish the WAR9 and WAR10 spectra from the central $^{14}N_S^0$ peak. This is a strong indication of why these defects have not been previously reported.

The WAR9 and WAR10 EPR spectra are detected after electron irradiation

[3]The hyperfine interaction for WAR9 and WAR10 has been scaled with the nuclear Zeeman interaction of ^{15}N to ^{14}N.

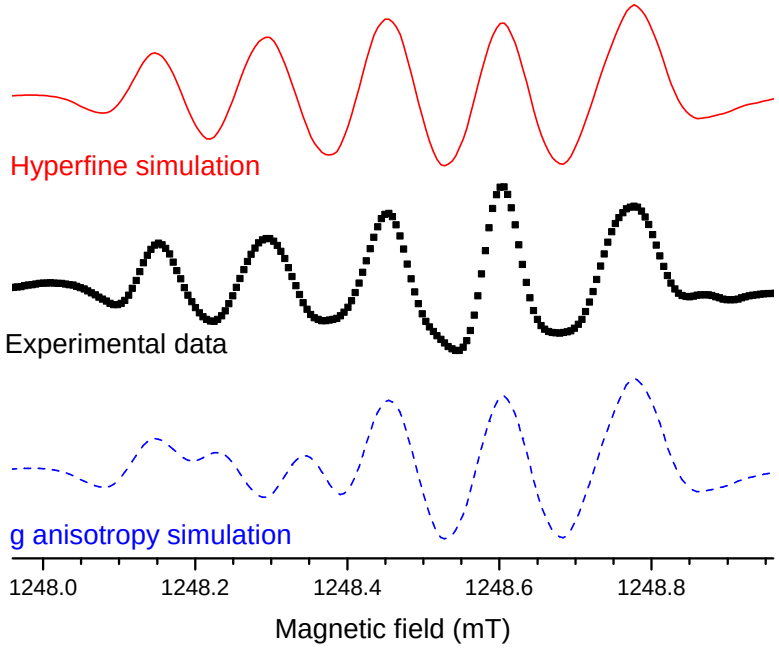

Figure 8-11: Q-band second derivative experimental and simulated EPR spectra at a microwave frequency of 35 GHz for WAR9, WAR10 and $^{14}N_S^0$ with the magnetic field applied parallel to a ⟨111⟩ crystallographic direction. The upper solid line (red when in colour) shows a simulation using the WAR10 parameters from Table 8-2 and the lower dashed line (blue when in colour) shows a simulation using a spin Hamiltonian with lower g-symmetry and no WAR10 hyperfine interaction, which fits the X-band data. The parameters for WAR9 and $^{14}N_S^0$ are the same for both simulations. Only the simulation including a hyperfine interaction for WAR10 yields a satisfactory fit to the experimental data.

and annealing to 1100 K. However, since the EPR signal from negatively charged isolated vacancies [7] appears in the same region of the spectrum as WAR9 and WAR10, these defects would not be detected until the vacancies have been annealed out. Therefore, there are several possible formation requirements for the WAR9 and WAR10 defects. The centres could be formed directly after the irradiation. This could explain why in samples where $[N_S^0] > [I], [V]$ no R1 is formed after electron irradiation [42] and WAR9 and WAR10 are formed instead. Another possibility is that WAR9 and WAR10 are formed after annealing at a temperature up to 1100 K (the annealing temperature used here). For example, the isolated, neutral ⟨100⟩-split self-interstitial (I_{001}) giving rise to the R2 EPR spectrum is stable up to 700 K [11, 43]. The WAR9 and WAR10 defects could be formed as

I_{001} becomes mobile. It is possible that WAR9 and WAR10 are only formed at the 1100 K annealing temperature, but if they were formed below this, the V^- EPR signal would mask the defects.

The EPR line-width is dependent upon the local paramagnetic defect concentration and the 0.02 mT line-width observed for WAR9 and WAR10 suggests that the defects are located in a low concentration region or sector. It is not known if the WAR9 and WAR10 defects are also present in the high concentration region since the line-width of the defects might be ~0.1 mT making the lineshapes too broad to observe at low concentrations. No optical features have been shown to be confined to a single sector.

Variation in the H1a and H1b signal strength with annealing temperature is consistent with that previously reported[4] for such sample types [39, 40]. However no significant variation in this concentration of WAR9 or WAR10 is observed, suggesting they are both stable to at least 1600 K. Further experiments by Liggins [44] have suggested the WAR9 and WAR10 defects are stable to 1800 K.

H1a, H1b and H2 cannot be optical analogues of either the WAR9 or WAR10 defects. H1a has been shown by Liggins [44] to have D_{2d} symmetry which is inconsistent with either the WAR9 or WAR10 defect. The H1b defect showed significant enhancement with annealing unlike WAR9 and WAR10 signals. The H2 defect has been shown to originate from a negatively charged H3 centre [38] and contains two nitrogen atoms which would be distinguishable by EPR [24].

8.4.1 WAR9 model

A ⟨001⟩ split nitrogen-carbon interstitial, N_I, would have C_{2v} symmetry and contain a single nitrogen atom. The N_I defect could be formed by irradiation, but may require further annealing to allow an interstitial to migrate and be captured by N_S. The N_I structure is depicted in Figure 8-1(c) and (d) in two and three dimensions respectively and is described in detail in Section 8.1.

The neutrally charged N_I^0 model is an analogue of the EPR active defect labelled NIRIM-4 [7] which has been observed in electron irradiated, boron doped, synthetic diamond. This defect has been modelled as a ⟨100⟩-split nitrogen-boron

[4] H1a is stable to 1100°C and anneals out at 1400°C.

interstitial in the positive charge state. In this defect centre the majority of the unpaired electron density is localised on the nitrogen atom.

In N_I^0, it would be expected that the EPR active π-orbital on the nitrogen atom will be filled and the π-orbital on the carbon atom half filled, resulting in the majority of the electron probability density being isolated on the unique carbon atom (c.f. to the nitrogen atom in the EPR-active NIRIM-4 defect). Comparing the two models by scaling the magnitude of the hyperfine interactions from ^{11}B to ^{15}N produces ^{15}N hyperfine interactions of $A_1 = 13.5\,\text{MHz}$, $A_2 = 10.4\,\text{MHz}$ and $A_3 = 7.9\,\text{MHz}$. These magnitudes are comparable with the ~8 MHz observed for the WAR9 defect (see Table 8-2). The observations of the WAR9 defect are consistent with the proposed N_I^0 model.

The WAR9 spectrum has a narrow line-width indicating the signal to come from the low N_S regions of the sample. If the concentration of N_S^0 is sufficiently high, the N_I^0 defect may accept an electron from N_S^0 and become diamagnetic (as well as having broader EPR lines). If the model by Goss *et al.* [24], of the H1a IR absorption centre [26] as a di-nitrogen interstitial (N_{2I}) is correct it is likely that the formation mechanism in type Ib diamond is the trapping of an N_I defect by N_S. Since H1a is formed on annealing at 950 K in type Ib material, this suggests that the nitrogen interstitial is mobile at this temperature in the negative charge state. However, the neutral charge state of N_I may have a much higher thermal stability so this formation mechanism does not rule out the assignment of WAR9 to N_I^0.

The nitrogen atom appears to stabilise the interstitial in the same fashion as it would stabilise a vacancy. The R2 defect (I_{001}^0) has been shown to anneal out at 700 K, whereas the WAR9 defect is certainly stable to above 1800 K [44].

8.4.1.1 WAR10 model

For a nearest neighbour ⟨001⟩-split nitrogen interstitial – self interstitial pair (N_I–I_{001}) (see Figure 8-2) in the neutral charge state, we expect, as for N_I^0, a filled π-orbital on the nitrogen atom and a half-filled π-orbital on the carbon atom, yielding a defect with C_{1h} symmetry and an $S = \frac{1}{2}$ ground state.

If we view the $[N_I\text{–}I_{001}]^0$ defect as analogous to the R1 EPR centre it is pos-

sible to estimate the hyperfine interaction by a simple dipole-dipole calculation between the unpaired electron probability density and the nitrogen nucleus. The inter-radical distance of the R1 centre has been calculated to be 0.17 nm [12]. Setting this to be the distance between the nitrogen atom and the carbon atom with the partially filled π-orbital. From the ^{13}C hyperfine interaction in the R1 centre it has been estimated that approximately 70% of the unpaired electron probability density is in the partially filled π-orbitals. Following Hunt *et al.* [11] and assuming that 35% of the unpaired electron probability density is centred at a distance of 0.06 nm on either side of the carbon nucleus along the $[1\bar{1}0]$ direction; this yields two contributions to the hyperfine interaction. Transforming these contributions into a common coordinate axes system and summing them produces the principal values of the hyperfine tensor, $A_1 = 1.6\,\text{MHz}$, $A_2 = -1.0\,\text{MHz}$ and $A_3 = -0.6\,\text{MHz}$ with A_3 parallel to the $[1\bar{1}0]$ crystallographic direction. Assuming that 0.4% of the unpaired electron probability density is localised on the nitrogen atom, this yields an additional uniaxial hyperfine contribution of the form, $A_\parallel = -2b$ and $A_\perp = b$ with $b = -0.3\,\text{MHz}$ and $A_\parallel$ along the $[1\bar{1}0]$ crystallographic direction. Adding this to the hyperfine tensor from the electron dipole calculation results in a calculated hyperfine tensor with $A_1 = -A_2 = 1.3\,\text{MHz}$ and $A_3 = 0\,\text{MHz}$, with A_3 still parallel to the $[1\bar{1}0]$ crystallographic direction. This is of the same form and magnitude as the experimentally determined hyperfine interaction for WAR10. The numerical values in the hyperfine calculation are very sensitive to the angle of the interaction. This angle is determined by the assumed carbon–nitrogen distance and position of the unpaired electron probability density along the p_π-orbital. Hence, the good numerical agreement between the calculated and experimental hyperfine interaction should be viewed as fortuitous. However, this calculation does show that a N_I–I_{001} model in the neutral charge state has a hyperfine interaction which is consistent with that observed for the WAR10 defect.

Similarly to the WAR9 defect, the narrow EPR line-width for WAR10 shows that it is only present in the low N_S concentration sectors. If N_I–I_{001} were present in the high N_S concentration sectors, it would probably not be detectable, since in these regions, it would be in the negative charge state and therefore diamagnetic. Even if $[N_I\text{–}I_{001}]^0$ was present, the EPR linewidths are likely to be broadened,

making observation impossible given the likely concentrations. In addition, since N_I^- is mobile below the temperatures the sample has been annealed at, N_I–I_{001} and may not be present in the high N_S sectors at all.

8.5 Conclusion

Two defects were observed by EPR in a type Ib synthetic HPHT diamond sample after the sample had been electron-irradiated and annealed. These defects have been labelled WAR9 and WAR10. The structures of WAR9 and WAR10, as well as the method of generation is consistent with them being the ⟨100⟩ carbon-nitrogen split interstitial (N_I) and the nearest neighbour ⟨001⟩-split nitrogen interstitial – self interstitial pair (N_I–I_{001}) respectively, both in the neutral charge state.

The narrow line widths of WAR9 and WAR10 indicate that the defects are only present in the low nitrogen concentration regions of the sample, suggesting that both N_I and N_I–I_{001} are electron acceptors and exist in the negative charge state in the presence of N_S. This also means that even though the average bulk concentration of WAR9 and WAR10 is only ~ 0.1 ppm, they are important irradiation products in low nitrogen concentration sectors of diamond.

WAR9 and WAR10 were shown to be stable to 1800 K [44]. The difference in mobility of N_I^0 and N_I^- has been suggested by theory [24], but nevertheless at first sight the survival of N_I^0 and $[N_I\text{–}I_{001}]^0$ is surprising. It is possible that in the low nitrogen sectors N_I^0 is mobile, but unable to find a trap at 1800 K.

Further work is required on both the annealing of N_I^0 and $[N_I\text{–}I_{001}]^0$, and determining the fraction of nitrogen involved in the interstitial complexes. The work presented here suggests that interstitial complexes are not necessarily minor players and should be considered when using ion-implantation to produce useful colour centres in diamond (e.g. NV^-). An experiment to investigate the annealing behaviours of N_I^0 and $[N_I\text{–}I_{001}]^0$ would be more easily carried out on a homogenously ^{15}N doped sample rather than the sample used here.

No optical analogue of the WAR9 and WAR10 defects have yet been observed. Such an analogue would help determine the formation temperatures of WAR9 and WAR10 by avoiding the difficulty caused by the V^- overlap in the EPR spectrum.

References

[1] I. Kiflawi and S. C. Lawson, in *The Properties, Growth and Application of Diamond*, edited by M. H. Nazare and A. J. Neves (INSPEC, the Institution of Electrical Engineers, London, 2001), vol. 26 of *EMIS Datareview Series*, pp. 130–133.

[2] G. Davies and E. C. Lightowlers, J. Phys. C: Solid State Phys. **3**, 638 (1970).

[3] C. D. Clark and J. Walker, Proc. R. Soc. Lond. A. Mat. **334**, 241 (1973).

[4] G. Davies and C. M. Penchina, Proc. R. Soc. Lond. A. Mat. **338**, 359 (1974).

[5] G. Davies, Nature **269**, 498 (1977).

[6] G. Davies and C. Foy, J. Phys. C: Solid State Phys. **13**, 2203 (1980).

[7] J. Isoya, H. Kanda, Y. Uchida, S. C. Lawson, S. Yamasaki, H. Itoh, and Y. Morita, Phys. Rev. B **45**, 1436 (1992).

[8] J. A. van Wyk, O. D. Tucker, M. E. Newton, J. M. Baker, G. S. Woods, and P. Spear, Phys. Rev. B **52**, 12657 (1995).

[9] G. Davies, S. C. Lawson, A. T. Collins, A. Mainwood, and S. J. Sharp, Phys. Rev. B **46**, 13157 (1992).

[10] D. J. Twitchen, M. E. Newton, J. M. Baker, T. R. Anthony, and W. F. Banholzer, Phys. Rev. B **59**, 12900 (1999).

[11] D. C. Hunt, D. J. Twitchen, M. E. Newton, J. M. Baker, T. R. Anthony, W. F. Banholzer, and S. S. Vagarali, Phys. Rev. B **61**, 3863 (2000).

[12] J. P. Goss, B. J. Coomer, R. Jones, T. D. Shaw, P. R. Briddon, M. Rayson, and S. Öberg, Phys. Rev. B **63**, 195208 (2001).

[13] G. Davies, H. Smith, and H. Kanda, Phys. Rev. B **62**, 1528 (2000).

[14] M. E. Newton, B. A. Campbell, D. J. Twitchen, J. M. Baker, and T. R. Anthony, Diamond Relat. Mater. **11**, 618 (2002).

[15] D. J. Twitchen, M. E. Newton, J. M. Baker, O. D. Tucker, T. R. Anthony, and W. F. Banholzer, Phys. Rev. B **54**, 6988 (1996).

[16] L. Allers, A. T. Collins, and J. Hiscock, Diamond Relat. Mater. **7**, 228 (1998).

[17] C. A. J. Ammerlaan, *Paramagnetic centers in diamond* (Springer, 2001).

[18] A. Pu, T. Bretagnon, D. Kerr, and S. Dannefaer, Diamond Relat. Mater. **9**, 1450 (2000).

[19] V. Avalos and S. Dannefaer, Diamond Relat. Mater. **14**, 155 (2005).

[20] D. C. Hunt, D. J. Twitchen, M. E. Newton, J. M. Baker, J. K. Kirui, J. A. van Wyk, T. R. Anthony, and W. F. Banholzer, Phys. Rev. B **62**, 6587 (2000).

[21] G. S. Woods, Proc. R. Soc. Lond. A. **407**, 219 (1986).

[22] A. T. Collins, J. Phys. C: Solid State Phys. **13**, 2641 (1980).

[23] Y. Mita, Y. Nisida, K. Suito, A. Onodera, and S. Yazu, J. Phys. Condens. Matter **2**, 8567 (1990).

[24] J. P. Goss, P. R. Briddon, S. Papagiannidis, and R. Jones, Phys. Rev. B **70**, 235208 (2004).

[25] D. J. Twitchen, M. E. Newton, J. M. Baker, W. F. Banholzer, and T. Anthony, Diamond Relat. Mater. **8**, 1101 (1999).

[26] G. S. Woods and A. T. Collins, J. Phys. C Solid State p. L949 (1982).

[27] R. C. Burns, V. Cvetkovic, C. N. Dodge, D. J. F. Evans, M. T. Rooney, P. M. Spear, and C. M. Welbourn, J. Cryst. Growth **104**, 257 (1990).

[28] C. V. H. Stroemann, F. Tshisikhawe, J. O. Hansen, and R. C. Burns, International Patent Application: WO2006061672 (15/06/2006).

[29] S. Felton, A. M. Edmonds, M. E. Newton, P. M. Martineau, D. Fisher, and D. J. Twitchen, Phys. Rev. B **77**, 081201 (2008).

[30] T. Evans, in *The Properties of Natural and Synthetic Diamond*, edited by J. Field (Academic Press Limited, London, 1992), pp. 259–290.
[31] T. Evans and Z. Qi, Proc. R. Soc. Lond. A. Mat. **381**, 159 (1982).
[32] D. Twitchen, D. Phil. Thesis, University of Oxford (1997).
[33] J. A. van Wyk, E. C. Reynhardt, G. L. High, and I. Kiflawi, J. Phys. D: Appl. Phys. **30**, 1790 (1997).
[34] W. V. Smith, P. P. Sorokin, I. L. Gelles, and G. J. Lasher, Phys. Rev. **115**, 1546 (1959).
[35] W. A. Runciman and T. Carter, Solid State Commun. **9**, 315 (1971).
[36] C. D. Clark, R. W. Ditchburn, and H. B. Dyer, Proc. R. Soc. Lond. A. **234**, 363 (1956).
[37] A. T. Collins and M. Stanley, J. Phys. D: Appl. Phys. p. 2537 (1985).
[38] S. C. Lawson, G. Davies, A. T. Collins, and A. Mainwood, J. Phys. Condens. Matter p. 3439 (1992).
[39] I. Kiflawi, D. Fisher, H. Kanda, and G. Sittas, Diamond Relat. Mater. **5**, 1516 (1996).
[40] G. S. Woods, Phil. Mag. B **50**, 673 (1984).
[41] D. R. Lide, *CRC handbook of chemistry and physics* (CRC Press, Boca Raton, FL, USA, 2006), 87th ed.
[42] G. A. Watt, M. E. Newton, and J. M. Baker, Diamond Relat. Mater. **10**, 1681 (2001).
[43] A. T. Collins and A. Dahwich, Diamond Relat. Mater. **13**, 1959 (2004).
[44] S. Liggins (2009), private communication.

Chapter 9

WAR5

9.1 Overview

9.1.1 Effect of oxygen on CVD growth

The chemical vapour deposition (CVD) growth of diamond is usually carried out using a hydrogen rich plasma which contains a small concentration of a carbon-species. Attempts to enhance growth rates and improve diamond purity has led to the investigation of alternative growth chemistries, using hydrocarbon and hydrogen gas mixtures.

One specific addition to microwave plasma synthesis, which is of interest here, is oxygen. The affect of oxygen in the growth environment of diamond thin films was investigated in the 1990's. This research focussed upon the affect of oxygen on the diamond-stable region of the CVD phase diagram [1–3]. It has been shown that the addition of oxygen can help to facilitate diamond formation [4] and improve growth rates [5]. The addition of oxygen can also hinder the generation of cracks, thereby promoting growth of thicker single-crystal diamond layers [6, 7]. The addition of oxygen has been shown to allow diamond films to be grown under conditions which otherwise would produce largely non-diamond carbon [6]. Oxygen cannot be used in conjunction with a hot filament reactor, because it leads to oxidation and the rapid destruction of the filament [8, 9].

Bachmann *et al.* [2] analysed the results of over 75 CVD experiments which used a variety of gas mixtures and reactors. These were summarised in an atomic carbon-hydrogen-oxygen (C-H-O) phase diagram - a simplified version of which is shown in Figure 9-1. Each side of the equilateral triangle shown in Figure 9-1 represents the fraction of atoms in the gas phase of one of the binary systems, C-H, H-O and O-C, which range from 0–100%. Any gas composition which contains all

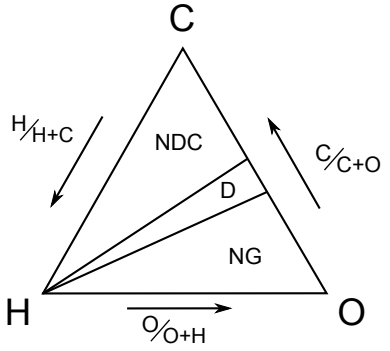

Figure 9-1: Simplified Bachmann diagram adapted from [2]. Each side representing the amount of atomic hydrogen, carbon or oxygen in the CVD growth phase. Regions of inside the diagram are labelled with the type of growth expected, NDC (non-diamond carbon), D (diamond) and NG (no growth).

three elements will be located inside the triangle. For example, carbon monoxide (CO) is located half way along the C-O side and pure acetylene (C_2H_2) half way along the C-H side. The hydrogen corner is the most densely populated region of the diagram since this composition is the most popular growth gas mixture.

Bachmann *et al.* [2] concluded that under typical process conditions, the exact nature of the source gases was largely unimportant and that it was only the relative ratios of the three elements that controlled deposition. Bachmann *et al.* [2] concluded that successful diamond growth was only possible within a well-defined region of the diagram (labelled D in Figure 9-1) where the ratio of carbon to oxygen is approximately equal.

Confirmatory and developmental work relating to the Bachmann diagram has been performed by Marinelli *et al.* [10], Beckmann *et al.* [11], Ford [12], Eaton and Sunkara [13], and Petherbridge *et al.* [14]. Their results support the findings of Bachmann *et al.* [2] and suggested physical processes which give rise to the three different sectors of the triangle.

It has been suggested that the enhancement in growth rates, as a result of the addition of oxygen [5], is the result of the formation of gas phase OH [6] that selectively etches sp_2 (non-diamond carbon) over sp_3 (diamond) material [4]. Therefore, growth rates can be increased whilst keeping crystal quality high [4, 15]. It has also been reported that the addition of oxygen to the growth gas has led to a reduction in the concentration of silicon and hydrogen-related defects [16].

More recent publications have revisited the use of oxygen in the CVD growth environment and have reported the growth of large, near-colourless, gem-quality, single-crystal CVD diamonds [17]. Ho *et al.* [17] used oxygen in various stages of CVD growth with no additional nitrogen added and achieved growth rate in excess of 40 μm/h with 'smooth' {100} surface morphology [17, 18].

To date there have been no reports of the incorporation of significant concentrations of oxygen into the diamond lattice. This is perhaps surprising, since if diamond source gases contain both nitrogen and oxygen, then for a typical nitrogen incorporation of 10 ppm, if the incorporation of oxygen were a factor of 1000 smaller than that of nitrogen, given the sensitivity of experimental techniques (EPR <1 ppb), it would be expected that oxygen is present and observable.

In this work samples synthesised from an experimental chemistry involving oxygen were shown to contain a previously unreported EPR-active defect, which has been labelled WAR5.

9.1.2 Oxygen related defects

Previous studies [19–21] have suggested the presence of oxygen contained within the lattice of natural diamonds, but have not conclusively identified any specific defects that contain oxygen.

In the case of EPR, the identification of oxygen related defects is made difficult because the dominant isotope of oxygen, ^{16}O, has zero nuclear spin ($I = 0$). Therefore there are no additional line splittings and so the presence of oxygen cannot be confirmed. The ^{17}O isotope, with $I = \frac{5}{2}$, makes up only 0.038% of the natural abundance meaning that any ^{17}O EPR line will only be ~0.006% the size of a ^{16}O EPR line[1]. Consequently, for ^{17}O hyperfine structure to be observed, isotopic enrichment with ^{17}O would be required. In some cases the lack of observed hyperfine structure has been used to infer the presence of an oxygen impurity in the defect structure. Two examples of this are the OK1 and N3 EPR centers which have been tentatively associated with nitrogen-oxygen complexes [22–24]. Irradiation-generated defects have also been suggested to be oxygen-vacancy related, e.g. the

[1]Compared to the ^{13}C satellites even a unique carbon would be ~0.05% the size of the main line.

R5–R11 defects all with C_{1h} symmetries [25]. The R9 defect has been suggested to be the vacancy-oxygen centre [25, 26]. However, Goss *et al.* [27] disagree with this assignment and argue that in order to conserve the C_{1h} symmetry of the defect, the oxygen atom could not be located in the, more energetically favourable, nearest neighbour site to the vacancy.

Implantation of CVD diamond films with ^{17}O has been completed by Iakoubovskii *et al.* [28]. Following implantation and a 1150°C anneal, a defect was observed with S=$\frac{1}{2}$ which displayed ^{17}O hyperfine structure. This ^{17}O hyperfine structure unambiguously showed the presence of oxygen in the lattice but thus far no model has been suggested for this defect.

Ruan *et al.* [29] has attributed some CL features in CVD diamond to oxygen-related centers. A CL line at 543.2 nm in CVD diamond has also been reported by Janssen [30], which was only observed in diamond grown with oxygen present in the source gas.

Theoretical calculations have suggested a structure in which substitutional oxygen is paired with substitutional nitrogen [31, 32]. However, this defect has not been conclusively observed by EPR, although the same model had previously been suggested for the OK1 defect [22].

9.1.2.1 OV^0 versus NV^-

The oxygen-vacancy (OV^0) and nitrogen-vacancy (NV^- - labelled W15 in EPR [33]) defects, are effectively a negatively charged vacancy (V^-) with four electrons in three of the dangling carbon orbitals and an O^+ or N^0 impurity at the remaining neighbouring site. This fourth 'site' is essentially diamagnetic and it can be assumed, to first order, that the four electrons in the three dangling orbitals lead to the same sort of state. However, there will be subtle differences in the zero field splitting (D), the electronic Zeeman interaction, the ^{13}C hyperfine structure and the energies of the excited states. These differences result from the slightly different perturbations caused by the differing species at the fourth 'site'.

Both defects have C_{3v} symmetry and $S = 1$. For the NV^- defect the majority of unpaired electron probability density is localised on the three carbon dangling orbitals from the C_a atoms as shown in Figure 9.2(a). The NV^- defect has been

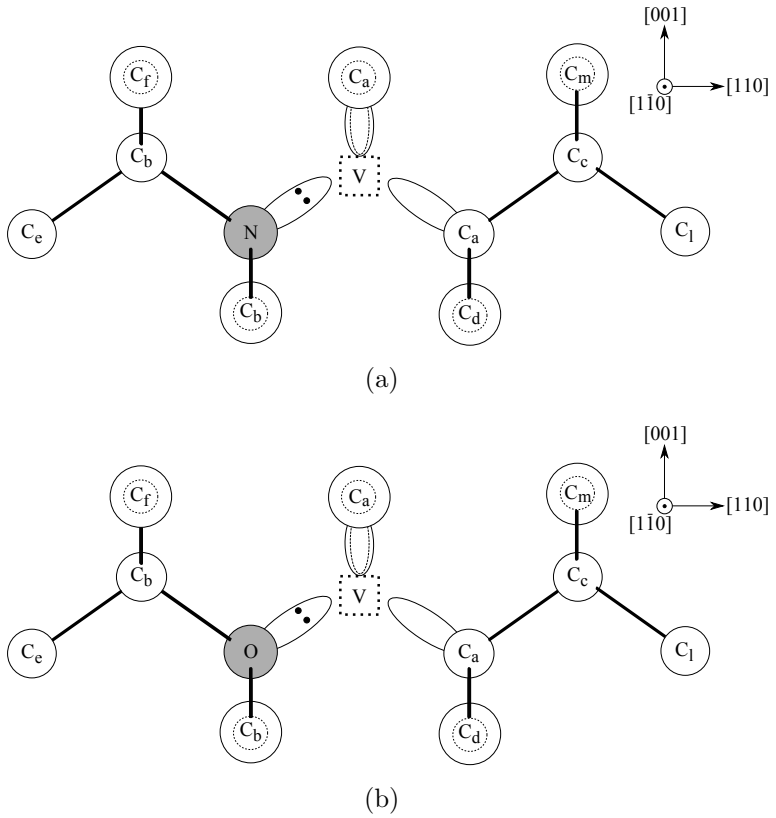

Figure 9-2: Cartoon depiction of the (a) NV^- and (b) OV^0 defects in diamond, projected in the $(1\bar{1}0)$ plane (adapted from [34]). The broken squares represent vacancies and the shaded circle represents the impurity atom. The larger circles represent those carbon atoms in the foreground, the smaller dotted circles represent those in the plane behind when viewed in this direction.

extensively studied and its electronic structure is well understood. This extensive study has originated because of the defect's potential quantum bit which occurs on account of its $S = 1$ ground state, long spin coherence time [35] and the efficient optical detection of the magnetic state. The electronic structure of NV^- has also been extensively modelled using the defect-molecule method [36], which assumes that the defect's properties are determined by the electrons in dangling orbitals.

From group theory, if a defect with four dangling orbitals were to have T_d symmetry, such as the isolated vacancy, the resulting linear combinations of orbitals would transform as a singlet (a) and a triplet (t). Lowering the symmetry from T_d to C_{3v} (the symmetry of NV^-) splits one t-state into a singlet (a) and a doublet (e). In the negative charge state of the NV^- defect there are six electrons to accommodate (three from the vacancy, two from the nitrogen and one making the defect negatively charged). Assuming the energy levels are ordered

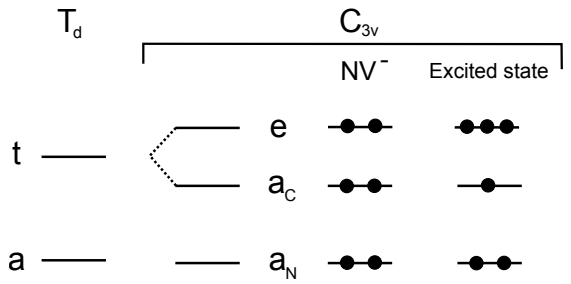

Figure 9-3: Depiction of the energy states of a T_d and C_{3v} defect. The occupation of energy levels in the NV^- defect is shown. The electrons which occupy the e level could be parallel or anti-parallel to one another resulting in an $S = 1$ or $S = 0$ defect respectively. On the right side of the Figure the occupation of the energy level after the promotion of an electron from a_c to e is shown .

$a_{1N} < a_{1C} < e$, where the subscripts N and C indicate the origin of those levels (nitrogen or carbon dangling orbitals respectively) then we would expect the configuration $a_{1N}^2 a_{1C}^2 e^2$. The singlet energy levels (a) accommodate two electrons each, their spins being antiparallel. The doublet (e) can accommodate two electrons parallel or anti-parallel to one another in an $S = 0$ or $S = 1$ state, see Figure 9-3.

This energy configuration gives rise to the many-electron states, $^1A_1$, $^3A_2$ and $^1E_1$. Through optical excitation of the NV^- centre an electron can be promoted from a singlet to a doublet state (Figure 9-3) giving the configuration $a_{1N}^2 a_{1C}^1 e^3$ and the resulting many-electron states, ^1E and ^3E, marked on Figure 9.4(a).

A spin triplet has been established as the NV^- ground state by many different experiments [37–40]. Using uniaxial stress the 1.945 eV (637 nm) NV^- ZPL line, has been associated with an $^3A_2$ to ^3E transition as shown in Figure 9.4(a). The zero field splitting (D) as shown on Figure 9.4(a), has been experimentally determined as positive by low temperature observations [41].

As a result of inter-system crossing between $^3A_2$ and meta-stable singlet state, ^1A, after excitation of the NV^- defect, preferential relaxation results in population of the $M_S = 0$ state [41, 42]. This is observed in the EPR experiment as absorption ($M_S = 0 \rightarrow M_S = +1$) and emission ($M_S = 0 \rightarrow M_S = -1$) lines, an effect known as spin polarisation. From such measurements Harrison *et al.* [43] have determined that at 2 K the preferential population of the $M_S = 0$ state is 80%. This ability to preferentially populate one of the spin states is an important property of any

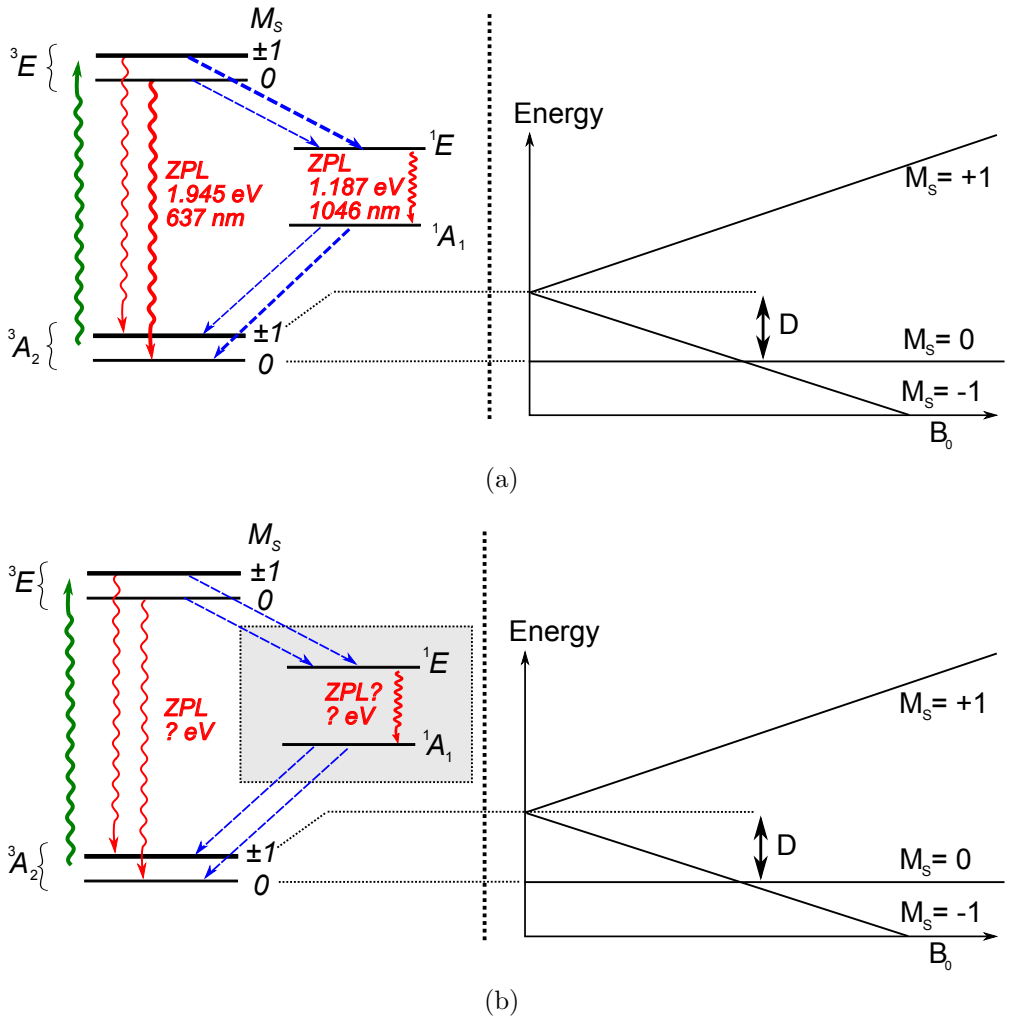

Figure 9-4: Depiction of the energy levels of the (a) NV^- and (b) OV^0 defects. Excitation from the $^3A_2$ ground state to an ^3E level results in the 1.945 eV ZPL in the NV^- defect shown in (a). The ZPL is yet to be confirmed for OV^0 shown in (b). Relaxation is possible via the ^1A level, which in (a) leads to preferential population of the $M_S = 0$ level, resulting in spin polarisation. In (b) relaxation could be possible via the ^1A level or other states designated by the unknown (shaded) region. The splitting of the $^3A_2$ level is determined by the magnitude of the zero field splitting, D. Transitions between the $^3A_2$ sub-levels gives rise to the observed EPR transitions. The energy level diagram for the EPR transitions is shown on the right of both Figures, with a different energy scale against an increasing external magnetic field.

potential quantum bit.

The OV^0 defect, as depicted in Figure 9.2(b), would have six electrons to accommodate (three from the vacancy and three from the oxygen impurity). Goss *et al.* [27] suggested that NV^- and OV^0 defects would be isoelectronic with one another.[2] The same many-electron states at the NV^- defect are also predicted, ^1A, $^3A_2$ and ^1E although there is uncertainly as to which would be the ground state.

An excited state has not been modelled, but the same many-electron states as the NV^- defect would come from the $a_{1C}^2 a_{1O}^1 e^3$ configuration, namely ^1E and ^3E. Also a very similar energy level diagram (Figure 9.4(b)) to that of the NV^- defect (Figure 9.4(a)) would be expected for the OV^0 defect.

As with the NV^- defect, in Figure 9.4(a), it has been assumed that $^3A_2$ is the ground state of the OV^0 defect, Figure 9.4(b). There might be an observable ZPL which will result from the excitation to a ^3E state, although there are no theoretically calculated values for this. Furthermore, the relaxation mechanism suggested in Figure 9.4(b) mirrors that of the NV^- centre, although there may be other states and multiple relaxation pathways within the shaded region of Figure 9.4(b).

The likelihood of the formation of the OV defect was discussed by Goss *et al.* [27] who suggested that the substitutional oxygen is more energetically favourable than the OV defect by 1.3 eV. Substitutional oxygen is expected to be diamagnetic and so EPR-silent in its neutral charge state and in the negative charge state, DFT calculations suggest a C_{2v} structure is strongly preferred [27].

Goss *et al.* [27] used a 64 atom cubic supercell to calculate geometric and electronic properties of the OV defect and compared these with a bulk diamond supercell of the same size. Goss *et al.* calculated the stability of the OV^0 defect to be 4.7 eV. This value was obtained by combining the binding energies of O_S and OV within the supercell and using the binding energy of a vacancy previously determined from quantum Monte Carlo calculations [44].

[2] The oxygen-vacancy will have further empty bands higher in the gap and consequently a $a_1^2 a_1^2 e^2 a_1^0 e^0$ electronic structure. These additional states reside predominantly on the oxygen-carbon bond, hence from the defect-molecule model the same $a_1^2 a_1^2 e^2$ structure is considered.

By using the same method the OV structure has also been calculated to be more energetically favourable than the split oxygen-vacancy (V-O-V) by 2.71 eV [27]. It is worthy of note that these calculations are for a bulk cluster and that the presence of a surface, as during CVD growth, could result in vastly different formation energies. For example there is evidence that this might be the case for phosphorous related defects [45].

It is possible that the NV^- and the OV^0 defects are formed by the migration of a vacancy to a substitutional impurity or the defects could be grown-in as a unit.

Gali *et al.* [46] modelled the hyperfine interactions resulting from the ^{13}C neighbours of the NV^- defect using DFT calculations. Felton *et al.* [47] observed two of these ^{13}C neighbours suggested by Gali *et al.* with the largest hyperfine interactions. Any ^{13}C structure for a defect with C_{3v} symmetry would have the same number of equivalent carbons, hence the same pattern is expected for the OV^0 defect. In addition, given the similar electronic structure the interactions might be expected to be of similar magnitudes.

9.2 Experimental

Three nitrogen-doped single crystal CVD samples were investigated, (samples J, I and δ, in Table 9-1), using EPR, FTIR absorption spectroscopy, and PL. Room temperature EPR spectra were recorded using an EMX X-band spectrometer with a 60 dB bridge and HQ cavity as discussed in Section 4.1.4. All three samples were grown using an experimental chemistry involving oxygen. All three samples contained an unknown defect which has been labelled WAR5 in comparable concentrations. Nevertheless, all of the spectra presented in this Thesis are from Sample J, see Table 9-1.

9.3 Results

9.3.1 EPR - WAR5 defect

EPR spectra have shown a previously unreported set of lines at full and half field, resulting from an $S = 1$ defect with C_{3v} symmetry, this defect has been labelled

Table 9-1: Concentrations in parts per billion (ppb) of the EPR-active defects mentioned in this chapter and observed in samples δ, I and J. (See Chapter 2 for details of these defects.) All concentrations were determined after the sample had been illuminated with a HgXe arc lamp for ~5 minutes, see Section 6.2.

Sample	Mass (mg)	$[N_S^0]$	$[NVH^-]$	$[NV^-]$	$[V_nH^-]$	[WAR5]
δ	38	1460(150)	500(50)	18(2)	25(3)	15(2)
I	40	1680(170)	330(35)	13(2)	12(2)	9(1)
J	43	2570(260)	370(40)	31(3)	25(3)	14(2)

WAR5. EPR transitions from the WAR5 defect are observed at similar fields to the NV^- defect, but have no observable hyperfine splitting. In addition the spectra from the NV^- defect saturates at a much lower microwave power and so is easily distinguished from the WAR5 spectra.

The spectra shown in Figure 9-5(a), and points shown in Figure 9-5(b) to indicate peak positions, were used to determine the spin Hamiltonian parameters g and D given in Table 9-2.

The interactions g and D, were constrained to be axially symmetric around [111]. Relaxing this constraint produced no statistically significant improvement in the fit. The simulated roadmap and transition probabilities are in good agreement with the observed spectra and marked peak positions are shown in Figures 9-5(a) and 9-5(b) respectively.

9.3.2 WAR5 ^{13}C hyperfine satellites

The WAR5 EPR signal is sufficiently strong for four sets of ^{13}C hyperfine satellites to be resolved from the main transition. These are labelled 'a', 'g', 'l' and 'c' for comparison with the NV^- paper by Felton *et al.* [34]. The spin Hamiltonian parameters used for the simulations of the WAR5 ^{13}C spectra in Figures 9-6 and 9-7 are given in Table 9-3. The hyperfine interactions (A) for the ^{13}C satellites labelled a and g are close to being axially symmetric about a $\langle 111 \rangle$ direction, but not the same $\langle 111 \rangle$ as the symmetry axis of g and D interactions, see Table 9-2.

The WAR5(i) simulation in Figure 9-6 is generated from the WAR5 spin Hamiltonian parameters given in Table 9-2 and the ^{13}C hyperfine parameters given in Table 9-3 rows a(i) and g(i). The ^{13}C hyperfine parameters given in these rows

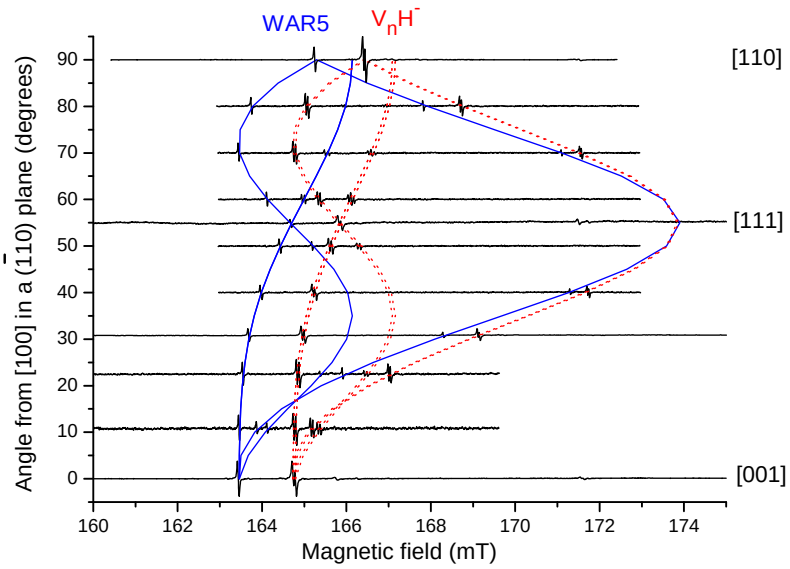

(a)

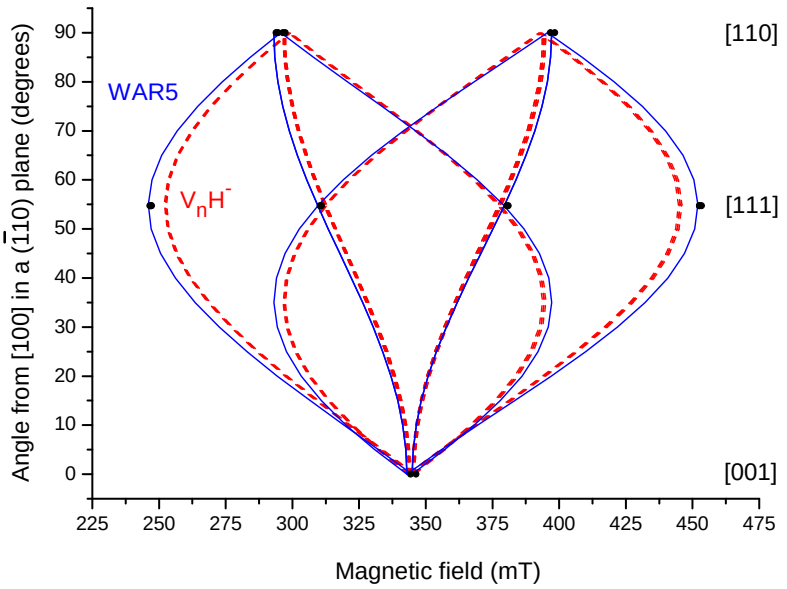

(b)

Figure 9-5: (a) Half and (b) full-field X-band roadmaps generated from Sample J. Experimental EPR spectra are shown in (a) and line positions of the WAR5 defect shown in (b) at different orientations of the applied magnetic field in the crystallographic $(1\bar{1}0)$ plane, with the microwave frequency corrected to 9.752 GHz. The lines in both Figures represent simulated peak positions of the WAR5 defect (solid line, blue when in colour) and V_nH^- defect (dashed line, red when in colour). These simulations are made using the fitted parameters given in Table 9-2.

Table 9-2: Experimentally determined spin Hamiltonian parameters for the WAR5 defect determined here compared to those experimentally determined for V_nH^- and NV^- and theoretically determined values for NV^-. The zero field splitting, D, has been constrained to be axially symmetric and in each case $E = 0$ [51].

Structure	* $g_\parallel$	$g_\perp$	* $D_\parallel = \frac{3}{2}D_z$	$D_x = D_y$
$V_nH^-{}_{exp}$ [48]	2.0034(2)	2.0026(2)	±2706(2)	∓902(2)
$NV^-{}_{exp}$ [29]	2.0029(2)	2.0031(2)	2872(2)	-958(2)
$WAR5_{exp}$	2.0029(2)	2.0025(2)	±2888(2)	∓962(2)
$NV^-{}_{theory}$ [27]	-	-	3218	-1073

*Parallel to ⟨111⟩

are constrained to be along ⟨111⟩. The WAR5(ii) simulation has been generated from the parameters given in Table 9-2 and those given in Table 9-3 rows a(ii) and g(ii) where the interactions are allowed to deviate from ⟨111⟩. The lowering of the symmetry improves the quality of the fit to the experimental data. The deviation of the hyperfine axis from the principal ⟨111⟩ direction with the ^{13}C satellites labelled 'a' and 'g' results in no affect at the other principal directions ⟨110⟩ or ⟨111⟩, the latter being demonstrated in Figure 9-7.

The remaining ^{13}C satellites, 'l' and 'c', were constrained to be axially symmetric about that same ⟨111⟩ direction. In both cases removal of this constraint does not improve the quality of the fit.

Comparing the relative intensities of the ^{13}C satellites to the appropriate central transition it is found that the magnitude of satellite 'a' ($^{13}C_a$), is the equivalent to the intensity arising from 2.3(10) (between two and three)[3] equivalent ^{13}C neighbours. This is determined from [001] and [110] half-field and [111] full-field spectra. Using the same spectra the g, l and c satellites result from 6.7(14) (between five and eight), 2.4(8) (between two and three) and 3.0(15) (between two and four) equivalent neighbours respectively, see Table 9-3.

Further ^{13}C satellites are observed as shoulders to the main line (labelled 'y' in Figure 9-6), but are not observed at sufficient orientations to determine the appropriate spin Hamiltonian parameters. Any satellites with smaller hyperfine interactions are not observed since they will overlap with the central line. One feature that remains unassigned is that labelled 'z' in Figure 9-6.

[3] 2.3(10) notation is used to demote the value and error 2.3 ± 1.0

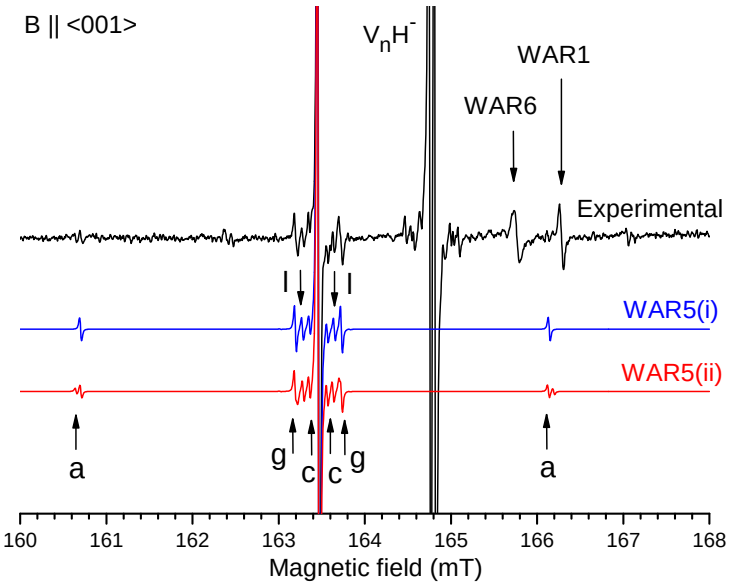

(a)

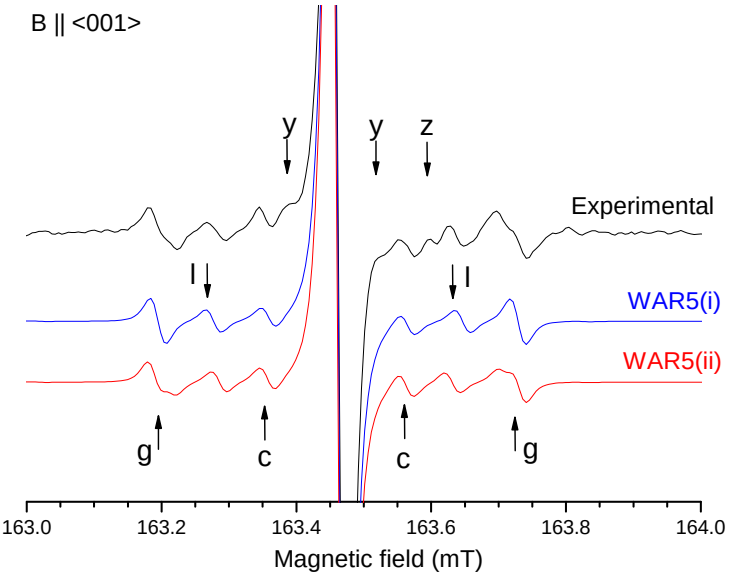

(b)

Figure 9-6: Half-field experimental and simulated spectra of the WAR5 defect with the external magnetic field aligned parallel to a ⟨001⟩ crystallographic direction. (b) shows a zoomed inversion of (a). The WAR5, V_nH^- [48], WAR6 [49] and WAR1 [50] defects are present in the experimental spectrum shown in (a). Spin Hamiltonian parameters used in the WAR5 simulations are given in Tables 9-2 and 9-3. WAR5 ^{13}C satellites are simulated and labelled 'a', 'g', 'l' and 'c', consistent with Table 9-3. In the WAR5(ii) simulation the symmetry has been relaxed to allow a splitting of the ^{13}C satellites labelled 'a' and 'g'. Additional shoulders on the central line have not been simulated, but are labelled 'y'. The label 'z' designates an unidentified feature.

Table 9-3: WAR5 ^{13}C hyperfine parameters. θ is the angle from the crystallographic [001] direction and φ is the angle from [100] measured towards [010] in the (100) plane. The ^{13}C label refers to those used in Figures 9.9(a) and 9.9(b) (c / h suggests either set of atoms might be responsible), and [Z] designates the number of equivalent carbons from this assignment. $\mathbf{N}_{\mathrm{eqC}}$ designates the experimentally determined number of equivalent carbon atoms when compared to the main peak intensity. η^2 is the unpaired electron probability density (on one of the equivalent carbon atoms) calculated from the hyperfine constants in the usual way [52].

^{13}C label	[Z]	$\mathbf{N}_{\mathrm{eqC}}$	$\mathbf{A}_1(A_\parallel)$ **(MHz)**	θ / °	φ / °	$\mathbf{A}_2$ **(MHz)**	θ / °	φ / °	$\mathbf{A}_3$ **(MHz)**	θ / °	φ / °	$\mathrm{Z}\eta^2$
a (i)	3	1.8(6)	196.0(3)	54.74(7)	225.26	115.8(2)	144.74	225	119.1(2)	90	135	~0.84
a (ii)	3	2.3(10)	197.4(2)	53.86(4)	225.26	117.3(2)	143.86(4)	225	118.2(3)	90	135	~0.84
g (i)	6	6.5(15)	17.6(1)	54.7(4)	225.26	12.3(2)	144.74	225	12.3(2)	90	135	~0.13
g (ii)	6	6.7(14)	17.5(1)	60.4(2)	225.26	11.7(1)	150.4(2)	225	13.0(1)	90	135	~0.13
l	3	2.4(8)	12.6(1)	54.7(6)	225.26	8.5(2)	144.74	225	8.5(2)	90	135	~0.05
c / h	3	3.0(15)	7.4(1)	54.7(6)	225.26	4.3(1)	144.74	225	4.3(1)	90	135	~0.03

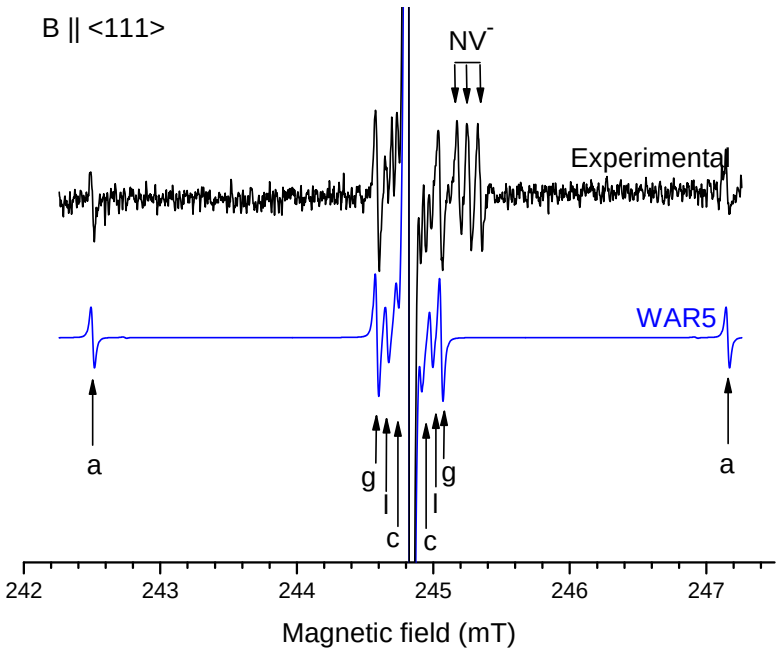

Figure 9-7: Full-field experimental and simulated spectra of the WAR5 defect and WAR5 ^{13}C satellites with the external magnetic field aligned parallel to a ⟨111⟩ crystallographic direction. Spin Hamiltonian parameters used in the WAR5 simulations are given in Tables 9-2 and 9-3. WAR5 ^{13}C satellites are simulated and labelled 'a', 'g', 'l' and 'c', consistent with Table 9-3. The microwave power used is such that the NV^- defect is observed, and labelled.

Table 9-4: Calculated ^{13}C hyperfine parameters for the atoms shown in Figures 9.2(b), and 9-9 for the NV^- defect as determined theoretically by Gali *et al.* [46] and experimentally by Felton *et al.* [34], all given in MHz. The ^{13}C label refers to those used in Figures 9.9(a) and 9.9(b), and [Z] designates the number of equivalent carbon atoms from this assignment.

		Theoretical			Experimental	
^{13}C label	[Z]	$\mathbf{A}_{11}$	$\mathbf{A}_{22}$	$\mathbf{A}_{33}$	$A_\parallel$	$A_\perp$
a	3	109.5	110.2	185.4	199.7(2)	120.3(2)
b	3	-	-	-	-	-
c	3	-7.4	-7.3	-5.8	-	-
d	6	-4.8	-3.7	-1.5	-	-
e	3	-	-	-	-	-
f	6	-	-	-	-	-
g	6	13.5	14.2	19.4	18.49(5)	13.26(5)
h	3	3.4	4.7	4.9	-	-
l	3	12.8	12.8	18	-	-
m	3	1.4	2.4	2.9	-	-
a (OV^0)	3	117 *		201 †	197.4(2)	118.8(4) ‡

* Perpendicular to $\mathbf{A}_{33}$
† One degree off ⟨111⟩
‡ Average of $\mathbf{A}_2$ and $\mathbf{A}_3$ from Table 9-3.

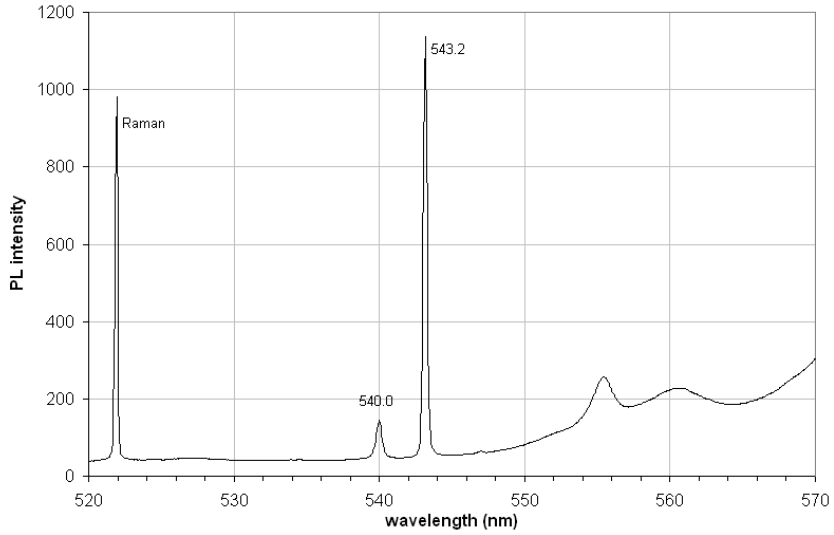

Figure 9-8: Photoluminescence spectrum of Sample J, recorded by Dr. R. U. A Khan using a LabramHR with a 488 nm excitation at 77 K. Only this partial spectrum has been made available of publication which displays a strong 543.2 nm excitation.

9.3.3 Photoluminescence

A PL spectrum of Sample J at 77 K (recorded by Dr. R. U. A Khan at the DTC Research Centre), with 488 nm excitation showed a strong feature at 543.2 nm, see Figure 9-8. Only a partial spectrum has been made available for publication by the DTC Research Centre.

9.4 Discussion

Defects V_nH^-, NV^- and WAR5 are all EPR-active with $S = 1$ and C_{3v} symmetry[4]. The magnitudes of the zero field splitting (D) are comparable for all three defects, (see Table 9-2). The ^{13}C satellite [29, 33] data suggests that unpaired electron probability density for each of the defects is localised on three dangling orbitals pointing into the vacancy. A potential model of the WAR5 defect is a trigonally distorted impurity-vacancy centre (XV) in an EPR-active charge state.

[4] V_nH^- may be time averaged to produce the C_{3v} structure observed in EPR. In an experiment performed on a shorter time scale a lower symmetry may be observed if the defect is dynamic as suggested by the di-vacancy model [53].

No impurity hyperfine splitting is observed for the WAR5 defect. If a hyperfine splitting is present it must be < 0.5 MHz, and so contained within the 0.02 mT line width. Alternatively, the impurity could be a nucleus with $I = 0$, resulting in no hyperfine interaction. The impurity atom (X) must have a low natural abundance of $I \neq 0$ isotopes otherwise, given the signal strength, hyperfine interactions would have been detected. For large atoms it is energetically favourable to adopt the split-vacancy formation [27], which does not display C_{3v} symmetry, e.g. the silicon split vacancy [54]. Therefore, the impurity atom cannot be too large in order to remain on the substitutional site. Potential candidates for the impurity atom in the WAR5 defect are:

1. Helium or neon - as these are noble gases, such impurities are unlikely to bond with the carbon lattice.
2. Silicon - known to form a split-vacancy structure [54]. Also, ^{29}Si is 4.7% abundant with $I = \frac{1}{2}$, therefore, satellites would be observable since ^{13}C satellites on the WAR5 defect are observed where the natural abundance is 1.1%.
3. Magnesium - is a larger atom than silicon and so would be expected to form a split vacancy structure [27]. In addition, magnesium would produce sufficient signals from the 10.0% abundant, $I = \frac{5}{2}$ of ^{25}Mg isotope to be observed.
4. Oxygen - No hyperfine interaction would be observed due to the 0.038% natural abundance of $I = \frac{5}{2}$ of ^{17}O. The oxygen atom would be small enough for the single vacancy, C_{3v} symmetry, structure to be energetically preferred [27].

The neutral vacancy oxygen (OV^0) centre adequately describes the observations of the WAR5 defect.

O_S^0, not OV^0, is predicted to be the most stable oxygen related defect in diamond [27], and so might also be expected to be present and observable. However, the defect is thought to be diamagnetic in its neutral charge state. It may be possible to produce an EPR-active charge state of O_S through charge transfer, but this has not been achieved to date.

The charge transfer results discussed in Chapter 6 show a reversible decrease in the concentration of WAR5 to zero after an 850 K heat treatment (Figure 6.6(b)). In Section 6.4.1 it is suggested that the WAR5 defect is accepting an electron from the valence band and lies ~1.1(2) eV from the top of it. Goss *et al.* [27] calculate that the (0/+) charge state of the OV defect would lie 1.6 eV above the valence band top. Thus experimental and theoretical values are in broad agreement.

The stability of the WAR5 defect is yet to be experimentally determined. Stabilities of the OV^0 centre have been calculated by Goss *et al.* [27], in three charge states, positive (3.6 eV), neutral (4.7 eV) and negative (4.5 eV). These values are similar to the experimentally determined stability of the V_nH^- defect (4.3(2) eV [50]). It is known that the WAR5 defect is stable at growth temperatures, which are typically of the order 1100–1200 K.

9.4.1 Comparison of the OV^0 to the NV^- defect

The NV^- and OV^0 (WAR5) defects have the same structure and symmetry. Nevertheless, there are significant differences in the g-values which might result from the different electronic configuration of nitrogen and oxygen. The magnitude and directions of the zero field splitting are similar (to within 0.5%, see Figure 9.9(b)). The ZPL for NV^0 is observed at 637 nm and a potential candidate for the ZPL of OV^0 has been observed at 543.2 nm, Figure 9-8. This ZPL has previously been observed prior to this work in CVD diamond [55] grown in an oxygen rich environment. The author knows of no theoretically calculated and published values for the ZPL of the OV^0 defect for comparison.

The spin lattice relaxation rates of the OV^0 (WAR5) and NV^- defects differ significantly. NV^- experiences microwave power saturation at much lower powers than OV^0. It is suggested that the high power saturation of the WAR5 defect is the result of faster or more efficient relaxation mechanisms. This explains the unsuccessful attempts to spin polarise the defect even at temperatures as low as 10 K. Since the two defects are similar, the difference in relaxation rates is unlikely to be the result of different phonon energies. Consequently, the difference may result from different energy levels for OV^0 which provide a more efficient route for spin-lattice relaxation.

9.4.2 WAR5 ^{13}C hyperfine satellites

An identical diagram to that used to describe the NV$^-$ ^{13}C neighbours [34] can be used to describe those around the OV^0 defect, shown in Figures 9.9(a) and 9.9(b).

'a' satellites

It was shown in Section 9.3.2 that the best fit to the outermost WAR5 ^{13}C satellites was achieved with a hyperfine interaction which was tilted off a $\langle 111 \rangle$ crystallographic direction (not the C_{3v} axis of the defect) by $\sim 1^\circ$ and which was not quite axially symmetric.

In a trigonal defect, only sets of 1, 3 or 6 equivalent carbon atoms are possible. The satellites labelled 'a' are the result of three carbons atoms. Given the magnitude of the interaction, and the number of equivalent carbon atoms involved, by comparison with the simulations by Gali *et al.* [46], (Table 9-4) the atoms labelled 'a' in Figures 9.9(a) and 9.9(b) are suggested to be responsible for these ^{13}C satellites. Dr. J. Goss has modelled the ^{13}C interactions of the nearest neighbours to the OV^0 defect. The calculations have predicted that the hyperfine interaction of the WAR5 $^{13}C_a$ satellites will be similar to those of the NV$^-$ defect.

The direction of the hyperfine interaction of the OV^0 ^{13}C satellites 'a' and 'g' deviates slightly from $\langle 111 \rangle$. The theoretical calculation for the $^{13}C)_a$ atoms suggest a similar orientation [56]. This deviation could be a result of the relaxation of the atoms labelled 'a' into the (111) plane, perpendicular to the oxygen-vacancy bond. A similar affect is suggested for atoms labelled 'g'. No hyperfine interaction directions are given by Gali *et al.* [46], and no variation of the principal component of the $^{13}C_a$ hyperfine interaction from $\langle 111 \rangle$ was reported experimentally by Felton *et al.* [47]. However, in the work by Felton *et al.*, an alignment where the external magnetic field was aligned parallel to the [001] crystallographic direction was not used to determine the spin Hamiltonian parameters. The closest orientation achieved to [001] was 35° from it in a $(\bar{1}10)$ crystallographic plane. At this orientation no splitting of the WAR5 $^{13}C_a$ satellites would be observed. Thus it is suggested that the $^{13}C_a$ hyperfine interaction for NV$^-$ could show a similar distortion.

Gali *et al.* [46] calculate that the unpaired electron spin density mostly extends on a plane perpendicular to the (111) direction and no measurable spin density

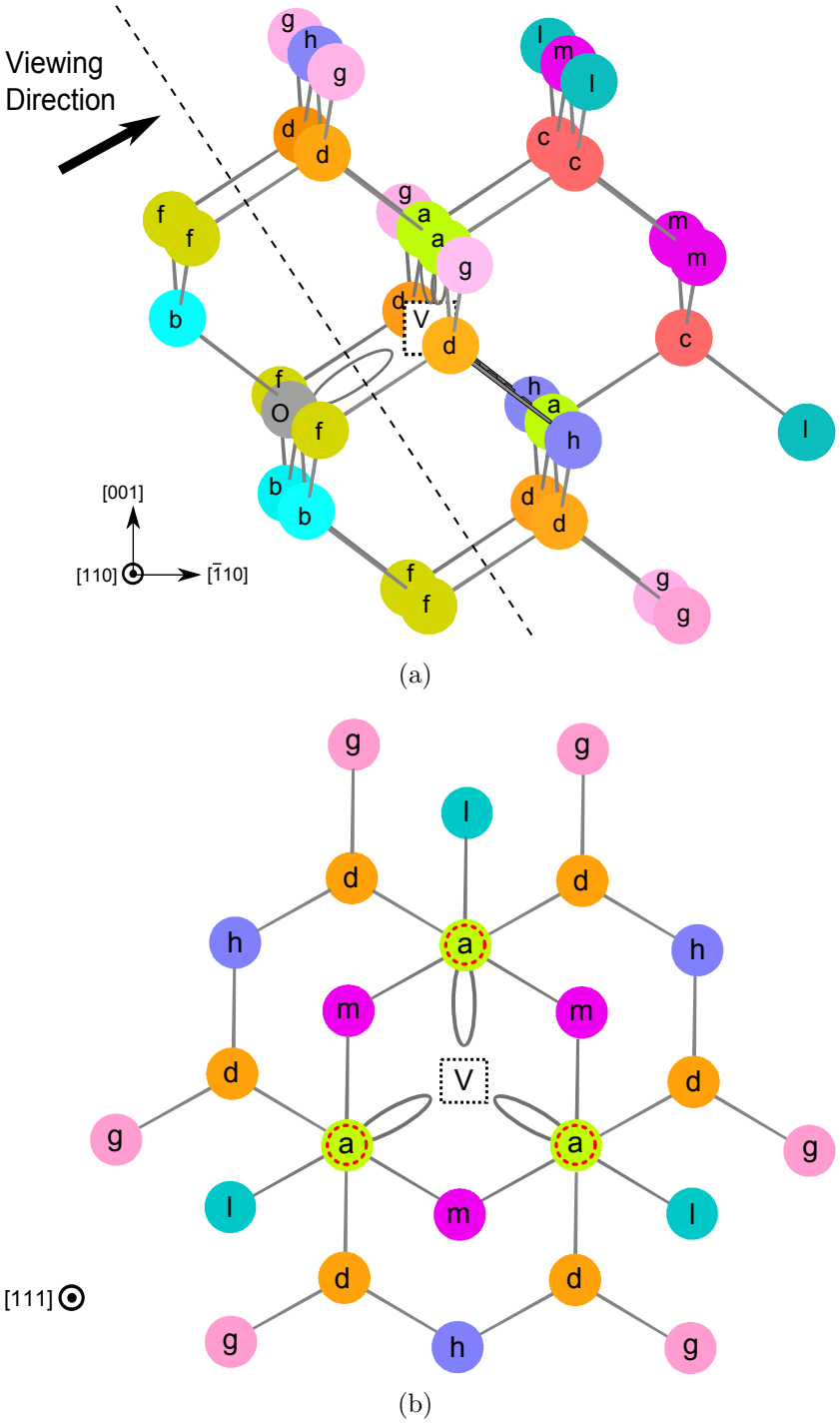

Figure 9-9: Cartoon depiction of the VO^0 defect in diamond and the surrounding carbon lattice. Equivalent carbon atoms are colour coded and labelled consistently with [47] and Tables 9-3 and 9-4. The vacancy is shown by a broken white square. (a) is a projection close to the $(1\bar{1}0)$ plane, the grey sphere represents the oxygen atom (labelled O). (b) is a slice through (a) along the broken line looking in the [111] direction. Carbon atoms labelled a, d, g, h, l and m are shown. Carbon atoms labelled c are depicted by a dotted (red when in colour) circle since they are hidden behind those labelled a in this projection.

can be found 'below' the nitrogen (impurity) atom.[5] This has also been assumed to be the case with OV^0, hence, the closest ^{13}C neighbours to the impurity, 'b' and 'f' in Figure 9-9, will not produce observable ^{13}C satellites.

'g' satellites

Those satellites labelled 'g' in Figure 9-9 have a larger intensity than those labelled 'a', 'l' and 'c'. The satellites labelled 'g' originate from between five and eight equivalent ^{13}C atoms.

Through comparison with the calculations by Gali *et al.* [46], the carbon atoms labelled 'g' in Figure 9-9 are predicted to be responsible for these ^{13}C satellites (six equivalent carbon atoms).

'l' and 'c' satellites

Two additional sets of ^{13}C satellites were observed, labelled 'l' and 'c'. No splittings were observed in the [001] direction and were both suggested to arise from three equivalent carbon atoms. Comparison with calculations by Gali *et al.* [46] suggests that those carbon atoms labelled 'l' on Figure 9-9 are responsible for the satellites with the larger of the two hyperfine interactions. Given that the sign of the hyperfine interaction is not known, the smaller could result from those labelled 'c' or 'h'. Atoms 'c' are suggested by Gali *et al.* to have $A_{\parallel} < A_{\perp}$, which is not observed for those satellites labelled 'c' here. Those labelled 'h' by Gali *et al.* [46] have $A_{\parallel} > A_{\perp}$, but unlike here, the interaction varies significantly from axial. Given the uncertainty in both theoretical calculations and the experimental parameters neither option can be ruled out, but the satellite has been named after one for simplicity.

The hyperfine parameters determined from $^{13}C_a$ and $^{13}C_g$ are very similar to those experimentally observed from the NV^- defect [33, 47]. This might be expected if the defects are isoelectronic and structurally similar.

[5] In this case 'below' means any atom to the oxygen side of a {111} plane if the plane bisects the oxygen-vacancy bond

9.5 Conclusion and further work

A previously unreported $S = 1$ defect, with C_{3v} symmetry, has been observed in CVD diamond that has been grown from an experimental chemistry containing oxygen. The observations are consistent with the OV^0 defect, but given the low natural abundance of ^{17}O no confirming hyperfine interaction has been observed. As a result, the strongest case that can be made is that of 'what else could WAR5 be?' No other models have been suggested that explain the observed experimental data. The more energetically favourable O_S structure [27] has not been observed but may be diamagnetic.

The spin Hamiltonian parameters are similar to those of the NV^- defect. ^{13}C hyperfine parameters also correspond well to the experimental NV^- values available [47] and the theoretically calculated parameters from Gali *et al.* [46].

The WAR5 defect has been observed in only three samples. However, it is possible that the defect is present in other samples at much lower concentrations but has not been observed to date given the unusual experimental conditions used here[6]. The 543.2 nm PL line, which is observed in these samples, may be the ZPL of the WAR5 (OV^0) defect. If the 543.2 nm PL line in an optical analogue of the OV^0 defect it and the WAR5 signal could act as a marker of oxygen-assisted CVD growth.

There has been much interest in the NV^- centre as a potential quantum bit. Given the similarities between WAR5 and NV^- it is perhaps reasonable to investigate potential uses for the WAR5 defect further. In the present work it has not been possible to spin-polarise the WAR5 defect but further investigation in varying sample grades may prove fruitful.

The OV^0 model is consistent with the experimental data for the WAR5 defect, however, to conclusively show the involvement of oxygen, isotopically enriched gas would have to be used to enable observation of ^{17}O hyperfine structure. This might result in confusion between the hyperfine structure of ^{17}O and ^{13}C neighbours, in groups of three and six. To avoid this confusion an enrichment of >20% would be required. In addition, a ^{13}C depleted carbon source could be used during the

[6]Much higher powers were used in this work than would normally be used for fear of saturating the NV^- signal.

diamond synthesis. There are currently no plans to grow such samples enriched with ^{17}O. Alternatively, implantation of ^{17}O, as performed by Iakoubovskii and Stesmans [28] could be attempted followed by annealing in an attempt to form the defect.

With irradiation and annealing of this sample it might be possible to determine how much substitutional oxygen has been incorporated by artificially increasing the concentration of WAR5 through vacancy migration and capture by substitutional oxygen.

References

[1] C. Benndorf, I. Schmidt, and P. Joeris, Phys. Status Solidi A **154**, 5 (1996).

[2] P. K. Bachmann, D. Leers, and H. Lydtin, Diamond Relat. Mater. **1**, 1 (1991).

[3] Z. Liu, D. Wei Zhang, P. Wang, S. Ding, J. Zhang, J. Wang, and K. Kohse-Hoinghaus, Thin Solid Films **368**, 253 (2000).

[4] Y. Liou, A. Inspektor, R. Weimer, D. Knight, and R. Messier, J. Mater. Res. **5**, 2305 (1990).

[5] S. Kapoor, M. A. Kelly, and S. B. Hagstrom, J. Appl. Phys. **77**, 6267 (1995).

[6] S. J. Harris and A. M. Weiner, Appl. Phys. Lett. **55**, 2179 (1989).

[7] A. Tallaire, J. Achard, F. Silva, R. S. Sussmann, A. Gicquel, and E. Rzepka, Phys. Status Solidi A **201**, 2419 (2004).

[8] T. Kawato and K. Kondo, Jpn. J. Appl. Phys. Pt.1 **26**, 1429 (1987).

[9] S. Kapoor, M. A. Kelly, and S. B. Hagstrom, J. Appl. Phys. **77**, 6267 (1995).

[10] M. Marinelli, E. Milani, M. Montuori, A. Paoletti, A. Tebano, G. Balestrino, and P. Paroli, J. Appl. Phys. **76**, 5702 (1994).

[11] R. Beckmann, B. Sobisch, and W. Kulisch, Diamond Relat. Mater. **4**, 256 (1995).

[12] I. J. Ford, J. Phys. D: Appl. Phys. p. 2229 (1996).

[13] S. C. Eaton and M. K. Sunkara, Diamond Relat. Mater. **9**, 1320 (2000).

[14] J. R. Petherbridge, P. W. May, and M. N. R. Ashfold, J. Appl. Phys. **89**, 5219 (2001).

[15] C. J. Tang, A. J. Neves, and A. J. S. Fernandes, Diamond Relat. Mater. **13**, 203 (2004).

[16] I. Sakaguchi, M. Nishitani-Gamo, K. P. Loh, S. Hishita, H. Haneda, and T. Ando, Appl. Phys. Lett. **73**, 2675 (1998).

[17] S. Ho, C. Yan, Z. Liu, H. Mao, and R. Hemley, Ind. Diamond Rev. **66**, 28 (2006).

[18] Q. Liang, C. Yan, Y. Meng, J. Lai, S. Krasnicki, H. Mao, and R. J. Hemley, Diamond Relat. Mater. **18**, 698 (2009).

[19] W. Kaiser and W. L. Bond, Phys. Rev. **115**, 857 (1959).

[20] C. Melton, C. Salotti, and A. Giardini, A, Am. Mineral. **57**, 1518 (1972).

[21] J. P. F. Sellschop, D. M. Bibby, C. S. Erasmus, and D. W. Mingay, Diamond Research p. 43 (1974).

[22] M. E. Newton and J. M. Baker, J. Phys. Condens. Matter **1**, 10549 (1989).

[23] J. A. van Wyk, J. H. N. Loubser, M. E. Newton, and J. M. Baker, J. Phys. Condens. Matter **4**, 2651 (1992).

[24] G. J. Hill, J. A. van Wyk, and M. J. R. Hoch, Radiat. Eff. Defect. Solid. **156**, 221 (2001).

[25] C. A. J. Ammerlaan, *Paramagnetic centers in diamond* (Springer, 2001).

[26] V. S. Vavilov, Defect. Radiat. Eff. Semicon. pp. 74–81 (1978).

[27] J. P. Goss, P. R. Briddon, M. J. Rayson, S. J. Sque, and R. Jones, Phys. Rev. B **72**, 035214 (2005).

[28] K. Iakoubovskii and A. Stesmans, Phys. Rev. B **66**, 045406 (2002).

[29] J. Ruan, W. J. Choyke, and K. Kobashi, Appl. Phys. Lett. **62**, 1379 (1993).

[30] G. Janssen, W. Vollenberg, L. J. Giling, W. J. P. van Enckevort, J. J. D. Schamine, and M. Seal, Surf. Coat. Tech. **47**, 113 (1991).

[31] A. Gali, J. E. Lowther, and P. Deak, J. Phys. Condens. Matter p. 11607 (2001).

[32] J. E. Lowther, Phys. Rev. B **67**, 115206 (2003).

[33] J. H. N. Loubser and J. A. van Wyk, Diamond Research **11**, 11 (1977).

[34] S. Felton, A. M. Edmonds, M. E. Newton, P. M. Martineau, D. Fisher, and D. J.

Twitchen, Phys. Rev. B **77**, 081201 (2008).
[35] T. A. Kennedy, J. S. Colton, J. E. Butler, R. C. Linares, and P. J. Doering, Appl. Phys. Lett. **83**, 4190 (2003).
[36] C. Coulson and M. Kearsley, Proc. R. Soc. Lond. A. Mat. **241**, 433 (1957).
[37] N. R. S. Reddy, N. B. Manson, and E. R. Krausz, J. Lumin. **38**, 46 (1987).
[38] E. van Oort, N. B. Manson, and M. Glasbeek, J. Phys. C Solid State **21**, 4385 (1988).
[39] D. A. Redman, S. Brown, R. H. Sands, and S. C. Rand, Phys. Rev. Lett. **67**, 3420 (1991).
[40] N. B. Manson, X. F. He, and P. T. H. Fisk, J. Lumin. **53**, 49 (1992).
[41] J. Harrison, M. J. Sellars, and N. B. Manson, J. Lumin. **107**, 245 (2004).
[42] L. J. Rogers, S. Armstrong, M. J. Sellars, and N. B. Manson, New J. Phys. p. 103024 (2008).
[43] J. Harrison, M. J. Sellars, and N. B. Manson, Diamond Relat. Mater. **15**, 586 (2006).
[44] R. Q. Hood, P. R. C. Kent, R. J. Needs, and P. R. Briddon, Phys. Rev. Lett. **91**, 076403 (2003).
[45] Y. Yan, S. B. Zhang, and M. M. Al-Jassim, Phys. Rev. B **66**, 201401 (2002).
[46] A. Gali, M. Fyta, and E. Kaxiras, Phys. Rev. B **77**, 155206 (2008).
[47] S. Felton, A. M. Edmonds, M. E. Newton, P. M. Martineau, D. Fisher, D. J. Twitchen, and J. M. Baker, Phys. Rev. B **79**, 075203 (2009).
[48] C. Glover, M. E. Newton, P. M. Martineau, S. Quinn, and D. J. Twitchen, Phys. Rev. Lett. **92**, 135502 (2004).
[49] B. L. Cann, S. Felton, M. E. Newton, J. M. Baker, P. M. Martineau, R. U. A. Khan, and D. J. Twitchen, *WAR6, 7 and 8: Three new point defects in CVD diamond*, The 59$^{\text{th}}$ Diamond Conference, Oxford, poster presentation (2008).
[50] R. J. Cruddace, PhD. Thesis, University of Warwick (2007).
[51] J. A. Weil, J. R. Bolton, and J. E. Wertz, *Electron paramagnetic resonance* (Wiley-Interscience, New York, 1994), 2nd ed.
[52] J. R. Morton and K. F. Preston, J. Magn. Reson. **30**, 577 (1978).
[53] M. J. Shaw, P. R. Briddon, J. P. Goss, M. J. Rayson, A. Kerridge, A. H. Harker, and A. M. Stoneham, Phys. Rev. Lett. **95**, 105502 (2005).
[54] A. M. Edmonds, M. E. Newton, P. M. Martineau, D. J. Twitchen, and S. D. Williams, Phys. Rev. B **77**, 245205 (2008).
[55] G. Janssen, W. J. P. van Enckevort, J. J. D. Schamine, W. Vollenberg, L. J. Giling, and M. Seal, J. Cryst. Growth **104**, 752 (1990).
[56] J. Goss (2009), private communication.

Chapter 10

V_nH^- ^{13}C satellites

10.1 Overview

The observation of the vacancy-hydrogen complex in as grown CVD diamond was first reported by Glover *et al.* [1]. This defect has C_{3v} symmetry, $S = 1$ and a small hyperfine interaction with a single hydrogen atom. Glover *et al.* [1] identified this defect as the VH^- defect, but Shaw *et al.* [2] later proposed a V_2H^- model with the hydrogen tunnelling between three equivalent sites on the end of the di-vacancy, see Section 2.4.1 and Figure 2-5.

Modelling has been an effective partner to experimentation in recent years. One example of this partnership is the NVH^- defect where theoretical calculations accurately predicted the motional averaging observed in EPR [2, 3]. Another example is the prediction of the silicon split-vacancy and approximate spin Hamiltonian parameters which preceded its subsequent experimental observation [4, 5]. In light of these agreements, it is difficult not to accept the theoretically proposed V_2H^- model [2] for the defect observed by Glover *et al.* [1]. However, the model leaves unanswered questions, specifically, why is the V_1H^- defect not observed? And how would V_2H^- form?

The VH^- defect, or certainly the VH^0 defect would be expected to be observed by EPR. It is likely that VH^- would have $S = 1$ and be EPR-active, and VH^0, would have $S = \frac{1}{2}$, also being EPR-active. It might be that the latter is hidden by any N_S^0 signal in the $g \approx 2.00$ region.

In as-grown CVD diamond, isolated vacancies are not observed, although many vacancy-related defects are. It appears that when a vacancy is 'grown-in' it is decorated with an impurity atom (e.g. hydrogen) which stabilises it. Alternatively, if a vacancy is grown-in it may migrate at the growth temperature to a trap. How a V_2H^- defect might be grown-in as a unit is not clear, but would require

a vacancy which contains a carbon-hydrogen unit on the growth surface which would somehow inhibit continued growth resulting in an additional vacancy and forming the V_2H^- defect. An alternative formation mechanism is that the VH^- defect grows in and captures an additional vacancy. However, where this vacancy would come from, if vacancies can be trapped by any impurity is an issue for this formation model. It is also possible that VH is mobile at growth temperatures and two of them combine. However, it is questionable why V_2H^- would form in preference to V_2H_2.

These discussions highlight remaining challenges for the V_2H model, but do not suggest that its formation is impossible. For this reason, the defect is referred to in this Thesis as the V_nH^- defect, with an unspecified number of vacancies 'n'.

To the author's knowledge no ^{13}C hyperfine parameters have previously been reported for the V_nH^- defect. Any differences between the observed hyperfine interactions when compared to the OV^0 (WAR5 - see Chapter 9) and NV^- [6, 7] defects may provide further evidence to support or refute the VH^- or V_2H^- models.

10.2 Results

The experimental procedures were identical to those outlined in Chapter 9. The V_nH^- signal strength from Sample J was sufficient to distinguish three sets of ^{13}C satellites.

The V_nH^- ^{13}C neighbours are labelled 'a', 'g' and 'x', in keeping with the labelling nomenclature used elsewhere [8]. (The label x has been used where the ^{13}C neighbours responsible are unclear.) The spin Hamiltonian parameters given in Table 10-1 were determined by fitting the predicted EPR transition fields to experimental full and half-field EPR spectra, simulations are shown in Figure 10-1. The hyperfine interaction (A) for the ^{13}C satellites labelled 'a' ($^{13}C_a$) is close to axial, the unique direction being close to a $\langle 111 \rangle$ crystallographic direction, (not the same $\langle 111 \rangle$ crystallographic direction as the symmetry axis of the electronic Zeeman (g) and zero field splitting (D) interactions, see Table 9-2). Deviation of the hyperfine interaction from axial symmetry results in additional splitting, beyond that due to the hydrogen hyperfine interaction, of the transitions when the

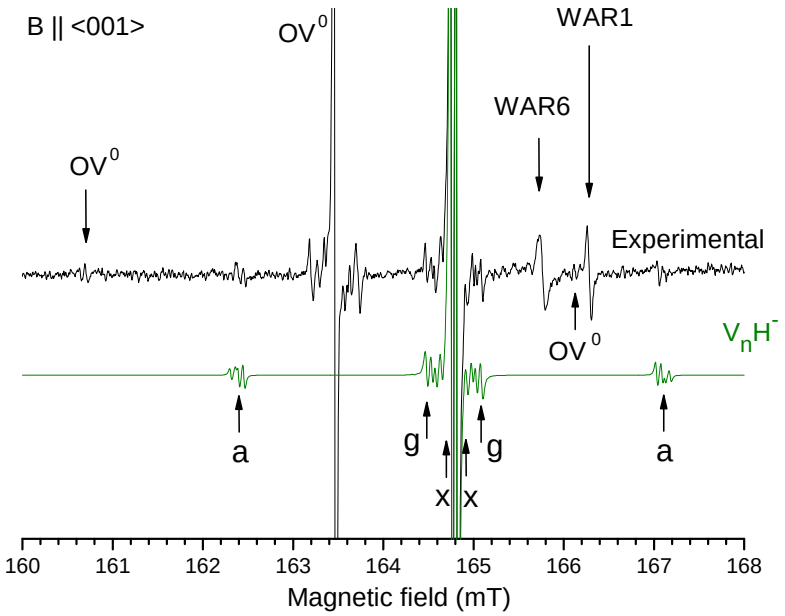

(a)

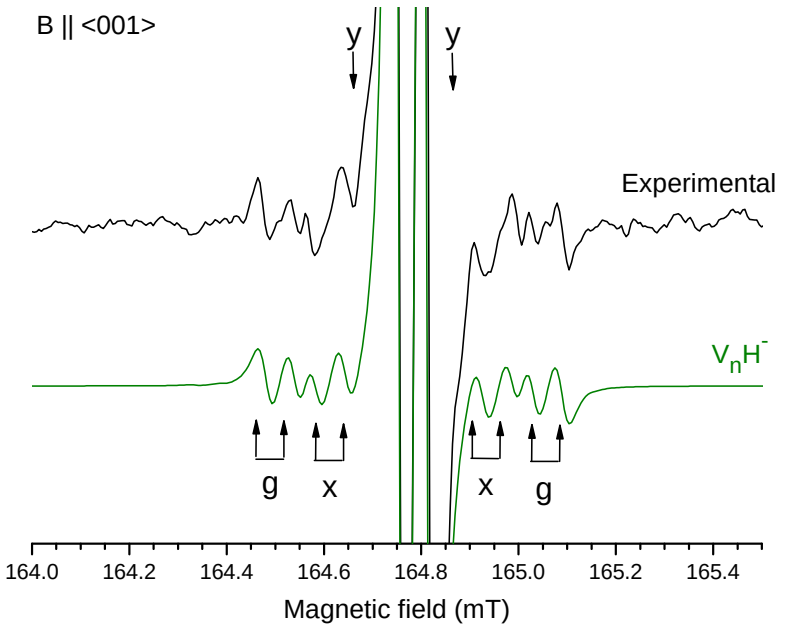

(b)

Figure 10-1: Experimental and simulated half-field spectra of the V_nH^- defect from Sample J. The magnetic field is applied parallel to a ⟨001⟩ crystallographic direction. (a) shows a wide field scan range, and (b) the region around 164.8 mT. The simulated spectra are produced using the spin Hamiltonian parameters given in Tables 9-2, 9-3 and 10-1. ^{13}C satellites are labelled 'a', 'g' and 'x' (see text) consistent with Figure 10-2. Small shoulders to the main line have not been fitted but are labelled 'y'.

external magnetic field is aligned parallel to the [001] crystallographic direction (see Figure 10-1). The remaining hyperfine interactions for the ^{13}C satellites 'g' and 'x', are constrained to be axially symmetric, again about a ⟨111⟩ crystallographic direction, which is not parallel to the C_{3v} symmetry axis of the defect. Removal of this constraint does not improve the quality of the fit.

Comparing the intensities of the ^{13}C satellites to the appropriate central ^{12}C transition, it is found that the 'a' satellites arise from 3.4(10) (three or four) equivalent ^{13}C neighbours. The 'g' and 'x' satellites result from 5.5(5) (five or six) and 7(2) (between five and nine) equivalent neighbours respectively, see Table 10-1.

Additional shoulders on the main line are observed, labelled 'y' on Figure 10-1(b). Any satellites with smaller hyperfine interactions are not observed and considered buried underneath the main ^{12}C transition.

10.3 Discussion

The V_nH^- ^{13}C structure is discussed using the models and labels given in Figures 10-2. The outermost ^{13}C hyperfine satellites, shown in Figure 10.1(a) have been shown to be a result of three or four equivalent carbon neighbours. Assuming three equivalent carbon neighbours (which fits with the C_{3v} symmetry), this interaction can be interpreted in the usual way to show that ~80% of the unpaired electron probability density is localised on these carbon neighbours. As with the NV^- [6, 7] and OV^0 (Chapter 9) models, the three carbon neighbours labelled C_a in Figure 10-2 are suggested to be responsible for these carbon satellites. This is consistent with the prediction of both VH^- and V_2H^- models.

The $^{13}C_a$ satellite transitions are split in addition to the hydrogen hyperfine splitting. As was observed for the OV^0 defect (Chapter 9) this suggests there is distortion of the 'a' atoms towards the (111) plane, which is perpendicular to the carbon-hydrogen bond (in the VH^- model).

The majority of the remaining unpaired electron probability density for OV^0, NV^- and V_nH^- defects is localised on a set of six equivalent carbon neighbours. For NV^- the predictions from DFT [6] have led to the assignment of this set of

Table 10-1: V_nH^- ^{13}C hyperfine parameters. θ is the angle from the crystallographic [001] direction and φ is the angle from [100] measured towards [010] in the (100) plane. The ^{13}C label refers to those atoms indicated in Figures 10-2, and [Z] designates the number of equivalent carbons from this assignment. $\mathbf{N}_{eqC}$ is the experimentally determined number of equivalent carbon atoms. η^2 is the unpaired electron probability density (on one of the equivalent carbon atoms) calculated from the hyperfine constants in the usual way [9].

^{13}C label	[Z]	$\mathbf{N}_{eqC}$	$\mathbf{A_1}(A_\parallel)$ **(MHz)**	θ / °	φ / °	$\mathbf{A_2}$ **(MHz)**	θ / °	φ / °	$\mathbf{A_3}$ **(MHz)**	θ / °	φ / °	$Z\eta^2$
a(ii)	3	3.4(10)	175.8(4)	52.91(6)	225	96.8(4)	142.9(7)	225	96.9(4)	90	135	~0.83
g	6	5.0(5)	18.40(5)	54.7(2)	225	12.96(7)	144.74	225	12.96(7)	90	135	~0.13
x	6	6.6(19)	14.5(1)	54.73	225	5.8(1)	144.74	225	5.8(1)	90	135	~0.02

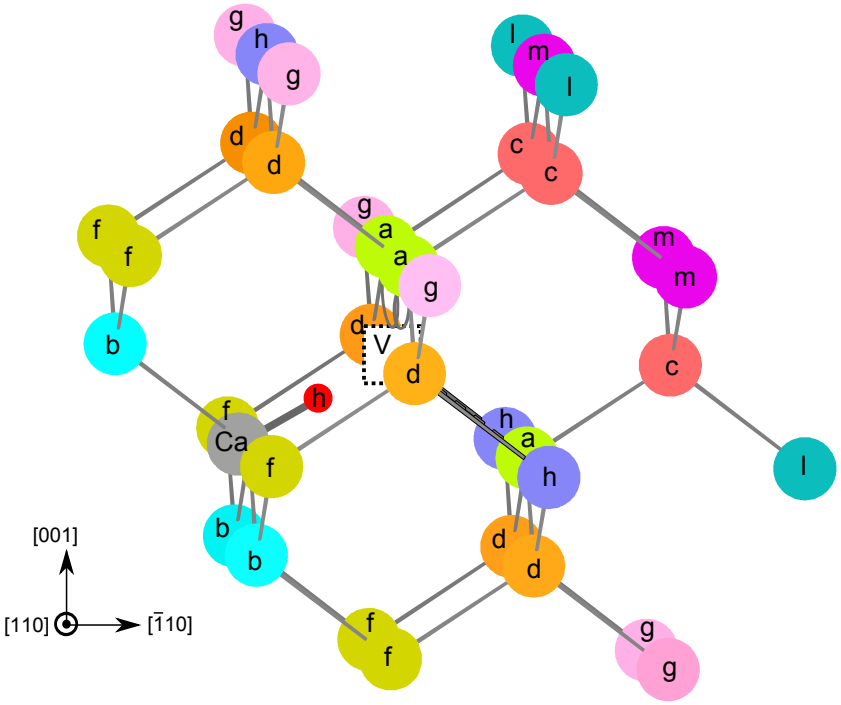

(a)

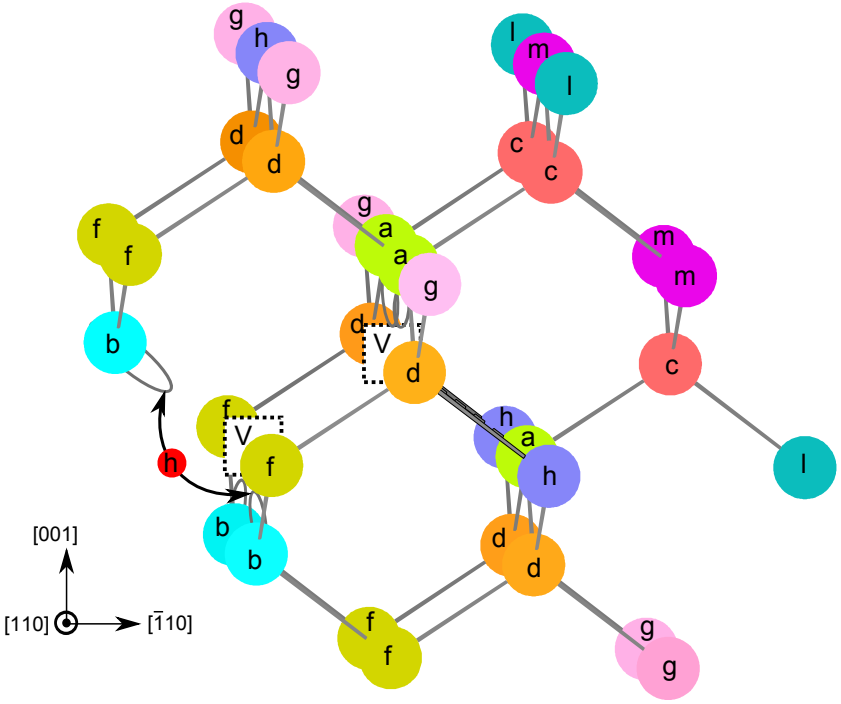

(b)

Figure 10-2: Cartoon depictions the (a) VH^- and (b) V_2H^- defects in diamond and the surrounding carbon lattice. The image is projected close to the $(1\bar{1}0)$ plane. Equivalent carbon atoms are colour coded and labelled consistently with [7] and Table 10-1. The vacancies are shown by broken white squares. Figure (a) represents the single vacancy model with a static carbon-hydrogen configuration oriented parallel to the [111] crystallographic orientation and a single vacancy. The unique carbon is labelled Ca. Figure (b) represents the di-vacancy model where the hydrogen atom is tunnelling around three C_b-hydrogen configurations.

six carbon neighbours to those atoms labelled 'g' in Figure 10-2. An identical assignment was made for the OV^0 defect (see Chapter 9). For the VH^- model (and possibly the V_2H^- model) the same assignment would seem appropriate (see Figure 10-2).

For the V_nH^- defect the third largest ^{13}C hyperfine splitting originates from a set of six equivalent carbons, whereas for the NV^- and OV^0 defects this splitting originates from a set of three equivalent carbon atoms. Unfortunately, for both the VH^- and V_2H^- model structures there are several sets of six equivalent carbon neighbours that could plausibly be assigned to explain the observed, small localisation of unpaired electron probability density of the measured satellites (e.g. sets 'd', 'f' and 'h'). Therefore, we cannot, on the basis of the measured ^{13}C splittings distinguish between the VH^- and V_2H^- models.

Given the available signal to noise ratio and the imperfect quality of the fit it is possible that another set of ^{13}C satellites is present. It is possible that from an additional ^{13}C satellite one of the hyperfine split lines is superimposed with the innermost line assigned to the satellite 'x'. The second line from this additional ^{13}C satellite could be assigned to the shoulder labelled 'y' on the main line, (see Figure 10-1). However, given the signal to noise ratio the best fit still appears to be consistent with two sets of six equivalent carbon atoms, giving rise to the 'g' and 'x' ^{13}C satellites.

10.4 Conclusion and further work

The observation of three sets of ^{13}C neighbours for the V_nH^- defect arising from three, six and six equivalent carbon neighbours has not permitted either of the VH^- or V_2H^- models to be ruled out. However, this work has provided valuable information which will allow for future theoretical comparison of the localisation of the unpaired electron probability in the VH^- and V_2H^- structures.

References

[1] C. Glover, M. E. Newton, P. M. Martineau, S. Quinn, and D. J. Twitchen, Phys. Rev. Lett. **92**, 135502 (2004).

[2] M. J. Shaw, P. R. Briddon, J. P. Goss, M. J. Rayson, A. Kerridge, A. H. Harker, and A. M. Stoneham, Phys. Rev. Lett. **95**, 105502 (2005).

[3] A. M. Edmonds, PhD. Thesis, University of Warwick (2008).

[4] J. P. Goss, P. R. Briddon, and M. J. Shaw, Phys. Rev. B **76**, 075204 (2007).

[5] A. M. Edmonds, M. E. Newton, P. M. Martineau, D. J. Twitchen, and S. D. Williams, Phys. Rev. B **77**, 245205 (2008).

[6] A. Gali, M. Fyta, and E. Kaxiras, Phys. Rev. B **77**, 155206 (2008).

[7] S. Felton, A. M. Edmonds, M. E. Newton, P. M. Martineau, D. Fisher, D. J. Twitchen, and J. M. Baker, Phys. Rev. B **79**, 075203 (2009).

[8] S. Felton, A. M. Edmonds, M. E. Newton, P. M. Martineau, D. Fisher, and D. J. Twitchen, Phys. Rev. B **77**, 081201 (2008).

[9] J. R. Morton and K. F. Preston, J. Magn. Reson. **30**, 577 (1978).

Chapter 11

Summary

The main experimental technique used in the studies reported in this Thesis is electron paramagnetic resonance (EPR). It has been used to:

- Elucidate the structure of previously unidentified point defects in diamond.
- Study charge transfer between defects in diamond.
- Quantify the incorporation of neutrally charged single substitutional nitrogen (N_S^0) down to sub part per billion (ppb) concentration levels.

11.1 Identification and characterisation

Four previously unreported EPR-active defects have been identified in single crystal synthetic diamond; spin Hamiltonian parameters have been determined and models suggested. Two have been observed in high pressure high temperature (HPHT) and two in chemical vapour deposition (CVD) diamond.

11.1.1 Defects in nitrogen doped HPHT diamond

The detection of paramagnetic defects with $S = \frac{1}{2}$ and small Zeeman and hyperfine splittings in nitrogen doped diamond is challenging because the central EPR transition from the ubiquitous $^{14}N_S^0$ defect dominates the spectral region close to $g \approx 2.00$. Whilst removing nitrogen from the diamond synthesis source material and thus growing nitrogen free diamond removes the $^{14}N_S^0$ defect it does not facilitate the study of other nitrogen related defects. The solution to this problem is to dope the diamond exclusively with ^{15}N. The $^{15}N_S^0$ defect with $S = 1$ has no EPR transition in the $g \approx 2.00$ region, allowing the study of other possibly nitrogen related defects.

In this spectral region two new paramagnetic defects have been observed and labelled WAR9 and WAR10. It has been shown that the properties of these defects are consistent with their identification as the neutral nitrogen interstitial, N_I^0, (WAR9) and the neutral nitrogen di-interstitial, N_I–I_{001}, (WAR10). Before the studies reported here, little was known about the interaction of nitrogen with the interstitial or the self-interstitial. This is despite the combination of vacancies with nitrogen related defects being well studied. The experimental data presented here supports the proposals that N_I^0 is more stable than N_I^- and that $[N_I–I_{001}]^0$ is considerably more stable than $[I_{001}–I_{001}]^0$ the R1 defect [1].

These observations add to the description of nitrogen aggregation in diamond, which to date has largely neglected the involvement of nitrogen-interstitials.

11.1.2 Defects in diamond grown by CVD

Two new paramagnetic defects have been observed in different CVD diamond samples which were produced using different growth conditions and chemistries. The first defect, labelled WAR2, has been observed in tens of homoepitaxial CVD diamond samples produced in three different laboratories. The WAR2 defect is preferentially aligned with respect to the [001] crystallographic direction. In each sample, WAR2 is observed in has been grown on (001) oriented substrates which indicates that the defect was 'grown-in' as a unit rather than being formed by the diffusion and aggregation of sub-units. The EPR spin Hamiltonian parameters show that the defect has S=$\frac{1}{2}$, a {110} mirror plane of symmetry and involves a single hydrogen atom. Based on this information and the observed preferential alignment, the $(V\text{-}(CH)\text{-}V)^0$ structure has been proposed for the WAR2 defect. Preferential alignment of other defects in (001) grown single crystal CVD diamond, observed by cathodoluminescence spectroscopy, have recently been reported [2] and should be investigated for correlations with the WAR2 defect. Further studies of WAR2, and other preferentially oriented defects are anticipated in an attempt to improve the understanding of the processes occurring on the (001) growth surface. Experiments are also planned to investigate any preferential alignment of NV^-, V_nH^- and NVH^- in CVD diamond grown on a {110} oriented substrate. From these experiments it may be possible to determine if the defects in question are

'grown-in' as a unit or formed by the diffusion of sub-units.

The second defect, labelled WAR5, has only been observed in CVD diamond samples produced using an experimental oxygen-carbon-hydrogen chemistry. It has often been speculated that oxygen is a constituent of unidentified EPR-defects, but the involvement of oxygen has only been confirmed for one defect [3]. This defect was produced by ^{17}O implantation and the involvement of an oxygen atom was confirmed by the observation of ^{17}O hyperfine structure. This is not the same defect as observed in this work. In this Thesis, a compelling case is made for the identification of WAR5 as the OV^0 defect. WAR5/OV^0 is structurally and electronically similar to the NV^- defect, [4] but spin polarisation of WAR5 has not yet been observed.

The addition of oxygen to source gases used in the CVD growth of diamond can be beneficial [5, 6]. However, if oxygen related defects are easily incorporated, this may have an affect on any potential applications of the material.

11.2 Charge transfer

The electronic properties of diamond can be adversely affected by the presence of defects which trap and scatter charge carriers. Changes in the concentration of N_S^0 with heat treatment indicates the existence of a trap(s) 0.5–1.2 eV above the top of the valence band in many CVD diamond samples. NVH^0 was identified as one of these traps, and through combined EPR and infra-red absorption studies, it was shown that the 3123 cm^{-1} absorption line originates from the NVH^0 defect. Other traps may include vacancy clusters, but more work is required to confirm the nature of the electronic traps in CVD diamond.

11.3 Sub ppb EPR detection of N_S^0

For electronic grade intrinsic CVD diamond, defect concentrations maybe below a single part per billion. Quantitative detection of paramagnetic defects in diamond at such low concentrations is a challenge for conventional continuous wave EPR. Hence, the rapid passage (RP) EPR technique has been investigated in an attempt

reduce the detection limit for N_S^0 in diamond. It has been shown that with RP-EPR it is possible to detect concentrations of N_S^0 at tens of parts per trillion, this is close to a factor of 100 improvement on standard slow passage EPR. RP-EPR is thus a suitable complementary technique to photoluminescence with which to monitor the quality of electronic grade CVD diamond.

References

[1] D. J. Twitchen, M. E. Newton, J. M. Baker, O. D. Tucker, T. R. Anthony, and W. F. Banholzer, Phys. Rev. B **54**, 6988 (1996).

[2] D. Charles, PhD. Thesis, King's College London (2008).

[3] K. Iakoubovskii and A. Stesmans, Phys. Rev. B **66**, 045406 (2002).

[4] J. P. Goss, P. R. Briddon, M. J. Rayson, S. J. Sque, and R. Jones, Phys. Rev. B **72**, 035214 (2005).

[5] Y. Liou, A. Inspektor, R. Weimer, D. Knight, and R. Messier, J. Mater. Res. **5**, 2305 (1990).

[6] S. Kapoor, M. A. Kelly, and S. B. Hagstrom, J. Appl. Phys. **77**, 6267 (1995).

Appendix A

Samples

Table A-1: Table of sample used in this work, see relevant chapter for defect concentrations. Mass is given to the nearest mg and the diamond type as synthetic CVD or HPHT.

Code	Mass (mg)	Supplier	Type	Relevant Chapter
A	48	DTC / E6	SC-CVD	7,6,5
B	14	IMOMEC	SC-CVD	7
C	36	DTC / E6	SC-CVD	7,6
D	9	LIMHP	SC-CVD	7
E	80	DTC / E6	SC-CVD	7
F	146	DTC / E6	SC-CVD	7
G	52	DTC / E6	SC-CVD	7
H	70	DTC / E6	SC-CVD	7,6
I	40	DTC / E6	SC-CVD	6,9
J	43	DTC / E6	SC-CVD	6,9
K	64	DTC / E6	SC-CVD	6
L	63	DTC / E6	SC-CVD	6
M	51	Apollo	SC-CVD	6
N	64	DTC / E6	SC-HPHT	6
P	14	DTC / E6	SC-HPHT	8
Q	80	DTC / E6	SC-CVD	5
R	88	DTC / E6	SC-CVD	5
S	56	E6	SC-CVD	5
T	57	E6	SC-CVD	5
U	53	E6	SC-CVD	5
V	51	E6	SC-CVD	5
W	35	Apollo	SC-CVD	5
X	64	DTC / E6	SC-CVD	5
Y	52	Apollo	SC-CVD	5
Z	59	Apollo	SC-CVD	5
α	64	Apollo	SC-CVD	5
β	81	Apollo	SC-CVD	5
γ	47	Apollo	SC-CVD	5
δ	38	DTC / E6	SC-CVD	9